# AGN at low and high redshifts:

*physical properties and co-evolution of galaxies and black holes*

By

MURILO MARINELLO

Coordenação de Astronomia e Astrofísica
OBSERVATÓRIO NACIONAL

A Thesis submitted to the Observatório Nacional in
accordance with the requirements of the degree of
DOCTOR IN ASTRONOMY.

FEBRUARY 2019

# Resumo

Núcleos ativos de galáxia (AGN) são os objetos astronomicos mais luminosos do no céu. Diferentes das galáxias normais, AGN são caracterizados por um núcleo extremamente brilhante o qual não pode ser associado com estrelas. Neste trabalho é estudado AGN em baixo e alto redshift. AGN em baixo são usadas com o objetivo de estudar em detalhes as propriedades físicas da região emissora de linhas largas (BLR), em particular a emissão de Fe II. Em alto redshift é apresentado a descoberta de uma nova e mais distante rádio galaxia conhecida, alem disso, quasares em alto redshift são usados com o intuito de estudar seus buracos negros super massivos (SMBH) e como eles crescem.

A tese começa com o estudo de galáxias Seyfert e quasares em baixo redshift a fim de analisar a BLR. O foco primário deste capítulo é usar espectros no infravermelho próximo (NIR) para estudar a emissão de Fe II e seu papel na BLR. Para analisar e emissão de Fe II em AGN é apresentado uma amostra de 25 AGN observado no NIR com SpeX no *Infrared Telescope Facility* (IRTF). A emissão de Fe II nestes AGN foi modelada usando o único template de Fe II disponível no NIR. Este template foi testado na amostra. Os resultados obtidos mostram que o template de Fe II no NIR modela bem a emissão em AGN, independentemente de sua luminosidade ou intensidade de Fe II. Foi detectado um excesso de Fe II em 9200 Å em todos os espectros da amostra, como predito pelos modelos teóricos de Fe II. Este resultado confirma fluorescência de Ly$\alpha$ como um mecanismo de excitação na produção da emissão de Fe II. A emissão de Fe II no NIR foi caracterizado através do excesso em 9200 Å e das linhas de 1 $\mu$m e foi encontrada uma forte correlação entre estas quantidades e a emissão óptica de Fe II, o que mostra que fluorescência de Ly$\alpha$ tem um papel importante na produção de Fe II. Foi estimado um limite inferior para a contribuição deste mecanismo de 18% na produção de Fe II óptico. A analise dos pefis das linhas de Fe II$\lambda$10502, O I$\lambda$11287, Ca II$\lambda$8664 e Pa$\beta$ mostram que as três primeiras possuem larguras similares. Em contra partida, Fe II é sistemáticamente mais estreita, por um fator 0.7, do que Pa$\beta$. Assumindo que as nuvens emissoras são virializadas, este resultado implica que o Fe II é formado em uma região duas vezes mais distante que Pa$\beta$, que pode variar entre 8.5 e 198.2 anos-luz. Este resultado é importante para colocar vínculos em modelos de fotoionização futuros que estudarão a emissão de Fe II.

O segundo resultado apresentado nesta tese é a descoberta de uma nova rádio galáxia, TGSS J1530+1049, em $z = 5.72$, a qual é a rádio galáxia mais distante já descoberta desde TN J0924-2201 em $z = 5.19$ em 1999. Esta galáxia foi descoberta através de observações específicas de galáxias com espectro ultra inclinados selecionadas em 150 MHz. A análise deste índice espectral entre 150 MHz e 1.4 GHz mostrou um $\alpha_{1.4\mathrm{GHz}}^{150\mathrm{MHz}} = -1.4$, e imageamento com em 1.4 GHz mostrou uma estrutura compacta e não resolvida espacialmente. A espectroscopia foi realizada com o telescópio GEMINI usando o *GEMINI Multi-Object Spectrograph* (GMOS) e revelou a presença de uma única linha de emissão observada em $\lambda = 8170$ Å. O perfil assimétrico da linha, a ausência de outras linhas na região do óptico, e alta largura equivalente levou a conclusão

de que esta linha é Ly$\alpha$, em $z = 5.72$. Foi medido uma luminosidade de $5.7 \times 10^{42}\,\mathrm{erg\,s^{-1}}$, uma FWHM de $370\,\mathrm{km\,s^{-1}}$, uma extensão espacial de 3.5 Kpc, e uma luminosidade em rádio de $L_{150\mathrm{Mhz}} = 29.1\mathrm{W\,Hz^{-1}}$. Apesar da luminosidade da linha e FWHM serem comparáveis à aquelas de galáxias emissoras de Ly$\alpha$ rádio silenciosas, o tamanho e a luminosidade em rádio são comuns em outras rádio galáxias em $z > 4$. Imagemento no NIR em $J$ e $K$ com o *Large Binocular Telescope* (LBT) usando *LBT Utility with CAM and Integral FIELD* (LUCI) não detectou a galáxia hospedeira a um limite de $3\sigma$ de $J > 24.4$ e $K > 22.4$mag. Estes limites são consistentes com aqueles esperados para uma rádio galáxia em $z > 5$, e em acordo com a relação $K - z$ para rádio galáxias. Foi estimado um limite para a massa estelar usando modelos de população estelar e encontrou-se $M_{stars} < 10^{10.5}\mathrm{M}_{\odot}$, o que sugere que a rádio galáxia está em uma fase ainda jovem de sua evolução.

O terceiro resultado principal desta tese é relacionado a quasares em alto redshift e seus SMBH. Foi usado uma amostra de 35 quasares radio-altos em alto redshift ($2.2 < z < 3.5$) selecionados do levantamento *Clusters Around Radio Loud AGN* (CARLA) e observados com *Very Large Telescope* (VLT) usando *Spectrograph for INtegral Field Observations in the Near Infrared* (SINFONI). Foi usado a linha de H$\alpha$ para se estimar massas de BH precisas e compara-las com resultados anteriores usando C IV. Os resultados mostram que o espalhamento estre estes dois métodos é de 0.27 dex. Foi encontrado que a taxa de Eddington se correlaciona fortemente com H$\alpha$ e $\mathrm{L}_{5100}$ mas apenas moderadamente com $\mathrm{M}_{\mathrm{BH}}$. Por outro lado, foi encontrado que a potência de rádio não se correlaciona com os principais observáveis. Foi etimado a taxa de crescimento dos BH da amostra e encontrou-se uma média abaixo da idade cósmica no redshift dos quasares, no entanto uma porção significante deles possuem idades maiores que esta. Os resultados sugerem que as massas destes BH experienciaram um crescimento próximo ao limite de Eddington no passado, seguido por uma fase de acrescimo reduzido com o $\mathrm{L/L}_{\mathrm{Edd}}$ medido em $z \sim 2$. Este capítulo é concluído revisitando a correlação entre $\mathrm{M}_{\mathrm{BH}}$ e o ambiente medido pelo levantamento CARLA e os resultados são discutidos no contexto do relação M–$\sigma$ observada localmente.

## Abstract

Active galactic nuclei (AGN) are the most luminous astronomical objects in the sky. Different from normal galaxies, AGN are characterized by a strong luminous nucleus which can not be associated with its stars. In this work we study AGN at low and high redshift. We use low redshift AGN in order to study in detail the physical properties of the broad line region (BLR), in particular its Fe II emission. Moving to the high redshift universe we present a new discovery of the most distant radio galaxy known and we use high redshift quasars in order to study their central supermassive black holes (SMBH) and how they grow.

We start this thesis by studying low redshift Seyfert galaxies and quasars to probe their broad line region (BLR). Our primary focus here is to use near-infrared (NIR) spectra to study the Fe II emission and its role in the BLR. In order to analyse Fe II emission in AGN we present a sample of 25 AGN observed with the SpeX at the *Infrared Telescope Facility* (IRTF) in the NIR. We modeled the Fe II emission in these AGN using the only NIR template available. We tested the NIR Fe II template for our entire sample. The results obtained show that the NIR Fe II template successfully reproduces the NIR Fe II emission in AGN, independent of their luminosity and Fe II intensity. We detected the Fe II bump at 9200 Å in all spectra of our sample, as predicted by theoretical models. This result confirms Ly$\alpha$-fluorescence as one of the excitation mechanisms responsible for the production of the Fe II emission. We analysed the Fe II emission in the NIR through the 9200 Å bump and the 1 $\mu$m lines and find a strong correlation between these features and the optical Fe II emission, proving that Ly$\alpha$-fluorescence plays an important role in the Fe II production. We estimate an inferior limit of 18% for the contribution of this mechanism to the production of the optical Fe II emisison. The analysis of the line profiles of the Fe II$\lambda$10502, O I$\lambda$11287, Ca II$\lambda$8664 and Pa$\beta$ lines shows that the first three ones have similar widths. On the other hand, Fe II is systematically narrower by a factor of 0.7 than Pa$\beta$. Assuming the emitting clouds are virialized, this result implies that the Fe II is formed in a region that is twice more distant than Pa$\beta$, ranging 8.5 to 198.2 light-days. This is important for constraining future photoionization models aimed to study the Fe II emission.

The second main result of this thesis is the discovery of a new radio galaxy, TGSS J1530+1049, at $z = 5.72$ which is the most distant radio galaxy to be discovered since TN J0924-2201 at $z = 5.2$ in 1999. This galaxy was discovered through the follow up of ultra-steep spectrum galaxies selected at 150 MHz. The analysis of the spectral index at 150Mhz and 1.4GHz shows an $\alpha_{1.4\mathrm{GHz}}^{150\mathrm{MHz}} = -1.4$, and images with the *Very Large Array* (VLA) at 1.4 GHz show an unresolved compact structure. The spectroscopic follow up was carried out with the GEMINI telescope using the *GEMINI Multi-Object Spectrograph* (GMOS) and revealed the presence of a single emission line at the observed wavelength of $\lambda = 8165$ Å. The asymmetric shape of the line, absence of other optical lines, and high equivalent width lead us to conclude that this line is Lyman-alpha, at $z = 5.72$. We measured a line luminosity of $5.7 \times 10^{42}$ erg s$^{-1}$, a FWHM of 370 km s$^{-1}$, a deconvolved physical extent of 3.5 kpc, and a radio luminosity of $L_{150\mathrm{Mhz}} = 29.1$W Hz$^{-1}$. Although the line

luminosity and full width at half maximum (FWHM) are comparable to those of other non-radio Lyman alpha galaxies the size and radio luminosity are common to those of other $z > 4$ radio galaxies. NIR imaging in $J$ and $K$ with *Large Binocular Telescope* (LBT) using *LBT Utility with CAM and Integral FIELD* (LUCI) did not detect the host galaxy at the $3\sigma$ detection limit of $J > 24.4$ and $K > 22.4$mag. These limits are consistent with those expected for a radio galaxy at $z > 5$ in accordance with the radio galaxy $K - z$ relation. We estimate the stellar mass limit using simple stellar population models finding $M_{stars} < 10^{10.5} \mathrm{M}_{\odot}$, which suggests a radio galaxy in an early phase of evolution.

The third maing result of this thesis relates to high redshift quasars and their supermassive black holes (SMBH). We used a sample of 35 high redshift radio loud quasars ($2.2 < z < 3.5$) from the *Clusters Around Radio Loud AGN* (CARLA) survey observed with the *Very Large Telescope* (VLT) using the *Spectrograph for INtegral Field Observations in the Near Infrared* (SINFONI). We used the H$\alpha$ line for accurate estimates of the BH masses and compare with previous results using C IV. Our results show a reduced scatter of 0.27 dex of C IV compared to H$\alpha$. We found that the Eddington ratio strongly correlates with H$\alpha$ and $\mathrm{L}_{5100}$ and only moderately with $\mathrm{M}_{\mathrm{BH}}$. On the other hand, the radio power does not correlate with the main observables. We estimate the growth time of the BH and found a median below the cosmic age at the redshift of the quasars, but with a significantly fraction of them having longer times. Our results suggest that the BH mass of these quasars experienced a near-Eddington growth in the past, followed by a slower accretion phase at the measured $\mathrm{L}/\mathrm{L}_{\mathrm{Edd}}$ until $z \sim 2$. We finish this chapter revisiting the correlation between the $\mathrm{M}_{\mathrm{BH}}$ and environment as measured by the CARLA survey and discuss our results in the context of the local M–$\sigma$ relation.

## Dedication and acknowledgements

I am thankful to everyone that helped to make this work possible, especially:

- To my mother, Mari Marinello, and my sister, Ana Marinello, for always believing in my work;
- To my PhD supervisor, Roderik Overzier, for the excellent job supervising and guiding me during these past four years;
- To my friends from Rio and the Apartment 301: Hélio Perottoni, Mauricio Thiel, Gustavo Rossi, Mario De Prá, Diogo Souto, Yuri, Gabriela Antunes, Carmen Ayala, Mathias Garcia, for all the good moments and patience with me during the PhD;
- To Huub Röttgering, for hosting me during my trip to the Netherlands;
- To Aayush Saxena, for the friendship and collaboration;
- To Gemma Gill, Ben Pepper and Hisakazu Uchiyama, for the friendship, funny moments in Rio and collaboration;
- To Lieke Van Son, for the friendship and the good moments in Rio and Leiden;
- To Alberto Ardila, for all these years of collaboration and guidance;
- To Rodrigo Lorencini and Patricia Lorencini, for the all the help and friendship in the past 12 years;
- To my climbing partners, Cassius Palauro, Adrimara Radim, Felipe Orlando, Bruno, Pedro, and Alexandre Magalhães, for all the mountains climbed and good moments;
- To all my professors at UNIFEI, for providing all the knowledge that brought me here;
- To all my friends from Ouro Fino, especially the VACAS, for the good moments and support;
- To all my brothers from Republica Lahma, for the good moments during my visits to Itajubá;
- To all staff members from Observatório Nacional, for working hard to make it a good work place;
- To CAPES for providing the funding to complete this project.

To all of you, Thanks.

# TABLE OF CONTENTS

**Page**

**List of Tables** **ix**

**List of Figures** **xi**

**1 Introduction** **1**
1.1 AGN: A Historical perspective . . . . . 1
1.2 AGN in a nutshell . . . . . 3
1.3 The Unified Model of AGN . . . . . 5
1.4 The inner region of the AGN . . . . . 7
1.4.1 The Black Hole Paradigm . . . . . 8
1.4.2 The Fe II Emission in AGN . . . . . 15
1.5 High Redshift Radio Galaxies . . . . . 18
1.6 In This Thesis . . . . . 20

**2 The Fe II Emission in Active Galactic Nuclei: Excitation Mechanisms and Location of the Emitting Region** **23**
2.1 Introduction . . . . . 24
2.2 Observations and Data Reduction . . . . . 26
2.2.1 Near-infrared Data . . . . . 28
2.2.2 Optical and Ultraviolet Data . . . . . 28
2.3 Analysis Procedure . . . . . 31
2.3.1 NIR Fe II Template Fitting . . . . . 31
2.3.2 Emission-line Fluxes of the BLR in the NIR . . . . . 39
2.4 Fe II Excitation Mechanism: Lyman-$\alpha$ fluorescence and Collisional Excitation . . . 42
2.5 Location of the Fe II Emission Line Region . . . . . 51
2.6 Final Remarks . . . . . 58

**3 Discovery of a radio galaxy at z = 5.72** **61**
3.1 Introduction . . . . . 62
3.2 Source Selection . . . . . 64

3.3 Observations . . . 66
3.3.1 Gemini GMOS spectroscopy . . . 66
3.3.2 Large Binocular Telescope NIR imaging . . . 67
3.4 Redshift Determination . . . 69
3.4.1 Skewness and equivalent width . . . 71
3.4.2 K-z relation for radio galaxies . . . 72
3.5 Discussion . . . 73
3.5.1 Emission Line Measurements . . . 73
3.5.2 Radio Properties . . . 74
3.5.3 Stellar mass limits . . . 76
3.6 Conclusions . . . 78

**4 A VLT/SINFONI study of black hole growth in high redshift radio-loud quasars from the CARLA survey 81**
4.1 Introduction . . . 82
4.2 Observations and data reduction . . . 85
4.3 Analysis . . . 89
4.3.1 H$\alpha$ Line Fitting . . . 89
4.3.2 C IV Line Fitting . . . 89
4.3.3 Monochromatic Luminosity . . . 91
4.4 Results . . . 97
4.4.1 Black hole masses . . . 97
4.4.2 Eddington Ratio . . . 101
4.4.3 Growth Time . . . 103
4.4.4 Black holes and radio power . . . 108
4.5 Discussion . . . 108
4.5.1 Black hole mass determinations based on C IV and H$\alpha$ . . . 108
4.5.2 The growth history of CARLA quasars . . . 111
4.5.3 Does black hole mass correlate with environment? . . . 114
4.6 Conclusions . . . 116
4.7 Additional Figures: Sample Spectra . . . 117

**5 Conclusions 125**

**A Appendix: Publication List 129**

**Bibliography 131**

# List of Tables


**Table** **Page**

2.1 Basic Information on the IRTF Observations. . . . . 27
2.2 Optical and UV data obtained from the literature. . . . . 29
2.3 Measurements of the most relevant BLR features used in this work. . . . . 38
2.4 Values of the parameters used to convolve the NIR Fe II template. . . . . 40
2.5 Fluxes of the 1$\mu$m Fe II lines measured with the template. . . . . 41
2.6 Fluxes for the Fe II+Pa9 Bump at $\lambda$9200. . . . . 42
2.7 Fluxes for the optical Fe II and H$\beta$. . . . . 47
2.8 Number of photons for the Fe II emission. . . . . 49
2.9 Distance of the H$\beta$ and Fe II Emission Line Regions . . . . . 58

3.1 Observation log. . . . . 69
3.2 Spectroscopic results from Gemini/GMOS . . . . . 72
3.3 Ly$\alpha$ properties of TGSS J1530+1049 and other $z > 4$ galaxies . . . . . 73
3.4 Radio properties of TGSS J1530+1049 and other HzRG . . . . . 74

4.1 Sample Information. . . . . 88
4.2 Results of the H$\alpha$ and C IV line fitting. . . . . 96
4.3 Peak ratio and UV and optical continuum luminosities. . . . . 98
4.4 Black Hole masses, Eddington ratios and growth times. . . . . 107

# List of Figures


**Figure** **Page**

1.1 Example of a Seyfert galaxy and a quasar . . . . . 2
1.2 Example of AGN and normal galaxy SEDs . . . . . 3
1.3 The spectral differences of AGN . . . . . 4
1.4 Sketch of the unified model for AGN . . . . . 7
1.5 Reverberation mapping technique. . . . . 9
1.6 Continuum-BLR variability correspondence. . . . . 10
1.7 $R_{\rm BLR}$–$L$ for AGN. . . . . 11
1.8 FWHM correlations. . . . . 13
1.9 Fe II emission in the I Zw 001 spectrum. . . . . 17
1.10 $K-z$-diagram for radio galaxies. . . . . 19

2.1 Example of continuum subtraction . . . . . 30
2.2 Convolution of the NIR Fe II template . . . . . 34
2.3 Continuation of Figure 2.2 . . . . . 35
2.4 Continuation of Figure 2.2 . . . . . 36
2.5 Continuation of Figure 2.2 . . . . . 37
2.6 Example of line fitting . . . . . 43
2.7 Partial Gothrian diagram for Fe II . . . . . 44
2.8 Convolution of the optical Fe II template . . . . . 45
2.9 Correlation between $R_{1\mu m}$ and $R_{4570}$. . . . . 48
2.10 Correlation between $R_{1\mu m}$ and $R_{9200}$. . . . . 50
2.11 Correlation between $R_{9200}$ and $R_{4570}$. . . . . 50
2.12 Correlation between the FWHM of Fe II and the FWHM of O I. . . . . 52
2.13 Comparison between the broad line profiles . . . . . 53
2.14 Continuation of Figure 2.13 . . . . . 54
2.15 Continuation of Figure 2.13 . . . . . 55
2.16 Continuation of Figure 2.13 . . . . . 56
2.17 Correlation between the FWHM of Fe II and the FWHM of Ca II . . . . . 57
2.18 Correlation between the FWHM of Fe II and the FWHM of Pa$\beta$ . . . . . 57

3.1 The location of TGSS J1530+1049 in the flux density–spectral index parameter space 65
3.2 Stacked *y, J, H* and *K* image of TGSS J1530+1049 . . . . . 66
3.3 Gemini individual exposures of TGSS J1530+1049 . . . . . 68
3.4 Observed spectrum of TGSS J1530+1049 . . . . . 69
3.5 LBT *K*-band image of TGSS J1530+1049 . . . . . 70
3.6 Ly$\alpha$ profile and best-fit . . . . . 71
3.7 The '$K-z$' diagram for radio galaxies . . . . . 77

4.1 Sample parameters distribution . . . . . 87
4.2 Line fitting example. . . . . 90
4.3 FWHM of C IV and H$\alpha$ . . . . . 91
4.4 Predicted versus observed flux at 5100 Å. . . . . 93
4.5 Examples of SED fitting . . . . . 94
4.6 Optical versus UV rest-frame luminosities . . . . . 95
4.7 Black hole masses estimated using H$\alpha$ and C IV. . . . . 99
4.8 Rehabilitation methods for C IV-based $M_{BH}$ estimates. . . . . 100
4.9 Distribution of $L/L_{Edd}$ for the quasars. . . . . 102
4.10 Quasar properties as function of Eddington ratio. . . . . 104
4.11 Distribution of the quasar growth times. . . . . 105
4.12 Quasar properties as function of the growth time. . . . . 106
4.13 Radio power versus other quasar properties . . . . . 109
4.14 Blueshift of C IV as a function of the Eddington ratio. . . . . 110
4.15 Black hole masses and possible evolutionary tracks . . . . . 112
4.16 Galaxy surface density . . . . . 114
4.17 H$\alpha$ fit for the entire CARLA sample . . . . . 118
4.18 Continuation of Figure 4.17 . . . . . 119
4.19 Continuation of Figure 4.17 . . . . . 120
4.20 C IV fit for the entire CARLA sample . . . . . 121
4.21 Continuation of Figure 4.20 . . . . . 122
4.22 Continuation of Figure 4.20 . . . . . 123

CHAPTER 1

# INTRODUCTION

Peterson (1997) in his seminal text book defines an active galactic nucleus (AGN) as *"Extraordinary energetic phenomenon in the center region of some galaxies, which can not be attributed exclusively to their stellar contents"*. The enormous amount of energy (with typical values of $10^{46}$–$10^{47}$ erg s$^{-1}$, when integrated within $10^{10}$–$10^{25}$ Hz) is emitted in a very compact region (<< 1 pc). These galaxies are divided in several sub-groups or families regarding their physical and observational characteristics. As we will see in this chapter, AGN can take the form of type–1 (emitting both narrow and broad lines) or type–2 (exclusively narrow lines that are visible). Type–1 AGN are most commonly seen as Seyfert galaxies and quasars, with the main difference related to the amount of energy emitted in the optical spectral region (3800 Å–7000 Å) by their nuclei. While the luminosity of Seyfert galaxies is of the same order of magnitude as the host galaxies themselves, quasars emit energy that can exceed the host galaxy by a factor of 100-1000. In high redshift AGN only a point source is usually observed, since the starlight is obfuscated by the brightness of the nucleus. Figure 1.1 shows an example of a Seyfert galaxy and a quasar. In this chapter, a general overview of the AGN and their physical structure is presented. Starting from their discovery and going through their physical structure, we present the main components, their subtypes, and the open questions that we intend to adress in this study.

## 1.1 AGN: A Historical perspective

The history of the study of AGN starts early in the 20th century. The first spectrum of an AGN was observed 110 years ago, by Edward A. Fath in 1908. In observations of "spiral nebulae" using a small spectrograph, Fath noticed six emission lines in one of his sources, NGC 1068. It was almost ten years later that Slipher, in 1917, with a better spectrograph realized that the lines observed in NCG 1068 were very similar to those observed in planetary nebulae, with one big difference

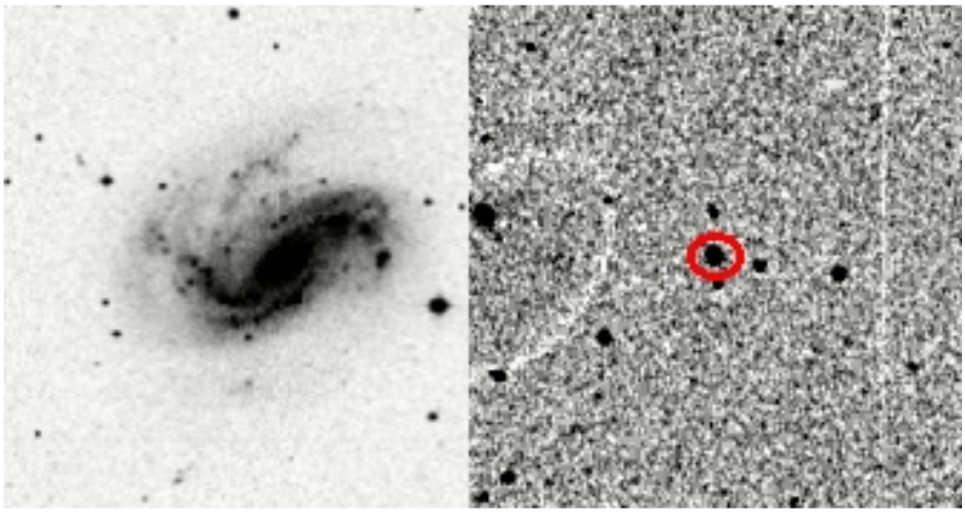

FIGURE 1.1. Example of two subtypes of AGN. On the left is shown a Seyfert galaxy, NGC 4051. On the right, a quasar, PG 1415+451. The figure clearly demostrate visible presence of the host galaxy in the case of the Seyfert galaxy and a point source in the case of the quasar. Images taken from the *"Nasa Extragalactic Database"* (NED) public archive.

– the lines had widths of hundreds of $\mathrm{km\,s^{-1}}$. In 1926, Edwin Hubble studying *"extragalactic nebulae"*, observed two other sources displaying similar characteristics to NGC 1068 – NGC 4051 and NGC,4151. His results led him to suggest that these spiral nebulae were objects outside of the Milky Way.

Carl Seyfert (1943), almost two decades later, noticed that a small group of galaxies had very peculiar characteristics compared to normal galaxies. Seyfert observed an intense brightness coming from the nuclear region ($> 10^{12}\,\mathrm{L_\odot}$). This region was emitting high ionization lines, broader than usual, with full width at half maximum (FWHM) of 200–1000 $\mathrm{km\,s^{-1}}$. The Hydrogen lines, had even more extreme values, reaching 10000 $\mathrm{km\,s^{-1}}$.

Schmidt (1963) discovered a type of source having properties even more extreme than the galaxies observed by Carl Seyfert twenty years before. Observing the radio source 3C 273, Schmidt noticed that this source had an even more compact and bright nucleus than the Seyfert galaxies. The apparent pointlike shape, reminiscent of stars, and the strong radio emission led him to name this galaxy a quasi-stellar radio source (quasar).

In the following decades several other classes were created to classify the several kinds of AGN observed (Khachikian & Weedman, 1974). Despite their spectroscopic differences, today it is well established that all AGN share common characteristics (Peterson, 1997; Ferrarese & Ford, 2005), such as:

- Broader emission lines than normal galaxies. The typical width of the narrower lines (such as the ones present in type–2 AGN) is typically of the order of $10^2\,\mathrm{km\,s^{-1}}$ (but reaching

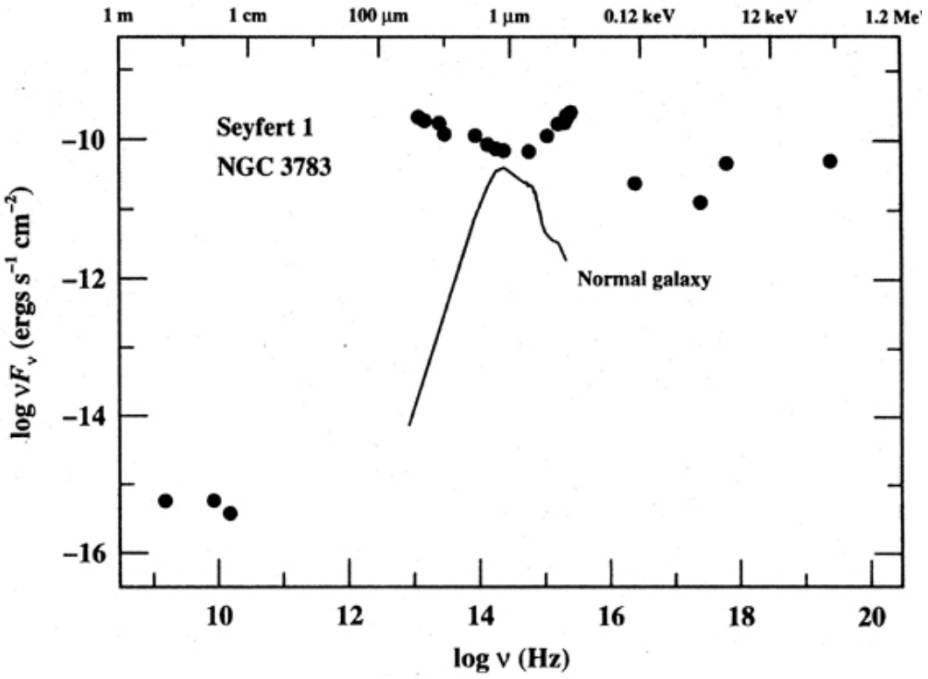


FIGURE 1.2. Example comparing the SED of an AGN and a normal galaxy, NGC 3783 (Alloin, 1995).

widths of 1500 km s$^{-1}$ in high-redshift radio-galaxies, De Breuck 2001). Permitted lines are seen in type–1 AGN with even broader widths, reaching $10^3 - 10^4$ km s$^{-1}$(Peterson et al. 1997, Marziani 2005, Shen et al. 2011, Rakshift et al. 2017).

- Flux variability in the continuum and broad emission lines (Peterson et al. 1997, Kaspi et al. 2001, Bentz et al. 2009, Barth et al. 2015, Park et al. 2017).
- Spectral energy distribution (SED) dominated by non-stellar emission, with emission excesses in the X-Ray, ultraviolet (UV), infrared, and radio (see Figure 1.2).
- Pointlike, spatially unresolved, high luminosity emission from the nucleus (that could reach $\sim 10^{12}$ L$_\odot$), concentrated in very a compact region of sub-parsec scale.

## 1.2 AGN in a nutshell

Seyfert galaxies are active nuclei of low luminosity (typically $M_B > -21.5 + h_0$, where $M_B$ is the absolute magnitude in the $B$ band and $h_0$ is the Hubble constant) and the host galaxy is easily seen (Peterson, 1997). Their morphology is usually spiral, with the addition of a bright nucleus characterized by its variability in the X-Ray and UV bands, and low (or no) emission in radio frequencies (typically radio-quiet AGN). The spectrum of a Seyfert galaxy is rich in

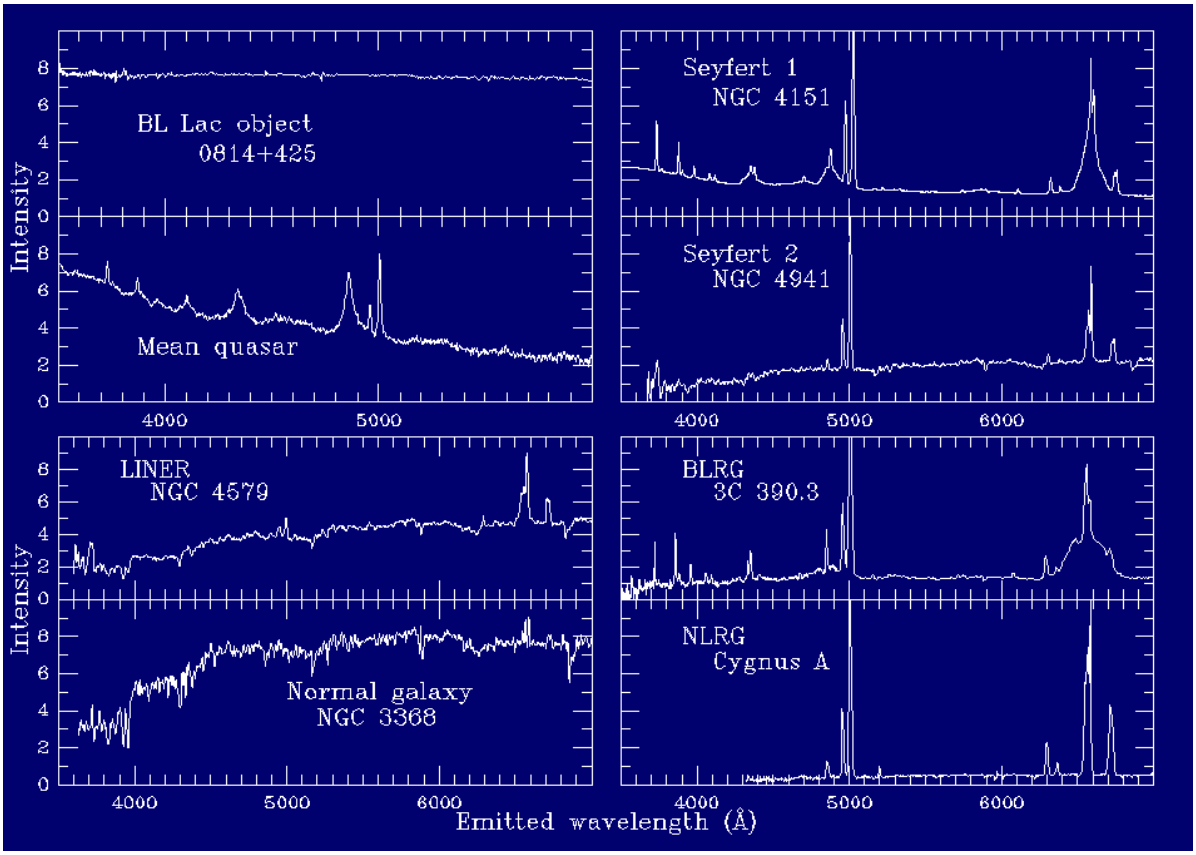


FIGURE 1.3. Comparison of the spectra of several types of AGN. Copyright: William C. Keel.

emission lines of low ionization, such as Fe II, H$\alpha$ and He I. High ionization lines such [Ar V] and [Fe XI] are also present, although not common (Elvis et al. 2014, Rose et al. 2014, 2015). Figure 1.3 show example spectra of Seyfert galaxies. The width of the emission lines present in the spectrum of Seyfert galaxies follows two very distinct patterns: They can be broad ($\sim 10^3\,\mathrm{km\,s^{-1}}$) or narrow ($\sim 10^2\,\mathrm{km\,s^{-1}}$). This difference separates the Seyfert galaxies in two groups: Seyfert–1 and Seyfert–2. Spectroscopically, the differences between them is related to the presence of broad lines. Seyfert–1's are characterized by the presence of both groups of emission lines, broad and narrow. Seyfert–2's, on the other hand, only show narrow emission lines. It is believed that these two types of Seyfert galaxies have the same inner structure and the differences observed between them are caused by orientation effects.

Quasars are among the most luminous sources in the universe. In contrast to the Seyferts they have a highly luminous nucleus (typically $M_B < -21.5 + h_0$) and typically an unresolved star-like morphology, sometimes showing nebular structures only in nearby sources or when they are expelling large amounts of energy. The quasar spectrum is similar to that observed in Seyfert

galaxies, but typically shows weaker narrow lines and strong radio emission. The brightness of the nucleus is much stronger than the host galaxy, thereby its spectrum is usually dominated by the non-stellar component and an excess emission in the UV attributed to accretion disk. The quasars are among the most common AGN observed in the early universe, being observed as far as $z > 7$ (Fan, 2001; Iye et al., 2006; Bradley et al., 2008; Lehmert et al., 2010).

Objects having Low-ionization nuclear emission-line regions (LINERs) were defined by Heckman (1980) as galaxies with emission line ratios [O II]$\lambda$3727/[O III]$\lambda$5007 > 1 and [O I]$\lambda$6300/[O III] $\lambda$5007 > 1/3. This kind of AGN are the most common (Ho 2008). The emission of these galaxies can be explained by an AGN, supported by the observation of broad emission lines in their spectrum (Storchi-Bergmann, 1993; Bower et al., 1996). On the other hand, hard ionizing photons from Wolf-Rayet, OB stars, or poststarburst in the central region explain the emission lines observed in the circumnuclear region (Shields, 1992; Barth et al., 2000). Recently, however, the hypothesis of the AGN-ionization has been questioned. Discoveries of inconsistency in line ratios and distribution of LINER-like emission in spatially distributed regions in the host galaxy support this questioning (Cid-Fernandes et al. 2011, Sarzi et al. 2010, Yan & Blanton 2012). A complete sample with spatial and spectral observations is necessary for a more robust conclusion. Recent works from the DeepDiving3D and CALIFA surveys are addressing these issues (Ricci et al. 2014, Singh 2014)

Radio-galaxies are objects characterized by their strong emission in the radio frequencies ($L_{1.4GHz} > 10^{25} W\,Hz^{-1}$, Blandford et al. 1990). In the local universe, they are typically associated with a giant elliptical morphology. The strong radio emission typically consists of a radio core radio jet and giant lobes, extending to kiloparsec scales (Blandford et al. 1990). As the quasars and Seyfert galaxies, their optical spectrum can be divided in two groups: Narrow-Line radio-galaxies (NLRG) and Broad-line Radio-Galaxies (BLRG)

BL Lac and Optical Violent Variables (OVV) are AGN characterized by a high amplitude of variability in short time scales. Collectively these objects are called Blazars. The variability in these sources is so extreme that it can reach amplitudes of 0.1 mag on the scale of a day. Moreover the blazars show highly polarized emission (> 3%), which also can vary both in magnitude and in angular position. Blazars are always strong radio-sources and show typically a featureless spectrum, without emission or absorption lines, dominated by the continuum.

## 1.3 The Unified Model of AGN

Despite the existence of several different types of AGN a general scenario was developed to explain this diversity – the unified model of AGN. In this model all AGN have the same internal structure and energy emitting source acting roughly in the same way. In this model the diversity between the several types of AGN from Section 1.2 is explained by varying the viewing angles towards the central emitting source that is being observed (Antonucci & Miller 1985, Urry &

Padovani, 1995, Cepa, 2009). The AGN components are sketched in Figure 1.4. This model has been supported by more than three decades of observations and its components are described in this section (Peterson, 1997, Osterbrock 1989, Cepa, 2009).

The structure in Figure 1.4 starts in the most central region with a super massive black hole (SMBH) with typically $M_{BH} > 10^6 M_\odot$ accreting matter from the interstellar medium of the host galaxy. This gas is accumulated around the SMBH in a disk structure called the 'Accretion Disk'.

The accretion disk surrounding the black hole is responsible for the continuum emission. The viscosity of the matter in the disk heats it, converting gravitational potential energy into thermal energy as the matter falls towards the black hole. This process is responsible for about 80% of the energy emitted in X-Ray. The outer regions of the disk emit continuum that dominates the optical and UV spectral regions.

Accelerated charges in the disk produce magnetic fields which boost the protons and electrons in the gas in perpendicular directions, producing the radio-jets observed at radio frequencies. In the unified model, when we observe sources directly along these jets, we are observing the object described by BL Lacs. Notice that not all the AGN have this emission, and the mechanism behind it is still under debate (Storchi-Bergmann et al., 1999; Winge et al., 2000; Riffel et al., 2006b).

The radiation emitted in the inner region of the accretion disk heats the cold gas surrounding it, which re-radiate it in the form of emission lines. This gas has two main components. The first is made of dense clouds closer to the central source (< 1pc), which emit the broad lines, and the second is composed by lower density clouds far from the central source ($\sim 10 - 10^2$pc), which emits the narrow lines.

The inner region described above is called the 'Broad Line Region' (BLR). Because it is very close to the central source the analysis of this region carries fundamental information regarding the physical processes of the AGN. Emission lines in this region have typical velocities of $10^3$ – $10^4\,\mathrm{km\,s^{-1}}$ and are ruled by the gravitational potential of the SMBH. This region was spatially unresolved until 2018 (GRAVITY colaboration, 2018), and its dense clouds ($n_e > 10^9\,\mathrm{cm^{-3}}$) are concentrated in a region smaller than 1 pc (Osterbrock, 1989). The proximity to the accretion disk makes the emission lines sensitive to the variability effects of the continuum. This variability is delayed due to the propagation velocity inside the BLR and can be studied through the reverberation mapping technique which provides important information about the distance of the emitting clouds and the SMBH mass (Peterson et al. 1999).

Surrounding the BLR exists a torus shaped structure composed of dust and molecular gas. This structure provides an anisotropic cover of the central emitting region. In the unified model, the torus is the main responsible by the differences observed between Seyfert 1 and 2 (Osterbrock, 1978). The torus emission can be described by a black body function that peaks in the near-infrared (NIR) at $\lambda > 2\,\mu$m. The dust in the torus is usually warm, and can reach temperatures around 2000 K. This limit is due to the sublimation temperature of the dust grains. The existence of the torus is supported by polarimetric studies (Antonucci & Miller, 1995) and the first modeling

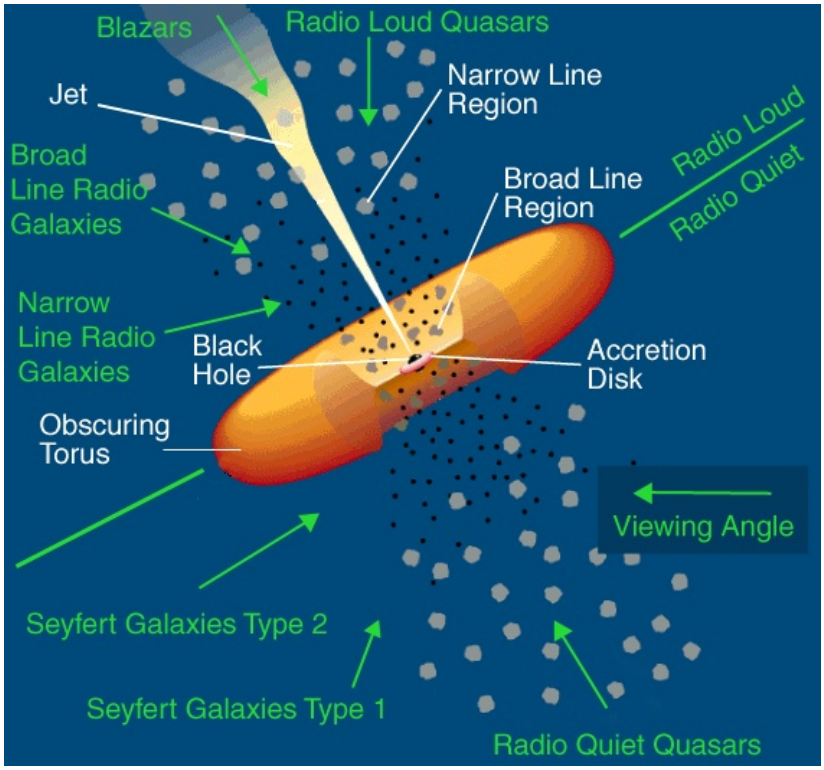


FIGURE 1.4. Artistic representation of the internal structure and different types of AGN depending on the viewing angles according to the unified model of AGN (Urry & Padovani 1995)

studies dating to the early 1990's (Pier & Krolik, 1992). The observations in nearby Seyfert galaxies show that this structure is confined in a region smaller than 10pc (Packham et al., 2005; Tristram et al., 2007; Radomski et al., 2008).

In contrast to the compact structure of the BLR, the narrow line region (NLR) is spread out over a much more extended region. The NLR is the only region that can be spatially resolved directly from ground observations. Its extent can reach hundreds of parsecs, with a roughly conic morphology. The emission lines from this region are one order of magnitude narrower than those from the BLR, with typical values of 200–1000 km s$^{-1}$. Forbidden emission lines are also observed which suggests low densities, $n_e < 10^4$ cm$^{-3}$, and high temperature, $T_{NLR} \sim 12000$ K.

## 1.4 The inner region of the AGN

One of the most puzzling aspects of the unified model of AGN is their inner region, < 1 pc. This portion of the AGN is usually inaccessible by spatially resolved observational methods, even for the most nearby AGN. Two main structures are responsible for the physics observed in the optical and NIR spectral regions addressed in this thesis, the SMBH and the BLR. While the

BLR is responsible for the observed emission lines, which are used to probe the physics of this regions, the SMBH mass, rules the sub-parsec region of the AGN. Many aspects of SMBH and BLR still remain unsolved. In the next sections we address some of the most important aspects of the SMBH and BLR subjects relevant to this thesis.

### 1.4.1 The Black Hole Paradigm

There are still many open questions regarding the black hole in the center of the AGN: what are their masses and spin parameters? How do they form and evolve? What is the relation between the SMBH and the host galaxy?

#### 1.4.1.1 The Black Hole Mass

The most direct method to estimate the parameters within the BLR is through the reverberation mapping (RM) technique. This technique is based on the fact that the BLR can not be spatially resolved and uses basic inferences about its structure and time resolved spectroscopic observations to probe this region.

The first attempts to measure the time variations in the continuum and its effect on broad lines were made by Lyutyj & Cherepashchuk (1974). Using a sample of narrow line Seyfert's 1, Lyutyj & Cherepashchuk showed the existence of some kind of 'response' of the broad line to continuum variations. The results from Bahcall et al. (1972) already predicted that a BLR driven by photoionization should produce variable emission lines, responding to the continuum. Bahcall et al. (1972) suggested that due to the time travel of the light within the BLR the variations in the broad lines should be observed with some lag. Time resolved campaigns have been monitoring several AGN using optical spectroscopy, and have found a widely accepted correlation between broad lines and continuum variations (Blandford & McKee 1982, Kaspi et al. 2000, Barth et al. 2013, Park et al. 2017). These campaigns were called 'Reverberation Mapping' (RM). this technique is a powerful tool to analyse the fundamental properties of the BLR, allowing a reconstruction of the kinematics and structure. Today this technique is widely applied in several nearby AGN in order to estimate their BLR size and the AGN central SMBH mass (Peterson et al. 2004, Kaspi et al. 2000, Park et al. 2017).

Reverberation mapping consists simply of a long term campaign monitoring a specific AGN. During the campaign a high temporal cadence is made in order to measure the continuum variations. Together with the continuum, emission line (typically H$\beta$) fluxes are measured and their variations analysed. Figure 1.5 shows a sketch of the BLR and central source and how the reverberation mapping works. The central source (blue) produces an ionizing continuum which is observed. The same continuum spreads and ionizes the BLR cloud surrounding the central source, and emits the broad lines observed. The time travel from the central source to the BLR clouds is translated in the observed time delays in the observed variations between the

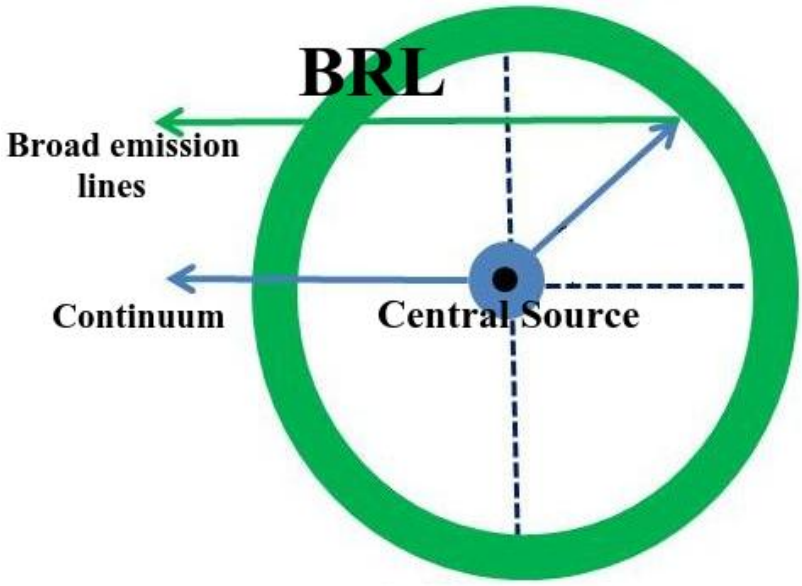


FIGURE 1.5. Sketch of the AGN structure for reverberation mapping technique. The blue circle show the ionizing central source surrounding the black hole (black circle) emitting. Its emission, represented by the blue arrows, reach the observer and the BLR clouds (green circle). The continuum ionize the clouds, which emits the broad lines observed. The time travel between the central source and the BLR clouds is the time lag observed in a RM campaign.

continuum and broad lines. An example of the time lags can be observed in Figure 1.6 for the AGN Mrk 335 (Peterson 2001).

To estimate BH masses from the results of RM campaigns, it is necessary to make the assumption that the clouds in BLR are virialized and their movements are ruled by the gravitational potential of the SMBH. The symmetry of the observed lines (usually H$\beta$, but note that is not true for C IV, which is believed to have at least one non-reverberating component, Runnoe et al, 2013), the lack of centroid shifts, and their intrinsic proximity to the central SMBH gives support to these assumptions. Since the light speed is constant, the time delays measured by RM can be converted in the distance where the emitting clouds are located, e.g. the size of the BLR. The black hole mass can be estimated by (Peterson 1997):

$$M_{RM} = \frac{V_{vir}^2 R}{G} = f\frac{FWHM^2 R}{G} \tag{1.1}$$

Where $V^2$ is the Virial velocity, $R$ is BLR radius, and G is the gravitational constant. The FWHM of the variable line can be used as a proxy of the Virial velocity (Peterson 1997). $f$ is a multiplicative factor introduced to parameterize our ignorance about the BLR geometry. For randomly oriented clouds, $f$ is approximately 3/4 (Netzer 1990).

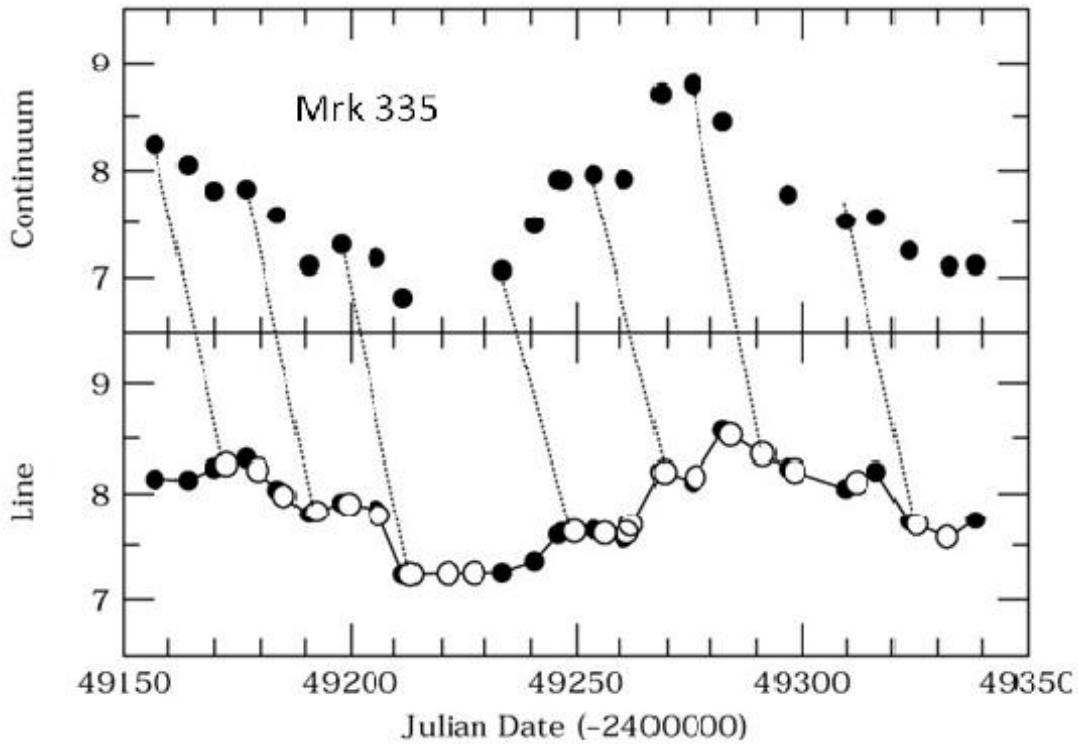


FIGURE 1.6. Continuum-BLR variability correspondence for Mrk 335. Top panel shows the continuum fluxes measured in a RM campaign and bottom panel shows the H$\beta$ fluxes. The rise and drops fluxes of the lines follow the continuum variations. Dotted lines were traced to identify some of these variations in the temporal axis. Figure from Peterson (2001).

Despite the importance of reverberation mapping in estimating BLR sizes, and BH masses, the technique comes at a high observational price. Several constraints make RM unfeasible to be applied to large samples, and only smaller follow-ups were made so far (less than 80 AGN up to date) (Bentz 2015, Park et al. 2013, Park et al. 2017, Barth et al. 2013). Among the challenges in RM we can list (Bentz 2015): (i) total length of the campaign – since the variability has a random behavior longer campaigns will optimize the chance to observer and map the variations of the continuum and emission lines. Horne et al. (2004) suggests a RM campaign at least three times longer than the expected time delays derived from single epoch spectra; (ii) the cadence of the observations – the sampling of the observations must be frequent enough to avoid losing variability information between two observations. Longer times between observations could produce data without variability or results that do not probe small variations in the continuum or line, leading to a misinterpretation of the results; (iii) high signal/noise spectra – S/N>50 in the continuum. Variability amplitudes on the emission lines are smaller than the continuum, for instance H$\beta$ amplitudes are on average smaller than 10% (Kaspi et al. 2000). Therefore the exposure times for the observations must be long enough to reach this S/N; (iv) spectral resolution

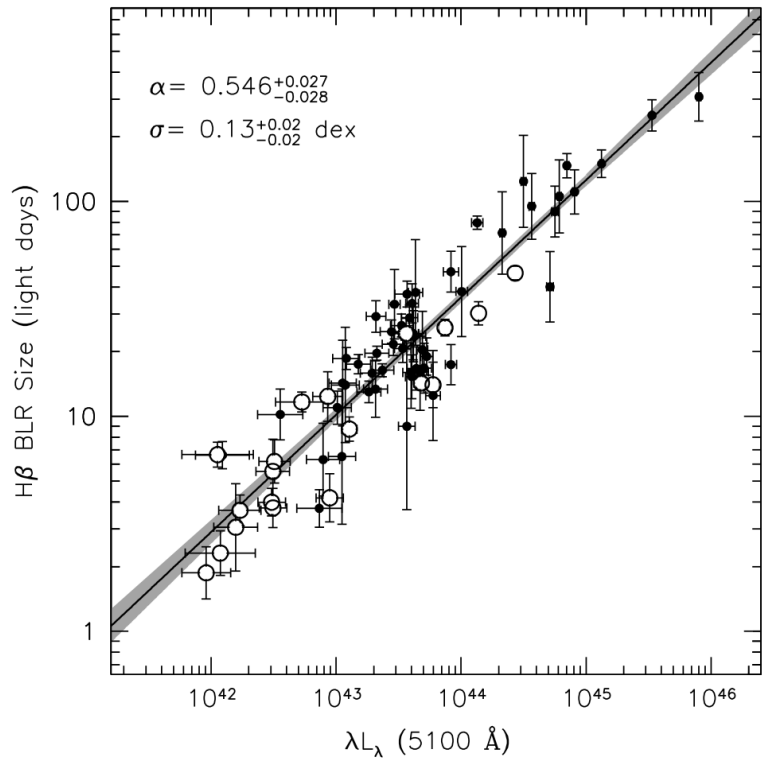


FIGURE 1.7. Relationship between the BLR radius measured by H$\beta$ line and the continuum luminosity at 5100 Å. All intensities were corrected for the host galaxies starlight contamination. Figure from Bentz et al. (2013)

– This is usually considered the easiest of the challenges, due to the intrinsically broad profiles of the observed lines. However at least a medium resolution must be applied to these observations, since narrow components lines can be blended and other contaminant agents may be present (such as Fe II and He I redwards H$\beta$); and (v) precise flux calibration – observations must have a relative flux calibration of at most 2% from each other (Peterson 2004). In addition to these constraints, other challenges apply, such as bad weather or even a non-detection of variability during the campaign. For these reasons another method to estimate BH masses has come into practice, the single epoch (SE) method.

One of the most important products of the reverberation mapping results was the discovery of the relationship between the time delay (e.g. radius of the BLR) for a specific line, and the luminosity of the central ionizing source of the AGN at some particular wavelength (Kaspi et al. 2000). This relation was well established with observations of AGN over a broad range of intensities ($10^{41}$–$10^{46.5}$erg s$^{-1}$) by Kaspi et al. (2000). This result was expected based on photoionization arguments and probed even when the RM sources were just few (Koratkar & Gaskell, 1991). Figure 1.7 shows the relationship between these two quantities.

The tightness of this relation led to the SE method. Since the BLR radius can be estimated

from the continuum luminosity of the AGN, it is possible to calibrate an equation that can be applied to very large samples of quasars. Combining the width of a specific line and the continuum luminosity we can estimate the single epoch SMBH mass ($M_{SE}$) using the following equation (Shen 2011):

$$\log\left(\frac{\mathrm{M_{SE}}}{M_\odot}\right) = a + b \times \log\left(\frac{\lambda L_\lambda}{10^{44}\mathrm{erg\,s^{-1}}}\right) + c \times \log\left(\frac{FWHM}{\mathrm{km\,s^{-1}}}\right) \tag{1.2}$$

In this equation $\lambda \mathrm{L}_\lambda$ is the luminosity of the AGN at a given wavelength, FWHM is the full width at half maximum of a broad line, and the parameters a,b and c are calibrated such that the SE BH masses match with RM BH masses. The parameters a,b and c will depend on the line and continuum wavelength used for the calibration. In theory, any broad line and featureless continuum wavelength can be used to calibrate Equation 1.2. Due to the extreme majority of the RM campaigns being based on the H$\beta$ and continuum luminosity at 5100 Å, these parameters are considered to be the most reliable for estimating SE BH masses (Vestergaard & Peterson 2006, Shen et al. 2011).

Several authors presented calibrations for the parameters of Equation 1.2 for different lines. Vestergaard & Peterson (2006) show that the FWHM of the broad component of H$\alpha$ is, on average, slightly narrower than H$\beta$, but strongly correlated, which makes it a reliable line for estimating BH masses using the single epoch method. This behavior was expected since both lines correspond to the same gas, and small variations (whithin the errors) can be explained by the line fitting method. For instance, H$\beta$ is surrounded by another contaminant ion, Fe II, which can produce variations in the FWHM of the lines (Lipari et al. 2005). On the other hand, the only contaminant blended with H$\alpha$ is the [N II] doublet but the separation in wavelength makes it easy to resolve, or it is so weak that its flux is irrelevant for the line fitting (Marziani et al. 2004). Another line used is Mg II. This line became important in intermediate redshift AGN ($0.8 < z < 2.0$) when the lines of H$\alpha$ and H$\beta$ are redshifted to the NIR spectral region. McLure & Dunlop (2004) derived the calibration for this line and successfully applied it to a sample of more than 10000 quasars in SDSS out to $z \sim 6$.

While the Balmer lines are reliable for SMBH mass estimates and Mg II also can be used with great accuracy, for $z > 4.5$ the only line available for such estimate is C IV, and a lot of controversial results are derived based on this line as an estimator (Baskin & Laor 2005, Netzer et al. 2007). The C IV line differs from the low ionization lines in ionization potential, shape of the line profile, emitting region and by the presence of non-reverberating components (Runnoe et al. 2013, Denney 2012, Sulentic et al. 1999). For instance, the FWHM of C IV is much weaker correlated with those lines (see figure 1.8 (Shen et al. 2008, Fine et al. 2008). Another prominent feature of the C IV line is its blueshift (Gaskell 1982, Richards et al. 2011). Several effects can cause the observed blueshift, which suggests non-gravitational effects playing an important role in the C IV emission. The most common mechanisms invoked to explain the asymmetrical profile of C IV is an outflowing gas (Gaskell 1982, Marziani et al. 1996) and electron/Rayleigh scattering

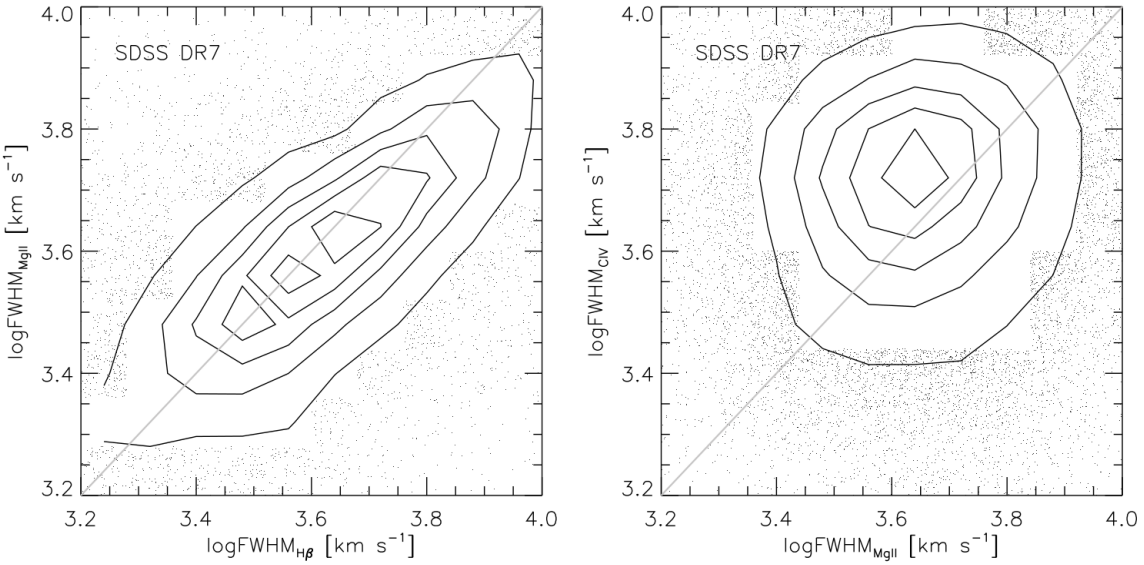


FIGURE 1.8. Correlations between FWHM of of low and high ionization lines. Left panel shows the FWHM of H$\beta$ versus the FWHM of Mg II (two low ionization lines). Right panel shows the FWHM of C IV versus the FWHM of Mg II. It is clear that the presented low ionization lines have a strong correlation. On the other hand high and low ionization present a much more scattered correlation. Figure adapted from Shen et al. (2008)

(Gaskell & Goosmann, 2008). Several authors have tried to rehabilitate the C IV line to improve its application to SE BH mass determinations, trying either to find an empirical correlation between the quasar spectral feature or increasing the C IV RM sample. Denney et al. (2012) suggested that the asymmetrical profile shape of C IV was causing the scatter in the correlation between H$\beta$ and C IV. They presented a correction term to equation 1.2, which consists of adding the velocity dispersion of the line in order to compute the FWHM difference. Runnoe et al. (2013) found an empirical correlation between the peak ratio of S IV$\lambda$1400Å and C IV with the FWHM of H$\beta$. Their method to correct the C IV SE BH mass consists of adding an extra term to compute this missing value. Coatman et al. (2017) found that the main cause of lack of correlation between the FWHM of C IV and FWHM of H$\beta$ is related to the blueshift of C IV. Their rehabilitation method for the SE masses consists of correcting the FWHM of C IV, keeping the equation 1.2 unchanged. Park et al. (2017) followed a different approach, using data from a RM campaign for C IV they obtained different [a,b,c] parameters for the C IV method. The main difference in the equation is the reduction of the FWHM term and increasing the luminosity contributions to the equation.

The SDSS survey mapped the optical spectra of over 100.000 quasars covering a wavelength range from 3000 Å–9000 Å, from local AGN ($z \sim 0$) to very high redshift ones ($z > 5$). The SE

method was used to estimate the SMBH mass of these quasars using several broad emission lines, depending on the redshift. For $z < 0.4$, H$\beta$ can be used for estimates. However, when we look to higher redshifts, this line may not be available. Other lines, though, can be used for SE BH mass estimates. The H$\alpha$ line for example can be observed up to redshift 0.8. Typically UV lines are redshifted to optical wavelength for in higher redshift quasars. For instance, Mg II falls in the SDSS spectral range for quasars up to $z = 2$ and above that only C IV is available. Therefore, for $z > 5$ AGN, the BH mass estimates are compromised by usage of C IV, which is the most unreliable of the lines. To access the reliable lines and obtain accurate BH mass estimates it is necessary to observe the AGN in NIR.

#### 1.4.1.2 The Black Hole Growth

Black hole masses can be estimated by the means presented in the previous section, but how do black holes achieve their masses?

One of the most important applications of SE BH masses is the capability of estimating accurately the BH masses from thousands of quasars, in a wide range of redshift, which allows an analysis of their evolution through time. The analysis of quasars at redshifts up to $\sim 7$ carries important information of how AGN and their SMBHs during the first Gyr of cosmic age. This information can be tracked to the population of SMBHs in local galaxies, tracing the evolution of their central SMBH (Vestergaard 2004). The SDSS data has provide powerful spectroscopic information for high redshift quasars up to z$\sim$ 6. The optical spectra of tens of thousands of quasars were used to successfully estimate the black holes of these AGN (McLure & Dunlop 2004, Netzer & Trakhtenbrot 2007, Shen et al. 2008, Shen et al. 2011, Labita et al. 2009). On the other hand, to observe quasars at higher redshifts, dedicated and deeper optical and NIR observations are required and necessary to fully understand the origin of the SMBH (Jiang et al. 2007, Kurk et al. 2007, Willott et al. 2010, Mortlock et al. 2011).

One of the current challenges in understanding the black hole growth is the discovery of quasars at redshift higher than seven (the record is held by the quasar at 7.54, Banãdos et al. 2018). At this redshift the universe was only 800 Myr old, and the measured black hole masses are higher than $10^9$ M$_\odot$, with some quasars reaching a luminosity close to the Eddington limit (i.e. the maximum luminosity at which gravitational infall and radiation pressure are balanced).

Traditional models consider that most of the growth of the SMBH happens via accretion of matter coming from the accretion disk. In this model the mass growth rate is:

$$\dot{M}_{\rm BH} = \lambda L_{Edd} \frac{(1-\epsilon)}{\epsilon c^2} \tag{1.3}$$

where $L_{Edd} = L_{bol}/1.26 \times 10^{38} (M_{\rm BH}/{\rm M}_\odot)\,{\rm erg\,s^{-1}}$ is the Eddington luminosity of the BH, $\lambda$ =L/L$_{\rm Edd}$ is the Eddington ratio, and $\epsilon$ is the efficiency of the conversion of matter in radiation. As explained by Shen (2013), if the Eddington ratio and the efficiency are not evolving, the

black hole mass grows in one $e$-fold, on a characteristic timescale (also known as Salpeter time or $e$-folding time, Salpeter 1964):

$$t_e = \frac{\epsilon c^2}{(1-\epsilon)\lambda L_{bol}} \approx 4.5 \times 10^8 \frac{\epsilon}{\lambda(1-\epsilon)} \tag{1.4}$$

Therefore, the black hole growth starting from a seed black hole with mass $M_{seed}$ at an initial time $t_i$ will increase its mass until their measured mass at given $z$ (final time, $t_f$). The equation below translates this into the growth of the BH mass with time:

$$M_{BH} = M_{seed} exp \frac{t_f - t_i}{t_e} \tag{1.5}$$

Two of the main concerns regarding the evolution of the black holes are the mass and formation epoch of the seeds. Theoretical models consider two main types of black hole seeds, light or heavy seeds (Volonteri et al. 2004, Volonteri et al. 2005). Light seeds are those with $M_{seed} \sim 10 - 100 M_\odot$. These black holes are produced from Population III (PopIII) star remnants. The relic SMBH found in the center of massive local elliptical galaxies must have their progenitors at already massive objects in higher redshifts, possibly being formed in luminous quasars at high redshift. Recent observations of quasars at $z > 6$ with $M_{BH} > 10^9 M_\odot$ show already formed BHs within ~ 1Gyr after the formation of the universe (Mortlock et al. 2011, Wu et al. 2015, Banãdos et al. 2018). Scenarios where the growth of a light seed could reach this order of magnitude in mass in such a short time is a challenge for theoretical models. One theoretical support for the light seed scenario were presented by Volonteri & Rees (2005) is that supercritical accretion plays a role in the growth of the seed. A black hole accreting in a supercritical regime has a $L/L_{Edd} >> 1$, which would reduce the $e$-folding time allowing to grow a $M_{BH} \sim 10^9 M_\odot$ by $z \sim 6 - 7$.

Another possibility is that the black hole seed starts heavy. In this case its initial mass is one to three orders of magnitude higher, e.g., $M_{seed} = 10^4 - 10^5 M_\odot$. Three main scenarios could produce this kind of seed: (i) Direct collapse of un-enriched pre-galactic disks (Begelman et al. 2006); (ii) Direct collapse of primordial gas clouds into a black hole (Johnson et al. 2012); and (iii) Collapse of a very massive star produced in a dense stellar cluster (Davies et al. 2011). The main consequence of a heavy seed is that its initial mass would boost the early growth in equation 1.5. One of the main arguments in support of the heavy seed scenario is that the formation environments of these seeds is highly dense, increasing the probability the feeding starts early (Pacucci et al. 2016). Superaccretion also can play a role for these seeds until the black hole achieve a more massive profile, to slow down until it becomes quiescent. The main take away from this scenario is that a higher $M_{seed}$ will require less $e$-folds to grow to $10^9 M_\odot$.

### 1.4.2 The Fe II Emission in AGN

The BLR in AGN has been extensively studied from the X-Ray to the NIR in the past few decades (see Gaskel 2009, for an extensive review). Despite of that, several aspects of its physical

properties are still under debate. One of the most puzzling aspects of the BLR is the Fe II emission, which forms a pseudo-continuum due to its hundreds of thousands of multiples that extend from the UV to the NIR (Sigut & Pradhan, 2003). The blend of more than 344000 multiplets close in wavelength, and their intrinsic broad nature, poses a challenge to model and subtract it from the AGN spectrum.

The Fe II emission is important for at least four reasons: (i) It represents one of the most conspicuous cooling agents of the AGN. The energy emitted by Fe II can be up to 25% of the total energy emitted by the BLR (Wills et al. 1985). (ii) The Fe II pseudo-continuum is the strongest contaminant agent in the AGN spectrum. Without a proper modeling and subtraction, a spectral analysis can be compromised, leading to a wrong description of the physical parameters and emission line features present in the inner region of the AGN (Marziani et al. 2001). (iii) The Fe II emitting region is located in the BLR and can provide clues about the structure and kinematics of the BLR and central source. Despite several results concerning the Fe II emitting region (Kuehn et al. 2008, Matsuoka et al. 2008, Sluse et al. 2007, Hu et al., 2008, Kovacevic et al., 2010) the blended Fe II lines in the optical and UV still present a challenge, and its physical properties and excitation mechanisms are under discussion. (iv) The relative intensity of Fe II to the peak of [O III]$\lambda$5007 is associated with important parameters of the BH accretion process (Sulentic et al. 2000, Boroson & Green 1992, Boroson 2002). The ratio Fe II/H$\beta$ is the dominant variable in the principal component analysis (PCA) presented in the seminal work of Boroson & Green (1992). It is believed that this parameter can be used to trace a 'main sequence' for quasars, analogous to the H-R diagram for stars (Marziani et al. 2001, Shen & Ho 2014).

The Fe II emission lines were observed for the first time in 1964, by Greenstein & Schmidt. Few years later Wampler & Oke (1967) found a new source with the peculiar emission, 3C 273. Sargent (1968) found for the first time the Fe II emission in high proportions in the source I Zw 001. The Fe II emission in this source was so strong that it was stronger than the Balmer lines, such as H$\beta$, by 2.5 times. In the next few years several other works reported Fe II emitting sources and performed detailed studies of their physical properties (Osterbrock, 1977; Meyers & Peterson, 1985; Grandi, 1981; Joly, 1991; Boroson & Green, 1992).

The Fe II intensity in AGN is usually measured in the optical, using the flux ratio between the Fe II bump centered at $\lambda$4570 Å and the broad component of H$\beta$ ($R_{4570}$). Figure 1.9 shows the Fe II bump in the I Zw 001 spectrum, with its strong Fe II emission in the optical region. Typically, AGN have, on average, $R_{4570} \sim 0.4$ with 90% of them with values between 0.1–1 (Bergeron & Kunt 1984). Strong Fe II emitting AGN have $R_{4570} > 1$, and occur only in roughly 5% of the sources (Lawrence et al. 1988). Just a few ultra strong Fe II emitting AGN ($R_{4570} > 2$) have been reported in the literature, and their presence is one order of magnitude rarer (Lipari et al. 1993, Moran et al. 1996, Xia et al. 1999, Marziani et al. 2001, Kovacevic et al. 2010, Shen et al. 2014). The $R_{4570}$ correlates with several physical properties of the AGN. For instance, Boroson & Green (1992) found that the $R_{4570}$ is anti-correlated with the width of H$\beta$, the peak of [O III], and

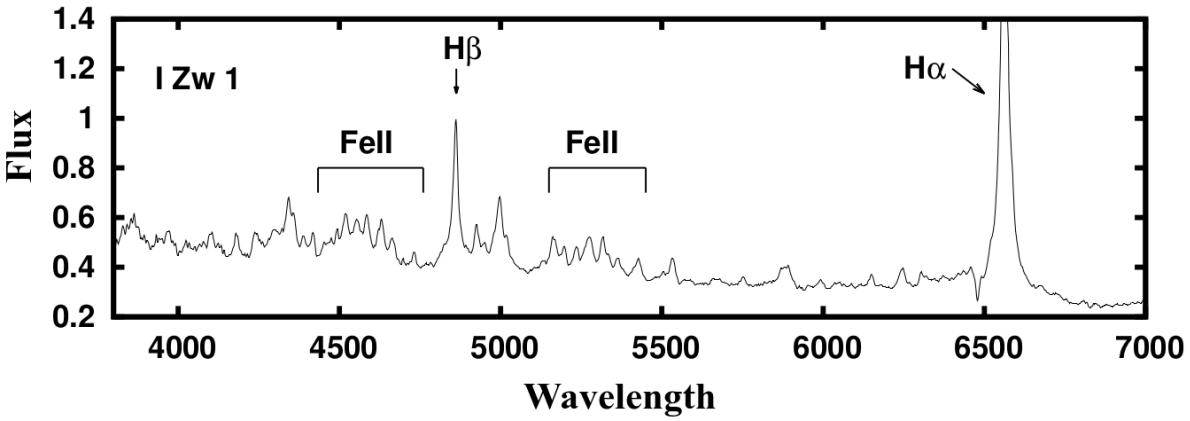


FIGURE 1.9. Example of the Fe II emission in the optical region. The blend of several multiplets form a pseudo continuum in the I Zw 001 spectrum. Around the H$\beta$ lines clear strong Fe II bumps can be seen.

asymmetries redwards of H$\beta$. The variability of the X-Ray photon index is also correlated with $R_{4570}$ (Moran et al. 1996, Wilkes et al. 1987, Wang et al. 1996, Sultentic et al. 1999). Moreover, the Fe II emission appears stronger in AGN with broad absorption lines (Hartig & Baldwin 1986, Boroson & Meyers 1992). All these correlations show that understanding the Fe II emission is of fundamental importance for an accurate description of the BLR.

After the discovery of the Fe II emission in the AGN spectrum many of theoretical models were developed. These works attempted to model, unsuccessfully, the Fe II emission using photoionization models for the BLR (Netzer 1980, Kwan & Krolik 1981). The failure of the Fe II model led to the discussion of other excitation mechanisms capable of producing such emission. Phillips (1978, 1979) showed that collisional excitation would not be sufficient to reproduce the observed Fe II intensity and suggested continuum fluorescence (e.g. absorption of the continuum photons by Fe II transitions) as an important mechanism for Fe II production. Netzer & Wills (1983) models had more sophisticated mechanisms, and included the continuum fluorescence, collision excitation and self-fluorescence via UV-overlapping Fe II photons. Despite that, the model still was not able to reproduce the total flux of Fe II observed in AGN. The total Fe II flux predicted by the model estimated values of $R_{4570} \sim 3-5$, while observations have shown that this values can be up to 12.

Penston (1987) suggested that the presence of unexpected Fe II multiplets in the UV spectrum of the symbiotic star RR Tel can be explained by the cascading from upper energy levels excited by the absorption of photons of Ly$\alpha$. Penston also argued that these levels could not be excited by the traditional excitation mechanisms presented by Wills et al. (1985) and Netzer & Wilkes (1983) since these levels needed energies higher than 10 eV to be excited. Graham et al. (1996) were the first to observe these multiplets in the AGN spectrum in a ultra Fe II emitter, QSO 2226–

3905. Sigut & Pradhan (1998) used an Fe II atomic model with 262 fine-structure levels with Ly$\alpha$-fluorescence as an additional excitation mechanism. They show that this mechanism is of fundamental importance for the Fe II production in the BLR. Sigut & Pradhan (1998) show that the key feature to characterize the Ly$\alpha$-fluorescence was the NIR Fe II bump at $\lambda$9200 Å. The bulk of the Fe II emission in this region would cause a rise in the optical and UV emission through the fluorescence process. Rodriguez-Ardila et al. (2002) were the first to identify such transitions in a small sample of 4 AGN.

Due to the complexity and uncertainties in the Fe II transition the most efficient way to study this emission is through empirical templates, constructed from observed spectra. The discovery of Boroson & Green (1992) that the relative intensity of the Fe II emission lines remains roughly constant from source to source, independent from luminosity, allowed them to create and apply an Fe II template to large samples of quasars (Boroson & Green 1992, Kovacevic et al. 2010, Kovacevic et al. 2015, Shen et al. 2011, Shen & Ho 2014, Rakshit et al. 2017). Boroson & Green (1992) used the optical spectrum of I Zw 001 to construct an Fe II template for the region between $\lambda\lambda$4400–5600 Å. Their approach was to model and subtract all unidentified emission lines but Fe II. The remaining spectrum was a pure Fe II emission template. Veron-Cetty et al. (2004) extended this concept to the entire optical region, successfully reproducing the Fe II emission for more than 4000 AGN (Hu et al. 2008, Dong et al. 2011). Vestergaard & Wilkes (2001) extended this template to the UV, using a high resolution Hubble Space Telescope (HST) spectrum of I Zw 001.

Almost one decade later, Garcia-Rissmann et al. (2012) used a moderate resolution spectrum of I Zw 001 combined with the theoretical model of Sigut & Pradhan to develop the first semi-empirical NIR Fe II template. This template was able to reproduce the NIR Fe II emission in Ark 564, another NLS1 known by its strong Fe II emission (Joly 1991, Rodriguez-Ardila et al. 2002). As in the optical region, they found that NIR Fe II emission also forms a pseudo-continuum in the wavelength range 8800–11600 Å. On the other hand, the NIR Fe II emission shows strong isolated or moderately blended lines, allowing an accurate characterization of its profiles and to compare with other prominent lines emitted by the BLR. This makes the NIR region a powerful tool in the study of the Fe II emission, with the possibility of constraining the most likely Fe II emitting region.

## 1.5 High Redshift Radio Galaxies

High redshift radio galaxies (HzRG) are powerful sources of energetic outputs at radio frequencies. As the quasars their power is driven by the accretion of matter onto SMBH in the nuclei of massive galaxies. Radio galaxies are among the most luminous sources in the universe. Their powerful radio emission ($L_{500MHz} > 10^{27}$ W Hz$^{-1}$) rises from a non-thermal spectrum in a usually extend morphology reaching $\sim 10^2$Kpc (Miley & De Breuck 2008).

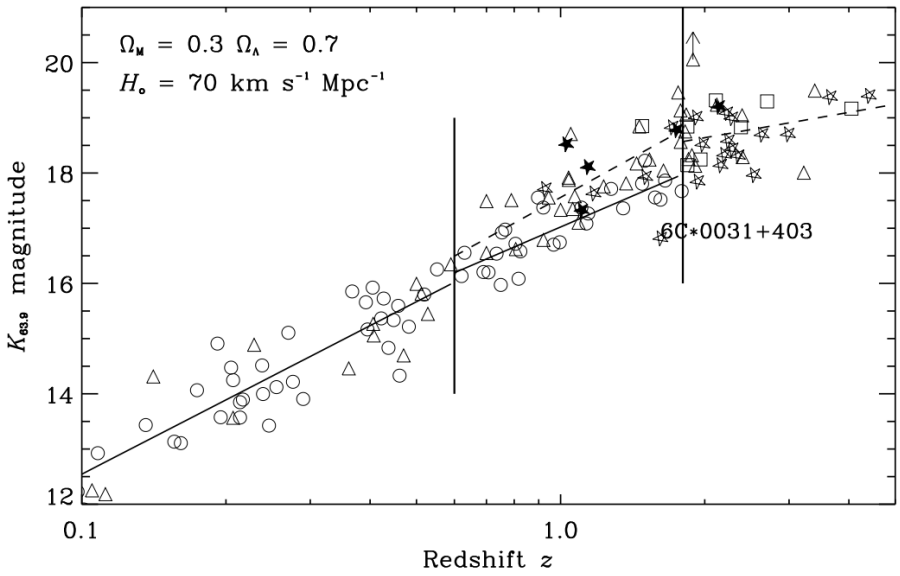


FIGURE 1.10. $K-z$-diagram for radio galaxies from the 3CRR (circles, 6DE (triangles), 6C* (stars) and 7C–III (squares) samples. Figure from Jarvis et al. (2001)

Distant radio galaxies started to call attention after the discovery of Cygnus A (Baade & Minkowski 1954). Due to the observational limitations early finds of high redshift radio sources were at maximum at $z \sim 0.45$. The increase of telescope sizes made it possible explore even more distant radio galaxies at $z \sim 1$ (Spinrad 1977). With the evolution of the optical CCD detectors HzRG were discovered up to $z \sim 4$ (De Breuck et al. 1999, De Breuck et al. 2001). Evolution in the search techniques, such as the photometric dropout method and narrow band search of Lyman alpha sources, allowed the discovery of several other HzRG. Until recently the most distant radio galaxy observed was at $z = 5.19$. (van Breugel et al. 1999, Jarvis et al. 2009, Waddington et al. 1999).

One of the most interesting relations of HzRG is the $k-z$ relation (Laing et al. 1983). Results from Dunlop & Peacock (1993) using the 3CRR sample showned a correlation between the $K$-band emission from radio sources and their radio luminosity. Eales et al. (1997) measured the dispersion in the $K$-band magnitude and their results showed and increase of the latter with redshift. The high end of the $K-z$ diagram suggests that this region probes the epoch of formation of massive radio galaxies. Figure 1.10 shows the $k-z$-diagram. Supporting this result, van Breugel et al. (1998) found that the NIR colors of HzRG (at $z > 3$) are very blue, which indicates the presence of young stellar populations. Moreover, Lacy et al. (2000) found that radio galaxies hosts are more luminous at higher redshift in the 7C–III sample, indicating a passive evolution of the population formed at redshift higher than 3.

Finding HzRG is quite challenging. The luminous steep-spectrum of radio galaxies typically has $L_{2.7GHz} > 10^{33}$erg s$^{-1}$ and the number density for this luminosity is smaller than $10^{-7}$ Mpc$^{-3}$

in the redshift range of $2 < z < 5$ (Dunlop & Peacock 1990, Venemans et al. 2007). The number density peak at $z \sim 2$ corresponds to an important age of the universe when quasars also had their maximum peak density, the star formation reached its peak and galaxy clusters started to form (Fan et al. 2001, Madau et al. 1998, Hickock et al. 2011). Finding HzRG is a task that requires several techniques, involving filtering large radio samples, removing background sources, improving the astrometric accuracy and finally confirming the redshift via spectroscopic observations. Low frequency radio observations contain radio sources in a wide range of redshift. To separate HzRG candidates typically two criteria are used, sources with ultra-steep spectrum and small angular sizes (Röttgering et al. 1994, De Breuck et al. 2000, De Breuck et al. 2004). Once these sources are selected, a cross-match with optical and NIR catalogs are used to discard bright and likely nearby sources. Then, accurate astrometric identification on arcsecond scale in the NIR $K$-band is made to identify faint host galaxies (Cruz et al. 2004). At this point an initial lower limit for the redshift can be estimated using the $K-z$-relation. Finally, follow up observations using optical and/or NIR spectroscopy of the candidates will reveal the real redshift of the source by comparing the emission lines in the spectrum (De Breuck et al. 2001, Jarvis et al. 2001, Bornancini et al. 2007). Typically only two different emission lines are needed in this last step. Since the wavelength ratio of the lines remains constant with redshift, comparing this quantity will give the redshift of the source.

## 1.6 In This Thesis

AGN are among the most bright, massive, and amazing objects in the universe. Their role in the formation and evolution of large scale structure makes them important for understanding the universe from its beginning, to the reionization epoch and to local galaxies. Despite its importance a lot of details on the structure and evolution of AGN remains under debate. For instance, their most central region hosting the SMBH and BLR, is still out of reach of observational techniques, and its analysis is crucial to understanding how the AGN works. The early birth and growth of obscured high redshift radio galaxies are fundamental pieces to understanding the reionization epoch and galaxy evolution. Massive and highly accreting quasars observed at redshifts $2-7$ pose a challenge to our understanding of the growth of SMBH. We will address several of these problems in this thesis. Our goal is to contribute by studying low and high redshift AGN to better understand their internal structure and how they evolve.

The crucial point to study AGN in low and high redshift is the large amount of information we can get from the synergy of these two cosmic times. The analysis of the three topics presented in the next three chapters will give us a deep understanding of the AGN and their role in the universe. The approach taken here is cyclic in the sens that studying low redshift AGN gives access to a their internal structure, e.g. BLR, NLR and SMBH. This knowledge is extended to high redshfit quasars and radio galaxies to understand their formation, physical structure,

evolution and impact in their surrounding environment in large scale. The understanding of these parameters allow us to see how the low redshift AGN are placed in the universe. In this context in the chapter 2 we study the physical properties of a sample of low redshift AGN in order to understand their physical structure. The large wavelength coverage available for these AGN can probe several parts of their structure, from the inner and most energetic region within the BLR (through the UV) to the outer and low ionization ruled portion of this region (through the optical and NIR). The host galaxy can be also studied in this redshift. The knowledge of low redshift AGN (Seyfert, quasars and local radio galaxies) is applicable to the high redshift radio galaxies in order to understand their physical properties, as presented in chapter 3. The high redshift quasars of the sample presented in chapter 4 allow us understand how massive elliptical galaxies form and how their BH evolve to their $10^{10}M_{\odot}$. Moreover, local massive galaxies live in dense clusters, and the analysis of the environment of the quasars in $z \sim 2$ allow us understand how the large overdense regions around them evolve to mentioned local structures. After the introduction to topics of this thesis presented above in chapter 1 the structure of this thesis is as follows

In chapter 2 we analyse a sample of 25 low redshift Seyfert galaxies and quasars in the NIR in order to better understand the BLR, in particular its Fe II emission. Since this emission arises from the BLR and can not be spatially or spectroscopically resolved its study is made through templates. Despite of the success of the template there are still unresolved questions, such as the excitation mechanism and the location of the emitting region. This emission contains important clues about the physics of the BRL and is the main contaminant agent in type-I AGN, especially when observed in low S/N spectra, such as for high redshift quasars. Despite several studies of the Fe II emission in large samples in the optical, NIR analysis of this emission is not very common. The NIR offers several advantages over the optical wavelength, such as isolated BLR lines. Our goal in this chapter is: (i) characterize the AGN Fe II emission using a template from the literature in the optical and NIR region – allowing us to quantify the multiwavelength emission; (ii) compare the optical and NIR Fe II emission – using the template we can analyse the Fe II and determine what excitation mechanisms are behind its production; (iii) Characterize and compare the Fe II line profiles with other BLR lines – because the Fe II lines are isolated in the NIR this will provide us with a much more accurate description of the BLR; (iv) Find the probable location where the Fe II is emitted – this is possible by comparing the Fe II line width with at of other lines and from reverberation mapping results.

In chapter 3 we present the discovery of the most distant radio galaxy observed. HzRG are obscured AGN characterized by strong radio luminosity. The study of HzRG offers important probes of several aspects of AGN. For instance, they present a unique opportunity to study the host galaxy, which is typically not possible for quasars. Moreover, their high redshift nature puts them close to the reionization epoch, and follow up radio spectroscopy can be used to give cosmological constraints. In this chapter we: (i) report the discovery of the radio galaxy

TGSS J1503+1049, at $z = 5.72$ – This galaxy is the most distant radio galaxy to date; (ii) Use optical spectroscopy, combined with multi-band image observations to set accurately its redshift; (iii) Characterize its line emission and radio emission and discuss its properties; (iv) Constrain its stellar mass and place it in the galaxy evolution scenario.

In chapter 4 we analyse a sample of 35 high redshift radio loud quasars from the CARLA survey in order to analyse their SMBH. Single epoch black hole masses using optical spectra are estimated from H$\alpha$ and H$\beta$ lines for low redshift quasars, and Mg II for intermediate redshift up to $z = 2$. Above this redshift the BH estimates are made using the C IV lines. With the SDSS survey thousands of high redshift quasars had their BH masses estimated with C IV. This line, however, is the least reliable SE BH mass estimator since it is affected by non-gravitational broadening effects. This lack of accuracy is problematic when analysing the evolution and properties of BHs. In this chapter we use NIR $K$-band observations from VLT/SINFONI in a sub-sample of quasars from CARLA in order to accurately estimate their BH masses. Our goal here is threefold: (i) use these new measurements to derive several properties of the BHs, such as their accretion rate and growth histories. (ii) look for correlations between these properties and the radio power of the quasars; and (iii) revisit the correlation between the BH mass and the environment of the quasar. In this chapter we also present an extensive study of the methods to estimate BH masses and the corrections that can be applied to the C IV-method to match BH masses based on H$\alpha$.

In chapter 5 we present a summary of this thesis and the main results from the three previous chapters.

CHAPTER 2

# THE FE II EMISSION IN ACTIVE GALACTIC NUCLEI: EXCITATION MECHANISMS AND LOCATION OF THE EMITTING REGION

**M. Marinello** [1], A. Rodríguez-Ardila [2], A. Garcia-Rissman [2],
T. T. A. Sigut [3], A. K. Pradhan [4]

[1] Observatório Nacional, Rua José Cristino, 77. CEP 20921-400, São Cristóvão, Rio de Janeiro-RJ, Brazil
[2] Laboratório Nacional de Astrofísica, Rua Estados Unidos 154, Itajubá, MG, 37504-364, Brazil
[3] The University of Western Ontario, London, ON N6A 3K7, Canada
[4] McPherson Laboratory, The Ohio State University, 140 W. 18th Ave., Columbus, OH 43210-1173, USA

Published in the Astrophysical Journal, 2016, 820, 116M

We present a study of Fe II emission in the near-infrared region (NIR) for 25 active galactic nuclei (AGNs) to obtain information about the excitation mechanisms that power it and the location where it is formed. We employ an NIR Fe II template derived in the literature and find that it successfully reproduces the observed Fe II spectrum. The Fe II bump at 9200 Å detected in all objects studied confirms that Ly$\alpha$ fluorescence is always present in AGNs. The correlation found between the flux of the 9200 Å bump, the 1 $\mu$m lines, and the optical Fe II implies that Ly$\alpha$ fluorescence plays an important role in Fe II production. We determined that at least 18% of the optical Fe II is due to this process, while collisional excitation dominates the production of the observed Fe II. The line profiles of Fe II $\lambda$10502, O I $\lambda$11287, Ca II $\lambda$8664, and Pa$\beta$ were compared to gather information about the most likely location where they are emitted. We found that Fe II, O I and Ca II have similar widths and are, on average, 30% narrower than Pa$\beta$. Assuming that the clouds emitting the lines are virialized, we show that the Fe II is emitted in a region twice as far from the central source than Pa$\beta$. The distance, though, strongly varies: from 8.5 light-days for NGC 4051 to 198.2 light-days for Mrk 509. Our results reinforce the importance of the Fe II in the NIR to constrain critical parameters that drive its physics and the underlying AGN kinematics, as well as more accurate models aimed at reproducing this complex emission.

## 2.1 Introduction

The broad-line region (BLR) in active galactic nuclei (AGNs) has been extensively studied from X-rays to the near-infrared region (NIR) during recent decades (see Gaskell 2009, for a review), but several aspects about its physical properties remain under debate. That is the case of the Fe II emission, whose numerous multiplets form a pseudo-continuum that extends from the ultraviolet (UV) to the NIR owing to the blending of over 344,000 transitions Bruhweiler & Verner 2008), although it is not clear that even that number of lines could denote adequate coverage. This emission is significant for at least four reasons: (i) It represents one of the most conspicuous cooling agents of the BLR, emitting about 25% of the total energy of this region (Wills et al. 1985). (ii) It represents a strong contaminant because of the large number of emission lines. Without proper modeling and subtraction, it may lead to a wrong description of the BLR physical conditions. (iii) The gas responsible for the Fe II emission can provide important clues on the structure and kinematics of the BLR and the central source. However, despite the extensive study of the Fe II emission(Popovic et al. 2007; Sluse et al. 2007; Hu et al. 2008; Kuehn et al. 2008; Matsuoka et al. 2008; Kovacevic et al. 2010),the strong blending of the lines prevents an accurate study of its properties and excitation mechanisms. (iv) The strength of Fe II relative to the peak of [O III], the so-called Eigenvector 1 (E1), which consists of the dominant variable in the principal component analysis presented by Boroson & Green (1992), is believed to be associated with important parameters of the accretion process (Boroson & Green 1992; Sulentic et al. 2000).

Owing to its complexity and uncertainties in transition probabilities and excitation mechanisms, the most successful approach to model the Fe II emission in AGNs consists of deriving empirical templates from observations. Among the most successful templates for the optical region are the ones of Boroson & Green (1992) and Veron-Cetty et al. (2004), which were developed using the spectrum of I Zw 1, the prototype of NLS1 that is widely known for its strong iron emission in the optical and UV regions (Joly 1991; Lawrence et al. 1997; Rudy et al. 2000; Tsuzuki et al. 2006; Bruhweiler & Verner 2008). Other works also successfully employ templates to quantify the optical Fe II emission in larges samples of AGNs (Tsuzuki et al. 2006; Popovic et al. 2007; Dong et al. 2010, 2011; Kovacevic et al. 2010). For the UV region, Vestergaard & Wilkes (2001) extended the Fe IItemplate using Hubble Space Telescope (HST)/FOS spectra of I Zw 1, presenting the first UV template for this emission.

Two decades after the seminal work by Boroson & Green (1992) on the optical Fe II emission template, the first semi-empirical NIR Fe II template was derived by Garcia-Rissmann et al. (2012) using a mid-resolution spectrum of I Zw 1 and theoretical models of Sigut et al. (2004) and Sigut & Pradhan (2003). They successfully modeled the Fe II emission in that galaxy and in Ark 564, another NLS1 known for its conspicuous iron emission (Joly 1991; Rodriguez-Ardila et al. 2002). Similar to the optical, they found that the Fe IIspectrum in the NIR forms a subtle pseudo-continuum that extends from 8300 up to 11800 Å. However, unlike in the optical, the NIR Fe IIspectrum displays prominent lines that can be fully isolated, allowing the characterization of Fe II emission line profiles and its comparison to other BLR emission features. That property confers an advantage to the NIR over the optical, making the Fe II emission in that region a powerful tool to study and understand this complex emission. It can be used, for instance, to observationally constrain the most likely location of the region emitting this ion. Previous works in the NIR carried out on a few targets (Rodriguez-Ardila et al. 2002) suggest that the Fe II lines are preferentially formed in the outer part of the BLR. Studies on a larger number of sources are necessary to confirm this trend and compare it to results obtained in the optical (Boroson & Green 1992; Popovic et al. 2007; Kovacevic et al. 2010).

Despite the wide and successful use of templates to reproduce, measure, and subtract the Fe II emission in AGNs (Boroson & Green 1992; Vestergaard & Wilkes 2001; Veron-Cetty et al. 2004; Garcia-Rissmann et al. 2012), attempts on determining the mechanisms that drive this emission continue to be an open issue. Current models (Verner et al. 1999; Baldwin et al. 2004; Bruhweiler & Verner 2008) include processes such as continuum fluorescence, collisional excitation, and self-fluorescence among Fe II transitions. They are successful at reproducing the emission-line strengths for the UV and optical lines, but results for the NIR are not presented, very likely because the relevant transitions in that region are not included. Penston (1987) proposed that Ly$\alpha$ fluorescence could be a key process involved in the production of Fe II. Indeed, models developed by Sigut & Pradhan (1998, 2003) and Sigut et al. (2004) showed that this mechanism is of fundamental importance in determining the strength of Fe II in the NIR. The

key feature that would reveal the presence of such a mechanism is the detection of the Fe II blend at 9200 Å, first identified by Rodriguez-Ardila et al. (2002) in AGNs. The bulk of this emission would be produced by primary cascades from the upper $5p$ levels to $e^4D$ and $e^6D$ levels after the capture of an Ly$\alpha$ photon.

Additional NIR features resulting from secondary cascading after the Ly$\alpha$ fluorescence process are the so-called 1 $\mu$m Fe II lines ($\lambda$9997, $\lambda$10502, $\lambda$10862, and $\lambda$11127), which are the most prominent Fe II features in the whole 8000–24000 Å region (Sigut & Pradhan 2003; Pradhan & Nahar 2011). The importance of the 1 $\mu$m lines resides in the fact that they are produced by the decay of the $e^4D$ and $e^6D$ levels down to the $z^4D^0$ and $z^4F^0$ levels. Transitions downward from the latter two populate the upper levels responsible for nearly 50% of all optical Fe II emission (Veron-Cetty et al. 2004). If Ly$\alpha$ fluorescence plays a key role as an excitation mechanism of Fe II in AGNs, a direct correlation should be observed between the strength of the 9200 Å blend and the 1 $\mu$m Fe II lines in the NIR. This issue should be investigated in detail because it can provide useful constraints to the Fe II problem.

In this paper, we describe for the first time a detailed application of the semi-empirical NIR Fe II template developed by Garcia-Rissmann et al. (2012) to a sample of 25 AGNs. The aims are threefold: (i) provide a reliable test for the NIR Fe II template and verify its capability to reproduce the numerous Fe II emission lines in a sample of Type 1 AGNs, (ii) measure the NIR Fe II flux and compare it to that of the optical region to confirm model predictions of the role of Ly$\alpha$ fluorescence in the total Fe II strength, and (iii) compare the Fe II emission line profiles with other broad line features to probe the BLR structure and kinematics.

This paper is structured as follows: Section 2 describes the observations and data reduction. Section 3 presents the methodology adopted to convolve the NIR Fe II template and its application to the galaxy sample and results. Section 4 discusses the excitation mechanisms of the NIR Fe II emission. Section 5 discusses the kinematics of the BLR based on the Fe II lines and other BLR emission, as well the distance of the Fe II emission line region. Conclusions are given in Section 6.

## 2.2 Observations and Data Reduction

The 25 AGNs that compose our sample were selected primarily from the list of Joly (1991), who collected data for about 200 AGNs (Seyfert 1 and quasars) to study the relationship between Fe II and radio emission. Additional selection criteria were applied to that initial sample, such as that the targets have to be brighter than $K = 12$ mag to obtain a good compromise between signal-to-noise ratio (S/N) and exposure time for the NASA 3 m Infrared Telescope Facility (IRTF) atop Mauna Kea. We also applied the restriction that the FWHM of the broad H$\beta$ component of the galaxies be smaller than 3000 km s$^{-1}$ in order to avoid severe blending of the Fe II lines with adjacent permitted and forbidden features. Because of the last criterion, our final sample was naturally dominated by narrow-line Seyfert 1 galaxies. Basic information for the galaxy sample

is listed in Table 2.1.

The NIR observations and data reduction for the above sample will be described first. Noncontemporaneous optical and UV spectroscopy obtained mostly from archival data (as well as pointed observations) was also collected for most sources of the sample for the purpose of assessing the optical and UV Fe II emission. Since the data reduction of the latter data was described elsewhere, we will discuss here only their sources and any particular issue we found interesting to mention.

Table 2.1: Basic Information on the IRTF Observations.

| AGN | Type | z | Date | Exp. Time(s) | E(B-V)$_G$ |
|---|---|---|---|---|---|
| Mrk 335 | NLS1 | 0.02578 | 2000 Oct. 21 | 2400 | 0.030 |
| I Zw 1 | NLS1 | 0.06114 | 2003 Oct. 23 | 2400 | 0.057 |
| Ton S180 | NLS1 | 0.06198 | 2000 Oct. 11 | 2400 | 0.013 |
| Mrk 1044 | NLS1 | 0.01645 | 2000 Oct. 11 | 1800 | 0.031 |
| Mrk 1239 | NLS1 | 0.01927 | 2002 Apr. 21 | 1920 | 0.065 |
| | | | 2002 Apr. 23 | 1920 | |
| Mrk 734 | S1 | 0.05020 | 2002 Apr. 23 | 2400 | 0.029 |
| PG 1126-041 | QSO | 0.06000 | 2002 Apr. 23 | 1920 | 0.055 |
| | | | 2002 Apr. 24 | 2160 | |
| H 1143-182 | S1 | 0.03330 | 2002 Apr. 21 | 1920 | 0.039 |
| NGC 4051 | NLS1 | 0.00234 | 2002 Apr. 20 | 1560 | 0.013 |
| Mrk 766 | NLS1 | 0.01330 | 2002 Apr. 21 | 1680 | 0.020 |
| | | | 2002 Apr. 25 | 1080 | |
| NGC 4748 | NLS1 | 0.01417 | 2002 Apr. 21 | 1680 | 0.052 |
| | | | 2002 Apr. 25 | 1440 | |
| Ton 156 | QSO | 0.54900 | 2002 Apr. 25 | 3600 | 0.015 |
| PG 1415+451 | QSO | 0.11400 | 2002 Apr. 24 | 3960 | 0.009 |
| | | | 2002 Apr. 25 | 1440 | |
| Mrk 684 | S1 | 0.04607 | 2002 Apr. 21 | 1440 | 0.021 |
| Mrk 478 | NLS1 | 0.07760 | 2002 Apr. 20 | 3240 | 0.014 |
| PG 1448+273 | QSO | 0.06522 | 2002 Apr. 24 | 2160 | 0.029 |
| PG 1519+226 | QSO | 0.13700 | 2002 Apr. 25 | 4000 | 0.043 |
| Mrk 493 | NLS1 | 0.03183 | 2002 Apr. 20 | 1800 | 0.025 |
| | | | 2002 Apr. 25 | 900 | |
| PG 1612+262 | QSO | 0.13096 | 2002 Apr. 23 | 2520 | 0.054 |
| Mrk 504 | NLS1 | 0.03629 | 2002 Apr. 21 | 2100 | 0.050 |
| 1H 1934-063 | NLS1 | 0.01059 | 2004 Jun. 02 | 2160 | 0.293 |
| Mrk 509 | S1 | 0.34397 | 2003 Oct. 23 | 1440 | 0.057 |
| | | | 2004 Jun. 01 | 2160 | |
| 1H 2107-097 | S1 | 0.02652 | 2003 Oct. 23 | 1680 | 0.233 |
| Ark 564 | NLS1 | 0.02468 | 2002 Oct. 10 | 1500 | 0.060 |
| | | | 2003 Jun. 23 | 2160 | |
| NGC 7469 | S1 | 0.01632 | 2003 Oct. 23 | 1920 | 0.069 |

### 2.2.1 Near-infrared Data

NIR spectra were obtained at IRTF from 2002 April to 2004 June. The SpeX spectrograph (Rayner et al. 2003) was used in the short cross-dispersed mode (SXD, 0.8–2.4 $\mu$m). In all cases, the detector employed consisted of a 1024×1024 ALADDIN 3 InSb array with a spatial scale of 0.15"pixel$^{-1}$. A 0.8×15 slit was used giving a spectral resolution of 360 km s$^{-1}$. This value was determined from both the arc lamp spectra and the skyline spectra and was found to be constant with wavelength within 3%. During the different nights, the seeing varied between 0.7" and 1". Observations were done nodding in an ABBA source pattern along the slit with typical integration times from 120 to 180 s per frame and total on-source integration times between 35 and 50 minutes. Right before/after the science frames, an A0V star was observed near each target to provide a telluric standard at similar airmass. It was also used to flux-calibrate the corresponding object.

The spectral reduction, extraction, and wavelength calibration procedures were performed using SPEXTOOL, the inhouse software developed and provided by the SpeX team for the IRTF community (Cushing et al. 2004). One-dimensional (1D) spectra were extracted using an aperture window of 0.8" in size, centered at the peak of the light distribution. Because all objects of the sample are characterized by a bright central nucleus compared with the galaxy disk, the light profile along the spatial direction was essentially point-like. Under this assumption, SPEXTOOL corrects for small shifts due to atmospheric diffraction in the position of the light peak along the different orders.

The extracted galaxy spectra were then corrected for telluric absorption and flux-calibrated using Xtellcor (Vacca et al. 2003), another inhouse software developed by the IRTF team. Finally, the different orders of each science spectrum were merged to form a single 1D frame. It was later corrected for redshift, determined from the average $z$ measured from the positions of [S III] $\lambda$9531, Pa$\gamma$, He I $\lambda$10830, Pa$\beta$ and Br$\gamma$. Galactic extinction corrections, as determined from the COBE/IRAS infrared maps of Schlegel et al. (1998), were applied for each target. The value of the Galactic E(B–V) used for each galaxy is listed in column (6) of Table 2.1.

### 2.2.2 Optical and Ultraviolet Data

Optical spectroscopy for a subsample of objects was obtained from different telescopes, including archival data from SDSS and HST, as well as our own observations. Column (2) of Table 2.2 lists the source of the optical spectroscopy. The purpose of these spectra is to determine the integrated flux of the Fe II blend centered at 4570 $\mu$m and H$\beta$, as well as $R_{4570}$, the flux ratio Fe II $\lambda$4570/H$\beta$.

In addition, UV spectroscopy for a subsample of sources taken with HST is also employed to compare the emission-line profiles of Fe II and other BLR features, including some high-ionization permitted lines.

As our interest is in the emission-line spectrum, it is necessary to remove the strong continuum emission in the optical and NIR, assumed to be primarily from the central engine. To

this purpose, we fit a polynomial function to the observed continuum using as anchor points regions free of emission lines and subtract it from the spectrum. Figure 2.1 shows an example of this procedure applied to 1H 1934-63A. This procedure proved to be successful for our purposes. The analysis of the individual continuum components (i.e., AGN, dust, and stellar population) is beyond the scope of this paper, so no effort was made at interpreting the physical meaning of the fit.

Table 2.2: Optical and UV data obtained from the literature.

| AGN | Optical data | UV data |
|---|---|---|
| Mrk 335 | Casleo | - |
| I Zw 1 | Casleo | HST FOS |
| Ton S180 | Casleo | HST STIS |
| Mrk 1044 | Casleo | HST COS |
| Mrk 1239 | Casleo | |
| Mrk 734 | KPNO | - |
| H 1143-182 | Casleo | - |
| NGC 4748 | Casleo | - |
| Ton 156 | SDSS | - |
| PG 1415+451 | SDSS | HST FOS |
| Mrk 478 | KPNO | HST FOS |
| PG 1448+273 | SDSS | - |
| PG 1519+226 | SDSS | - |
| Mrk 493 | SDSS | HST FOS |
| PG 1612+262 | SDSS | HST FOS |
| 1H 1934-063 | Casleo | - |
| Mrk 509 | - | HST COS |
| 1H 2107-097 | Casleo | - |
| NGC 7469 | Casleo | - |

In none of the cases were the NIR spectroscopy and optical/UV spectroscopy contemporaneous. Therefore, no effort was made to match the continuum emission in the overlapping regions of the spectra (i.e., NIR and optical and UV and optical) because of variability, seeing, and aperture effects. However, since the optical data are used to provide quantities to be compared to the NIR, it is important to consider variability effects on the emission lines that are being analyzed. Few works in the literature, though, have found optical Fe II variability, and the overall statistics are scarce.

Giannuzzo & Stirpe (1996), for example, reported variations of the Fe II bump at 5200 $\mu$m of less than 15%. Dietrich et al. (1993) detected no significant variations in the Fe II lines in NGC 5548. Bischoff & Kollatschny (1999) found that optical Fe II lines remained constant over a 10 yr monitoring campaign, even when the Balmer lines and continuum were seen to vary over a range of 2–5. Wang et al. (2005) found that the Fe II variations in NGC 4051 correlate with variations in the continuum and the H$\beta$ line. Similar results were found by Shapovalova et al.

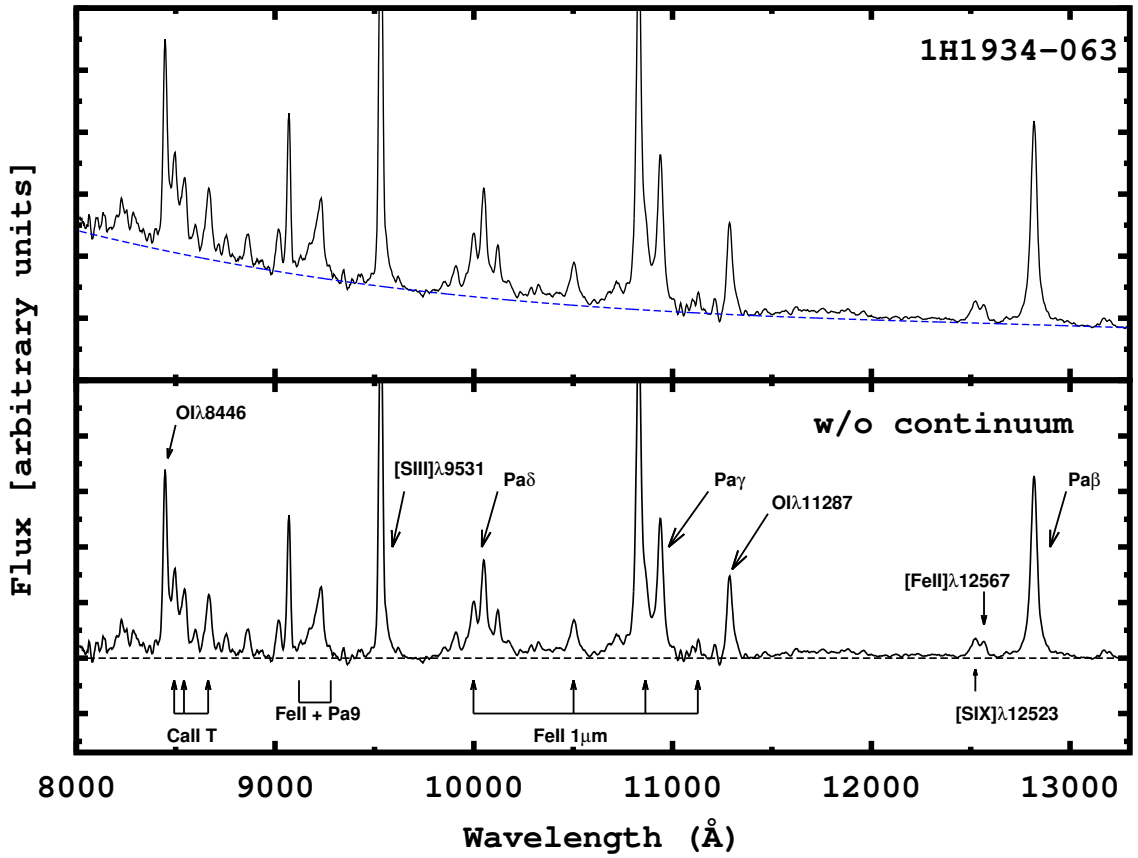


FIGURE 2.1. Example of continuum subtraction and the most relevant emission lines used in this work. Top panel: observed spectrum of 1H 1934–063 (in the rest frame)and the continuum fit (blue dashed line). Bottom panel: spectrum of 1H 1934–063 without the continuum. The black arrows point to the most relevant lines for this paper. The dashed black line indicates the zero continuum level.

(2012) for Ark 564.

Few AGNs show strong Fe II variations (larger than 50%), particularly in very broad line objects (FWHM of H$\beta > 4000\,\mathrm{km\,s^{-1}}$; Kollatschny et al. 1981; Kollatschny & Fricke 1985; Kollatschny et al. 2000). For example, Kuehn et al. (2008) carried out a reverberation analysis of Ark 120. They were unable to measure a clean reverberation lag for this object. Barth et al. (2013), though, detected Fe II reverberation for two broad-line AGNs, Mrk 1511 and NGC 4593, using data from the LICK AGN Monitoring Project. They found variability with an amplitude lower than 20% relative to the mean flux value. In addition, Hu et al. (2015) report the detection of significant Fe II time lags for a sample of nine NLS1 galaxies in order to study AGNs with high accretion rates. Difficulties in detect variations in the Fe II bump at 4570 $\mu$m are usually ascribed

to residual variations of the He II $\lambda$4686, which is blended with Fe II in this wavelength interval (Kollatschny & Dietrich 1996).

The general scenario that emerges from these works is that the amplitude of the Fe II variability (when it varies) in response to continuum variations is much smaller than that of H$\beta$. Indeed, the latter line is widely known to respond to continuum variability (Peterson et al. 1998, 2004; Kaspi et al. 2000; Kollatschny et al. 2000, 2006). Kollatschny et al. (2006) analyzed this effect using a sample of 45 AGNs in order to study the BLR structure. Considering the mean values of all fractional variabilities presented in their work as representative of the variability effect in our sample, we estimate an uncertainty of ~ 11% on the optical fluxes due to variability. This value is also in good agreement with the results of Hu et al. (2015), which found an average fractional variability of 10% for Fe II when compared with H$\beta$. This value is within the error in the line fluxes measured in this work; therefore, we conclude that variability is unlikely to impact our results.

## 2.3 Analysis Procedure

### 2.3.1 NIR Fe II Template Fitting

Modeling the Fe II pseudo-continuum, formed by the blending of thousands of Fe II multiplets, has remained a challenge for the analysis of this emission since it was first observed by Wampler & Oke (1967). Sargent (1968) noted that I Zw 1, for instance, had the same kind of emission but with stronger and narrower lines. The strength of the Fe II lines in that AGN made it a prototype of the strong Fe II emitters, as well as of the NLS1 subclass of AGNs, leading to the development of empirical templates of this emission based on this source (Boroson & Green 1992; Vestergaard & Wilkes 2001; Veron-Cetty et al. 2004; Garcia-Rissmann et al. 2012).

Sigut & Pradhan (2003) and Sigut et al. (2004) presented the first Fe II model from the UV to the NIR using an iron atom with 827 fine-structure energy levels and including all known excitation mechanisms (continuum fluorescence via the UV resonance lines, self-fluorescence via overlapping Fe II transitions, and collisional excitation) that were traditionally considered by Wills et al. (1985) and Baldwin et al. (2004) in addition to fluorescent excitation by Ly$\alpha$ as suggested by Penston (1987). Their models incorporates photoionization cross sections (references in Sigut et al. 2004) that include a large number of autoionizing resonances, usually treated as lines but too numerous to count explicitly, which means that they include many more photoexcitation transitions than the 23,000 bound–bound lines and would form part of the pseudo- continuum. Moreover, in their work they show how the Fe II intensity varies as a function of the ionization parameter ($U_{ion}$),[1] the particle density ($n_H$), and the microturbulence velociy ($\zeta_t$). Details of all the physics involved in the calculations are in Sigut & Pradhan (2003). Landt et al. (2008) were

[1]The ionization parameter $U_{ion}$ is correlated with $\Phi_H$, the flux of hydrogen-ionizing photons at the illuminated face of the cloud, by $U_{ion} = \Phi_H / n_H\, c$

the first to confront these models with observations, noting some discrepancies between the model and the observed emission lines. Bruhweiler & Verner (2008), using an Fe II model with 830 energy levels (up to 14.06 $eV$) and 344,035 atomic transitions, found that the model parameters that best fit the observed UV spectrum of I Zw 1 were $log(\Phi_H = 20.5$, $log(n_H) = 11.0\,\mathrm{cm}^{-3}$, and $\zeta_t = 20\,\mathrm{km\,s}^{-1}$. Garcia-Rissmann et al. (2012) modeled the observed NIR spectrum of I Zw 1 using a grid of Sigut & Pradhan's templates covering several values of ionization parameters and particle densities, keeping the microturbulence velocity constant at $\zeta_t = 10\,\mathrm{km\,s}^{-1}$. They found that the model with $U_{\mathrm{ion}} = -2.0$ (implying $log(\Phi_H) = 21.1$) and $log(n_H) = 12.6\,\mathrm{cm}^{-3}$) best fit the observations. Note that these values are comparable to those found by Bruhweiler & Verner (2008), suggesting that the physical conditions of the clouds emitting Fe II are similar.

The template developed by Garcia-Rissmann et al. (2012) is composed of 1529 Fe II emission lines in the region between 8300 and 11600 Å. In order to apply it to other AGNs, it is first necessary to convolve it with a line profile that is representative of the Fe II emission. At this point we are only interested in obtaining a mathematical representation of the empirical profiles. In order to determine the optimal line width, we measured the FWHM of individual iron lines detected in that spectral region. We assumed that each Fe II line could be represented by a single or a sum of individual profiles and that the main source of line broadening was the Doppler effect.

The Fe II emission lines $\lambda$10502 and $\lambda$11127 are usually isolated and allow an accurate characterization of their form and width. The LINER routine (Pogge & Owen 1993), a $\chi^2$ minimization algorithm that fits up to eight individual profiles (Gaussians, Lorentzians, or a linear combination of them as a pseudo-Voigt profile) to a single or a blend of several line profiles, was used in this step. We found that a single Gaussian/Lorentzian profile was enough to fit the two lines above in all objects in the sample. However, the difference between the rms error for the Gaussian and Lorentzian fit was less than 5%, which lies within the uncertainties. As Fe II $\lambda$11127 is located in a spectral region with telluric absorptions, residuals left after division by the telluric star may hamper the characterization of that line profile. For this reason, we considered Fe II $\lambda$10502 as the best representation of the broad Fe II emission. Note that Garcia-Rissmann et al. (2012) argued that Fe II $\lambda$11127 is a better choice than Fe II $\lambda$10502 because the latter can be slightly broadened owing to a satellite Fe II line at 10490 Å. However, Fe II $\lambda$10490 is at least 5 times weaker relative to $\lambda$10502 (Rodríguez-Ardila et al. 2002; Garcia-Rissmann et al. 2012). Therefore, we adopted the $\lambda$10502 line as representative of the Fe II profile because it can be easily isolated and displays a good S/N in the entire sample. The flux and FWHM measured for this line are shown in columns (2) and (3), respectively, of Table 2.3.

For each object, a synthetic Fe II spectrum was created from the template using the FWHM listed in Table 2.3 and then scaled to the integrated line flux measured for the $\lambda$10502 line.

In order to ensure that the line width used to convolve the template best represented the FWHM of the Fe II emission region, we generated for each galaxy a grid of 100 synthetic spectra with small variations in the line width (up to 10% around the best value) for three different

functions (Gaussian, Lorentzian, and Voigt). In all cases, the value of the FWHM that minimized the rms error after subtraction of the template was very close (less than 1%) to the width found from the direct measurement of the $\lambda$10502 line. Also, the best profile function found in all cases was the same one that fitted initially. The final parameters of the convolution of the template for each source are shown in Table 2.4.

Figures 2.2–2.5 show the observed spectra and the template convolved with the best parameters (upper panels for each source). The iron-free spectra after subtraction of the modeled Fe II emission are shown in the bottom panels for each source. It can be seen that overall the template nicely reproduces the observed Fe II in all AGNs. We measure the rms error of the subtraction of the template using as reference the regions around the 1 $\mu$m lines. The mean rms error of the template subtraction is shown in column (4) of Table 2.4.

From the best-matching template we estimated the flux of the 1 $\mu$m lines. Columns (2)–(6) of Table 2.5 show the fluxes of each line. We define the quantity $R_{1\mu m}$ as the ratio between the integrated flux of the 1 $\mu$m lines and the flux of the broad component of Pa$\beta$. This value is presented in column (7) of Table 2.5. We consider this ratio as an indicator of the NIR Fe II strength in each object. Sources with weak Fe II emission are characterized by low values of $R_{1\mu m}$ (0.1–0.9), while strong Fe II emitters display values of $R_{1\mu m} > 1.0$.

Two features in the residual spectra (after subtraction of the Fe II emission) deserve comments. The first one is the apparent Fe II excess centered at 11400 $\mu$m that is detected in some sources. We identify this emission with an Fe II line because it was first identified in I Zw 1 but it is absent in sources with small $R_{4570}$. Therefore, its detection may be taken as an indication of a I Zw 1-like source. The 11400 Å feature is formed by a blend of eight Fe II lines, with those located at 11381.0 and 11402.0 Å being the strongest ones. They both carry 95% of the predicted flux of this excess. Garcia-Rissmann et al. (2012) had to modify it to properly reproduce the observed strength in that object because the best-matching Fe II model severely underestimated it. Nonetheless, when the template was applied to Ark 564, the feature was over-estimated. Our results show that the peak at 11400 Å is present only in the following objects: Mrk 478, PG 1126–041, PG 1448+273, Mrk 493, and Ark 564. In the remainder of the sample it is absent.

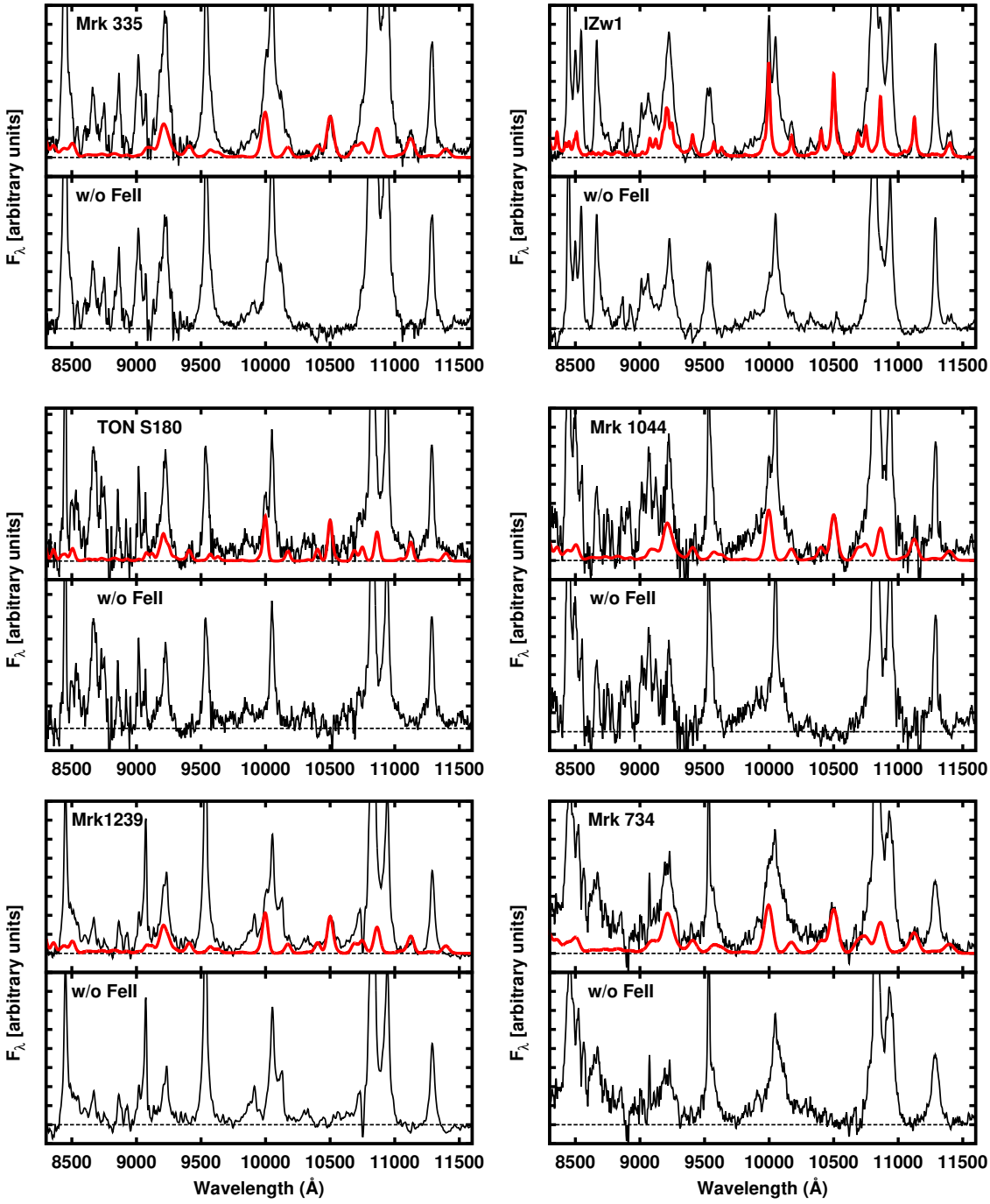


FIGURE 2.2. Top panels: continuum-subtracted spectrum (in the rest frame) of each object of the sample (black line), with the spectrum of Fe II calculated from the semi-empirical template (in bold) superposed. Bottom panels: spectrum of each object of the sample without this contribution.

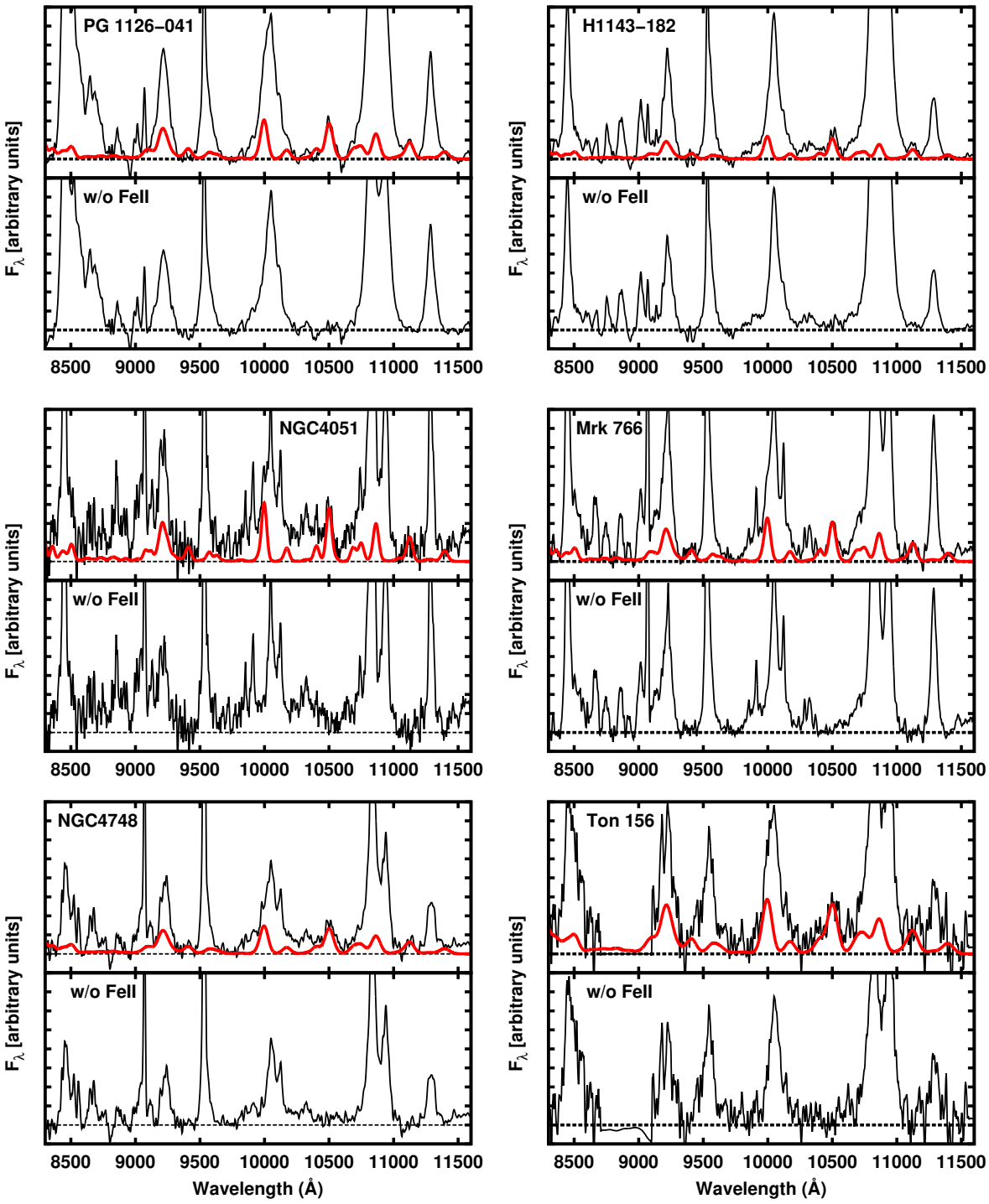


FIGURE 2.3. Continuation of Figure 2.2

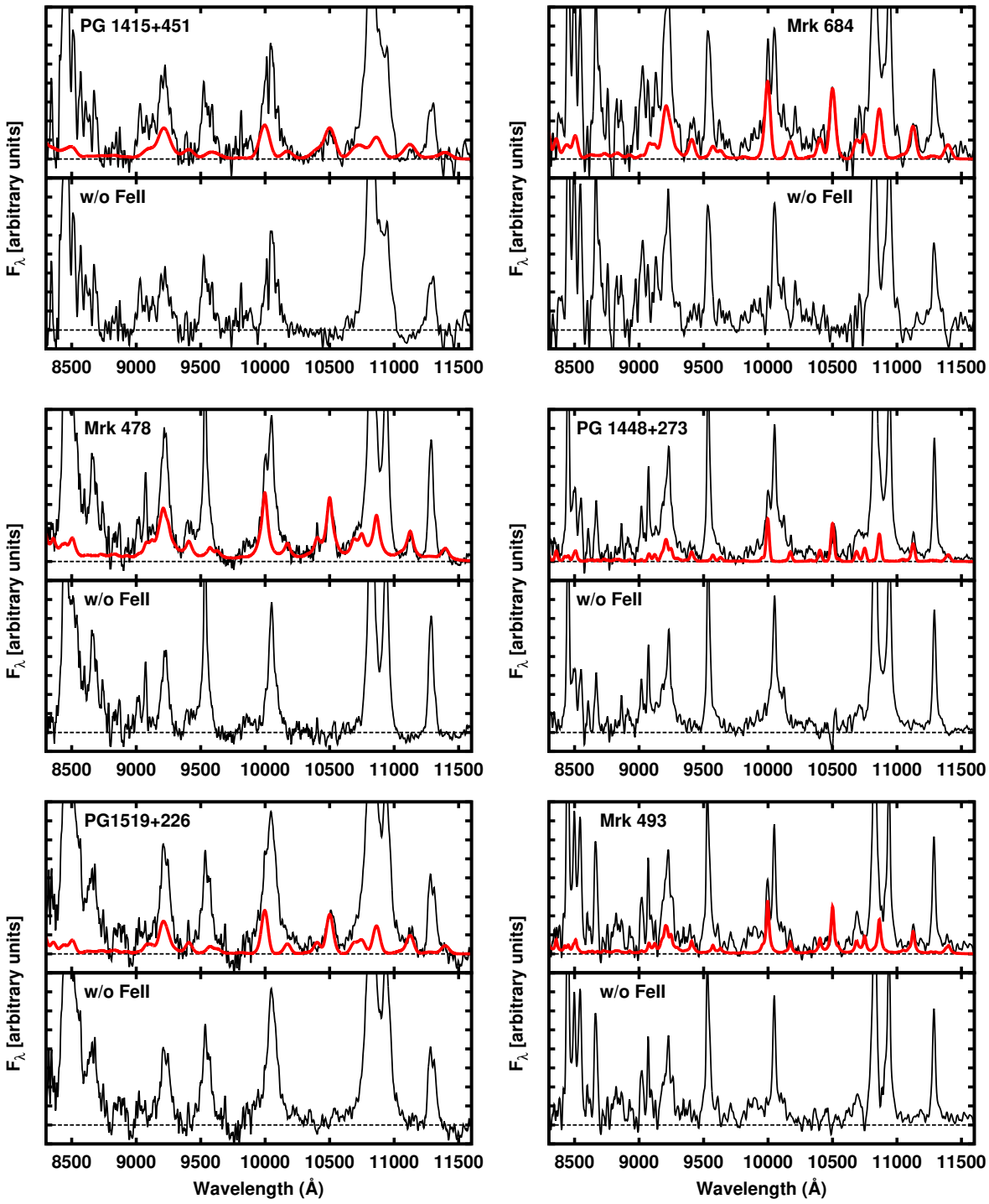


FIGURE 2.4. Continuation of Figure 2.2

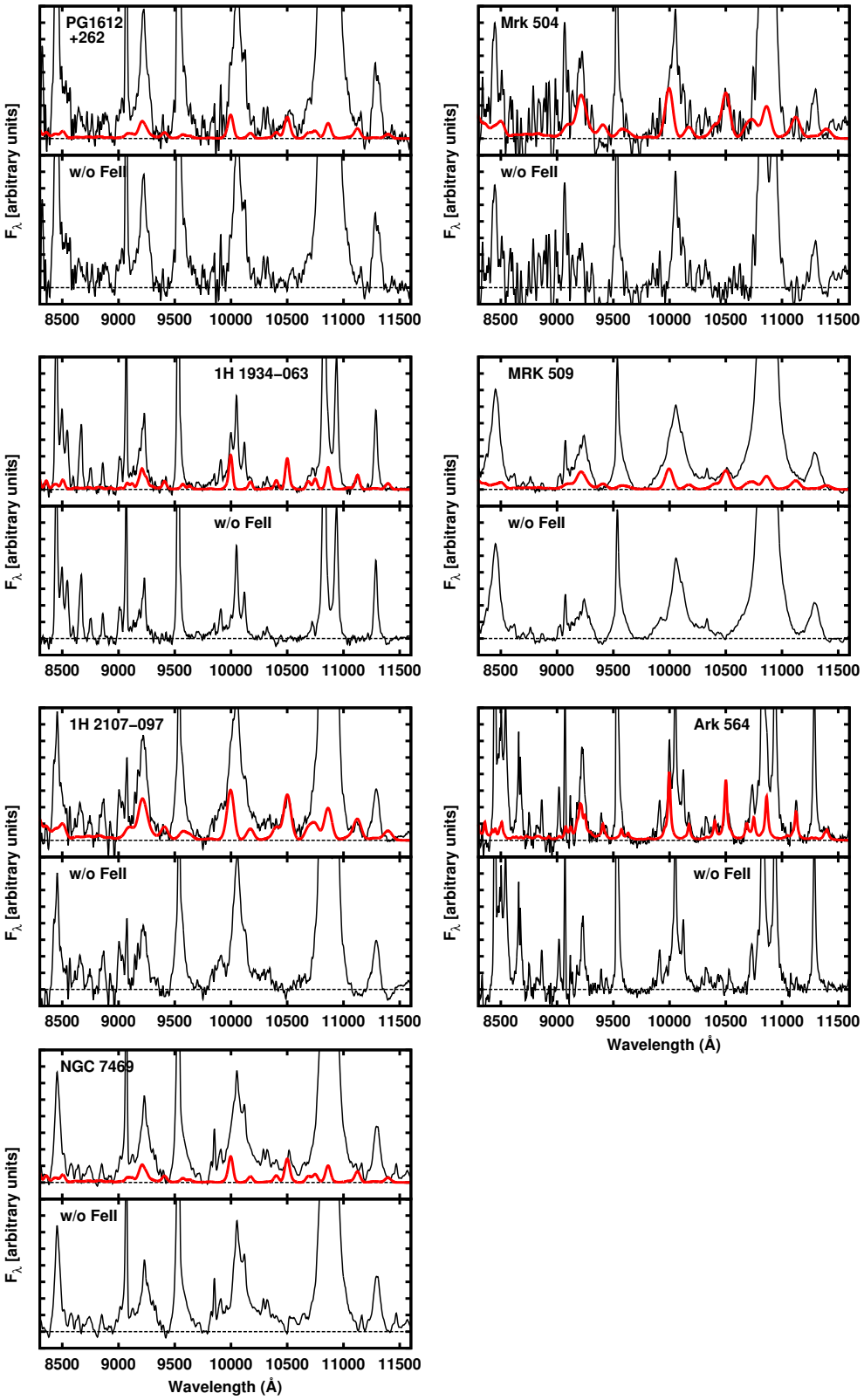


FIGURE 2.5. Continuation of Figure 2.2

Table 2.3: Measurements of the most relevant BLR features used in this work.

| | Fe II $\lambda$10502 | | O I $\lambda$11297 | | Ca II $\lambda$8663 | | Pa$\beta$ $\lambda$12218 | |
|---|---|---|---|---|---|---|---|---|
| Object | Flux | FWHM | Flux | FWHM | Flux | FWHM | Flux | FWHM |
| Mrk 335 | 14.4 ± 0.9 | 1230 ± 74 | 26.0 ± 2.3 | 1140 ± 103 | 14.7 ± 1.2 | 1490 ± 119 | 87.1 ± 5.2 | 2010 ± 121 |
| I Zw 1 | 39.8 ± 1.6 | 890 ± 36 | 29.9 ± 2.1 | 820 ± 57 | 28.6 ± 2.0 | 1100 ± 77 | 86.7 ± 3.5[a] | 1650 ± 66[a] |
| Ton S180 | 2.8 ± 0.1 | 1030 ± 52 | 5.5 ± 0.4 | 930 ± 74 | 5.2 ± 0.4 | 990 ± 69 | 24.0 ± 1.2[a] | 1660 ± 83[a] |
| Mrk 1044 | 9.7 ± 0.6 | 1480 ± 79 | 11.7 ± 0.7 | 1010 ± 61 | 7.2 ± 0.4 | 1200 ± 72 | 24.2 ± 1.4 | 1800 ± 119 |
| Mrk 1239 | 29.1 ± 1.7 | 1350 ± 81 | 50.1 ± 4.0 | 1220 ± 98 | 16,2 ± 1.0 | 1240 ± 74 | 135.5 ± 8.1 | 2220 ± 133 |
| Mrk 734 | 17.8 ± 2.1 | 1600 ± 192 | 17.3 ± 0.9 | 1670 ± 84 | - - | - - | 71.9 ± 8.6[a] | 1830 ± 220[a] |
| PG ,1126-041 | 25.0 ± 2.3 | 2000 ± 180 | 39.4 ± 2.4 | 1940 ± 116 | - - | - - | 128.6 ± 11.6[a] | 2600 ± 234[a] |
| H 1143-182 | 18.5 ± 1.7 | 2170 ± 195 | 34.5 ± 2.1 | 1720 ± 103 | - - | - - | 151.2 ± 13.6 | 2070 ± 186 |
| NGC 4051 | 20.0 ± 2.4 | 1430 ± 172 | 51.6 ± 2.6 | 1035 ± 52 | - - | - - | 65.1 ± 7.8 | 1530 ± 184 |
| Mrk 766 | 21.2 ± 2.5 | 1650 ± 198 | 50.9 ± 2.0 | 1380 ± 55 | 17.9 ± 1.6 | 1520 ± 137 | 115.4 ± 13.9 | 1780 ± 214 |
| NGC 4748 | 21.2 ± 1.9 | 1800 ± 162 | 24.7 ± 2.0 | 1650 ± 132 | - - | - - | 62.9 ± 5.7 | 2130 ± 192 |
| Ton 156 | 47.8 ± 5.7 | 2050 ± 246 | 38.1 ± 2.3 | 2070 ± 124 | - - | - - | 144.6 ± 17.4 | 3490 ± 419 |
| PG 1415+451 | 4.4 ± 0.4 | 2140 ± 171 | 5.3 ± 0.3 | 1780 ± 107 | - - | - - | 17.2 ± 1.4[a] | 2530 ± 202[a] |
| Mrk 684 | 43.5 ± 2.6 | 1430 ± 86 | 53.0 ± 2.7 | 1560 ± 78 | 64.2 ± 4.5 | 1520 ± 106 | 107.7 ± 6.5[a] | 2400 ± 144[a] |
| Mrk 478 | 50.7 ± 3.0 | 1400 ± 84 | 48.1 ± 3.4 | 1300 ± 91 | 40.3 ± 2.4 | 1560 ± 94 | 122.6 ± 7.4[a] | 1940 ± 116[a] |
| PG 1448+273 | 10.9 ± 0.5 | 950 ± 48 | 32.3 ± 1.3 | 880 ± 35 | 12.4 ± 0.6 | 885 ± 44 | 66.9 ± 3.3[a] | 2480 ± 124[a] |
| PG 1519+226 | 4.4 ± 0.4 | 2280 ± 182 | 7.9 ± 0.9 | 1890 ± 227 | - - | - - | 20.1 ± 1.6 | 2800 ± 224 |
| Mrk 493 | 16.2 ± 0.6 | 800 ± 32 | 26.1 ± 1.0 | 770 ± 31 | 29.4 ± 1.8 | 1065 ± 64 | 40.0 ± 1.6[a] | 1970 ± 79[a] |
| PG 1612+262 | 3.7 ± 0.3 | 1770 ± 124 | 10.9 ± 1.2 | 2310 ± 254 | - - | - - | 63.8 ± 4.5[a] | 2770 ± 194[a] |
| Mrk 504 | 6.0 ± 0.4 | 1630 ± 114 | 3.9 ± 0.3 | 1620 ± 130 | - - | - - | 20.5 ± 1.4[a] | 2390 ± 167[a] |
| 1H 1934-063 | 16.7 ± 1.5 | 1200 ± 108 | 35.7 ± 2.9 | 1000 ± 80 | 28.6 ± 2.0 | 1205 ± 84 | 62.8 ± 5.7 | 1520 ± 137 |
| Mrk 509 | 287.1 ± 12.6 | 2220 ± 178 | 640.2 ± 16.8 | 2390 ± 239 | - - | - - | 2474.0 ± 250.4[a] | 3720 ± 298[a] |
| 1H, 2107-097 | 29.9 ± 1.8 | 1800 ± 108 | 20.7 ± 1.7 | 1720 ± 138 | 10.8 ± 0.9 | 1700 ± 136 | 116.1 ± 7.0 | 2570 ± 154 |
| Ark 564 | 17.9 ± 0.9 | 800 ± 40 | 27.8 ± 1.4 | 820 ± 41 | 28.7 ± 1.7 | 990 ± 59 | 56.9 ± 2.8 | 1800 ± 90 |
| NGC 7469 | 24.3 ± 1.7 | 1860 ± 130 | 48.1 ± 2.9 | 1830 ± 110 | - - | - - | 174.9 ± 12.2 | 2800 ± 196 |

**Notes:** FWHM in km s$^{-1}$. Flux in units of $10^{-15}$ erg s$^{-1}$ cm$^{-2}$.

[a] For these objects, the measurements correspond to Pa$\alpha$, because Pa$\beta$ was not available owing to the redshift of the source.

The second feature is the Fe II bump centered at 9200 Å, which is actually a blend of aproximately 80 Fe II lines plus Pa9. The most representative Fe II transitions in this region are Fe II $\lambda$9132.36, $\lambda$9155.77, $\lambda$9171.62, $\lambda$9175.87, $\lambda$9178.09, $\lambda$9179.47, $\lambda$9187.16, $\lambda$9196.90, $\lambda$9218.25, and $\lambda$9251.72. In order to assess the suitability of the template to reproduce this feature, we modeled the residual left in the 9200 Å region after subtracting the template. The residual was constrained to have the same profile and FWHM as Pa$\beta$. The flux of the Pa9 line should be, within the uncertainties, the flux of Pa$\beta$ multiplied by the Paschen decrement factor (Pa$\beta$/Pa9$\sim$ 5.6; Garcia- Rissmann et al. 2012). The results obtained for each object are shown in column (3) of Table 2.6.

Column (4) of Table 2.6 shows the expected flux for that line. When we compare it to the measured flux, we find that the latter is systematically larger, which indicates that the template underestimates the value of the Fe II emission in this region. Similar behavior was observed by Martinez-Aldama et al. (2015) for a smaller spectral region (0.8–0.95 $\mu$m). They subtracted the NIR Fe II emission in 14 luminous AGNs using the template of Garcia-Rissmann et al. (2012) for this region and found an excess of Fe II in the 9200 Å bump after the subtraction.

Nevertheless, we can estimate the total Fe II emission contained in the 9200 Åbump using the residual flux left after subtraction of the expected Pa9 flux to "top up" the flux found in the Fe II template. Column (5) of Table 2.6 lists this total Fe II flux in the bump. We define the quantity $R_{9200}$as the flux ratio between the Fe II bump and the broad component of Pa$\beta$. The results are listed in column (6) of Table 2.6.

Except for the residuals in the $\lambda$9200 region, our results demonstrate the suitability of the semi-empirical NIR Fe II template in reproducing this emission in a large sample of local AGNs. The only difference from source to source are scale factors in FWHM and flux, meaning that the relative intensity between the different Fe II lines remains approxi mately constant, similar to what is observed in the UV and optical region (Boroson & Green 1992; Vestergaard & Wilkes 2001; Veron-Cetty et al. 2004). Figures 2.2–2.5 also confirm that the template developed for the Fe II emission in the NIR can be applied to a broad range of Type 1 objects.

The results obtained after fitting the Fe II template allow us to conclude that (i) without a proper modeling and subtraction of that emission, the flux and profile characteristics of other adjacent BLR features can be overestimated; (ii) once a good match between the semi-empirical Fe II template and the observed spectrum is found, individual Fe II lines, as well as the NIR Fe II fluxes, can be reliably measured; and (iii) the fact that the template reproduces well the observed NIR Fe II emission in a broad range of AGNs points to a common excitation mechanism for the NIR Fe II emission in Type 1 sources.

### 2.3.2 Emission-line Fluxes of the BLR in the NIR

Modeling the pseudo-continuum formed by numerous permitted Fe II lines in the optical and UV regions is one of the most challenging issues for a reliable study of the BLR. Broad optical

Table 2.4: Values of the parameters used to convolve the NIR Fe II template.

| AGN | Flux[a] | FWHM[b] | Function | rms[c] after subtraction | rms[c] around 1 $\mu$m lines |
|---|---|---|---|---|---|
| Mrk 335 | 14.1 ± 0.9 | 1220 ± 74 | Gaussian | 1.60 | 1.42 |
| I Zw 1 | 38.8 ± 1.6 | 870 ± 36 | Lorentzian | 2.60 | 2.40 |
| Ton S180 | 2.4 ± 0.1 | 1020 ± 52 | Gaussian | 0.29 | 0.35 |
| Mrk 1044 | 9.0 ± 0.6 | 1330 ± 79 | Gaussian | 0.55 | 0.65 |
| Mrk 1239 | 29.9 ± 1.7 | 1360 ± 81 | Gaussian | 2.70 | 2.50 |
| Mrk 734 | 16.8 ± 2.1 | 1620 ± 192 | Gaussian | 1.06 | 1.16 |
| PG ,1126-041 | 23.9 ± 2.3 | 2040 ± 180 | Gaussian | 1.87 | 1.83 |
| H 1143-182 | 17.9 ± 1.7 | 2150 ± 195 | Gaussian | 3.01 | 2.92 |
| NGC 4051 | 20.8 ± 2.4 | 1420 ± 172 | Gaussian | 0.90 | 0.70 |
| Mrk 766 | 20.8 ± 2.5 | 1620 ± 198 | Gaussian | 2.20 | 2.10 |
| NGC 4748 | 20.2 ± 1.9 | 1780 ± 162 | Gaussian | 1.20 | 1.26 |
| Ton 156 | 46.8 ± 5.7 | 2030 ± 246 | Gaussian | 2.20 | 2.03 |
| PG 1415+451 | 4.1 ± 0.4 | 2110 ± 171 | Gaussian | 0.48 | 1.60 |
| Mrk 684 | 43.1 ± 2.6 | 1420 ± 86 | Gaussian | 4.19 | 4.35 |
| Mrk 478 | 50.3 ± 3.0 | 1400 ± 84 | Gaussian | 2.30 | 2.35 |
| PG 1448+273 | 11.3 ± 0.5 | 920 ± 48 | Gaussian | 0.68 | 0.74 |
| PG 1519+226 | 4.6 ± 0.4 | 2230 ± 182 | Gaussian | 6.40 | 5.90 |
| Mrk 493 | 16.5 ± 0.6 | 800 ± 32 | Lorentzian | 2.80 | 2.71 |
| PG 1612+262 | 3.3 ± 0.3 | 1760 ± 124 | Gaussian | 0.56 | 0.48 |
| Mrk 504 | 6.2 ± 0.4 | 1620 ± 114 | Gaussian | 0.69 | 0.76 |
| 1H 1934-063 | 16.2 ± 1.5 | 1200 ± 108 | Gaussian | 1.70 | 1.65 |
| Mrk 509 | 290.0 ± 13.4 | 2250 ± 178 | Gaussian | 1.80 | 1.70 |
| 1H, 2107-097 | 29.5 ± 1.8 | 1810 ± 108 | Gaussian | 0.89 | 0.84 |
| Ark 564 | 17.1 ± 0.9 | 810 ± 40 | Lorentzian | 2.20 | 2.32 |
| NGC 7469 | 24.9 ± 1.7 | 1840 ± 130 | Gaussian | 1.17 | 1.05 |

[a] In units of $10^{-15}$ erg s$^{-1}$ cm$^{-2}$ Å$^{-1}$
[b] In units of km s$^{-1}$
[c] In units of $10^{-17}$ erg s$^{-1}$ cm$^{-2}$

emission lines of ions other than Fe II are usually heavily blended with Fe II multiplets and narrow-line region (NLR) lines. In order to measure their fluxes and characterize their line profiles, a careful removal of the Fe II emission needs to be done first. In this context, the NIR looks more promising for the analysis of the BLR at least for three reasons. First, the same set of ions detected in the optical are also present in that region (H I, He I, Fe II, He II, in addition to O I and Ca II, not seen in the optical). Second, the lines are either isolated or moderately blended with other species. Third, the placement of the continuum is less prone to uncertainties relative to the optical because the pseudo-continuum produced by the Fe II is weaker.

This section will describe the method employed to derive the flux of the most important BLR lines in the NIR after the removal of all the emission attributed to Fe II.

Table 2.5: Fluxes of the 1$\mu$m Fe II lines measured with the template.

| AGN | 9998 Å | 10502 Å | 10863 Å | 11127 Å | Pa$\beta$ | $R_{1\mu m}$ |
|---|---|---|---|---|---|---|
| Mrk 335 | 14.8 ± 0.6 | 13.9 ± 0.6 | 10.1 ± 0.4 | 6.8 ± 0.3 | 87.1 ± 5.2 | 0.52 ± 0.07 |
| I Zw 1 | 30.4 ± 1.2 | 29.4 ± 1.2 | 21.9 ± 0.9 | 14.2 ± 0.6 | 52.9 ± 2.1[a] | 1.81 ± 0.08 |
| Ton S180 | 2.5 ± 0.1 | 2.4 ± 0.1 | 1.8 ± 0.1 | 1.2 ± 0.1 | 14.6 ± 0.7[a] | 0.54 ± 0.07 |
| Mrk 1044 | 8.5 ± 0.3 | 8.0 ± 0.3 | 5.8 ± 0.2 | 4.0 ± 0.2 | 24.2 ± 1.4 | 1.08 ± 0.07 |
| Mrk 1239 | 29.7 ± 1.2 | 28.1 ± 1.1 | 20.2 ± 0.8 | 13.7 ± 0.5 | 135.6 ± 8.1 | 0.68 ± 0.07 |
| Mrk 734 | 15.1 ± 0.6 | 16.0 ± 0.6 | 10.7 ± 0.4 | 7.2 ± 0.3 | 43.9 ± 5.3[a] | 1.12 ± 0.09 |
| PG ,1126-041 | 14.5 ± 0.6 | 14.0 ± 0.6 | 10.0 ± 0.4 | 7.0 ± 0.3 | 78.4 ± 7.1[a] | 0.58 ± 0.06 |
| H 1143-182 | 12.0 ± 0.5 | 11.7 ± 0.5 | 8.3 ± 0.3 | 5.8 ± 0.2 | 151.2 ± 13.6 | 0.25 ± 0.02 |
| NGC 4051 | 20.0 ± 0.8 | 18.8 ± 0.8 | 13.6 ± 0.5 | 9.4 ± 0.4 | 65.1 ± 7.8 | 0.95 ± 0.11 |
| Mrk 766 | 18.3 ± 0.7 | 17.6 ± 0.7 | 13.1 ± 0.5 | 9.0 ± 0.4 | 115.4 ± 13.9 | 0.50 ± 0.06 |
| NGC 4748 | 18.0 ± 0.7 | 17.6 ± 0.7 | 12.7 ± 0.5 | 8.8 ± 0.4 | 62.9 ± 5.7 | 0.91 ± 0.07 |
| Ton 156 | 33.9 ± 1.4 | 30.1 ± 1.2 | 25.0 ± 1.0 | 17.3 ± 0.7 | 144.6 ± 17.4 | 0.74 ± 0.06 |
| PG 1415+451 | 4.5 ± 0.2 | 4.7 ± 0.2 | 3.2 ± 0.1 | 2.2 ± 0.1 | 10.5 ± 0.8[a] | 1.39 ± 0.07 |
| Mrk 684 | 44.6 ± 1.8 | 43.0 ± 1.7 | 30.9 ± 1.2 | 21.5 ± 0.9 | 65.7 ± 3.9[a] | 1.13 ± 0.13 |
| Mrk 478 | 51.7 ± 2.1 | 51.6 ± 2.1 | 38.7 ± 1.5 | 26.6 ± 1.1 | 74.7 ± 4.5[a] | 1.26 ± 0.14 |
| PG 1448+273 | 10.1 ± 0.4 | 9.9 ± 0.4 | 7.2 ± 0.3 | 4.9 ± 0.2 | 40.8 ± 2.0[a] | 0.79 ± 0.07 |
| PG 1519+226 | 3.7 ± 0.1 | 3.5 ± 0.1 | 2.6 ± 0.1 | 1.8 ± 0.1 | 20.1 ± 1.6 | 0.58 ± 0.06 |
| Mrk 493 | 11.6 ± 0.5 | 11.2 ± 0.4 | 8.2 ± 0.3 | 5.4 ± 0.2 | 24.4 ± 1.0[a] | 1.49 ± 0.09 |
| PG 1612+262 | 2.2 ± 0.1 | 2.1 ± 0.1 | 1.5 ± 0.1 | 1.0 ± 0.1 | 38.9 ± 2.7[a] | 0.18 ± 0.04 |
| Mrk 504 | 5.3 ± 0.2 | 5.4 ± 0.2 | 3.9 ± 0.2 | 2.6 ± 0.1 | 12.5 ± 0.9[a] | 0.49 ± 0.35 |
| 1H 1934-063 | 17.6 ± 0.7 | 16.9 ± 0.7 | 12.2 ± 0.5 | 8.4 ± 0.3 | 62.8 ± 5.7 | 0.88 ± 0.06 |
| Mrk 509 | 306.1 ± 16.7 | 295.8 ± 10.0 | 211.0 ± 11.7 | 141.1 ± 7.5 | 2474.0 ± 250.4[a] | 0.26 ± 0.10 |
| 1H, 2107-097 | 24.0 ± 1.0 | 23.6 ± 0.9 | 16.7 ± 0.7 | 11.7 ± 0.5 | 116.1 ± 7.0 | 0.65 ± 0.08 |
| Ark 564 | 11.6 ± 0.5 | 11.3 ± 0.5 | 8.3 ± 0.3 | 5.6 ± 0.2 | 56.9 ± 2.8 | 0.65 ± 0.01 |
| NGC 7469 | 17.1 ± 0.7 | 16.5 ± 0.7 | 11.9 ± 0.5 | 8.3 ± 0.3 | 174.9 ± 12.2 | 0.31 ± 0.04 |

**Notes:** FWHM in km s$^{-1}$. Flux in units of $10^{-15}$ erg s$^{-1}$ cm$^{-2}$.
[a] For these objects, the measurements correspond to Pa$\alpha$, because Pa$\beta$ was not available owing to the redshift of the source.

To this purpose, the presence of any NLR emission should be evaluated first and, if present, subtracted from the observed lines profiles. An inspection of the spectra reveals the presence of forbidden emission lines of [S III] $\lambda$9068 and $\lambda$9531 in all sources analyzed here. Therefore, a narrow component is also expected for the hydrogen lines that may contribute a non-negligible fraction to the observed flux. In order to measure this narrow component, we followed the approach of Rodriguez-Ardila et al. (2000), which consists of adopting the observed profile of an isolated NLR line as a template, scaling it in strength, and subtracting it from each permitted line.

Note that neither O I, Ca II, nor Fe II required the presence of a narrow component to model their observed profiles, even in the spectra with the best S/N. In all cases, after the inclusion and subtraction of a narrow profile, an absorption dip was visible in the residuals. Rodriguez-Ardila et al. (2002) had already pointed out that no contribution from the NLR to these lines is expected as high gas densities ($> 10^8$ cm$^{-3}$) are necessary to drive this emission. This result contrasts claims made by Dong et al. (2010), who include a narrow component, with origin in the NLR, in the modeling of the optical Fe II lines.

For consistency, O I $\lambda$8446[2] and Ca II $\lambda\lambda$8498,8542 had their widths (in velocity space) constrained to that of O I $\lambda$11287 and Ca II $\lambda$8662, respectively. The latter lines are usually isolated

[2]Note that this line is actually a closely spaced triplet of O I $\lambda$8446.25, $\lambda$8446.36, and $\lambda$8446.38.

Table 2.6: Fluxes for the Fe II+Pa9 Bump at $\lambda$9200.

| AGN | Fe II $\lambda$9200 bump[a] | Pa9+fit residuals | Expected Pa9[b] | Total Fe II at 9200 Å | $R_{9200}$ |
|---|---|---|---|---|---|
| Mrk 335 | 16.8 ± 0.7 | 45.8 ± 2.7 | 18.2 ± 1.1 | 44.4 ± 2.9 | 0.51 ± 0.03 |
| I Zw 1 | 30.5 ± 1.2 | 27.3 ± 2.3 | 11.1 ± 0.4 | 46.7 ± 3.4 | 0.88 ± 0.04 |
| Ton S180 | 2.6 ± 0.1 | 6.0 ± 0.3 | 3.1 ± 0.2 | 5.5 ± 0.3 | 0.33 ± 0.05 |
| Mrk 1044 | 9.4 ± 0.4 | 8.8 ± 0.5 | 5.0 ± 0.3 | 13.1 ± 0.9 | 0.54 ± 0.03 |
| Mrk 1239 | 30.9 ± 1.2 | 31.7 ± 1.9 | 28.3 ± 1.7 | 34.3 ± 2.3 | 0.25 ± 0.02 |
| Mrk 734 | 16.0 ± 0.6 | 18.6 ± 2.2 | 9.2 ± 1.1 | 25.4 ± 3.3 | 0.35 ± 0.04 |
| PG ,1126-041 | 15.5 ± 0.6 | 43.9 ± 3.9 | 16.5 ± 1.5 | 42.8 ± 4.2 | 0.33 ± 0.03 |
| H 1143-182 | 12.7 ± 0.5 | 51.1 ± 4.6 | 31.5 ± 2.8 | 32.4 ± 3.2 | 0.21 ± 0.02 |
| NGC 4051 | 22.7 ± 0.9 | 35.3 ± 4.2 | 13.6 ± 1.6 | 44.5 ± 5.9 | 0.68 ± 0.08 |
| Mrk 766 | 21.3 ± 0.9 | 53.7 ± 6.4 | 24.0 ± 2.9 | 51.0 ± 6.7 | 0.44 ± 0.05 |
| NGC 4748 | 20.4 ± 0.8 | 30.1 ± 2.7 | 13.1 ± 1.2 | 37.3 ± 3.7 | 0.59 ± 0.05 |
| Ton 156 | 38.1 ± 1.5 | 33.1 ± 4.0 | 30.1 ± 3.6 | 41.0 ± 5.4 | 0.28 ± 0.03 |
| PG 1415+451 | 5.7 ± 0.2 | 7.5 ± 0.6 | 2.2 ± 0.2 | 11.1 ± 1.0 | 0.64 ± 0.05 |
| Mrk 684 | 50.8 ± 2.0 | 44.2 ± 2.6 | 13.8 ± 0.8 | 81.1 ± 5.4 | 0.75 ± 0.05 |
| Mrk 478 | 50.5 ± 2.0 | 36.4 ± 2.2 | 15.7 ± 0.9 | 71.2 ± 4.7 | 0.58 ± 0.03 |
| PG 1448+273 | 11.4 ± 0.5 | 20.1 ± 1.0 | 8.6 ± 0.4 | 22.9 ± 1.3 | 0.34 ± 0.02 |
| PG 1519+226 | 4.2 ± 0.2 | 7.9 ± 0.6 | 4.2 ± 0.3 | 7.8 ± 0.7 | 0.39 ± 0.03 |
| Mrk 493 | 13.0 ± 0.5 | 29.0 ± 1.2 | 5.1 ± 0.2 | 36.8 ± 1.6 | 0.92 ± 0.04 |
| PG 1612+262 | 2.5 ± 0.1 | 12.0 ± 0.8 | 8.2 ± 0.6 | 6.3 ± 0.5 | 0.10 ± 0.01 |
| Mrk 504 | 6.7 ± 0.3 | 0.1 ± 0.0 | 2.6 ± 0.2 | 4.0 ± 0.3 | 0.20 ± 0.01 |
| 1H 1934-063 | 19.4 ± 0.8 | 31.4 ± 2.8 | 13.1 ± 1.2 | 37.7 ± 3.7 | 0.60 ± 0.05 |
| Mrk 509 | 336.2 ± 14.8 | 501.3 ± 42.2 | 441.7 ± 60.2 | 395.8 ± 51.7 | 0.16 ± 0.01 |
| 1H, 2107-097 | 26.1 ± 1.0 | 30.1 ± 1.8 | 24.2 ± 1.5 | 32.0 ± 2.1 | 0.28 ± 0.02 |
| Ark 564 | 13.0 ± 0.5 | 14.3 ± 0.7 | 11.8 ± 0.6 | 15.4 ± 0.8 | 0.27 ± 0.01 |
| NGC 7469 | 18.1 ± 0.7 | 44.7 ± 3.1 | 36.4 ± 2.6 | 26.3 ± 2.0 | 0.15 ± 0.01 |

**Notes:** Flux in units of $10^{-15}$ erg s$^{-1}$ cm$^{-2}$.
[a] Measure from the NIR Fe II template. [b] Based on the Paschen decrement.

and display good S/N. Note, however, that for a part of our sample, it was not possible to obtain a good simultaneous fit to the three calcium lines using this approach. We attribute this mostly to the fact that some of the AGNs have the Ca II lines in absorption (Penston 1987) and also to the lower S/N of Ca II $\lambda\lambda$8498,8542 as they are located in regions with reduced atmospheric transmission.

Table 2.3 lists the fluxes and FWHM measured for the most conspicuous emission lines of our sample. The errors presented are due to the small variations in establishing the continuum zero level for the fits. Figure 2.6 shows an example of the deblending procedure applied to each of the lines analyzed.

## 2.4 Fe II Excitation Mechanism: Lyman-$\alpha$ fluorescence and Collisional Excitation

The primary excitation mechanism invoked to explain most of the NIR Fe II lines is Ly$\alpha$ fluorescence (Sigut & Pradhan 1998, 2003; Rodríguez-Ardila et al. 2002). In this scenario the iron lines are produced by primary and/or secondary cascading after the absorption of an Ly$\alpha$ photon between the levels $a^4G \rightarrow (t,u)^4G^0$ and $a^4D \rightarrow u^4(P,D), v^4F$. As can be seen in Figure 2.7, there are two main NIR Fe II features in the range of 0.8–2.5 $\mu$m that arise from this process: the 1 $\mu$m

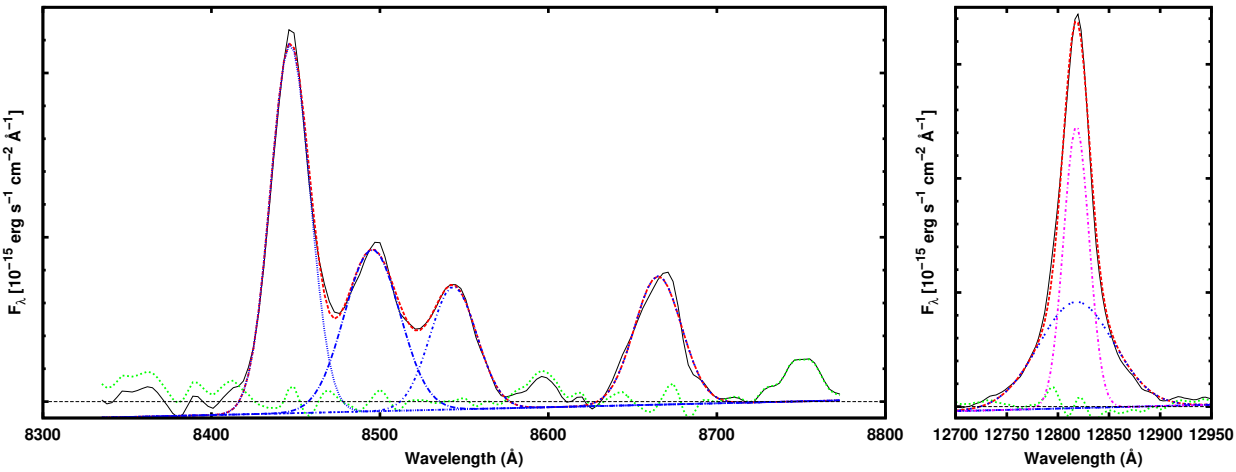


FIGURE 2.6. Example of line deblending for 1H 1934–063. The left panel shows each line of the Ca II triplet (blue dot-dashed line), the O I $\lambda$8446 line (blue dotted line), and the total fit of these lines (red dashed line). The right panel shows the deblend of the Pa$\beta$ line in broad (dotted blue line) and narrow (dot-dashed magenta line) components. The red dashed line is the sum of these two components.

lines and the bump centered in the 9200 Å region. The importance of this excitation channel is the fact that it populates the upper energy levels whose decay produces the optical Fe II lines, traditionally used to measure the intensity of the iron emission in AGNs (Sigut & Pradhan 2003). Much of the challenge to the theory of the Fe II emission is to determine whether this excitation channel is indeed valid for all AGNs and the degree to which this process contributes to the observed Fe II flux.

In order to answer these two questions, we will analyze first the 1 $\mu$m lines. hey result from secondary cascading after the capture of an Ly$\alpha$ photon that excites the levels $a^4G \rightarrow (t,u)^4G^0$ followed by downward UV transitions to the level $b^4G$ via 1870/1873 Å and 1841/1845 Å emission and finally $b^4G \rightarrow z^4F^0$ transitions, which produce the 1 $\mu$m lines. These lines are important for at least two reasons: (i) they are the most intense NIR Fe II lines that can be isolated; and (ii) after they are emitted, the $z^4F$ and $z^4D$ levels are populated. These levels are responsible for $\sim 50\%$ of the total optical Fe II emission. Therefore, the comparison between the optical and NIR Fe II emission can provide important clues about the relevance of the Ly$\alpha$ fluorescence process in the production of optical Fe II.

We measured the optical Fe II emission for 18 out of 25 AGNs in our sample by applying the Boroson & Green (1992) method to the optical spectra presented in Section 2. Boroson & Green (1992) found that a suitable Fe II template can be generated by simply broadening the

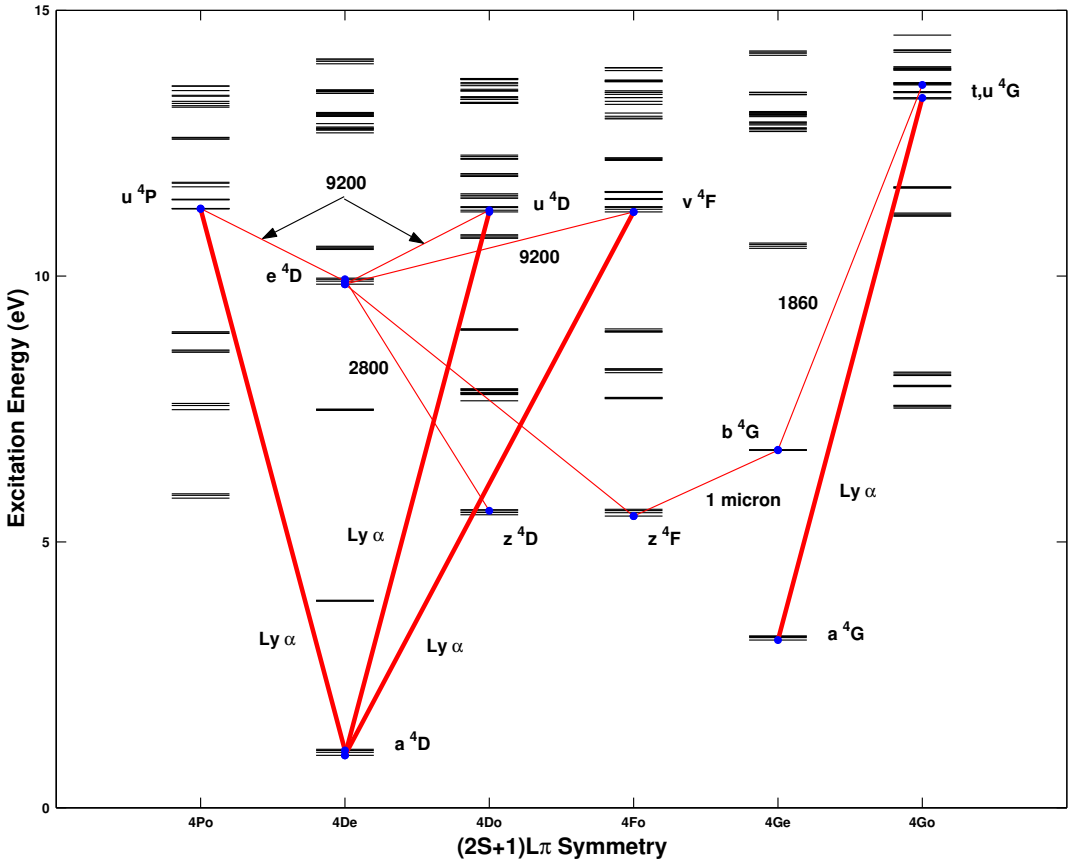


FIGURE 2.7. Partial Grothrian diagram for the Fe II system showing the transitions forming the 1 $\mu$m lines and the bump at 9200 Å. The red diagonal lines are the Ly$\alpha$ fluorescence route and the subsequent cascades. The 1 $\mu$m lines are produced by the multiplet transitions $b^4G \rightarrow z(^4F,^4D)$. The Fe II $\lambda$9200 bump is produced by the transitions $u(^4P,^4D), v^4F \rightarrow e^4D$. Figure from Sigut & Pradhan (2003)

Fe II spectrum derived from the observations of I Zw 1. The Fe II template strength is free to vary, but it is broadened to be consistent with the width found for the NIR iron lines. The best Fe II template is found by minimization of the $\chi^2$ values of the fit region, set to 4435–4750 Å. Half of the lines that form this bump come from downward cascades from the $z^4F$ levels. Figure 2.8 shows an example of the optical Fe II template fit to the observed spectrum. In addition, we measured the integrated flux of the H$\beta$ line after subtraction of the underlying Fe II emission.

Afterward, the amount of Fe II present in each source was quantified by means of $R_{4570}$, the flux ratio between the Fe II blend centered at 4570 Å and H$\beta$. Currently, this quantity is employed as an estimator of the amount of optical iron emission in active galaxies. Although values of $R_{4570}$ for some objects of our sample are found in the literature (Joly 1991; Boroson & Green 1992),

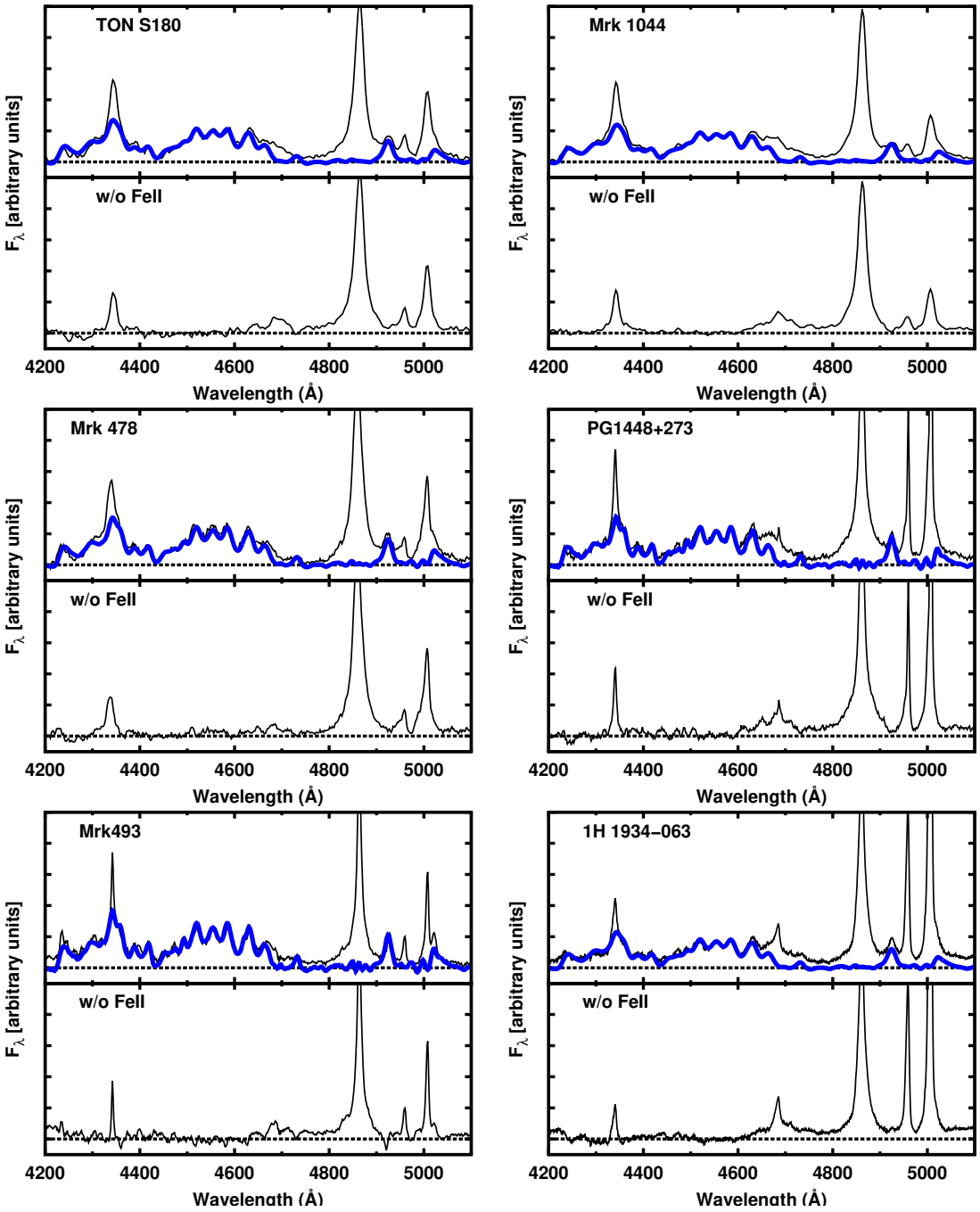


FIGURE 2.8. Examples of the convolved optical Fe II template. Top panels show the continuum-subtracted spectrum of the AGN (black line), with the optical spectrum of Fe II (blue line) superposed. Bottom panels show the spectrum of each object without this emission.

we opted for estimating it from our own data. Differences between values of $R_{4570}$found for the same source by different authors, the lack of proper error estimates in some of them, and the use of different methods to determine $R_{4570}$ (Persson 1988; Joly 1991) encouraged us to use this approach. The values found for $R_{4570}$ in our sample are listed in Table 2.7.

Model results of Bruhweiler & Verner (2008) show that both the BLR and the NLR contribute to the observed permitted Fe II emission in the 4300–5400 Å interval. The contribution of the NLR is particularly strong in the 4300–4500 Å region and would arise from the $a(^6S,^4G) \rightarrow a(^6D,^4F)$ and $b^4F \rightarrow a^6D$ transitions, in regions of low-density ($n_{\rm H} < 10^4$ cm$^{-3}$) gas. The iron BLR component, in contrast, dominates the wavelength interval 4500–4700 Å. This hypothesis was tested by Bruhweiler & Verner (2008) in the NLS1 galaxy I Zw 1. Our optical spectra include the interval of 4200–4750 Å, and recall that we followed the empirical method proposed by Boroson & Green (1992) to quantify this emission. In other words, no effort was made to separate the BLR and NLR components. Moreover, because the relevant optical quantity in our work is composed by the blends of Fe II lines located in the interval 4435–4750 Å, where the NLR almost does not contribute, we conclude that this NLR component, if it exists, does not interfere with our results. It is possible, however, to test the presence of NLR Fe II emission in the NIR. Riffel et al. (2006), for instance, in their NIR atlas of 52 AGNs clearly identified the forbidden [Fe II] lines at 12570 and 16634 Å in most objects of their sample, but did not find evidence of permitted Fe II emission from the NLR.

Here we also confirm this result. For none of the NIR spectra studied here was evidence of a narrow component found, even in isolated Fe II lines such as Fe II $\lambda$10502. If this contribution exists, it should be at flux levels smaller than our S/N.

Table 2.5 lists the fluxes of the 1 $\mu$m lines. As in the optical, we derive the quantity $R_{1\mu m}$. In order to determine whether both ratios are correlated, we plot $R_{1\mu m}$ versus $R_{4570}$ in Figure 2.9. Since the energy levels involved in producing the optical lines in the $R_{4570}$ bump are populated after the emission of the NIR Fe II 1 $\mu$m lines, a correlation between these quantities can be interpreted as evidence of a common excitation mechanism.

An inspection of Figure 2.9 shows that $R_{1\mu m}$ and $R_{4570}$ are indeed strongly correlated, at least for the range of values covered by our sample.

In order to obtain a linear fit and determine the correlation coefficient, we perform a Monte Carlo simulation with the bootstrap method (similarly to Beers et al. 1990). First, we run 10,000 Monte Carlo simulations in order to determine the effect of the $R_{1\mu m}$ and $R_{4570}$ uncertainties in the linear fit. For each realization, random values of these two quantities were generated (constrained to the error range of the measurements) and a new fit was made. The standard deviation of the fit coefficients $\epsilon_i$ , was determined and represents the uncertainty of the values over the linear fit coefficients. The next step was to run the bootstrap realizations in order to derive the completeness and its effects on the fit. For each run, we made a new fit for a new sample randomly constructed with replacement from the combination of the measured values of

Table 2.7: Fluxes for the optical Fe II and H$\beta$.

| AGN | Fe II $\lambda$4570 bump[a] | Broad H$\beta$[b] | $R_{4570}$ |
|---|---|---|---|
| Mrk 335 | 87.5 ± 6.6 | 11.8 ± 0.9 | 0.74 ± 0.11 |
| I Zw 1 | 32.0 ± 1.6 | 1.4 ± 0.1 | 2.32 ± 0.11 |
| Ton S180 | 19.7 ± 1.2 | 2.0 ± 0.1 | 1.01 ± 0.14 |
| Mrk 1044 | 30.7 ± 2.3 | 2.6 ± 0.2 | 1.16 ± 0.11 |
| Mrk 1239 | 33.5 ± 2.5 | 2.5 ± 0.2 | 1.33 ± 0.20 |
| Mrk 734 | 14.3 ± 2.1 | 1.2 ± 0.2 | 1.19 ± 0.10 |
| H 1143-182 | 6.3 ± 0.7 | 1.9 ± 0.2 | 0.34 ± 0.06 |
| NGC 4748 | 15.0 ± 1.7 | 1.7 ± 0.2 | 0.90 ± 0.12 |
| Ton 156 | 3.2 ± 0.5 | 0.4 ± 0.1 | 0.86 ± 0.18 |
| PG 1415+451 | 8.2 ± 0.8 | 0.6 ± 0.1 | 1.47 ± 0.15 |
| Mrk 478 | 16.1 ± 1.2 | 1.3 ± 0.1 | 1.24 ± 0.08 |
| PG 1448+273 | 13.2 ± 0.8 | 1.1 ± 0.1 | 1.22 ± 0.12 |
| PG 1519+226 | 8.5 ± 0.9 | 1.1 ± 0.1 | 0.76 ± 0.16 |
| Mrk 493 | 19.1 ± 1.0 | 1.1 ± 0.1 | 1.85 ± 0.14 |
| PG 1612+262 | 6.6 ± 0.6 | 1.5 ± 0.1 | 0.43 ± 0.06 |
| 1H 1934-063 | 37.9 ± 4.3 | 2.7 ± 0.3 | 1.38 ± 0.08 |
| 1H, 2107-097 | 15.7 ± 1.2 | 1.5 ± 0.1 | 1.07 ± 0.10 |
| NGC 7469 | 4.0 ± 0.4 | 0.5 ± 0.0 | 0.74 ± 0.06 |

[a] Fluxes in units of $10^{-14}$ erg s$^{-1}$ cm$^{-2}$.

[b] Fluxes in units of $10^{-13}$ erg s$^{-1}$ cm$^{-2}$.

$R_{1\mu m}$ and $R_{4570}$. The standard deviation of these coefficients, $\epsilon_e$ , gives us the intrinsic scatter of the measured values. Finally, the error in the coefficients is given by the sum of the $\epsilon_i$ and $\epsilon_e$ in quadrature, i.e., $\sqrt{\epsilon_i^2 + \epsilon_e^2}$. The strength of the correlation can be measured by the Pearson rank coefficient, which indicates how similar two sample populations are.

Following the method above, we found a Pearson rank coefficient of $P = 0.78$ for the correlation between $R_{1\mu m}$ and $R_{4570}$. This suggests that the two emissions are very likely excited by the same mechanisms. However, it does not prove that Ly$\alpha$ fluorescence is the dominant process. This is because collisional excitation is also an option. Rodriguez-Ardila et al. (2002), using HST/FOS spectra, found that the Fe II UV lines at 1860 Å were intrinsically weak, pointing out that Ly$\alpha$ fluorescence could not produce all the observed intensity of the 1 $\mu$m lines because a number of photons of the latter were significatively larger than those in the former (see Figure 2.7). They concluded that collisional excitation was responsible for the bulk of the Fe II emission.

We inspected the UV spectra available for our sample in the region around 1860 Å. The evidence for the presence of these lines is marginal. For four objects in our sample, though, it was possible to identify them: 1H 1934–063, Mrk 335, Mrk 1044, and Ark 564. The upper limit of such UV emission in these galaxies ranges from 0.6 to 13.2 ($10^{-14}$ erg cm$^{-2}$ s$^{-1}$) for Mrk,1066 and 1H,1934–063, respectively (Rodriguez-Ardila et al. 2002). This does not necessarily mean that

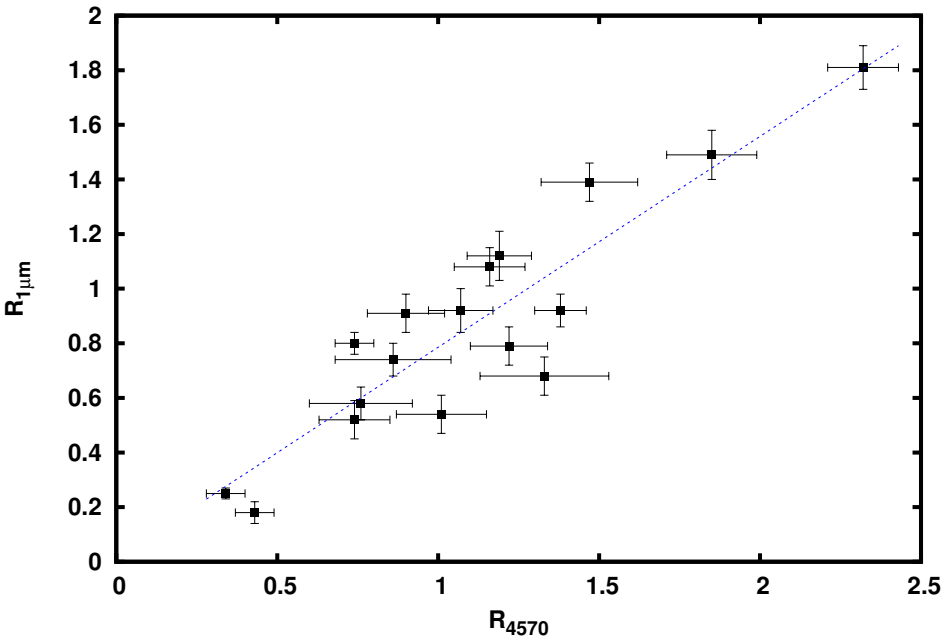


FIGURE 2.9. Correlation between $R_{1\mu m}$ and $R_{4570}$. The blue dotted line shows the best linear fit.

the lines are not actually emitted in the remainder of the sample. Extinction, for instance, can selectively absorb photons in the UV relative to that of the NIR. Also, the region where these UV lines are located, at least for the spectra we have available, is noisy and makes any reliable detection of these lines very difficult.

Taking into account that the 1 $\mu$m lines are strong in all objects while the primary cascade lines from which they originate are marginally detected, we conclude that Ly$\alpha$ fluorescence does not dominate the excitation channel leading to the NIR Fe II emission.

Here we propose that collisional excitation is the main process behind the iron NIR lines. This mechanism is more efficient at temperatures above 7000 K (Sigut & Pradhan 2003). Such values are easily found in photoinization equilibrium clouds (~10,000 K; Osterbrock 1989), exciting the bound electrons from the ground levels to those where the 1 $\mu$m lines are produced. The constancy of the flux ratios among Fe II NIR lines found from object to object of our sample supports this result.

Ly$\alpha$ fluorescence, though, should still contribute to the flux observed in the 1 $\mu$m lines even if it is not the dominant mechanism. This can be observed in Figure 2.10, where $R_{1\mu m}$ versus $R_{9200}$ is plotted. It can be seen that both quantities are correlated, with a Pearson coefficient of $P = 0.72$. However, in order to make a crude estimate of the contribution of the fluorescence process, we should look at other relationships between the iron lines, such as the bumps at 9200 and 4570 Å.

Recall that the former is produced after the absorption of an Ly$\alpha$ photon, exciting the levels

Table 2.8: Number of photons for the Fe II emission.

| AGN | Fe II photons in $\lambda$4570 bump[a] | Fe II photons in $\lambda$9200 bump[b] | $N_{9200}/N_{4570}$ [c] |
|---|---|---|---|
| Mrk 335 | 20 ± 2 | 10 ± 10 | 0.51 |
| I Zw 1 | 74 ± 8 | 36 ± 4 | 0.48 |
| Ton S180 | 46 ± 4 | 30 ± 3 | 0.65 |
| Mrk 1044 | 71 ± 8 | 31 ± 3 | 0.43 |
| Mrk 1239 | 77 ± 10 | 16 ± 2 | 0.20 |
| Mrk 734 | 33 ± 4 | 12 ± 1 | 0.35 |
| H 1143-182 | 14 ± 2 | 2 ± 1 | 0.10 |
| NGC 4748 | 35 ± 3 | 17 ± 2 | 0.50 |
| Ton 156 | 7 ± 1 | 2 ± 1 | 0.25 |
| PG 1415+451 | 19 ± 2 | 5 ± 1 | 0.27 |
| Mrk 478 | 37 ± 2 | 33 ± 1 | 0.89 |
| PG 1448+273 | 30 ± 3 | 11 ± 1 | 0.35 |
| PG 1519+226 | 20 ± 3 | 4 ± 1 | 0.18 |
| Mrk 493 | 44 ± 5 | 17 ± 2 | 0.38 |
| PG 1612+262 | 15 ± 2 | 3 ± 1 | 0.19 |
| 1H 1934-063 | 88 ± 11 | 18 ± 2 | 0.20 |
| 1H 2107-097 | 36 ± 4 | 15 ± 2 | 0.41 |
| NGC 7469 | 9 ± 1 | 2 ± 1 | 0.13 |

**Notes:** in units of $10^{13}$.
[a] Energy for one photon of Fe II $\lambda$4570 = 4.33x10$^{-28}$ erg s$^{-1}$ cm$^{-2}$.
[b] Energy for one photon of Fe II $\lambda$9200 = 2.15x10$^{-28}$ erg s$^{-1}$ cm$^{-2}$.
[c] Average N = 0.36.

$a^4D \rightarrow (u,v)^4(D,F)$ followed by downward transitions to the level $e^4D$ via the emission of the $\lambda$9200 lines. The latter level decays to $e^4D \rightarrow z^4(Z,F)$, via UV transitions emitting the lines at ~2800 Å. A further cascade process contributes to producing the $\lambda$4570 bump. However, collisional excitation may also populate the upper levels leading to the $\lambda$4570 bump. As the $\lambda$9200 bump is clearly present in all objects of the sample, the presence of this excitation channel is demonstrated. In order to assess the relative contribution of the Ly$\alpha$ fluorescence to the optical Fe II emission, we plot $R_{9200}$ and $R_{4570}$ in Figure 2.11. It can be seen that both quantities are indeed well correlated ($P = 0.76$), showing that part of the photons producing the $\lambda$9200 bump are converted into $\lambda$4570 photons.

It is then possible to make a rough estimate of the contribution of the Ly$\alpha$ fluorescence to the optical Fe II emission through the comparison of the number of photons observed in both transitions. Table 2.8 shows the number of photons in the $\lambda$4570 bump (column (2)) and that in the $\lambda$9200 bump (column (3)). The ratio between the two quantities is listed in column (4). From Table 2.8 we estimate that Ly$\alpha$ fluorescence is responsible for ~ 36% of the observed optical lines in the Fe II bump centered at 4570 Å. The optical Fe II bump at 4570 Å represents

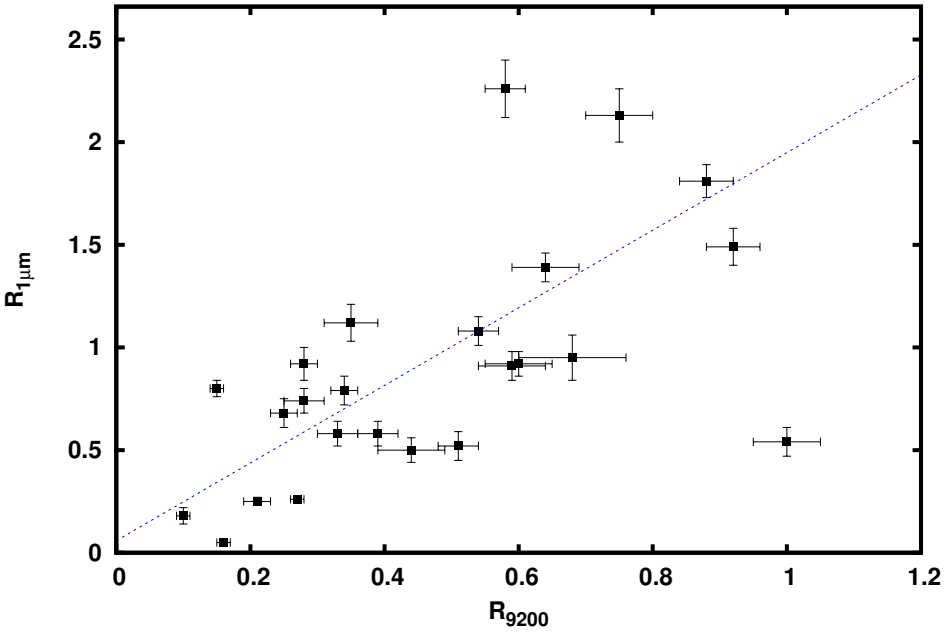


FIGURE 2.10. Correlation between $R_{1\mu m}$ and $R_{9200}$. The blue dotted line shows the best linear fit.

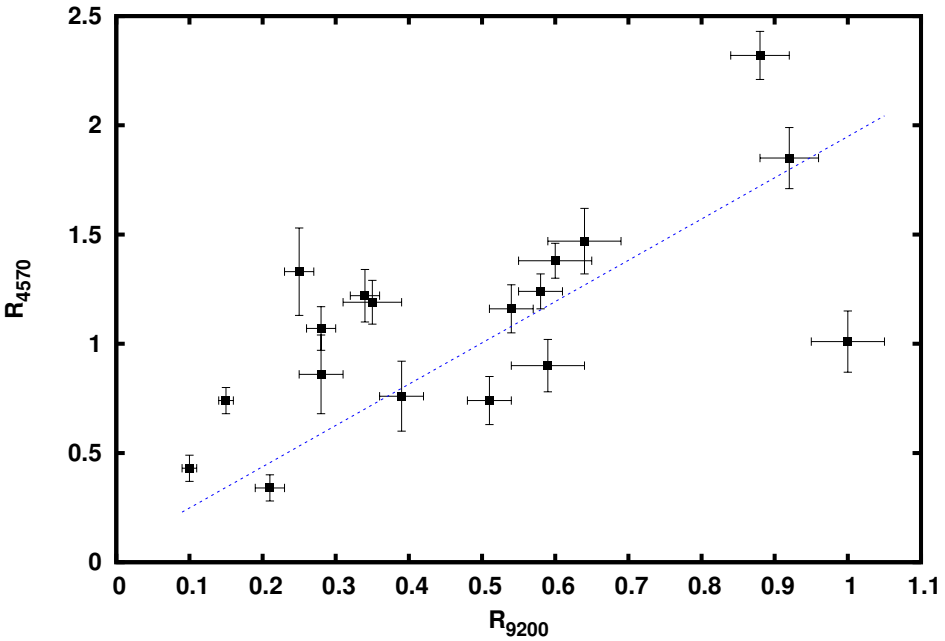


FIGURE 2.11. Correlation between $R_{9200}$ and $R_{4570}$. The blue dotted line shows the best linear fit.

~ 50% of the total optical Fe II emission (Veron-Cetty et al. 2004). This means that, on average, 18% of all optical Fe II photons observed are produced via downward transitions excited by Ly$\alpha$ fluorescence. This result is in agreement with that presented by Garcia-Rissmann et al. (2012), which estimated a contribution of 20% of this excitation mechanism in I Zw 1

## 2.5 Location of the Fe II Emission Line Region

The fact that the BLR remains unresolved for all AGNs poses a challenge to models that try to predict the spatial structure and kinematics of this region. In the simplest approach, we assume that the proximity of this region to the central source (black hole plus accretion disk) implies that the movement of the gas clouds is dominated by the gravitational potential of the black hole. Under this assumption, the analysis of the line profiles (form and width) can provide us with clues about the physical structure of this region.

We address the above issue using the most prominent lines presented in Table 2.3. The line profiles of Ca II $\lambda$8664, Fe II $\lambda$10502, O I $\lambda$11287, and Pa$\beta$ are relatively isolated or only moderately blended, making the study of their line profiles more robust than their counterparts in the optical. With the goal of obtaining clues on the structure and kinematics of the BLR, we carried out an analysis of these four line profiles detected in our galaxy sample.

Figure 2.12 shows the FWHM of O I versus that of Fe II. It is clear from the plot that both lines have very similar widths, with the locus of points very close to the unitary line (red line in the Figure 2.12). We run a Kolmogorov–Smirnov (K-S) test to verify the similarity of these two populations.

We found a statistical significance of $p = 0.74$, implying that it is highly likely that both lines belong to the same parent population. This result can also be observed in Figures 2.13–2.16, which show that both lines display similar velocity widths and shapes. Rodriguez-Ardila et al. (2002), analyzing a smaller sample, found that these two lines had similar profiles, suggesting that they arise from the same parcel of gas. Our results strongly support these hypotheses using a different and a more sizable sample of 25 AGNs.

A similar behavior is seen in Figure 2.17, which shows the FWHM of Ca II versus Fe IIṪhe lower number of points is explained by the fact that for a subsample of objects it was not possible to obtain a reliable estimate of the FWHM of Ca II either owing to poor S/N or because in some objects Ca II appears in absorption. As with O I and Fe II, we found that the width of Ca II is similar to that of Fe II. The K-S test reveals a statistical significance of $p = 0.81$. The combined results of Figures 2.12 and 2.17 support the physical picture where these three lines are formed in the same region. Since the analysis of the Fe II emission is usually more challenging, the fact that O I and Ca II are produced co-spatially with iron provides constraints on the use of these ions to study the same physical region of the BLR (Matsuoka et al. 2007, 2008).

In contrast to O I and Ca II, the Paschen lines display a different behavior. Figure 2.18 shows

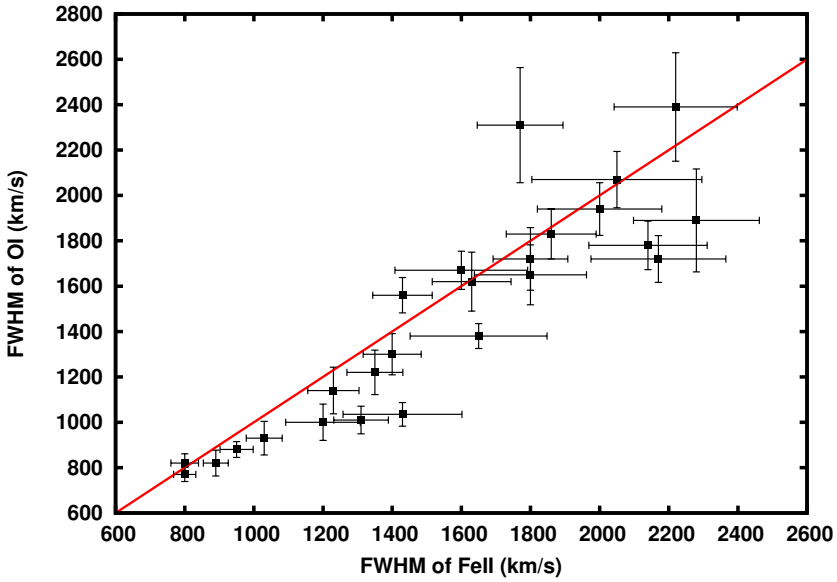


FIGURE 2.12. Correlation between the FWHM of Fe II and the FWHM of O I. The red line shows the unitary relationship.

the FWHM of Pa$\beta$ versus Fe IIİt is clear that the latter appears systematically narrower than the former, suggesting that the H I lines are formed in a region closer to the central source than Fe II and, by extension, O I and Ca II. The K-S test for these two populations resulted in a statistical significance of $p = 0.001$. The average FWHM value for Pa$\beta$ is $\sim 30\%$ larger than that of Fe II.

Assuming that the Fe II emitting clouds are virialized, the distance between the nucleus and the clouds is given by $D \propto v^{-2}$. Using in this equation the average difference in width (or velocity) between Fe II and H I, we found that the Fe II emitting region is twice as far from the nucleus compared to the region where hydrogen emission is produced.

The stratification of the BLR can also be observed in Figures 2.13–2.16, which compare the line profiles of the above four lines discussed in this section. We add to the different panels, when available, C IV $\lambda$1550, a higher-ionization emission line. The plots show that Fe II, O I, and Ca II have similar FWHM and profile shapes. Pa$\beta$ has a larger FWHM than Fe II, and the C IV line is usually the broadest of the five lines. Moreover, the C IV line profile is highly asymmetric. This result indicates that C IV is probably emitted in an inner region of the BLR, closer to the central source than Pa$\beta$, and is very likely affected by outflows driven by the central source, as well as electron or Rayleigh scattering (Baskin & Laor 2005; Gaskell 2009). An observational test of this scenario was provided by North et al. (2006), who detected P–Cygni profiles in this line in a sample of seven AGNs.

The above findings are in good agreement with those reported in the literature for different samples of AGNs and spectral regions. Hu et al. (2008) analyzed a sample of more than 4000 spectra of quasars from SDSS and verified that the FWHM of the Fe II lines was, on average, 3/4

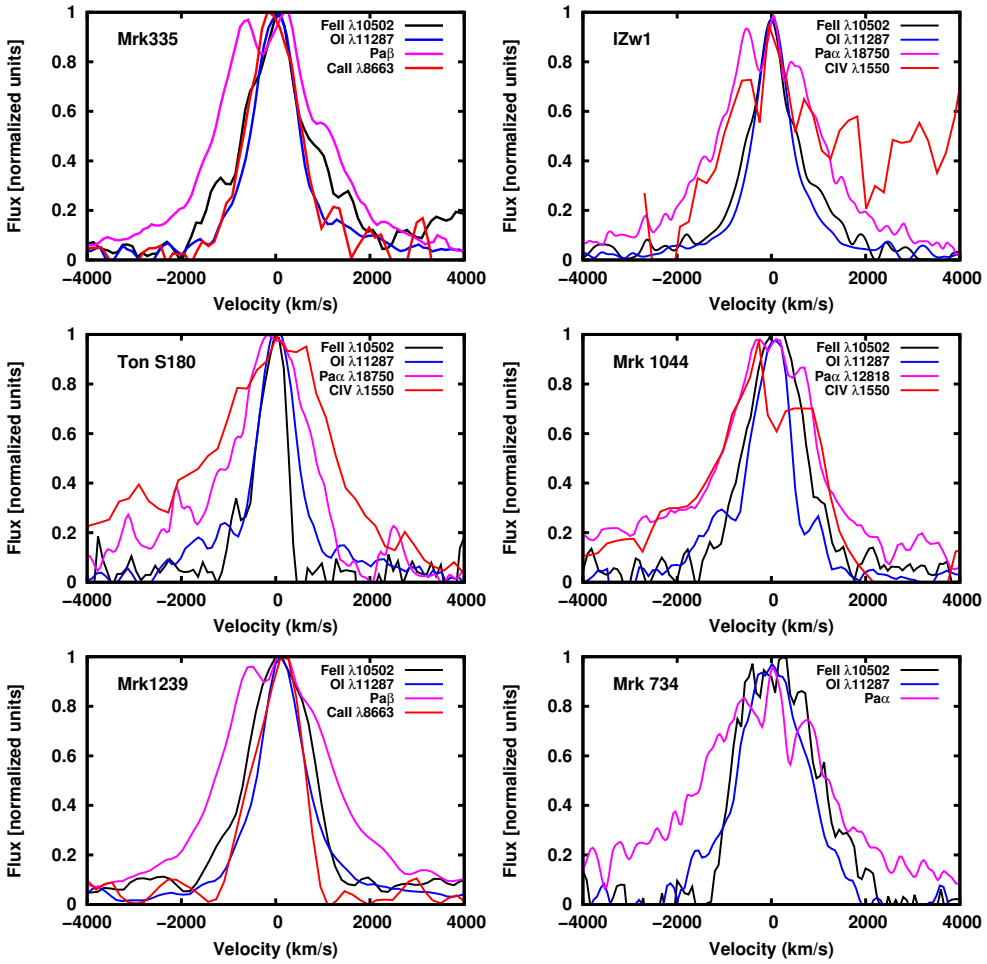


FIGURE 2.13. Comparison between the broad line profiles for the most important lines in this work for each object of the sample: Fe II (black line), O I (blue line), and Pa$\beta$ (magenta line). C IV (red line) was added for the objects in which it was available in order to have a high-ionization line to compare. In all cases, the lines were normalized to their peak intensity and Pa$\beta$ had its narrow component removed according to the procedure described in Section 2.3.

that of H$\beta$. Sluse et al. (2007), using spectroscopic microlensing studies for the AGN RXS J1131–1231, found that Fe II is emitted most probably in an outer region beyond H$\beta$. Matsuoka et al. (2008), comparing the intensities of Ca II/O I $\lambda$8446 and O I $\lambda$11287/O I $\lambda$8446 with those predicted by theoretical models, found for 11 AGNs that these lines are emitted in the same region of the BLR, with common location and gas densities. Martinez-Aldama et al. (2015) studied the emission of the Ca II triplet + O I $\lambda$8446 in a sample of 14 luminous AGNs with intermediate redshifts and found intensity ratios and widths consistent with the outer part of a high-density BLR, suggesting that these two emission lines could be emitted in regions with similar dynamics.

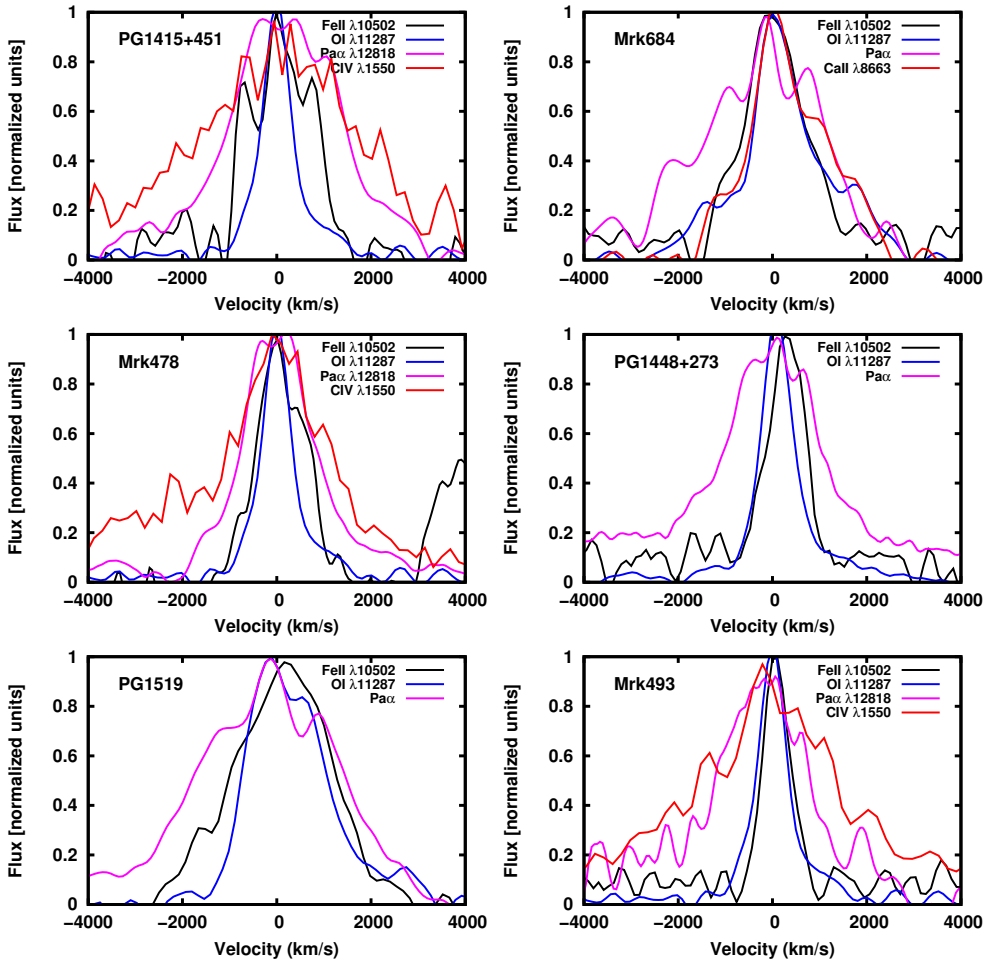


FIGURE 2.14. Continuation of Figure 2.13

Recent works based on variability studies indicate that Fe II and hydrogen are emitted at different spatial locations, with the former being produced farther out than the latter (Kaspi et al. 2000; Kuehn et al. 2008; Barth et al. 2013). Kuehn et al. (2008), for instance, studied the reverberation behavior of the optical Fe II lines in Akn 120. They found that the optical Fe II emission clearly does not originate in the same region as H$\beta$ and that there was evidence of a reverberation response time of 300 days, which implies an origin in a region several times farther away from the central source than H$\beta$. Barth et al. (2013) report similar results in the Seyfert 1 galaxies NGC 4593 and Mrk 1511 and demonstrate that the Fe II emission in these objects originates in gas located predomnantly in the outer portion of the BLR (see Table 2.9 for the values). Hu et al. (2015), however, analyzing the reverberation mapping in a sample of nine AGNs, identified as super-Eddington accreting massive black holes (SEAMBHs), found no difference between the time lags of Fe II and H$\beta$.

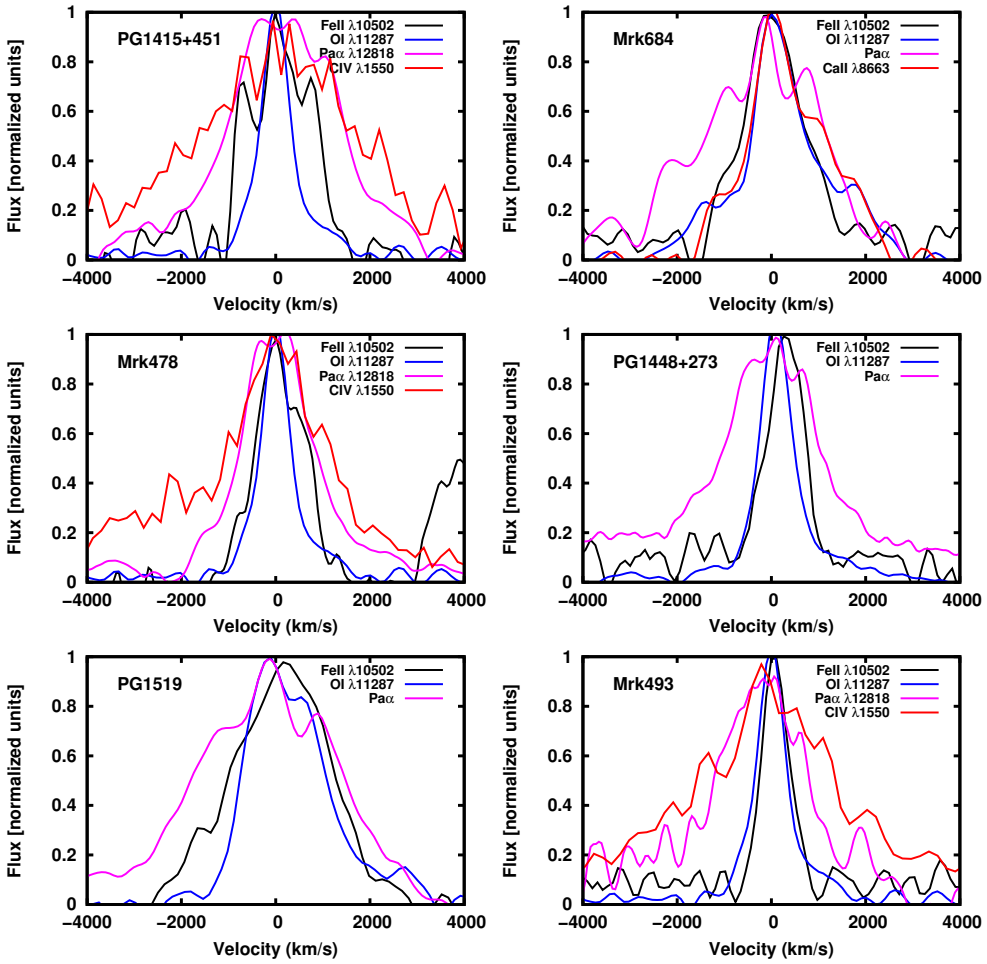


FIGURE 2.15. Continuation of Figure 2.13

Despite the fact that Fe II reverberation mapping results are quite rare in the literature, the reverberation of H$\beta$ is indeed more common (Peterson et al. 1998; Peterson & Wandel 1999; Kaspi et al. 2000). Peterson et al. (1998) present a reverberation mapping for nine AGNs obtained during an 8 yr monitoring campaign, where they derived the distance of the H$\beta$ emission line region. Kaspi et al. (2000) collected data from a 7.5 yr monitoring campaign in order to determine several fundamental properties of AGNs, such as BLR size and black hole mass. Four of their objects (Mrk 335, Mrk 509, NGC 4051, and NGC 7469) are common to our work, and they found the distance of the H$\beta$ emitting region using reverberation mapping. From the Hu et al. (2015) reverberation-mapped AGNs we identified three objects common to our sample (Mrk 335, Mrk 1044, and Mrk 493). From their results, and assuming that the Fe II emitting clouds are virialized, we may estimate the distance of these iron clouds to the central source using the relation between the measured FWHM of Fe II and H$\beta$ for these objects. The values that we find

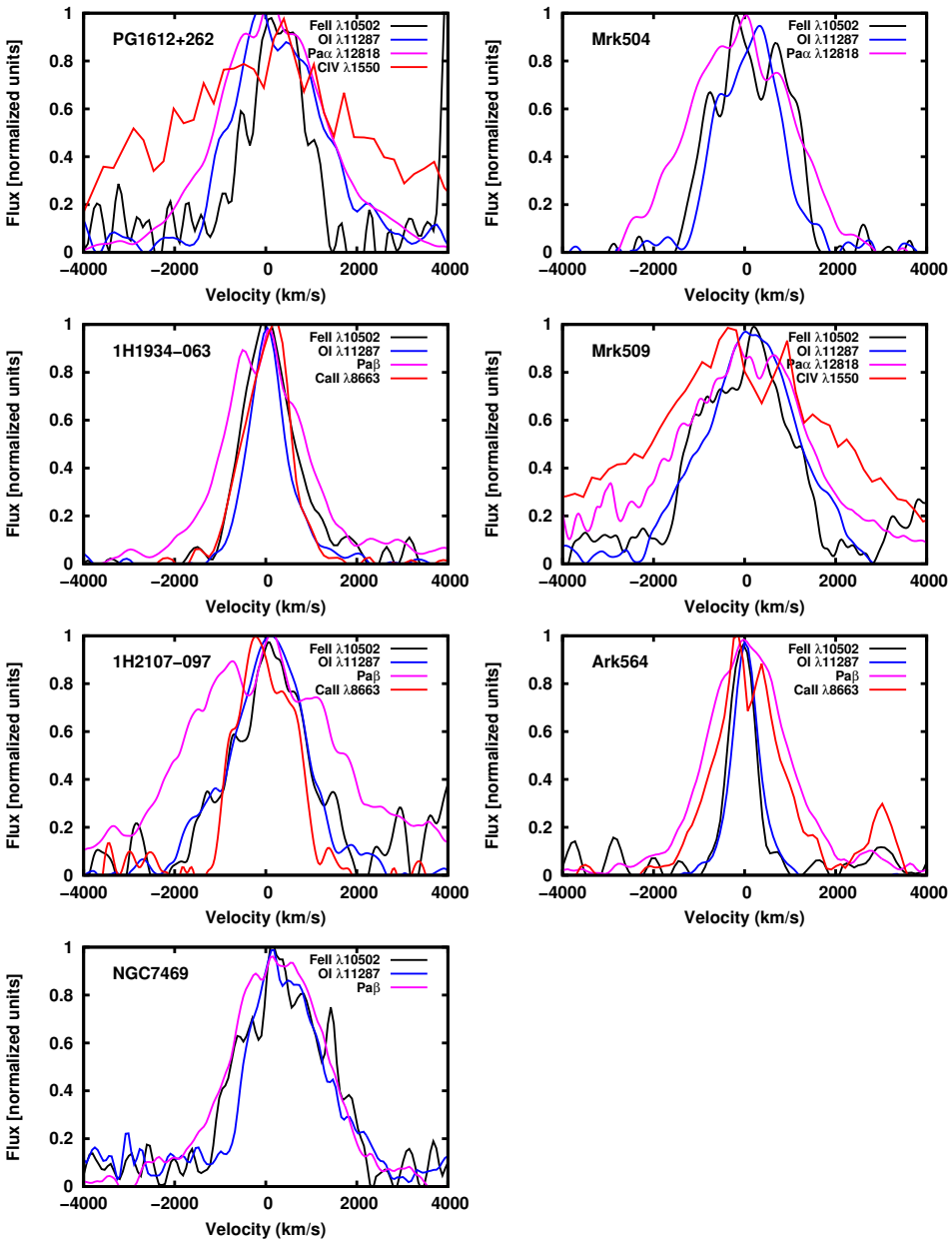


FIGURE 2.16. Continuation of Figure 2.13

are presented in Table 2.9.

Columns (2) and (3) of Table 2.9 show the distance of H$\beta$ and Fe II (Kaspi et al. 2000; Hu et al. 2015, determined by reverberation mapping), respectively. For Mrk 335, we notice discrepant values for the distance of H$\beta$ in the work of Hu et al. (2015) (8.7 light-days) and Kaspi et al. (2000) (16.8 light-days). Column (4) of Table 2.9 shows our estimations of the distance to the Fe II emission line region. Except for Mrk 493, our estimations are in good agreement with those

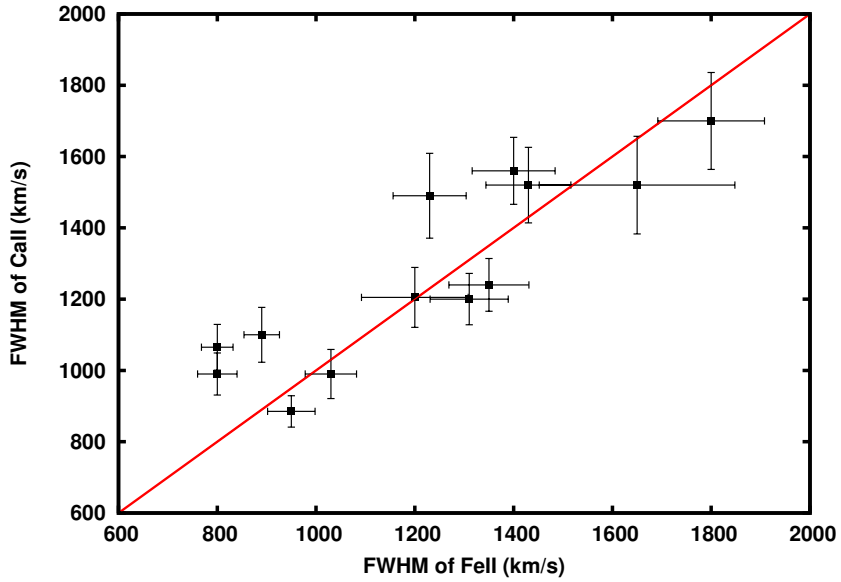


FIGURE 2.17. Correlation between the FWHM of Fe II and the FWHM of Ca II. The red line shows the unitary relationship.

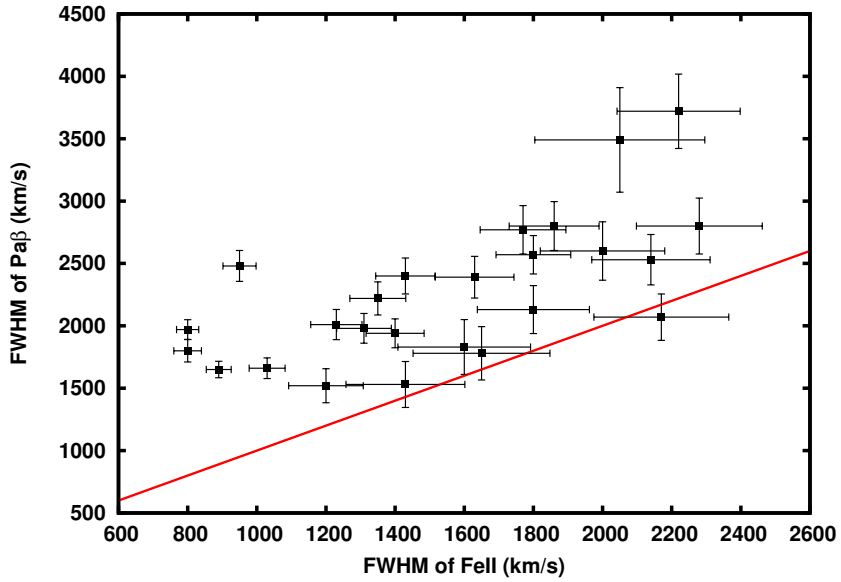


FIGURE 2.18. Correlation between the FWHM of Fe II and the FWHM of Pa$\beta$. The red line shows the unitary relationship.

measured from reverberation mapping, with a ratio between the distances of the Fe II and H$\beta$ emission line region of $\sim 2$, as we predict. Hu et al. (2015) point out that the distance of the Fe II emission line region may be related to the intensity of the Fe II emission. They noted that the time lags of Fe II are roughly the same as H$\beta$ in AGNs with $R_{4570} > 1$ (including Mrk 493, as well

Table 2.9: Distance of the H$\beta$ and Fe II Emission Line Regions

| | H$\beta$ | Fe II | Fe II |
|---|---|---|---|
| Object | Reverb. map. | Reverb. map. | Our estimations |
| Mrk 335$^{(a)}$ | $8.7^{+1.6}_{-1.9}$ | $26.8^{+2.9}_{-2.5}$ | $23.2^{+2.1}_{-2.1}$ |
| Mrk 1044$^{(a)}$ | $10.5^{+3.3}_{-2.5}$ | $13.9^{+3.4}_{-4.7}$ | $15.6^{+1.7}_{-1.7}$ |
| Mrk 509$^{(b)}$ | $79.3^{+6.3}_{-6.3}$ | - | $198.2^{+34.5}_{-34.5}$ |
| NGC 4051$^{(b)}$ | $6.5^{+5.1}_{-5.1}$ | - | $8.5^{+6.3}_{-6.3}$ |
| NGC 7469$^{(b)}$ | $4.9^{+0.8}_{-0.8}$ | - | $11.2^{+1.8}_{-1.8}$ |
| Mrk 493$^{(a)}$ | $11.6^{+1.2}_{-2.6}$ | $11.9^{+3.6}_{-6.5}$ | $49.3^{+5.6}_{-5.6}$ |

**Notes:** Distances in light-days.
[a] Reverberation mapping values from Hu et al.2015.
[b] Reverberation mapping values from Kaspi et al. 2000.

the other sources in their sample that are not common to ours), usually classified as strong Fe II emitters, and longer for those with normal/weak Fe II emission ($R_{4570} < 1$), as seen in the sample of Barth et al. (2013) (and most of our sample). This indicates that the physical properties of strong Fe II emitters may be different from the normal Fe II emitters. Observations of this kind of object are needed to confirm this hypothesis.

From the results of Kaspi et al. (2000),Barth et al. (2013), and Hu et al. (2015), we can also estimate a mean distance for the H$\beta$ and Fe II emission line region: $\tau$(H$\beta$) = 19.7 light-days and $\tau$(Fe II) = 40.5 light-days. If we include high-luminosity quasars (such as Mrk 509), the average values are significantly higher: $\tau$(H$\beta$) = 80.3 light-days and $\tau$(Fe II) = 164.6 light-days.

Assuming a Keplerian velocity field where the BLR emitting clouds are gravitationally bound to the central source, the above results suggest that the low-ionization lines (Fe II Ca II, and O I) are formed in the same outer region of the BLR. Moreover, the hydrogen lines would be formed in a region closer to the central source. This scenario is compatible with the physical conditions needed for the formation of Fe II and O I, that is, neutral gas strongly protected from the incident ionizing radiation coming from the central source. These conditions can only be found in the outer regions of the central source. Our work confirms results obtained in previous works using different methods in different spectral regions (Persson 1988; Rodriguez-Ardila et al. 2002; Sluse et al. 2007; Hu et al. 2008; Barth et al. 2013), but on significantly smaller samples.

## 2.6 Final Remarks

We analyzed for the first time an NIR sample of 25 AGNs in order to verify the suitability of the NIR Fe II template developed by Garcia-Rissmann et al. (2012) in measuring the Fe II strength in a broad range of objects. We also studied the excitation mechanisms that lead to this emission and derived the most likely region where it is produced. The analysis and results carried out in the previous sections can be summarized as follows:

1. We identified, for the first time in a sizable sample of AGNs, the Ly$\alpha$ excitation mechanism predicted by Sigut & Pradhan (1998). The key feature of this process is the Fe II bump at 9200 Å, which is clearly present in all objects of the sample.

2. We demonstrated the suitability of the NIR Fe II template developed by Garcia-Rissmann et al. (2012) in reproducing most of the iron features present in the objects of the sample. The template models and subtracts the NIR Fe II satisfactorily. We found that the relative intensity of the 1 $\mu$m lines remains constant from object to object, suggesting a common excitation mechanism (or mechanisms), most likely collisional excitation. Qualitative analysis made with the NIR and UV spectra led us to conclude that this process contributes to most of the Fe II production, but Ly$\alpha$ fluorescence must also contribute to this emission. However, the percentage of the contribution should vary from source to source, producing the small differences found between the predicted and observed $\lambda$9200 bump strengths. Despite this, it is still possible to determine the total Fe II intensity of the bump.

3. We found that the NIR Fe II emission and the optical Fe II emission are strongly correlated. The strong correlation between the indices $R_{1\mu m}$, $R_{9200}$, and $R_{4570}$ shows that Ly$\alpha$ fluorescence plays an important role in the production of the Fe II observed in AGNs.

4. Through the comparison between the number of Fe II photons in the $\lambda$9200 bump and that in the $\lambda$4570 bump, we determine that Ly$\alpha$ fluorescence should contribute with at least $\sim 18\%$ to all optical Fe II flux observed in AGNs. This is a lower limit, since UV spectroscopy at a spectral resolution higher than currently available is needed to estimate the total contribution of this process to the observed Fe II emission. This result is key to the development of more accurate models that seek to better understand the Fe II spectrum in AGNs.

5. The comparison of BLR emission line profiles shows that Fe II, O I, and Ca II display similar widths for a given object. This result implies that they all are produced in the same physical region of the BLR. In contrast, the Pa$\beta$ profiles are systematically broader than those of iron (30% broader, on average). This indicates that the former are produced in a region closer to the central source than the latter (2× closer, on average). These results and data from reverberation mapping allowed us to estimate the distance of the Fe II emitting clouds from the central source for six objects in our sample. The values found range from a few light-days ($\sim 9$ in NGC 4051) to nearly 200 (in Mrk 509). Overall, our results agree with those found independently via reverberation mapping, giving additional support to our approach. These results should also guide us to understanding why reverberation mapping has had little success in detecting cross-correlated variations between the AGN continuum and the Fe II lines.

CHAPTER 3

# DISCOVERY OF A RADIO GALAXY AT Z = 5.72

A. Saxena[1], **M. Marinello**[1,2], R. Overzier[2], P. N. Best[3], H. J. A. Röttgering[1], K. J. Kuncan[1], I. Prandoni[4], L. Pentericci[5], M. Magliocchetti[6], D. Paris[5], F. Cusano[7], F. Marchi[5], H. T. Intema[1], G. K. Miley[1]

[1] Leiden Observatory, Leiden University, P.O. Box 9513, 2300 RA Leiden, The Netherlands

[2] Observatório Nacional, Rua José Cristino, 77. CEP 20921-400, São Cristóvão, Rio de Janeiro-RJ, Brazil

[3] Institute for Astronomy, University of Edinburgh, Royal Observatory, Blackford Hill, EH9 3HJ Edinburgh, UK

[4] INAF-Instituto di Radioastronomia, Via P. Gobetti 101, I-40129 Bologna, Italy

[5] INAF-Osservatorio Astronomico di Roma, Via Frascati 33, I-00040 Monteporzio (RM), Italy

[6] IAPS-INAF, Via Fosso del Cavaliere 100, I-00133 Rome, Italy

[7] INAF-Osservatorio di Astrofisica e Scienza dello Spazio di Bologna, Via P. Gobetti 93/3, I-40129 Bologna, Italy

Published in the Monthly Notices of the Royal Astronomical Society, 2018, 480, 2733S

We report the discovery of the most distant radio galaxy to date, TGSS J1530+1049 at a redshift of $z = 5.72$, close to the presumed end of the Epoch of Reionisation. The radio galaxy was selected from the TGSS ADR1 survey at 150 MHz for having an ultra-steep spectral index, $\alpha_{1.4\,\mathrm{GHz}}^{150\,\mathrm{MHz}} = -1.4$ and a compact morphology obtained using VLA imaging at 1.4 GHz. No optical or infrared counterparts for the radio source were found in publicly available sky surveys. Follow-up optical spectroscopy at the radio position using GMOS on Gemini North revealed the presence of a single emission line. We identify this line as Lyman alpha at $z = 5.72$, because of its asymmetric line profile, the absence of other optical/UV lines in the spectrum and a high equivalent width. With a Ly$\alpha$ luminosity of $5.7 \times 10^{42}$ erg s$^{-1}$ and a FWHM of 370 km s$^{-1}$, TGSS J1530+1049 is comparable to 'non-radio' Lyman alpha emitters (LAEs) at a similar redshift. However, with a radio luminosity of $\log L_{150\,\mathrm{MHz}} = 29.1$ W Hz$^{-1}$ and a deconvolved physical size 3.5 kpc, its radio properties are similar to other known radio galaxies at $z > 4$. Subsequent $J$ and $K$ band imaging using LUCI on the Large Binocular Telescope resulted in non-detection of the host galaxy down to $3\sigma$ limits of $J > 24.4$ and $K > 22.4$ (Vega). The $K$ band limit is consistent with $z > 5$ from the $K - z$ relation for radio galaxies and helps rule out low redshifts. The stellar mass limit derived using simple stellar population models is $M_{\mathrm{stars}} < 10^{10.5}\ M_{\odot}$. Its relatively low stellar mass and small radio and Ly$\alpha$ sizes suggest that TGSS J1530+1049 may be a radio galaxy in an early phase of its evolution.

## 3.1 Introduction

High-redshift radio galaxies (HzRGs) are thought to be the progenitors of local massive elliptical galaxies and generally contain large amounts of dust and gas (Best et al. 1998; Carilli et al. 2002a; Reuland et al. 2004; De Breuck et al.2010). They are also among the most massive galaxies at their redshift (Overzier et al. 2009) and are often found to be located at the centre of clusters and proto-clusters of galaxies (Pentericci et al. 2000; Venemans et al. 2002; Röttgering et al. 2003; Miley et al. 2004; Hatch et al. 2011; Orsi et al.2016). Studies of their environment can give insights into the assembly and evolution of the large scale structure in the Universe. Miley & De Breuck (2008) provide an extensive review about the properties of distant radio galaxies and their environments.

Radio galaxies at $z$ >6, in the Epoch of Reionisation (EoR), are of particular interest as they could be used as unique tools to study the process of reionisation in detail. At these redshifts, the hyper-fine transition line from neutral hydrogen atoms, with a rest-frame wavelength of 21 cm, falls in the low-frequency radio regime and can be observed as absorption signals in spectra of luminous background radio sources such as radio galaxies (Carilli et al.2002b; Furlanetto & Loeb 2002; Xu et al. 2009; Mack & Wyithe 2012; Ewall-Wice et al. 2014; Ciardi et al. 2015). Such 21 cm absorption signals from patches of neutral hydrogen clouds in the early Universe could in principle be observed by current and next-generation radio telescopes such as the Giant

Metre-wave Radio Telescope (GMRT; Swarup et al. 1991), the Low Frequency Array (LOFAR; van Haarlem et al. 2013), the Murchinson Widefield Array (MWA; Tingay et al. 2013) and the Square Kilometer Array (SKA; Dewdney et al. 2009). This unique application motivates searches for bright enough radio galaxies at the highest redshifts from deep all-sky surveys at low radio frequencies.

Finding powerful radio galaxies at increasingly large distances or redshifts, however, is challenging. HzRGs are rare and flux-limited samples have shown that their space densities fall off dramatically at $z > 2-3$ (Dunlop & Peacock 1990; Willott et al. 2001; Rigby et al. 2011, 2015). Although a number of quasars at $z > 5$ are known, with a few also being radio-loud (see Bañados et al. 2015, for example), the same cannot be said for radio galaxies – previously, the only known radio galaxy at $z > 5$ was TN J0924–2201 at $z = 5.19$ (van Breugel et al. 1999). If the orientation-based unification of radio galaxies and quasars is valid (see Morabito et al. 2017, for example), the number of radio quasars and galaxies at any given epoch should be comparable and it may be possible that many of the already unidentified radio sources are at $z > 5$. The scarcity of $z > 5$ radio galaxies could therefore be due to the relative difficulty in first identifying these sources amongst the wider radio source population, and then obtaining spectroscopic redshifts for these radio galaxies, which are optically much fainter than quasars. Dedicated spectroscopic follow-up of radio sources such as the WEAVE-LOFAR survey (Smith et al. 2016), and the upcoming major optical facilities such as the Extremely Large Telescope (ELT), the Thirty Meter Telescope (TMT), the Giant Magellan Telescope (GMT) and the James Webb Space Telescope (JWST) will help overcome these difficulties and potentially help characterise a number of USS radio sources.

The key requirement for gathering enough statistics for meaningful studies of radio galaxies at high redshifts are deep low-frequency radio surveys covering large areas on the sky. Surveys such as the TIFR GMRT Sky Survey Alternative Data Release 1 (TGSS; Intema et al. 2017) and the currently ongoing surveys using LOFAR (Shimwell et al. 2017) are opening up new parameter spaces for searches for radio galaxies at $z > 6$. Using TGSS, which covers the entire radio sky north of $-53$ declination at a frequency of 150 MHz and achieving a median noise level of 3.5 mJy beam$-1$, we launched a campaign to hunt for fainter and potentially more distant HzRGs, with the ultimate aim of discovering radio galaxies that could be suitable probes of the EoR (Saxena et al. 2018). In this paper, we report the discovery of a radio galaxy at a redshift of $z = 5.72$, TGSS J1530+1049, which was pre-selected as part of our sample of high-redshift radio galaxy candidates.

The layout of this paper is as follows. In Section 2 we present details about the initial source selection criteria and follow-up radio observations at high resolution for TGSS J1530+1049. In Section 3 we present the new optical spectroscopy and infrared imaging obtained for TGSS J1530+1049 and expand upon the data reduction methods. In Section 4 we describe how the redshift for this source was determined. In Section 5 we study the emission line and radio properties of this source and set constraints on its stellar mass. We also compare the observed properties to galaxies

at the same epoch from the literature. Finally, in Section 6 we summarise the findings of this paper. Throughout this paper we assume a flat ΛCDM cosmology with $H_0 = 70\,\mathrm{km\,s^{-1}\,Mpc^{-1}}$ and $\Omega_m = 0.3$. Using this cosmology, at a redshift of 5.72 the age of the Universe is 0.97 Gyr, and the angular scale per arcsecond is 5.86 kpc.

## 3.2 Source Selection

Our two stage selection process is based on first isolating compact radio sources with an ultra-steep spectrum (USS; $\alpha < -1.3$, where $S_\nu \propto \nu_\alpha$) at radio wavelengths, that has historically been very successful at finding HzRGs from wide area radio surveys (Röttgering et al. 1994; Blundell et al. 1999; De Breuck et al. 2000; Afonso et al. 2011), and then combining it with optical and/or infrared faintness requirements. The relation that exists between the apparent K–band magnitude of radio galaxies and their redshift, known as the K–$z$ relation, (Lilly & Longair 1984; Jarvis et al. 2001; Willott et al. 2003; Rocca-Volmerange et al. 2004) gives further strength to the argument of selecting USS sources that are also faint at near-infrared wavelengths in a bid to isolate HzRGs (Ker et al. 2012). Deep near-infrared imaging of promising USS candidates can therefore serve as an independent way to set constraints on the redshifts of radio sources. HzRGs are expected to be very young and therefore, have small sizes at the highest redshifts (Saxena et al. 2017): implementing an additional criterion that puts an upper limit on the angular sizes of radio sources has the potential to increase the efficiency of pin pointing the highest-redshift sources in a wide area radio survey.

Combining all of these selection methods, we first shortlisted 588 candidates with an ultra-steep spectrum 150 MHz ($\alpha^{150\,\mathrm{MHz}}_{1.4\,\mathrm{GHz}} = -1.3$) and compact morphologies, out of a to tal of 65,996 sources that had spectral index information from TGSS and FIRST/NVSS. This sample probes fainter flux densities than previous large area searches and has flux limits that ensure that a new parameter space in flux density and spectral index is probed, where a large number of undiscovered HzRGs are expected to lie (Ishwara-Chandra et al. 2010). From this shortlist, we then retained in our sample only those radio sources that are blank in all available optical surveys such as the Sloan Digital Sky Survey DR12 (SDSS; Alam et al. 2015) and the Pan-STARRS1 survey (PS1; Chambers et al. 2016), and infrared surveys such as ALLWISE using the WISE satellite (Wright et al. 2010) and the UKIDSS surveys (Lawrence et al. 2007) to maximise the chances of finding radio galaxies at the highest redshifts. This led to a final sample of 32 very promising HzRG candidates. Details of the sample selection can be found in Saxena et al. (2018).

High resolution imaging using the Karl G. Jansky Very Large Array (VLA) for the 32 candidates, including for TGSS J1530+1049 (RA: 15:30:49.9, Dec: +10:49:31.1) is presented in Saxena et al. (2018), which was used to obtain morphologies and sub-arcsecond localisation of the expected positions of the host galaxies, enabling blind spectroscopic follow-up. TGSS J1530+1049 in particular showed a compact morphology, which was fitted with a single Gaussian. With a flux density

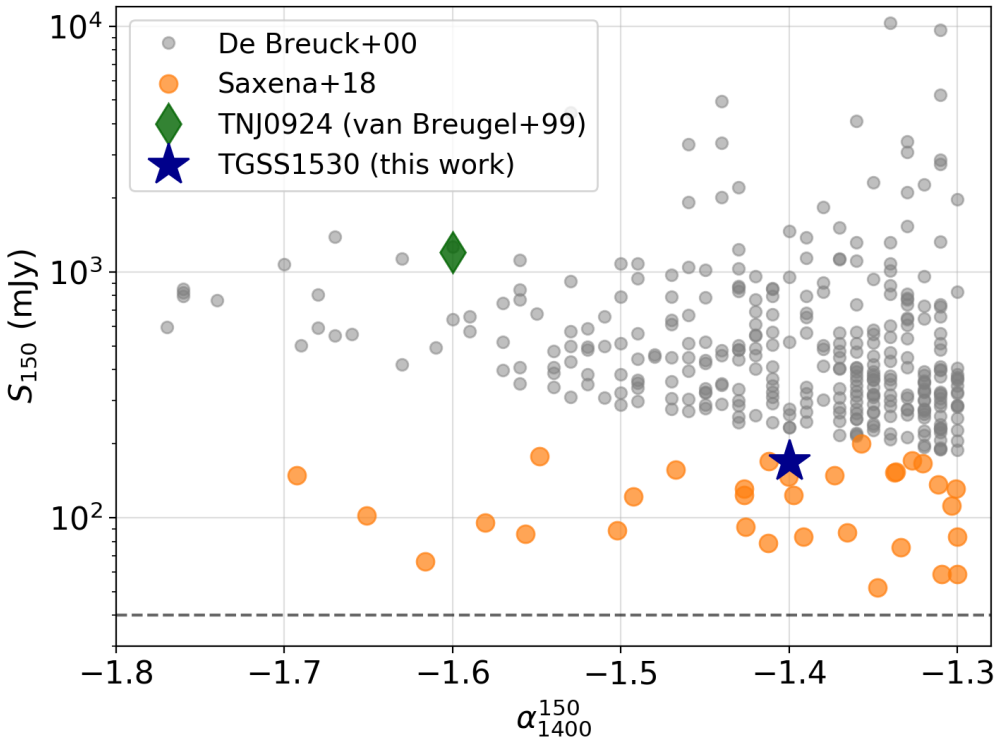


FIGURE 3.1. The location of TGSS J1530+1049 in the flux densityspectral index parameter space. The large orange points show the parameter space probed by the Saxena et al. (2018) sample and the smaller grey points show radio sources from De Breuck et al. (2000), scaled to an observed frequency of 150 MHz using the spectral indices provided for individual sources. Also shown for comparison is TN J0924–2201 at z = 5.2 (van Breugel et al. 1999). TGSS J1530+1049 is fainter than the previously studied large area samples and offers a new window into fainter radio galaxies at high redshifts.

of S 150 MHz= $170 \pm 34$ mJy, TGSS J1530+1049 is one of the brightest sources in the sample. At 1.4 GHz, it has a flux density $S_{1.4\mathrm{GHz}} = 7.5 \pm 0.1$ mJy, giving a spectral index of $\alpha = -1.4 \pm 0.1$. With a relatively small (deconvolved) angular size of $0.6 \pm 0.1$ arcsec, TGSS J1530+1049 was deemed to be a promising HzRG candidate. We show the location of TGSS J1530+1049 in the flux density-spectral index parameter space in Figure 3.1.

TGSS J1530+1049 is not detected in any of the PS1 bands (*g, r, i, z* and *y*). This source also happens to lie in the sky area covered by the UKIDSS Large Area Survey (LAS), and is not detected down to (Vega) magnitude limits of $y > 20.5$, $J > 20.0$, $H > 18.8$ and $K > 18.4$. We show the image obtained from stacking all of the LAS bands with radio contours overlaid in Figure 3.2. Lastly, this source is also not detected in any of the ALLWISE bands. These non-detections

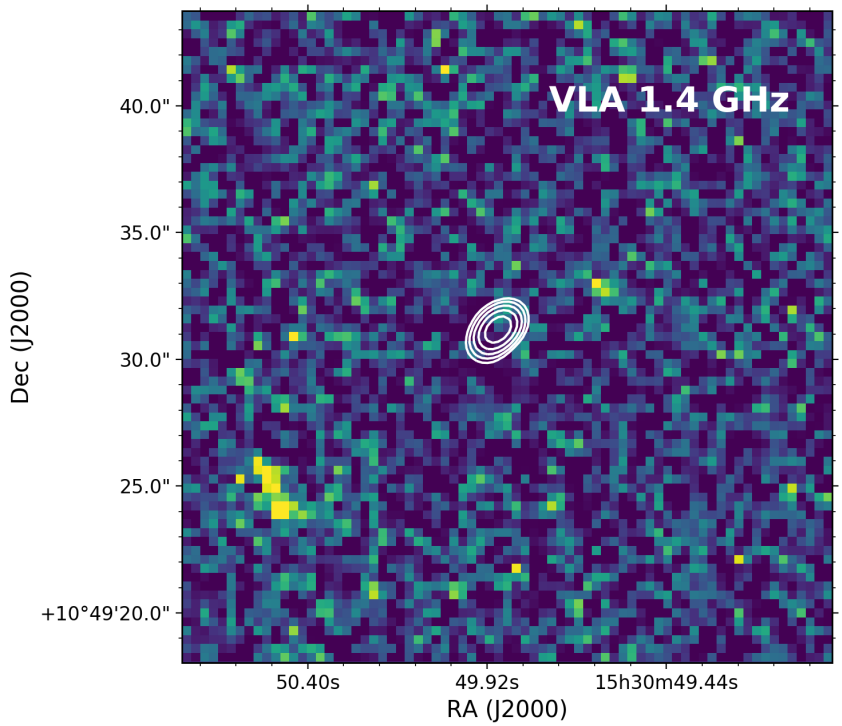


FIGURE 3.2. Stacked *y, J, H* and *K* band image from the UKIDSS Large Area Survey, with $\sqrt{2}$ contours (starting from 0.5 mJy, in a geometric progression of 2) from the 1.4 GHz VLA map (Saxena et al. 2018) overplotted for TGSS J1530+1049. The radio source is compact and has an ultra-steep spectral index. A non-detection in the UKIDSS LAS *K* band down to a magnitude limit of 18.4 Vega (~20.3 AB) made TGSS J1530+1049 a promising HzRG candidate and a prime target for spectroscopic follow-up.

coupled with the ultra-steep radio spectral index and compact radio morphology are in line with expectations of a high-redshift host galaxy and made TGSS J1530+1049 a prime candidate for follow-up spectroscopy.

## 3.3 Observations

### 3.3.1 Gemini GMOS spectroscopy

A long-slit spectrum of TGSS J1530+1049 was taken using GMOS on Gemini North on 28 April, 2017 (Program ID: GN-2017A-Q-8; PI: Overzier) using the filter GG455_G0305 and the R400_G5305 grating giving a wavelength coverage of 5400–10800 Å and a resolution of roughly R~1500. The central wavelength was set to 7000 Å. The total length of the slit was 300 arcseconds

and the slit width was chosen to be 1.5 arcseconds so that it covers the entire radio emission footprint detected in the VLA image. As the host galaxy of the radio source was undetected in all available all-sky optical/IR surveys, we performed blind offsetting from a bright star, which ensures positional accuracy to within 0.1 arcseconds, to the centroid of the radio emission. The VLA observations ensured sub-arcsecond localisation of the expected position of the host galaxy and the relatively large slit-width provided insurance against minor positional uncertainties. We took 3 exposures of 800 seconds each, giving a total of 2400 seconds of on-source exposure time. The standard star EG 131 was observed for flux calibration.

We used the Gemini IRAF package for reducing the data, which includes the standard steps for optical spectrum reduction. Briefly, the bias frames were mean stacked in a master bias which was subtracted from all other images acquired. Pixel-to-pixel sensitivity was corrected through the flat field image taken during the day of the observations. The wavelength solution was derived from the arc lamp frame taken immediately after the science observations, and applied to the science frame and standard star. The 2D images were then combined in a single frame, rejecting possible cosmic rays. The sky lines were removed and flux calibration was achieved using the standard star spectrum.

A single emission line with a peak at 8170 Å and a spatial extent of ~1 arcsecond was detected in the reduced 2D spectrum at the expected position of the radio galaxy. No other line associated with this source was detected. No continuum was detected either bluewards or redwards of this ine either. To ensure that the line detection is indeed real and not due to an artefact or contamination by cosmic rays, we looked at the individual frames, both raw and sky subtracted, to ensure that the detection (although marginal) was present in each science frame. The three frames are shown in Figure 3.3. The top panels show the raw frames and the bottom panels the sky subtracted frames. The emission line is clearly present in all three frames, ensuring that the detection is real. The extracted 1D spectrum with a 1 arcsecond aperture showing the detected emission line is shown in Figure 3.4. We give details about line identification in Section 4.

### 3.3.2 Large Binocular Telescope NIR imaging

Imaging in the J and K-s bands using LUCI (formerly known as LUCIFER; Seifert et al. 2003) on the Large Binocular Telescope (LBT) was carried out in two separate runs, with the first on 1 February 2018 and the second on 11 May 2018 (Program ID 2017 2018 43; PI: Prandoni). The average seeing throughout the observations was $0.6-0.8$ arcseconds. In the first run, the on-source exposure time was 720 ($12\times60$ s) seconds in $J$ (central wavelength of 1.247 microns) and 1200 ($20\times60$ s) seconds in $K-s$ (central wavelength of 2.194 microns). In the second run we obtained additional 3600 ($30\times120$ s) seconds in $J$ and 3000 ($50\times60$ s) seconds in $K-s$, giving a total on-source exposure time of 4320 seconds in $J$ band and 4200 seconds in $K-s$ band.

The LUCI data reduction pipeline developed at INAF-OAR was used to perform the basic reduction such as dark subtraction, bad pixel masking, cosmic ray removal, flat fielding and sky

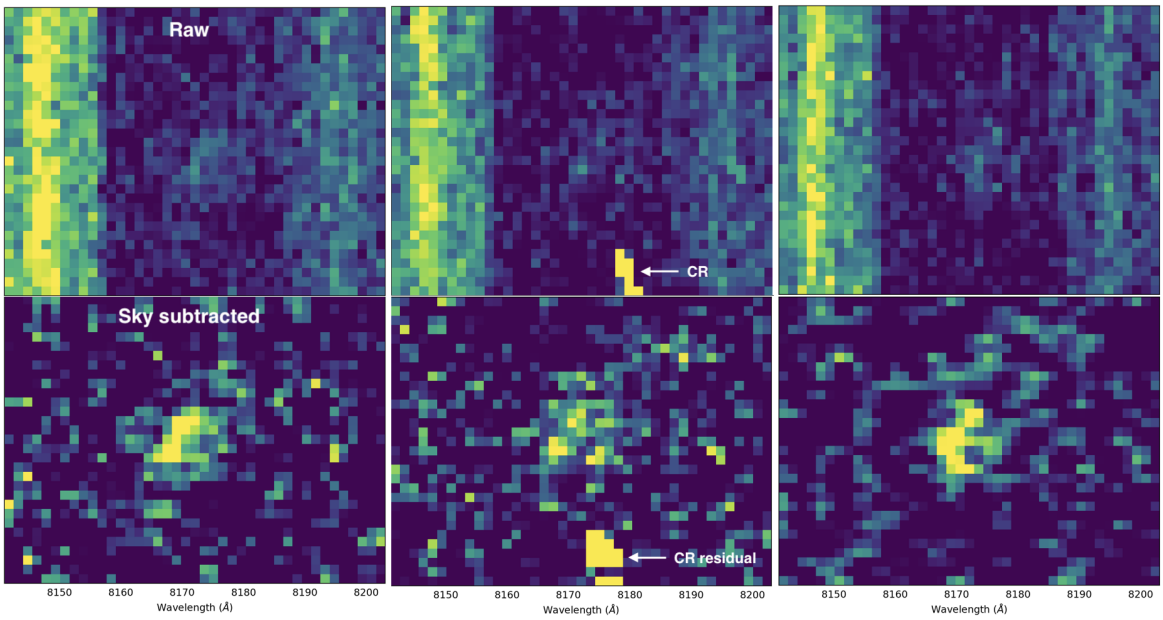


FIGURE 3.3. Raw (top panels) and sky subtracted (bottom panels) 2D frames shown for the three individual exposures taken using GMOS on Gemini. Traces of the emission line are visible in all three frames, ensuring that the detected line is real and not a consequence of cosmic rays or artefacts. There is some cosmic ray residual left over in the second frame but that does not contaminate the emission line signal.

subtraction. Astrometric solutions for individual frames were obtained and the single frames were then resampled and combined using a weighted co-addition to form a deeper image. [ The $4' \times 4'$ field-of-view of LUCI contained many bright objects detected in both 2MASS and the UKIDSS Large Area Survey, which were used to calibrate the photometry of the images in both bands.

The median and standard deviation of the background in both images was calculated by placing 5000 random apertures with a diameter of 1.5 arcseconds. We measure $3\sigma$ depths of $J = 24.4$ and $K - s = 22.4$. Aperture photometry performed on both $J$ and $K - s$ (from here on we denote $K - s$ as simply $K$) images using photutils (Bradley et al. 2017) at the peak of the radio emission using an aperture of diameter 1.5 arcseconds yield magnitudes that are lower than the $3\sigma$ depths in both images. Smoothing the $K$ band image with a $3\times3$ pixel Gaussian kernel reveals a faint source very close to the peak radio pixel, as shown in Figure 3.5, but it is not entirely clear if this indeed the host galaxy and there is no faint detection even in the smoothed $J$ band image. A summary of the observations is given in Table 3.1.

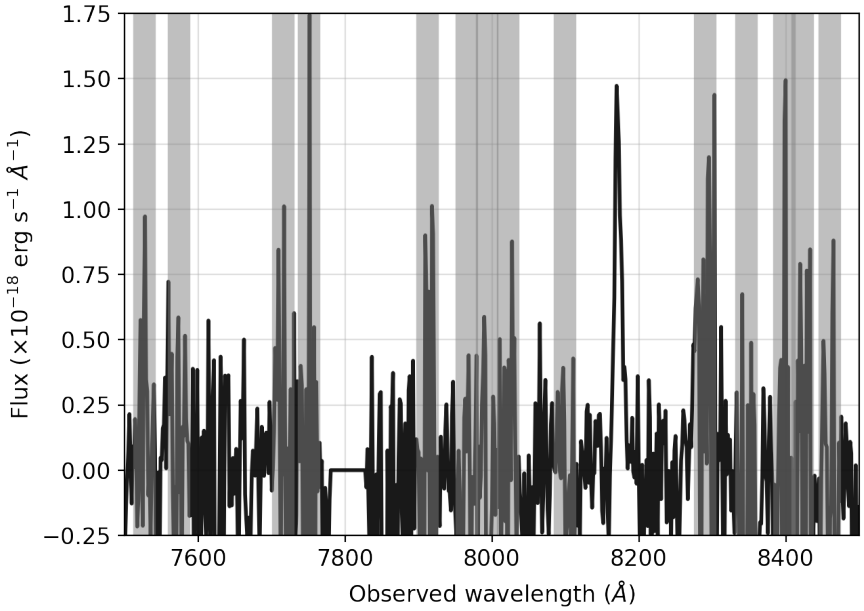


FIGURE 3.4. Extracted 1D spectrum showing the single emission line detection centred at 8170 Å from the GMOS 2D spectrum. No other line or continuum is detected. Shaded regions mark the presence of sky lines in the spectrum.

Table 3.1: Observation log.

| Telescope | Instrument | Date | Exp. time (sec) |
|---|---|---|---|
| Gemini N | GMOS long-slit | 28-04-2017 | 2400 (3 × 800s) |
| LBT | LUCI J-band | 01-02-2018 | 720 (12 × 60s) |
| | | 09-05-2018 | 3600 (30 × 120s) |
| | Total | | 4320 |
| LBT | LUCI Ks-band | 01-02-2018 | 1200 (20 × 60s) |
| | | 09-05-2018 | 3000 (50 × 60s) |
| | Total | | 4200 |

## 3.4 Redshift Determination

We identify the single emission line detected in the GMOS spectrum as Ly$\alpha$ $\lambda$1216, giving a redshift of $z = 5.720 \pm 0.001$, which is shown in Figure 3.6. Other plausible identifications of this emission line could be [O III] $\lambda$5007, giving a redshift of $z \sim 0.63$ or H$\alpha$ $\lambda$6563 at $z \sim 0.25$. These can be ruled out given the non-detection of other bright lines expected in the wavelength range covered. For example, if the observed line is [O III] at $z = 0.63$, then the [O II] $\lambda$3727 line would be observed at ~6075 Å, unless the galaxy has a particularly high [O III]/[O II] ratio as in the case of very low metallicity objects. An unresolved [O II] $\lambda\lambda$3726,3729 doublet at a redshift of $z \sim 1.2$ could be a possibility, but the absence of other expected UV/optical lines common in AGN and

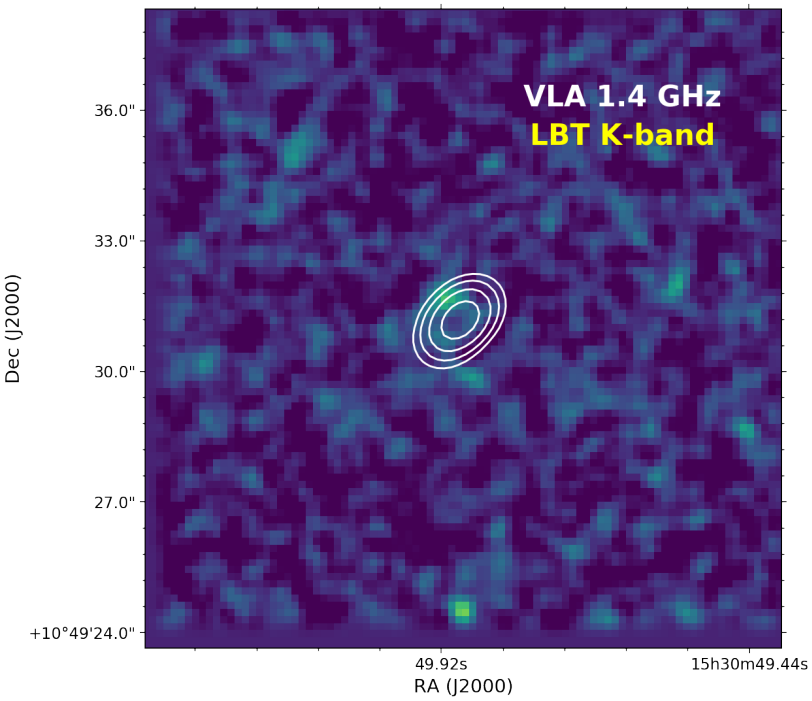


FIGURE 3.5. $K-$band image from the Large Binocular Telescope (LBT), which has been smoothed with a 3×3 pixel Gaussian kernel, with radio contours (same as Figure 3.2) from the VLA at 1.4 GHz overlaid. The measured magnitude at the radio position with a 1.5 arcsecond aperture is fainter than the $3\sigma$ depth of the image, giving $K > 22.4$. When the image is smoothed, however, faint emission is visible around the peak of the radio emission. The magnitude limit is consistent with $z > 5$ following the $K$–$z$ relation for radio galaxies. For comparison, the $z = 5.2$ radio galaxy TN J09224–2201 has a $K-$band magnitude of 21.3 (van Breugel et al. 1999).

radio galaxy spectra, such as C II] $\lambda$2326 or Mg II $\lambda\lambda$2797,2803, which are on average a factor of 2–4 times fainter than [O II] (De Breuck et al. 2001), makes this possibility unlikely. Another possibility could be C IV $\lambda$1549 giving $z = 4.27$, but this can be ruled out because in this case Ly$\alpha$, which is often much brighter (for example, there are no radio galaxies in De Breuck et al. (2001) with Ly$\alpha$ flux lower than C IV $\lambda$1549 flux), would be expected at ~6410 Å and we do not see any signs of an emission line in that region, which is free from bright sky lines.

We fit a Gaussian to the emission line (shown in Figure 3.6) to measure an integrated line flux of $F_{Ly\alpha} = 1.6 \pm 0.2 \times 10^{-17}$ erg s$^{-1}$ cm$^{-2}$. The total measured Ly$\alpha$ luminosity is $L_{Ly\alpha} = 5.7 \pm 0.7 \times 10^{42}$ erg s$^{-1}$. The full width at half maximum (FWHM) after correcting for the instrumental

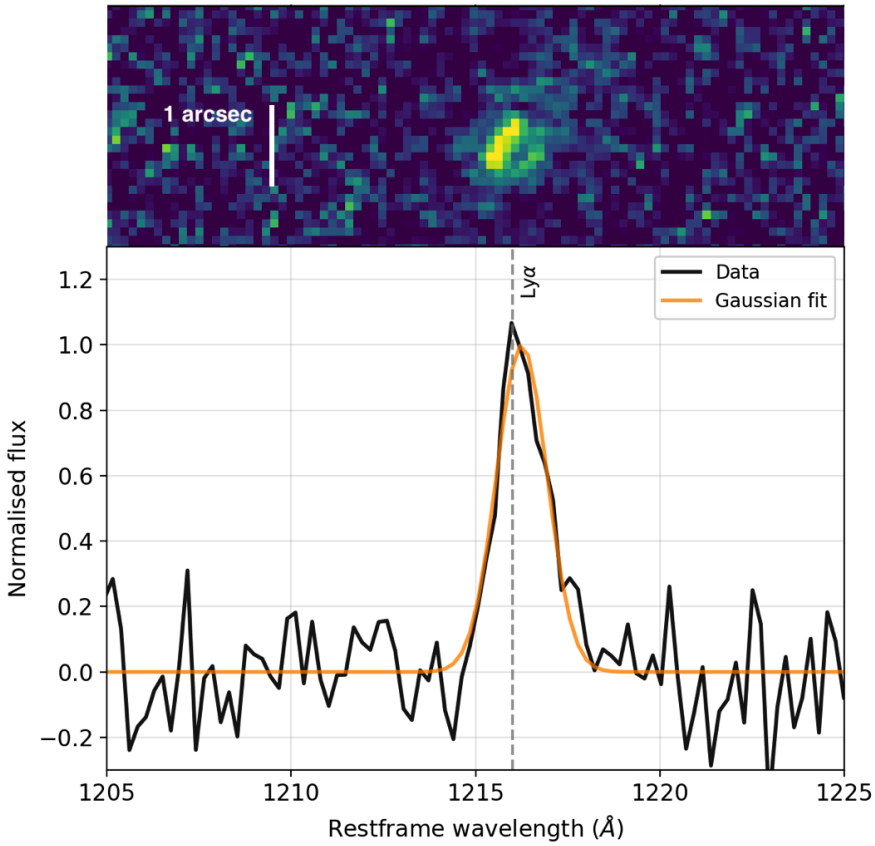


FIGURE 3.6. Rest-frame 1D spectrum showing the asymmetric Ly$\alpha$ line profile at a redshift of $z = 5.720$. Also shown is the best-fit Gaussian to the emission line. The peak of the fitted Gaussian is slightly redder than the peak of the line, suggesting asymmetry in the emission line. This is also clear from the excess towards the redder parts of the Gaussian. Top: The 2D GMOS spectrum showing the detected Ly$\alpha$ line. The spatial extent of the emission is roughly 1 arcsecond, which is also the aperture size used to extract the 1D spectrum.

FWHM is $370 \pm 30\,\mathrm{km\,s^{-1}}$. Since no continuum is detected in the spectrum (down to $1\sigma$ depth of $4.0\times10^{-19}\,\mathrm{erg\,s^{-1}\,cm^{-2}}$), we can only put a lower limit on the rest-frame equivalent width (EW) of the line, $\mathrm{EW}_0 > 40$ Å. Table 3.2 presents a summary of emission line measurements for TGSS J1530+1049.

### 3.4.1 Skewness and equivalent width

To further confirm our redshift determination, we quantify the asymmetry of the emission line following the prescriptions laid out by Kashikawa et al. (2006), by calculating the S-statistic and the weighted skewness parameter. A measure of the skewness of the emission line is particularly useful when dealing with spectra with a single emission line and can help differentiate Ly$\alpha$ emission at high redshifts from [O II], [O III] or H$\alpha$ emission from lower redshift galaxies (Rhoads

Table 3.2: Spectroscopic redshift and emission line measurements for TGSS J1530+1049 through GMOS spectroscopy.

| Property | Measurement |
|---|---|
| $z_{\rm spec}$ | $5.720 \pm 0.001$ |
| $F_{{\rm Ly}\alpha}$ | $1.6 \pm 0.2 \times 10^{-17}$ erg s$^{-1}$ cm$^{-2}$ |
| $L_{{\rm Ly}\alpha}$ | $5.7 \pm 0.7 \times 10^{42}$ erg s$^{-1}$ |
| FWHM | $370 \pm 30$ km s$^{-1}$ |
| EW$_{\rm obs}$ | $> 40$ Å |

et al. 2003; Kurk et al. 2004; Kashikawa et al. 2006). We measure the skewness $S = 0.31 \pm 0.14$ and the weighted skewness $S_w = 6.44 \pm 2.97$ Å, which are consistent with what is observed for confirmed Ly$\alpha$ emitters at high redshift (Kashikawa et al. 2006, 2011; Matthee et al. 2017).

To check what possible values of skewness could be obtained from an unresolved [O II] doublet, we simulated the doublet with all possible ratios ($0.35 < j_{\lambda 3729}/j_{\lambda 3726} < 1.5$), convolved with the instrument resolution. We find that the skewness measured for the emission line seen in the spectrum ($S = 0.31$) is only possible for $j_{\lambda 3729}/j_{\lambda 3726} < 0.7$. These line ratios correspond to the high electron density regime when the line would be collisionally de-excited, and hence unlikely to be as strong as observed, with previous studies of the [O II] doublet in high-z galaxies (Steidel et al. 2014; Shimakawa et al. 2015; Sanders et al. 2016) also finding much higher line ratios on average. This helps drive the interpretation of the observed emission line more towards a Ly$\alpha$ at high redshift.

Further, an EW$> 40$ Å for an [O II] line originating from a presumably massive radio galaxy at $z \sim 1.2$ would be at the extreme end of the EW distribution (Bridge et al. 2015), including for radio-loud quasars (Kalfountzou et al. 2012). This EW value is also incompatible with the line ratios that would give rise to the observed skewness, as in regions of very high electron densities the [O II] line is expected to be weaker due to collisional de-excitation. Therefore, we can practically rule out the [O II] doublet as a possible identification of this emission line. An EW$_0 > 40$ Å however, is typical for Ly$\alpha$ emission seen in galaxies at $z \sim 5.7$ (see Kashikawa et al. 2011, for example) and generally consistent with the $z \sim 6$ galaxy population (De Barros et al. 2017).

### 3.4.2 K-z relation for radio galaxies

Finally, a strong indicator of a high-redshift nature of the host galaxy is the non-detection in $K$ band down to a $3\sigma$ limiting magnitude of 22.4 (Figure 3.5) using aperture photometry at the peak pixel of the radio emission. For comparison, TN J0924–2201 at $z = 5.2$ has a magnitude of $K = 21.3 \pm 0.3$ and our measurement of $K > 22.4$ is consistent with $z > 5$ and helps rule out lower redshifts owing to the $K - z$ relation for radio galaxies (note that the luminosity and the spectral index rule out that it is a star-forming galaxy). We expand upon this point in Section 5.3. The

Table 3.3: Comparison of Ly$\alpha$ emission line properties of TGSS J1530+1049 reported in this paper with some of the known radio galaxies at $z > 4$, and the much fainter radio galaxy at $z = 4.42$ (all marked as RG), in addition to several confirmed LAEs at $z \approx 5.7$ from the literature.

| Name | $z$ | $F_{Ly\alpha}$ ($\times 10^{-17}$ erg s$^{-1}$ cm$^{-2}$) | $L_{Ly\alpha}$ ($\times 10^{42}$ erg s$^{-1}$) | FWHM$_{Ly\alpha}$ (km s$^{-1}$) | Reference |
|---|---|---|---|---|---|
| TGSS J1530+1049 | 5.72 | 1.6 | 5.7 | 370 | This work |
| TN J0924−2201 (RG) | 5.19 | 3.4 | 9.6 | 1500 | (van Breugel et al. 1999) |
| J163912.11+405236.5 (RG) | 4.88 | 18.5 | 47.0 | 1040 | (Jarvis et al. 2009) |
| VLA J123642+621331 (RG) | 4.42 | 0.6 | 2.0 | 420 | (Waddington et al. 1999) |
| LALA J142546.76+352036.3 | 5.75 | 1.6 | 6.7 | 360 | (Rhoads et a. 2003) |
| S11 5236 | 5.72 | 14.9 | 9.1 | 200 | (Lidman et al. 2012) |
| SDF J132344.8+272427 | 5.72 | 1.1 | 3.7 | 366 | (Kashikawa et al. 2011) |
| HSC J232558+002557 | 5.70 | 3.6 | 12.6 | 373 | (Shibuya et al. 2018) |
| SR6 | 5.67 | 7.6 | 25.0 | 236 | (Matthee et al. 2017) |

additional non-detection in $J$ band down to a $3\sigma$ limit of 24.3 further favours a high redshift galaxy and supports the argument that the line we see is indeed Ly$\alpha$ and not [O II].

## 3.5 Discussion

### 3.5.1 Emission Line Measurements

The Ly$\alpha$ luminosity and FWHM measured for TGSS J1530+1049 are lower than what is seen for typical HzRGs at $z > 4$ (see Spinrad et al. 1995; De Breuck et al. 1999; van Breugel et al. 1999; Miley & De Breuck 2008, for examples) and more consistent with those measured for 'non-radio' Ly$\alpha$ emitting galaxies (LAEs) at this redshift (Rhoads et al. 2003; Ouchi et al. 2008; Kashikawa et al. 2011; Lidman et al. 2012; Matthee et al. 2017). However, the FWHM for TGSS J1530+1049 is consistent with that of a very faint radio galaxy VLA J123642+621331, with a 1.4 GHz flux density of $S_{1.4\mathrm{GHz}} = 0.47$ mJy, discovered at $z = 4.424$ (Waddington et al. 1999). This galaxy has a FWHM of $\sim 420\,\mathrm{km\,s^{-1}}$ and a Ly$\alpha$ luminosity $\sim 2 \times 10^{42}\,\mathrm{erg\,s^{-1}}$, which is weaker than TGSS J1530+1049. VLA J123642+621331 is however, not detected in TGSS at 150 MHz down to a noise level of 3.5 mJy beam$^{-1}$, suggesting a relatively flat spectral index or a spectral turnover at low radio frequencies. We present some comparisons of the Ly$\alpha$ properties we measure for TGSS J1530+1049 with other HzRGs at $z > 4$ and also non-radio LAEs at $z = 5.7$ in Table 3.3.

A statistical sample of radio galaxies at $z \sim 6$ is needed to understand whether they are more like LAEs at high redshift or whether a majority of them continue being very different systems, surrounded by extremely overdense regions and forming stars intensively. The relatively underluminous Ly$\alpha$ would be one signature of a significantly neutral intergalactic medium (IGM) during the late stages of the EoR. Weaker Ly$\alpha$ emission may also be caused by significant absorption in a cold and dusty medium surrounding the radio galaxy. The presence of cold gas and dust has been reported in many HzRGs, including TN J0924–2201 (see Klamer et al. 2005, for example) and dedicated observations to look for molecular gas and dust in a statistically significant sample of radio galaxies at $z > 5$ are required to better characterise their surrounding

Table 3.4: A comparison of the radio properties of TGSS J1530+1049 with other known radio galaxies at $z > 4$. Flux densities at 150 MHz are measured from the TGSS catalog.

| Name | $z$ | $S_{150}$ (mJy) | $\log L_{150}$ (W Hz$^{-1}$) | $S_{1400}$ (mJy) | $\alpha_{1400}^{150}$ | Size (kpc) | Reference |
|---|---|---|---|---|---|---|---|
| TGSS J1530+1049 | 5.72 | 170 | 29.1 | 7.5 | −1.4 | 3.5 | This work |
| TN J0924−2201 | 5.19 | 760 | 29.6 | 71.1 | −1.1 | 7.4 | (van Breugel et al. 1999) |
| J163912.11+405236.5 | 4.88 | 103 | 28.2 | 22.5 | −0.7 | – | (Jarvis et al. 2009) |
| RC J0311+0507 | 4.51 | 5981 | 30.3 | 500.0 | −1.1 | 21.1 | (Parijskij et al. 2014) |
| VLA J123642+621331 | 4.42 | undetected | – | 0.5 | – | – | (Waddington et al. 1999) |
| 6C 0140+326 | 4.41 | 860 | 29.4 | 91.0 | −1.0 | 17.3 | (Rawlings et al. 1996) |
| 8C 1435+635 | 4.25 | 8070 | 30.4 | 497.0 | −1.2 | 21.1 | (Lacy et al. 1994) |
| TN J1123−2154 | 4.11 | 512 | 29.1 | 49.3 | −1.0 | 5.5 | (Reuland et al. 2004) |
| TN J1338−1942 | 4.10 | 1213 | 29.5 | 120.8 | −1.0 | 37.8 | (Reuland et al. 2004) |

medium.

### 3.5.2 Radio Properties

TGSS J1530+1049 has a flux density of 170 mJy at a frequency of 150 MHz and 7.5 mJy at 1.4 GHz (Saxena et al. 2018). Using the standard $K$-corrections in radio astronomy and assuming a constant spectral index of $\alpha = -1.4$, we calculate a rest-frame radio luminosity of $\log(L_{150\mathrm{MHz}} = 29.1$ and $\log(L_{1.4\mathrm{GHz}} = 28.2\,\mathrm{W\,Hz^{-1}}$, which places this ource at the most luminous end of the radio luminosity function at this epoch (Saxena et al. 2017). For comparison, TN J0924–2201 has a $K$-corrected radio luminosity of $\log(L_{1.4\mathrm{GHz}} = 29.3\,\mathrm{W\,Hz^{-1}}$ using a spectral index of $\alpha = -1.6$ (van Breugel et al. 1999). TGSS J1530+1049 is close to an order of magnitude fainter than TN J09224–2201 at 1.4 GHz, but remains by far the brightest radio source observed this close to the end of the epoch of reionisation.

The deconvolved angular size determined by Saxena et al. (2018) at 1.4 GHz for TGSS J1530+1049, which remains unresolved, is 0.6 arcseconds, which translates to a linear size of 3.5 kpc. This size is smaller than the size of TN J0924–2201 (van Breugel et al. 1999) and in line with predictions at $z \sim 6$ from Saxena et al. (2017), as radio galaxies in the early Universe are expected to be young and very compact (Blundell et al. 1999). In Table 3.4 we compare the radio properties of TGSS J1530+1049 with all currently known radio galaxies at $z \sim 4$. This was done by querying the TGSS ADR1 catalog to determine flux densities for all $z \sim 4$ radio galaxies at 150 MHz, which were then used to calculate radio powers using the standard $K$-corrections. We find that TGSS J1530+1049 is comparable to many of the $z \sim 4$ radio galaxies when looking at radio properties alone.

TGSS J1530+1049 has a spectral index of $\alpha_{1.4\ \mathrm{GHz}}^{150\ \mathrm{MHz}} = -1.4$, which is ultra-steep but flatter than TN J0924−2201 at $z = 5.19$, which was selected because of its spectral index of $\alpha_{1.4\ \mathrm{GHz}}^{365\ \mathrm{MHz}} = -1.6$. Interestingly, at lower radio frequencies the spectral index of TN J0924−2201 appears to flatten dramatically. The 150 MHz flux density measured in TGSS (Intema et al. 2017) for TN J0924−2201 is $760 \pm 76$ mJy, giving a low frequency spectral index $\alpha_{365\ \mathrm{MHz}}^{150\ \mathrm{MHz}} = -0.16$. If the spectral index were to be calculated only using the flux densities at frequencies of 150 MHz and 1.4 GHz,

the inferred spectral index would be $\alpha^{150\,\mathrm{MHz}}_{1.4\,\mathrm{GHz}} = -1.06$, making it not strictly ultra-steep ($\alpha < -1.3$). This implies that in a search for ultra-steep spectrum radio sources using data at 150 MHz and 1.4 GHz, such as (Saxena et al. 2018), TN J0924−2201 would be missed entirely. Indeed, an indication of a generally flatter spectral index at lower frequencies is visible in the spectral indices calculated for known $z > 4$ radio galaxies between frequencies of 150 MHz and 1.4 GHz in Table 3.4. A large majority of these radio sources were selected for having an ultra-steep spectral index in a higher frequency range, but appear to have a flatter spectral index when calculated between 150 MHz and 1.4 GHz.

Spectral flattening or even a turnover at low radio frequencies is expected in radio galaxies at increasingly higher redshifts due to: a) Inverse Compton (IC) losses due to the denser cosmic microwave background that affect the higher frequencies and result in a steeper high frequency spectral index, and b) free-free or synchrotron self absorption due to the compact sizes of radio sources at high redshifts that can lead to a turnover in the low frequency spectrum (see Callingham et al. 2017, and references therein). Saxena et al. (2018) have reported evidence of flattening of the low-frequency spectral index in candidate HzRGs and observations at intermediate radio wavelengths for sources like TGSS J1530+1049 are essential to measure spectral flattening and constrain various energy loss mechanisms that dominate the environments of radio galaxies in the early Universe. Additionally, search techniques for radio galaxies at even higher redshifts could be refined by possibly using radio colours instead of a simple ultra-steep spectral index selection. The LOFAR Two Metre Sky Survey (Shimwell et al. 2017, Shimwell et al. submitted) will eventually provide in-band spectral indices at 150 MHz and could potentially be used to identify HzRG candidates more efficiently.

We also draw attention towards the radio galaxy J163912.11+405236.5 at $z = 4.88$ (Jarvis et al. 2009), that has a spectral index of $\alpha^{325\,\mathrm{MHz}}_{1.4\,\mathrm{GHz}} = -0.75$ and is not an ultra-steep spectrum radio source. Interestingly, there is evidence of spectral flattening at lower frequencies with a 150 MHz flux density of 103.5 mJy, giving a spectral index $\alpha^{150\,\mathrm{MHz}}_{325\,\mathrm{MHz}} = -0.56$, which is flatter than that at higher frequencies. This source was targeted for spectroscopic follow-up owing to the faintness of its host galaxy at 3.6 $\mu m$. The very faint radio galaxy VLA J123642+621331 at $z = 4.42$ (Waddington et al. 1999)is also not strictly an ultra-steep spectrum source at high radio frequencies ($\alpha^{1.4\,\mathrm{GHz}}_{4.8\,\mathrm{GHz}} = -0.94$) and is too faint to be detected in TGSS. This source was also selected based on its optical and infrared faintness, suggesting that a considerable fraction of HzRGs may not be ultra-steep at all and therefore, be missed in samples constructed using the ultra-steep spectrum selection technique.

Indeed Ker et al. (2012) have shown that selecting infrared-faint radio sources (IFRS) could be more efficient at isolating HzRGs from large samples when compared to radio selection alone. This has been confirmed observationally through many previous studies (Norris et al. 2006; Collier et al. 2014; Herzog et al. 2014; Maini et al. 2016; Singh et al. 2017). However, the caveat is that deep infrared photometry over large sky areas is required to effectively implement such

a selection, which can be expensive. The recently concluded UKIRT Hemisphere Survey (UHS; Dye et al. 2018) has the potential to be extremely useful in the identification of promising HzRG candidates in the Northern Hemisphere, particularly from the LOFAR surveys (Shimwell et al. 2017, Shimwell et al. submitted), as a combination of a relaxed spectral index steepness criterion and infrared-faintness could be more effective at isolating HzRGs.

### 3.5.3 Stellar mass limits

The non-detection of the host galaxy down to a $3\sigma$ depth of $K = 22.4$ can be used to set limits on the stellar mass for TGSS J1530+1049 using simple stellar population synthesis modelling. To do this, we make use of the PYTHON package SMPY[1], which is designed for building composite stellar populations in an easy and flexible manner, allowing for synthetic photometry to be produced for single or large suites of models (see Duncan & Conselice 2015).

To build stellar populations, we use the Bruzual & Charlot (2003) model with a Chabrier (2003) initial mass function (IMF) and solar metallicity (Willott et al. 2003), a formation redshift $z_f = 25$ and as (Lacy et al.2000). We follow the Calzetti et al. (2000) law for dust attenuation and use values of $A_v = 0.15$ (moderate extinction) and 0.5 mag (dusty), which are commonly seen in massive galaxies at $5 < z < 6$ (McLure et al. 2006). The synthetic photometry is produced for different stellar masses, which we then convolve with the $K$ band filter to calculate apparent $K$ magnitudes over a redshift range $0-7$.

The $K$ magnitude limit for TGSS J1530+1049 fits well with a stellar mass limit of $M_{\rm stars} <\sim 10^{10.25}\ M_\odot$ for $A_v = 0.15$ mag, and $M_{\rm stars} <\sim 10^{10.5}$ for $A_v = 0.5$ mag. We note here that thanks to the excellent seeing for $K$-band observations ($0.6-0.8$ arcseconds), and since at $z \sim 6$ the host galaxy is expected to be small, any aperture correction is only expected to be at the level of a few tenths of a magnitude at most, or $0.1-0.2$ in the logarithmic stellar mass, which is smaller than the uncertainty from dust extinction corrections.

We find that the stellar mass limits we infer are in agreement with the $J$ band $3\sigma$ limit from LBT. The photometry predicted by the models in the optical bands from PS1 ($g$, $r$, $i$, $z$, $y$) is also consistent with the non-detections that we report. This stellar mass limit places TGSS J1530+1049 towards the $> M^*$ end of the galaxy stellar mass function at $z \sim 6$ (see Duncan et al. 2014, for example). For comparison, we show the apparent $K$ band magnitudes of other radio galaxies in the literature, taken from the 3CRR, 6CE, 6C* and 7C−I/II/III samples (Willott et al. 2003), in Figure 3.7. Also shown is the $K$ magnitude for TN J09224−2201 at $z = 5.2$ (van Breugel et al. 1999), which is best fit with a stellar mass of $10^{10.5}\ M_\odot$ for $A_v = 0.15$ mag and $10^{11}\ M_\odot$ for $A_v = 0.5$ mag.

We also show the $K$-band magnitude limit for the UKIDSS LAS as a dashed black line in Figure 3.7. TGSS J1530+1049 was initially selected due to its non-detection in LAS. However, these magnitude limits alone were not sufficient to constrain the very high redshift nature of the

[1] https://github.com/dunkenj/smpy

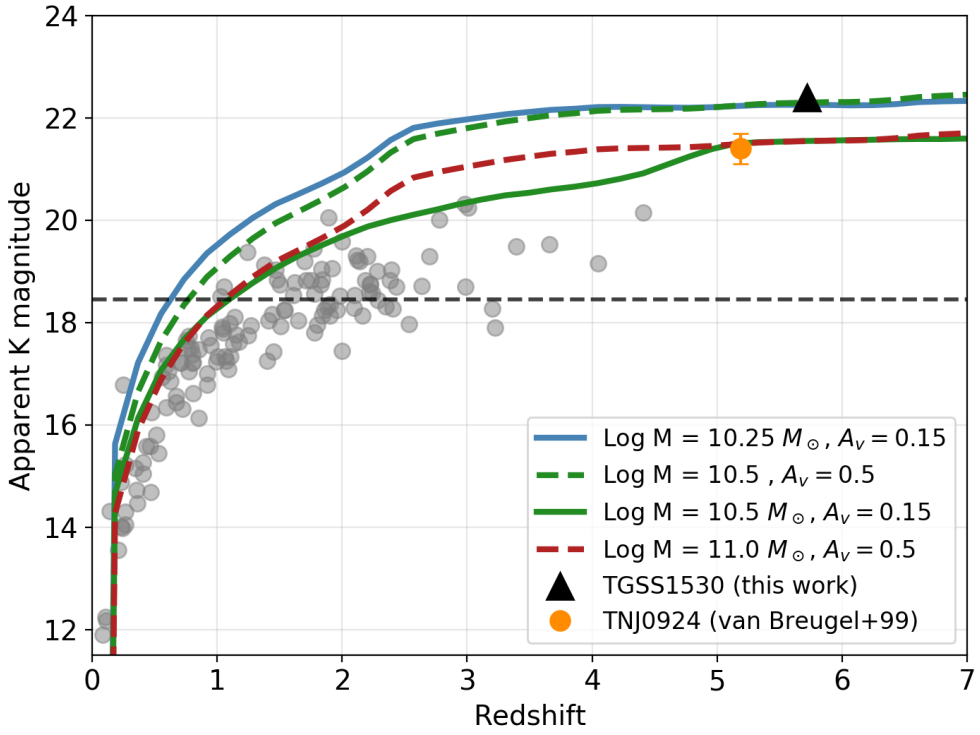


FIGURE 3.7. The '$K-z$' diagram for radio galaxies, showing stellar mass limits derived from stellar population synthesis modelling for TGSS J1530+1049 (black triangle). The $K$-band $3\sigma$ limit gives $M_{\rm stars} < 10^{10.25}\ M_\odot$ for $A_v = 0.15$ mag, and $M_{\rm stars} < 10^{10.5}$ for $A_v = 0.5$ mag. Also shown are $K$-band magnitudes and redshifts for known radio galaxies in the literature (grey points; see text), with TN J0924−2201 at $z = 5.19$ (orange circle). The $K$-band limits for TGSS J1530+1049 further help exclude lower redshift measurements from incorrect line identification.

host galaxy. With deeper LBT observations in $K$ band, we show that TGSS J1530+1049 follows the trend in the $K-z$ plot for radio galaxies. It is also clear that a low redshift solution that would arise if the detected emission line in Section 3.4 is not Lyman alpha (for example, $z \approx 1.2$ if the line is [O II]) would be hard to explain using galaxy evolution models with the inputs and assumptions outlined above and those generally used to model radio galaxy spectra (Overzier et al. 2009).

A stellar mass limit of $M_\star < 10^{10.5}\ M_\odot$ for TGSS J1530+1049 (based on the outlined assumptions) is almost an order of magnitude lower than the sample of radio galaxies studied by Rocca-Volmerange et al. (2004), where the highest stellar masses are seen for radio galaxies in the redshift range $2-4$. This suggests that TGSS J1530+1049 is still evolving and is in the process of building up its stellar mass. This interpretation is in line with TGSS J1530+1049

being a relatively young radio galaxy owing to its small radio size, and lower stellar masses may be expected from radio galaxies close to or into the epoch of reionisation. Robust detections at optical and infrared wavelengths are required to properly characterise the galaxy spectral energy distribution in order to understand better the star formation history of TGSS J1530+1049.

## 3.6 Conclusions

In this paper we have presented the discovery of the highest redshift radio galaxy, TGSS J1530+1049, at $z = 5.72$. The galaxy was initially selected at 150 MHz from TGSS (Saxena et al. 2018) and was assigned a high priority for spectroscopic follow-up owing to its compact morphology and faintness at optical and near-infrared wavelengths. The conclusions of this study are listed below:

1. Long-slit spectroscopy centered at the radio position of the source revealed an emission line at 8170 Å, which we identify as Lyman alpha at $z = 5.720$. We rule out alternative line IDs owing to the absence of other optical/UV lines in the spectrum, the asymmetrical nature of the emission line characteristic of Lyman alpha at high redshifts that we quantify using the skewness parameter and the high observed equivalent width of the emission line.

2. Deep $J$ and $K$ band imaging using the Large Binocular Telescope led to no significant detection of the host galaxy down to $3\sigma$ limits of $K > 22.4$ and $J > 24.4$. The limits in $K$ can be used as an additional constraint on the redshift, owing to the relation that exists between $K$ band magnitude and redshift of radio galaxies. The magnitude limit is consistent with $z > 5$, practically ruling out a redshift of $z \approx 1.2$ that would be expected if the emission line were an unresolved [O II] $\lambda\lambda 3726, 3729$ doublet, which is the most likely alternative line identification.

3. The emission line is best fitted with a skewed Gaussian, giving an integrated line flux of $F_{Ly\alpha} = 1.6 \times 10^{-17}$ erg s$^{-1}$ cm$^{-2}$, a Ly$\alpha$ luminosity of $5.7 \times 10^{42}$ erg s$^{-1}$, an equivalent width of EW $> 40$ Å and a FWHM of 370 km s$^{-1}$. These values are more consistent with those observed in non-radio Lyman alpha emitting galaxies at this redshift and much lower than those corresponding to typical radio galaxies at $z > 4$.

4. The radio luminosity calculated at 150 MHz is $\log L_{150} = 29.1$ W Hz$^{-1}$, which places it at the most luminous end of the radio luminosity function at this epoch. The deconvolved angular size is 3.5 kpc, which is in line with the compact morphologies expected at high redshifts. We find that the radio properties of TGSS J1530+1049 are comparable to other known radio galaxies at $z > 4$ but the compact size suggests that it is a radio galaxy in an early phase of its evolution. A joint study of the Ly$\alpha$ halo and the radio size of this source may provide one of the earliest constraints on the effects of radio-mode feedback.

5. We use the $K$ band limit to put constraints on the stellar mass estimate using simple stellar population synthesis models. Assuming a constant star formation history and a maximally old stellar population, we derive a stellar mass limit of $M_{\rm stars} <\sim 10^{10.25}\ M_{\odot}$ for $A_v = 0.15$ mag, and $M_{\rm stars} <\sim 10^{10.5}$ for $A_v = 0.5$ mag. These limits are almost an order of magnitude lower than typical radio galaxy masses in the redshift range $2-3$ and suggest that TGSS J1530+1049 may still be in the process of assembling its stellar mass, which is in line with it being a relatively young radio galaxy.

An effective application of deep radio surveys covering very large areas on the sky has been demonstrated by this discovery of the first radio galaxy at a record distance after almost 20 years. With the more sensitive, large area surveys currently underway with LOFAR (LoTSS; Shimwell et al. 2017, Shimwell et al. submitted), there is potential to push searches for radio galaxies to even higher redshifts. Discovery of even a single bright radio galaxy at $z > 6$ would open up new ways to study the epoch of reionisation in unparalleled detail, through searches for the 21cm absorption features left behind by the neutral hydrogen that pervaded the Universe at high redshifts.

CHAPTER 4

# A VLT/SINFONI STUDY OF BLACK HOLE GROWTH IN HIGH REDSHIFT RADIO-LOUD QUASARS FROM THE CARLA SURVEY

**Murilo Marinello** [1], Roderik Overzier [1,3], Huub Röttgering[2], Jaron Kurk[4], Carlos De Breuck[5], Joel Vernet[5], Dominika Wylezalek[5], Kenneth Duncan[2], Nina Hatch[9], Nobunari Kashikawa[8], Yen-Ting Lin[7], Rodrigo Nemmen[3], Aayush Saxena[2], Daniel Stern[6]

[1] Observatório Nacional, Ministry of Science, Technology, and Innovation, Rio de Janeiro, RJ 20921-400, Brazil

[2] Leiden Observatory, University of Leiden, PO Box 9513, 2300 RA Leiden, The Netherlands

[3] Institute of Astronomy, Geophysics and Atmospheric Sciences, University of São Paulo, São Paulo, SP 05508-090, Brazil

[4] Max–Planck–Institut fur Extraterrestrische Physik, Giessenbachstrasse, D-85741, Germany

[5] European Southern Observatory, Karl-Schwarzschild-Strasse 2, Germany

[6] Jet Propulsion Laboratory, California Institute of Technology, Pasadena, CA 91109, USA

[7] Academia Sinica Institute of Astronomy and Astrophysics, Taipei 10617, Taiwan

[8] Department of Astronomy, School of Science, The University of Tokyo, Tokyo, 113-0033, Japan

[9] School of Physics and Astronomy, University of Nottingham, Nottingham, United Kingdom

To be submitted to Monthly Notices of the Royal Astronomical Society, 2019

We present VLT/SINFONI observations of 35 high redshift ($2.2 < z < 3.5$) quasars selected from the *Clusters Around Radio-Loud AGN* (CARLA) survey. CARLA quasars have large black hole (BH) masses ($M_{BH} > 10^9$ $M_\odot$, based on the C IV line) and powerful radio emission ($P_{500MHz} > 27.5$ W Hz$^{-1}$). We estimate new BH masses based on H$\alpha$, and compare with previous results based on C IV, finding a scatter of 0.43 dex. With the improved masses we evaluate several of the recipes proposed for correcting C IV-based masses, finding a reduced scatter of 0.27 dex in the best case. We estimate Eddington ratios $L/L_{Edd}$ in the range 0.04–0.64 and find strong correlations with the H$\alpha$ width and $L_{5100}$, and a moderate correlation with $M_{BH}$. We find no correlation (or very weak ones) between the radio power and the other observables quantities, suggesting that these quantities are not governed by the same physical mechanisms Although the median black hole growth time ($t_{grow}$) is below the cosmic age at the redshift of the quasars, it is substantially longer in about half the sample, suggesting that these objects must have experienced near-Eddington growth in the past. If CARLA quasars have been growing from seed BHs before reionization, a possible scenario is one in which they grew at the Eddington limit to $\sim 10^9$ $M_\odot$ similar to the population of $z \sim 6-7$ quasars, and then continued at the $L/L_{Edd}$ observed until $z \sim 2-3$. Alternatively, the BHs in CARLA quasars formed much more recently by accreting near the Eddington limit from $\sim 1000$ $M_\odot$ seeds. Finally, using the results from this paper, we revisit the possible correlation between $M_{BH}$ and environment as measured by the CARLA survey, finding a weak positive correlation at low significance and discuss the results in the context of the local $M_{BH} - \sigma_*$ relation.

## 4.1 Introduction

Active galactic nuclei (AGN) are among the most luminous objects in the universe. At the center of an AGN, accretion of matter around a supermassive black hole (SMBH) powers luminous radiation that, in the case of quasars, typically outshines the host galaxy at optical wavelengths. The study of these SMBHs are important for galaxy evolution. Feedback from active SMBHs, which can be radiative or kinetic, can impact the surrounding media, and there is evidence that AGN are in symbiosis with their environments (Heckman et al. 2014 and references therein). Correlations between the black hole mass and the bulge mass ($M_{bulge}$) and velocity dispersion ($\sigma_*$) of galaxies, suggest co-evolution between SMBHs and their host galaxies (Magorrian et al. 1998, Ferrarese et al. 2000, Gebhardt et. al. 2000). However, the exact nature of this co-evolution is not yet understood.

The Clusters Around Radio-Loud AGN (CARLA) project was a 400 h Spitzer snapshot survey that targeted 419 powerful radio-loud AGN (radio galaxies and quasars) with $L_{500MHz} > 27.5$ W Hz$^{-1}$ in the redshift range $1.3 < z < 3.2$. The main goal of CARLA was to investigate for the first time systematically the environments of radio galaxies and quasars (Wylezalek et al. 2013, Wylezalek et al. 2014). By selecting galaxies on the basis of relatively red ([3.6] μm – [4.5] μm)

colors, the CARLA survey successfully identified excesses of galaxies in the fields around many of the radio-loud AGN (Galametz et al. 2012, Wylezalek et al. 2013). The luminosity function of the companion galaxies derived by Wylezalek et al. (2014) shows that the overdense regions have the expected luminosity function of a cluster de-evolved to the redshift of the radio-loud AGN (RLAGN). In a pilot study of 48 radio galaxies, Galametz et al. (2012) showed that radio galaxies tend to lie in average in overdense regions consistent with clusters and proto-clusters of galaxies. In one of the densest fields identified in the CARLA study, Cooke et al. (2015) found that massive galaxies assembled their stars faster compared to the field. Recently, Noirot et al. (2016) spectroscopically confirmed two structures around powerful $z = 2$ radio galaxies from CARLA. Using *Hubble Space Telescope* (HST) slitless spectroscopy they found 8 star-forming members in the field of MRC 2036–254 and 8 star-forming galaxies (and 2 AGN) in the field of B3 0756+406. The spectroscopic follow-up of CARLA overdensities has since been expanded to yield 16 galaxy structures at $1.8 < z < 2.8$ in 20 of the densest CARLA fields (Noirot et al. 2018). Although a proper interpretation of the CARLA results must await more complete spectroscopic follow-up, the results are consistent with numerous previous studies that found strong evidence for overdense environments and (proto-)clusters associated with powerful radio galaxies at high redshift (see Overzier 2016, for a review).

The local $M_{BH} - \sigma_*$ relation combined with the galaxy stellar-to-halo mass relation suggests that there is a connection, albeit an indirect one, between the mass of SMBHs and their large-scale environments (Ferrarese et al. 2000, Geghardt et al 2000, Kormendy & Ho 2013). The CARLA sample offers a unique chance to investigate at what redshifts these relations may have been established. The dense environments found around a significant fraction of RLAGN targeted by CARLA could be particularly conducive to galaxy major merging or halo gas accretion rates that are atypical for ordinary galaxies in the early universe. Although it is difficult to directly measure black hole masses for the radio-loud type–2 galaxies in the CARLA sample, black hole masses are available for the radio-loud quasars in CARLA. Measurements based on the width of the C IV line from the Sloan Digital Sky Survey (SDSS) indicate that CARLA quasars have very massive black holes ($\log(M_{BH}/M_\odot)>8.5$;Hatch et al 2014). It will therefore be interesting to study whether the black hole masses correlate with any other properties of the quasar hosts or their large-scale (cluster) environments provided by CARLA. Hatch et al. (2014) found a mild trend for more massive SMBHs to be located in denser environments. However, for CARLA sources located at high redshift, most of the BH mass estimates in that study were based on the C IV line, which is known to be problematic with large scatter and systematic offsets (Shen et al. 2008). Increasing the accuracy of the BH mass determination will be a crucial first step if one wants to study any correlations involving the BH mass (Uchiyama et al. 2018). Therefore, an accurate measurement of the black hole mass is necessary before we can properly assess possible correlations between the SMBHs and other properties of their host and environments.

Reverberation mapping (RM) is a powerful technique for probing the inner parsec of type-I

quasars (see Peterson 2014, for a review). Mapping the delay time between the variability of the continuum and the emission line response to this variation allows us to estimate fundamental parameters, such as the black hole mass and the size of the broad line region (BLR) (Kaspi et al. 2000). However, RM observations are time-consuming and the delay times can only be obtained for a relatively small sample of (nearby) sources. Alternatively, black hole masses can be estimated from single epoch (SE) spectra under the assumption of virial motions of the BLR gas, $M_{BH} \propto R_{BLR} v_{gas}^2/G$. The RM radius-luminosity ($R-L$) relation shows that the continuum luminosity at 5100 Å ($L_{5100}$) can be used as a proxy for the $R_{BLR}$, while the full width at half maximum (FWHM) of a BLR line, usually H$\beta$, is related to the velocity dispersion of the emitting gas (Kaspi et al. 2000). This technique was extended to other lines, such as H$\alpha$ and Mg II in the rest-frame optical and ultraviolet (UV), respectively, and is widely used to determine black hole masses from SE quasar spectra for quasars over a wide range of redshifts (Shen et al. 2011).

Vestergaard & Peterson (2006) presented a RM analysis of nearby AGN observed in the UV and H$\beta$, and found an empirical relation capable of estimating black hole masses based on C IV. With the increase of RM data this relation was later updated using a larger sample of 25 nearby AGN (Park et al. 2013). Using a similar approach, Wang et al. (2009) obtained an empirical relation between H$\beta$ and Mg II. The resulting Mg II–$M_{BH}$ calibration is considered to be very reliable, and has been applied to large samples of quasars (Shen et al. 2011, Marziani et al. 2013). Another reliable line that is frequently used is H$\alpha$. Green & Ho (2005) showed that the FWHM and luminosity of H$\alpha$ are good analogs of the FWHM(H$\beta$) and $L_{5100}$.

Despite the success of SE black hole mass determinations, the technique also has its limitations. Depending on the redshift of the quasars, rest-frame UV or optical lines may not be available. For instance, H$\alpha$ is available in optical spectra only at $z < 0.4$, while H$\beta$ can be detected only up to $z \sim 0.8$. At $0.8 < z < 2.2$ the black hole mass can be estimated reliably using the Mg II line detected in optical spectra, while at $z > 2.2$ only the C IV line can be used. Furthermore, the scaling relation for SE black hole mass determinations relies on the tightness of the $R-L$ relation, and has additional scatter when using lines other than H$\beta$. While results based on H$\alpha$, H$\beta$, and Mg II are usually consistent with those provided by RM results, and hence provide a good estimate for the black hole mass, the C IV line is affected by several non-gravitational broadening effects making this line the least reliable of all (Shen et al. 2008). Therefore, in order to obtain more accurate BH masses for high redshift using reliable lines, NIR observations are required. For instance, $K$-band spectroscopy is able to probe H$\alpha$ for $1.9 < z < 2.7$, H$\beta$ for $4.0 < z < 5.0$, and Mg II for $6.8 < z < 7.5$.

Several studies have attempted to correct the C IV-based estimates by determining empirical relations between the main observables used in the SE black hole mass estimate, e.g., FWHM and continuum luminosity. For instance, Park et al. (2017) obtained RM for an updated sample of AGN to improve the C IV black hole mass estimator using FHWM(C IV) and the luminosity at 1350 Å ($L_{1350}$) as BLR size proxy. Runnoe et al. (2013) proposed a correction to the C IV BH mass

estimator using the peak ratio between Si IV+O IV] and C IV. Assef et al. (2011) used a different approach, taking the ratio between $L_{5100}$ and $L_{1350}$ as an additional parameter in the SE BH mass determination. In yet another approach, Denney et al. (2012) constructed a correction factor based on the ratio of the FWHM and $\sigma$ of the line. Recently, Coatman et al. (2017) used NIR spectra for a large sample (230 quasars) in order to obtain a reliable relation between the $M_{BH}$ estimated from H$\alpha$ (and H$\beta$) and that obtained from C IV. Despite all these attempts to improve the black hole mass estimators based on C IV, the Balmer lines remain the most reliable for black hole mass determination as we will show in this paper.

In this paper we use NIR SINFONI/VLT observations to probe the optical rest-frame spectra of 35 high redshift ($z$ >2.2) radio-loud quasars from the CARLA survey. We use H$\alpha$ to estimate the black hole masses, and compare with the estimates from C IV and the various recipes that have been suggested to be able to correct the C IV-based measurements for non-virial contributions. Furthermore, we use the new $M_{BH}$ to study its relation to several other physical parameters of the CARLA quasars, such as their accretion rate, luminosity, radio power, growth time, and local environment.

This paper is organized as follows. In Section 2 we describe the selection of the sample targeted with SINFONI, the observations and the data reduction. In Section 3 we present a description of the techniques used for the BH mass determination. In Section 4 we present redshifts and black hole masses estimated from H$\alpha$, and compare the results with values obtained using several methods from the literature that were designed to correct estimates based on C IV for non-gravitational effects. Using the updated black hole masses we then estimate the Eddington ratio ($L/L_{Edd}$) and the black hole growth time. In Section 5 we study the correlations between the $M_{BH}$ and the luminosity, FWHM(H$\alpha$), radio power, $L/L_{Edd}$, and growth time. Finally, we use the accurate measurements of $M_{BH}$ based on H$\alpha$ to study the relation between the masses of the black holes and the Mpc-scale environment of their host galaxies using the galaxy surface density measurements from the CARLA survey. We give a summary of the results and concluding remarks in Section 6. In this paper, we adopt a $\Lambda$CDM cosmology with $H_0 = 70\,\mathrm{km\,s^{-1}\,Mpc^{-1}}$, $\Omega_M = 0.3$ and $\Omega_\Lambda = 0.7$. All magnitudes and colors are given in the AB photometric system.

## 4.2 Observations and data reduction

We used the Spectrograph for INtegral Field Observations in the Near Infrared (SINFONI; Eisenhauer et al. 2003) at UT4 of the Very Large Telescope (VLT) at the European Southern Observatory (ESO) to observe a sample of 35 high redshift quasars from CARLA. The purpose of the project was to obtain NIR spectra probing the rest-frame optical spectral region around H$\alpha$ in order to obtain more accurate black hole masses for quasars selected from the CARLA survey and the SDSS. The data were taken over 6 years (2009–2015) as part of programs 095.B-0323(A), 094.B-0105(A), 093.B-0084(A), 092.B-0565(A), 091.B-0112(A), 090.B-0674(A), and 089.B-0433(A)

(PI: Jaron Kurk). Except for 089.B-0433(A), all programs targeted radio-loud quasars from CARLA. The 089.B-0433(A) targets were selected from SDSS on the basis of their very high (C IV-based) BH masses but are not part of the CARLA sample. The redshift range of all but one of the targets is $z = 2.1 - 2.6$, and the H$\alpha$ line falls within the wavelength range 2.0–2.4 μm. One target (SDSS J094113+114532) has a higher redshift of $z = 3.19$, for which we observe H$\beta$ at 2.04 μm. In our analysis we assume that the FWHM of this line is roughly equivalent to that of H$\alpha$ measured for the other objects (Vestergaard & Peterson 2006, Coatman et al. 2017). Our final sample consists of 35 Radio-Loud Quasars (RLQs) at $z \sim 2 - 3$, covering the full range of parameter space of the CARLA sample (i.e., UV luminosities of $45.5 < L_{\rm UV} < 47.5$ erg s$^{-1}$, black holes masses of $8.5 < \log(M_{\rm BH}/M_\odot) < 10.5$, and radio power of $27.6 < P_{\rm 500MHz} < 29.2$ W Hz$^{-1}$). Figure 4.1 shows the sources selected for this work compared to the full sample of ~ 200 CARLA quasars in redshift, radio power, UV luminosity and black hole mass parameter space. The figure shows that the SINFONI subsample, while only ~10% the size of the full CARLA sample, is representative of the full sample in radio power, UV luminosity and black hole mass.

We used the SINFONI $K$-band (1.95–2.45 μm) with the spatial scale of $125 \times 250$ mas (without adaptive optics). This setup delivers a spatial aperture of 8"×8" with a spectral resolution of ~400 km s$^{-1}$, allowing a proper sky subtraction. The observational strategy includes on-source dithering (ABBA pattern) in order to optimize the exposure time on the source and sky subtraction, and a telluric standard star for telluric band removal and flux calibration. We took 14 to 16 individual exposures of 300 s each, resulting in a total integration time of 4200-4800 s. A complete list of the targets and relevant observational information is given in Table 4.1.

The data reduction was performed using the SINFONI pipeline v2.9.0 (Modigliani et al. 2007) with the *Reflex* interface. The pipeline creates master calibration images and applies them to the observations, starting with a non-linear map from the flat-field frames. A master dark frame is created from the dark frames and the hot pixels are mapped. Individual flat-field images are combined into a master flat. Optical distortion and slitlets distances are computed, and the dispersion solution for the wavelength calibration is determined from arc spectra. Finally, individual exposures of the quasar and standard star are stacked. We perform an extra sky background removal step by determining a median stack of the pixels surrounding the source and combining them to create a residual sky map. This map was then subtracted from the source spectrum to remove background residuals remaining in the final data cube (these residuals can be seen in the form of spikes in the uncorrected spectrum).

We determined the spatial location of each quasar using a 2-dimensional Gaussian fit, and extracted the spectrum from a $5\sigma$ pixel aperture around this position (which should contain 99.99% of the flux). Because this program was designed to operate in poor weather conditions, no effort was made to obtain spatially resolved information from the data cubes. We modeled and subtracted Paschen lines from the telluric standard spectrum and the removal of telluric absorption was performed by dividing the quasar spectrum by a scaled telluric template derived

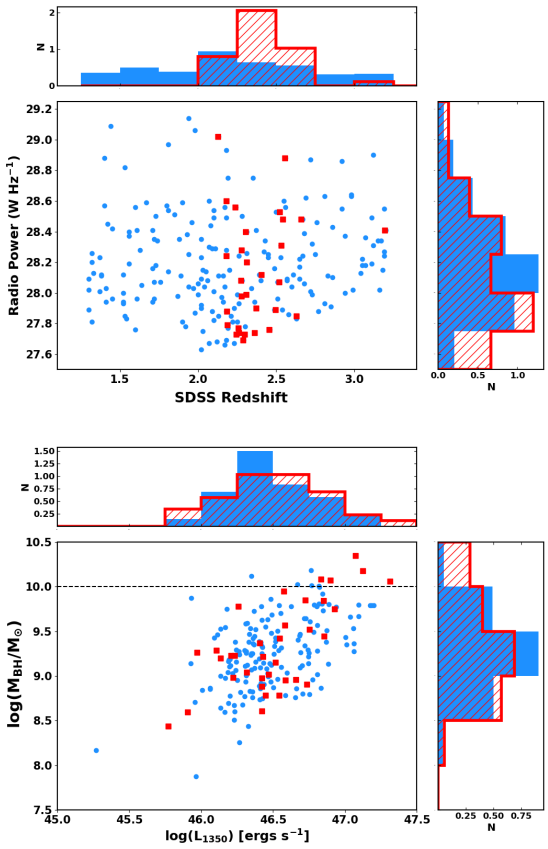


FIGURE 4.1. Sample parameters distribution showing redshift versus radio power (top panel) and UV luminosity versus CIV-based black hole mass (bottom panel). In both these panels, sources targeted with SINFONI and presented in this paper are indicated with red squares, while the full CARLA quasars sample is indicated with blue circles. The right and top histograms show that the SINFONI targets (red hatched histogram) form a fair subsample of the 10× larger CARLA sample (blue shaded histogram) in radio power, UV luminosity and black hole mass.

from the standard star using the task *Telluric* in the IRAF *onedspec* package. Finally, the spectrum was flux calibrated using the standard star. For quasars with photometry in the $K$-band available from UKIDSS or 2MASS, we scaled the final spectrum to have the same flux as expected based on the photometry. For the remaining 7 quasars for which no previous $K$-band photometry exists, we estimated the absolute scale of the continuum using a template fitting technique described in Section 3.3. Because we are interested only in the properties of the emission lines (i.e., flux and FWHM), we fit and subtract the underlying continuum near H$\alpha$. We modeled the continuum using a power law, fitting the regions free of emission lines between rest-frame 6250–6400Å and 6600–6750Å (redshifted using the redshifts from the SDSS catalog). The resulting final spectra around H$\alpha$ are shown in Figure 4.17.

Table 4.1: Sample Information.

| SDSS Name | R.A. (J2000) | Dec. (J2000) | $z_{SDSS}$ | $T_{exp}$ (s) | $P_{500MHz}$ ($WHz^{-1}$) | $u'$ (mag) | $g'$ (mag) | $r'$ (mag) | $i'$ (mag) | $z'$ (mag) | $J$ (mag) | $H$ (mag) | $K$ (mag) |
|---|---|---|---|---|---|---|---|---|---|---|---|---|---|
| Radio-loud quasars from CARLA | | | | | | | | | | | | | |
| J012514−001828 | 01:25:17.1 | −00:18:29 | 2.279054 | 4200 | 28.28 | 19.06 | 18.31 | 18.36 | 18.27 | 18.04 | 16.94 | 16.72 | 15.91 |
| J082707+105224 | 08:27:06.4 | 10:52:24 | 2.278000 | 4800 | 27.98 | 19.75 | 18.94 | 18.90 | 18.71 | 18.39 | – | – | – |
| J090444+233354 | 09:04:44.3 | 23:33:54 | 2.258323 | 4200 | 27.77 | 18.06 | 17.40 | 17.30 | 17.00 | 16.73 | 15.76 | 15.25 | 14.21 |
| J092035+002330 | 09:20:35.8 | 00:23:31 | 2.493972 | 4800 | 27.89 | 19.30 | 18.51 | 18.48 | 18.46 | 18.18 | 17.22 | 16.74 | 15.94 |
| J094113+114532 | 09:41:13.5 | 11:45:32 | 3.193793 | 4800 | 28.41 | 21.39 | 19.41 | 19.27 | 19.33 | 19.35 | 18.39 | 18.12 | 17.41 |
| J102429−005255 | 10:24:29.5 | −00:52:55 | 2.556504 | 4200 | 28.88 | 19.01 | 18.33 | 18.28 | 18.23 | 17.93 | 16.92 | 16.37 | 15.59 |
| J104257+074850 | 10:42:57.6 | 07:48:51 | 2.660536 | 4800 | 28.48 | 18.81 | 17.76 | 17.50 | 17.32 | 17.17 | 18.18 | 17.47 | 16.61 |
| J110344+023209 | 11:03:44.5 | 02:32:10 | 2.517125 | 4200 | 28.07 | 19.35 | 18.53 | 18.44 | 18.33 | 18.01 | 16.98 | 16.37 | 15.49 |
| J111857+123441 | 11:18:57.3 | 12:34:42 | 2.125651 | 4800 | 29.02 | 18.87 | 18.50 | 18.49 | 18.33 | 18.13 | 17.59 | 16.98 | 16.10 |
| J112338+052038 | 11:23:38.1 | 05:20:38 | 2.183412 | 4800 | 27.88 | 19.65 | 19.20 | 19.09 | 18.77 | 18.50 | 17.66 | 17.04 | 16.09 |
| J115901+065619 | 11:59:01.7 | 06:56:19 | 2.186956 | 4800 | 27.79 | 20.49 | 19.75 | 19.29 | 18.93 | 18.60 | 17.66 | 16.95 | 15.97 |
| J120301+063441 | 12:03:01.0 | 06:34:42 | 2.180930 | 4800 | 28.24 | 21.15 | 19.74 | 18.91 | 18.39 | 18.04 | 16.99 | 16.42 | 15.51 |
| J121255+245332 | 12:12:55.8 | 24:53:32 | 2.373100 | 4800 | 27.90 | 19.53 | 19.10 | 19.02 | 19.02 | 18.84 | – | – | – |
| J121911−004345 | 12:19:11.2 | −00:43:46 | 2.296210 | 4200 | 27.73 | 18.27 | 17.89 | 17.94 | 17.98 | 17.90 | 17.13 | 16.68 | 16.08 |
| J122836+101841 | 12:28:36.9 | 10:18:42 | 2.303086 | 4800 | 28.40 | 19.43 | 18.79 | 18.72 | 18.58 | 18.31 | 17.24 | 16.55 | 15.78 |
| J133932−031706 | 13:39:32.6 | −03:17:06 | 2.311469 | 4200 | 28.20 | 19.19 | 18.66 | 18.62 | 18.52 | 18.30 | 17.28 | 16.69 | 15.93 |
| J140445−013021 | 14:04:45.9 | −01:30:22 | 2.520401 | 4200 | 28.53 | 18.98 | 18.29 | 18.19 | 18.10 | 17.91 | 16.91 | 16.36 | 15.45 |
| J141906+055501 | 14:19:06.8 | 05:55:02 | 2.287456 | 4200 | 27.69 | 19.78 | 19.21 | 19.18 | 19.12 | 18.89 | 18.33 | 17.93 | 16.96 |
| J143331+190711 | 14:33:31.9 | 19:07:12 | 2.360114 | 4200 | 27.74 | 19.74 | 18.85 | 18.84 | 18.72 | 18.45 | – | – | – |
| J145301+103617 | 14:53:01.5 | 10:36:17 | 2.275276 | 4200 | 28.08 | 19.97 | 19.30 | 19.29 | 19.11 | 18.77 | 17.89 | 17.38 | 16.41 |
| J151508+213345 | 15:15:08.6 | 21:33:45 | 2.245700 | 4800 | 27.73 | 19.30 | 18.48 | 18.32 | 18.14 | 17.85 | 16.81 | 16.21 | 15.28 |
| J153124+075431 | 15:31:24.1 | 07:54:31 | 2.455450 | 4200 | 27.76 | 19.82 | 19.21 | 19.10 | 19.06 | 19.10 | 18.37 | 17.77 | 17.37 |
| J153727+231826 | 15:37:27.7 | 23:18:26 | 2.259551 | 4800 | 27.74 | 19.83 | 19.38 | 19.02 | 18.79 | 18.59 | – | – | – |
| J153925+160400 | 15:39:25.1 | 16:04:00 | 2.542400 | 4200 | 28.48 | 20.33 | 19.48 | 19.23 | 19.17 | 19.01 | – | – | – |
| J154459+040746 | 15:44:59.4 | 04:07:46 | 2.182000 | 4800 | 28.60 | 18.75 | 18.33 | 18.26 | 18.04 | 17.81 | 17.17 | 16.53 | 15.73 |
| J160016+183830 | 16:00:17.0 | 18:38:30 | 2.404757 | 4200 | 28.12 | 19.68 | 18.85 | 18.77 | 18.60 | 18.28 | – | – | – |
| J160154+135710 | 16:01:54.5 | 13:57:11 | 2.237000 | 4800 | 28.56 | 19.11 | 18.49 | 18.38 | 18.18 | 17.96 | 17.01 | 16.20 | 15.64 |
| J160212+241010 | 16:02:12.6 | 24:10:11 | 2.530514 | 4200 | 28.31 | 19.66 | 18.79 | 18.71 | 18.58 | 18.22 | 17.16 | 16.54 | 15.70 |
| J230011−102144 | 23:00:11.7 | −10:21:44 | 2.306749 | 4200 | 27.99 | 18.77 | 18.35 | 18.27 | 18.30 | 18.16 | – | – | – |
| J231607+010012 | 23:16:07.2 | 01:00:13 | 2.629261 | 4200 | 27.85 | 18.85 | 18.32 | 18.13 | 18.05 | 17.93 | 17.15 | 16.22 | 16.03 |
| Non-CARLA quasars having $M_{BH}(\mathrm{C\,IV}) > 10^{10}$ $M_\odot$ | | | | | | | | | | | | | |
| J005814+011530 | 00:58:14.3 | 01:15:30 | 2.519759 | 4200 | – | 18.71 | 17.86 | 17.66 | 17.66 | 17.53 | 16.64 | 16.11 | 15.45 |
| J081014+204021 | 08:10:14.6 | 20:40:21 | 2.506104 | 4200 | – | 17.79 | 17.31 | 17.28 | 17.27 | 17.11 | 16.16 | 15.67 | 14.86 |
| J115301+215117 | 11:53:01.6 | 21:51:18 | 2.367374 | 4200 | – | 17.21 | 16.67 | 16.69 | 16.63 | 16.43 | 15.54 | 15.03 | 14.26 |
| J130331+162146 | 13:03:31.3 | 16:21:47 | 2.276900 | 4200 | – | 18.80 | 18.21 | 18.05 | 18.01 | 17.84 | 17.05 | 16.44 | 15.61 |
| J210831−063022 | 21:08:31.5 | −06:30:23 | 2.348147 | 4800 | – | 17.90 | 17.38 | 17.20 | 17.16 | 17.03 | 16.42 | 15.77 | 15.01 |

## 4.3 Analysis

### 4.3.1 H$\alpha$ Line Fitting

H$\alpha$ is a recombination line that can be produced both in the BLR and in the NLR (Stern et al. 2013). Several authors have claimed the existence of multiple broad components of this line, suggesting that there are different emitting regions inside the BLR producing the observed emission. Surrounding H$\alpha$ are the lines of the  doublet emitted by the NLR. Because forbidden lines in powerful radio-loud AGN can be broadened by shocks to velocities as high as 1500 km s$^{-1}$ (De Breuck et al. 2001), we include a narrow component with FWHM$_{\rm narrow}$ <1500 km s$^{-1}$ and force the broad component to have FHWM$_{\rm broad}$ >1500 km s$^{-1}$. Taking into account these possible components, we fit H$\alpha$ by solving for the parameters of a multi-Gaussian fitting function that minimize the $\chi^2$.

We used one Gaussian for each of the lines of the  doublet and two broad Gaussians for the BLR component of H$\alpha$. However, in none of our quasars we detected any  emission above 3$\sigma$. Since no detections were found, we assumed one Gaussian profile for the NLR H$\alpha$ component and (at most) two Gaussians for the broad component of H$\alpha$. We selected just one broad Gaussian function when the difference in the $\chi^2$ was smaller than 10% compared to the fit with two Gaussians. Again, if the narrow component found was weaker than the 3$\sigma$ threshold we ignored this component and fit the profiles only with broad Gaussian lines. We found a narrow component in 8 out of the 35 sources in our sample. From the best fit we estimated the flux and FWHM of H$\alpha$. The velocity dispersion of H$\alpha$ was computed from the second moment of the line (Peterson et al. 2004). This approach is similar to Shen et al. (2011), and reproduces well the observed line profiles of H$\alpha$ in all our quasars. The results are summarized in Columns 2-5 of Table 4.2. An example of the best fit profiles can be seen in the top panels of Figure 4.2. The fits for the entire sample are presented in Figure 4.17.

In order to obtain accurate measurements of the blueshift of C IV (see Section 3.2), we need to estimate accurately the systemic redshift of the quasars. Coatman et al. (2016) show that redshifts can be reliably obtained from the centroid of H$\alpha$ defined as the intersection point that separates half of the flux of the line. Using the results from the H$\alpha$ fits we estimated the systemic redshifts for each source (Column 5 in Table 4.2).

### 4.3.2 C IV Line Fitting

In order to measure the properties of the C IV line, we first remove the underlying continuum. We fit a power law function to the line free regions at rest-frame 1400–1450Å and 1700–1705Å, corrected for the Doppler shift using the redshifts estimated from H$\alpha$ in the previous section (similar to Shen et al. 2011). We found a median value for the power law index of -1.2, which is consistent with the mean value for a composite quasar spectrum from SDSS/DR3 (Vanderberk et al. 2001). We subtracted the power law from each SDSS spectrum, resulting in a pure emission

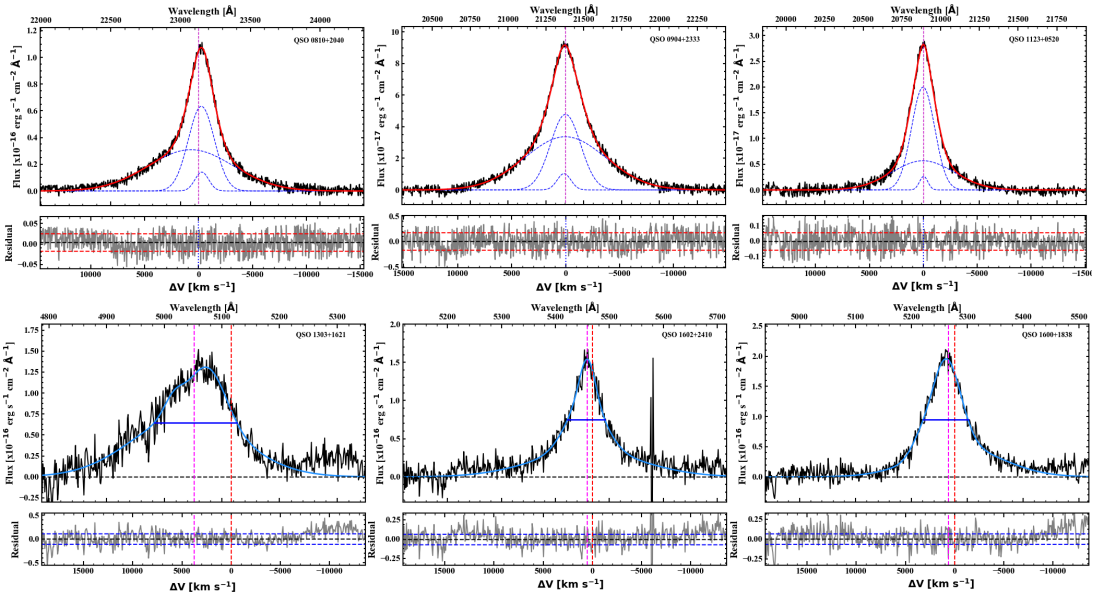


FIGURE 4.2. Results of the line fitting routine applied to the SINFONI spectra (H$\alpha$, top row of panels) and the SDSS spectra (C IV, bottom row of panels). The spectra and the residuals of the subtracted best fit model are shown in black and gray, respectively. The top panels show examples of H$\alpha$ in the SINFONI spectra. The bold red line shows the best fit, the dashed blue lines show the individual component of the model and the vertical dashed magenta line shows the centroid of H$\alpha$. The bottom panels show examples of C IV in the SDSS spectra of the same quasars. The blue line shows the best fit model, and the red and magenta vertical dashed lines show the central wavelength of C IV$\lambda$1549 as expected based on H$\alpha$ and the actual centroid of the C IV profile, respectively. The horizontal blue line shows the FWHM of C IV. Dashed red and blue horizontal lines in the rms panels show the 1-$\sigma$ level for H$\alpha$ and C IV, respectively.

line spectrum around C IV. Different from H$\alpha$, the profile of C IV exhibits a much more complex structure. Several physical phenomena can cause non-gravitational broadening of this line, resulting in an often asymmetrical profile. To model this line we used a similar approach as Shen et al. (2011), who considered a line profile composed of three Gaussians. While other authors have used a 6th-order Gauss-Hermite function to model C IV, these approaches are consistent with the difference between them smaller than 10% (Assef et al. 2011, Coatman et al. 2016).

We model C IV with three Gaussians in order to reduce the sensitivity of the fitting routine to high noise spikes and the presence of absorption features in the line. To fit C IV we perform two rounds of fitting. First we apply a 20-pixel boxcar filter to produce a smoothed spectrum. An initial fit is performed on the smoothed spectrum and any regions above and below 3$\sigma$ (i.e., strong noise spikes and absorption features) are masked. This mask was applied to the original spectrum and the final fit was performed.

The bottom row of panels of Figure 4.2 shows examples of the best fit profiles. The flux

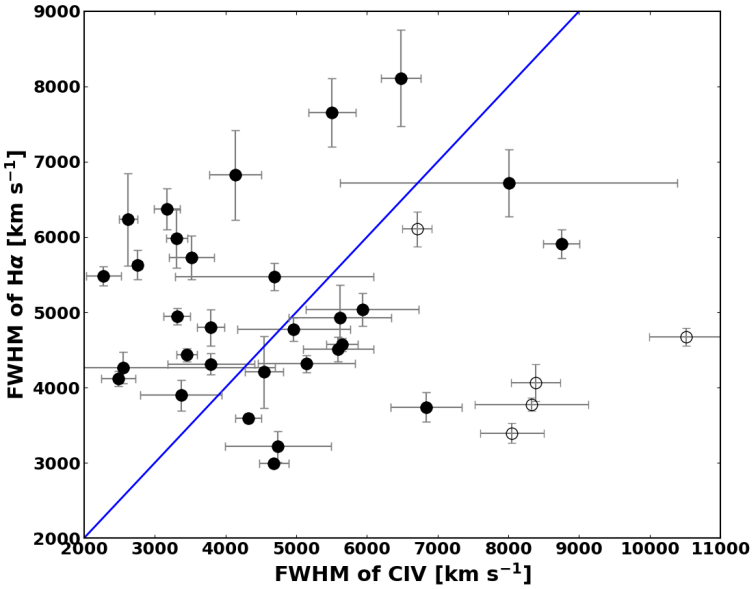


FIGURE 4.3. FWHM of C IV and H$\alpha$. The large scatter observed in the plot suggests a poor correlation between the width of these two lines. Filled circles are the CARLA sources in our sample. Empty circles show the observed quasars in our sample that do not belong to the CARLA survey. The blue line shows the unitary line. This suggests that different broadening mechanisms may be acting on C IV other than gravitational broadening.

and FWHM were estimated from the total fit of the profile. The C IV blueshift, defined as $BS_{CIV} = (\lambda_c - 1549.48)/c$, relative to the measured line centroid[1], $\lambda_c$, was also estimated. A positive value of $BS_{CIV}$ means that the centroid of C IV is shifted blueward of the expected rest-frame wavelength of the line as determined from H$\alpha$. The best fit model parameters including the blueshift are summarized in Table 4.2. Figure 4.3 shows a comparison between the FWHM determined from H$\alpha$ and C IV. The large scatter observed between the two values suggests that mechanisms, other than gravitational broadening, likely contribute to the C IV line profile.

### 4.3.3 Monochromatic Luminosity

In this work, our goal is to estimate the black hole mass using H$\alpha$ and compare it with the estimates based on C IV and the various methods that have been proposed to correct C IV-based measurements for non-gravitational contributions. The last piece of information needed for these black hole mass determinations is the rest-frame optical continuum luminosity, which is a proxy of the radius of the line emitting region in the BLR through the $R - L$ relation (Kaspi et al. 2005, Bentz et al. 2006). The C IV-based black hole mass relies on the FWHM of C IV and the continuum luminosity at 1350 Å ($L_{1350}$). Deriving $L_{1350}$ is straightforward if the spectrum is well

[1]The line centroid, $\lambda_c$, is wavelength which separate half of the flux of the line

flux-calibrated, and to estimate it we used the monochromatic flux at 1350 Å from the power law obtained in the previous section (Column 3 of Table 4.3).

Similarly, the luminosity at 5100 Å ($L_{5100}$) is necessary for the black hole mass estimate using the H$\alpha$ (or H$\beta$) line. Since our spectra do not cover the region around 5100 Å we used a similar approach as Hewett et al. (2006), fitting a model spectral energy distribution (SED) simultaneously to the spectrum and the available photometric data. This is an accurate method for estimating the shape of the SED and successfully reproduces the observed magnitudes of quasars with a precision better than 0.1 mag. Once the observed magnitudes are being reproduced well, $L_{5100}$ can be estimated from the best fit SED model. This method is the same as used by Coatman et al. (2016) to obtain the continuum luminosities for more than 200 high redshift quasars. We constructed a simple parametric quasar SED template consisting of a reddened power-law and a Balmer continuum. We used the reddening law for quasars derived in Zafar et al. (2015). The Balmer continuum was forced to have an integrated flux of 10% of the power-law in the region blueward of the Balmer edge (3646 Å) (as in Hewett et al. 2006). Emission lines were added to the template using the values listed for the SDSS composite from Vanderberk et al. (2001), which includes all broad and narrow lines and the Fe II pseudo-continuum. Each of the parameters were varied, and the resulting templates were used to compute synthetic magnitudes. The best fit model was found by comparing the modeled $g,r,i,z,J,H,K$ magnitudes to those given by the SDSS and UKIDSS surveys using a $\chi^2$ minimization routine. We excluded the $u$ filter from the fitting process because it is not sufficiently covered by the SDSS spectrum. Finally, the luminosity at 5100 Å was measured from the continuum component of the best fit SED. Overall, this method accurately reproduced the observed fluxes to $\sigma < 0.1$ mag per band. However, for a couple of quasars the $H$-magnitude was above this threshold (but still lower than 0.15 mag), and we note that a 0.15 mag error in magnitude translates to a 12% flux error.

For seven quasars, NIR photometry was not available. For these sources we therefore fit the SED template only to the SDSS optical magnitudes. In order to test if these results still reliably predict the luminosity at 5100 Å, we performed a test by fitting all quasars for which $J,H,K$ data does exist first with and then without the NIR magnitudes. The results are shown in Figure 4.4. The difference in the fluxes at 5100 Å determined for these objects using the two methods has a standard deviation of 18%. We used this value as the typical error for the seven sources for which NIR photometry is not available.

Figure 4.5 shows some examples of the SED fits obtained. The values found for $L_{5100}$ are given in Column 4 of Table 4.3. We plot the values obtained for the rest-frame optical and UV luminosities in Figure 4.6 together with the luminosities of all quasars in the Coatman et al. (2017) sample. Our values are consistent with their results and with the slope ($\alpha = 1.044$) obtained by Shen et al. (2011) for the SDSS sample.

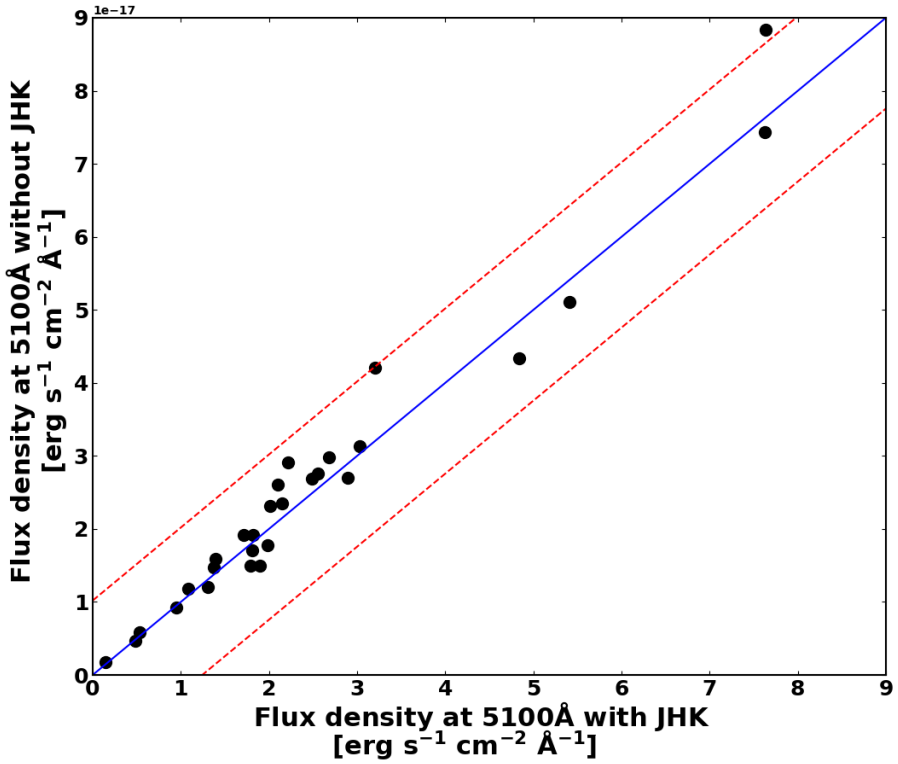


FIGURE 4.4. Measured flux densities at 5100 Å from the SED fitting performed in Section 3.3. The abscissa shows the values obtained from fits using the full optical+NIR photometry, while the ordinate shows the results without the $J$,$H$,$K$ photometry. The values are consistent within a standard deviation of 18%. See the text of Section 3.3 for details.

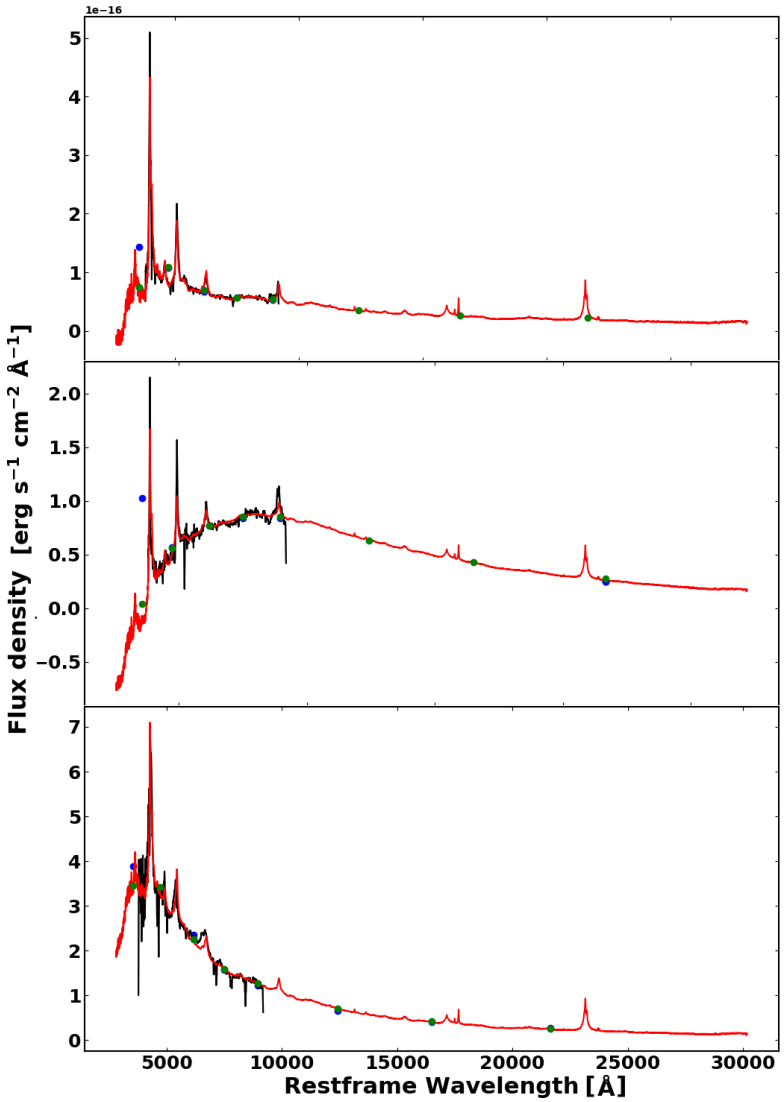


FIGURE 4.5. Examples of the SED template fit to the observed magnitudes. The blue and green dots, respectively, show the observed and modeled $u,g,r,i,z,J,H,K$ magnitudes. The best-fit template and the observed SDSS spectra are shown in red and black, respectively. See the text of Section 3.3 for details.

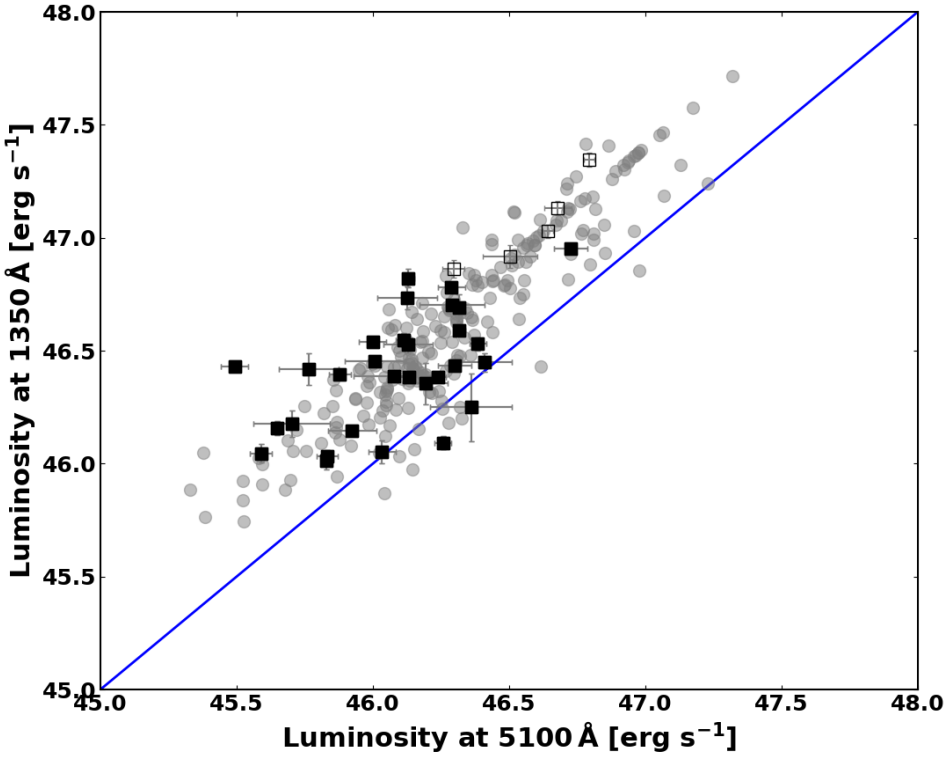


FIGURE 4.6. Optical versus UV rest-frame luminosities. The black filled squares show the values for $L_{5100}$ and $L_{1350}$ for the SINFONI targets studied in this paper that belongs to the CARLA sample. Empty squares show the quasars in our sample that are not in CARLA survey. The blue line shows the unitary line. The sources from Coatman et al. (2017) are shown in grey circles. See the text of Section 3.3 for details.

Table 4.2: Results of the H$\alpha$ and C IV line fitting.

| SDSS Name | H$\alpha$ | | | | | C IV | | | | |
|---|---|---|---|---|---|---|---|---|---|---|
| | Flux[a] | FWHM (km s$^{-1}$) | $\sigma_l$ (km s$^{-1}$) | $z$ | $S/N$ | Flux[a] | FWHM (km s$^{-1}$) | $\sigma_l$ (km s$^{-1}$) | Blueshift (km s$^{-1}$) | $S/N$ |
| Radio-loud quasars from CARLA | | | | | | | | | | |
| J012514−001828 | 8.24±0.16 | 4433±87 | 3126±61 | 2.27980450 | 50 | 37.08±1.36 | 3450.8±142 | 4278±157 | -0.39 | 27.18 |
| J082707+105224 | 8.97±0.29 | 4768±154 | 3046±98 | 2.28465762 | 30 | 17.97±0.69 | 4965.1±801 | 4450±170 | 235.75 | 26.04 |
| J090444+233354 | 35.68±0.66 | 4569±84 | 3151±58 | 2.25777869 | 53 | 53.24±1.69 | 5647.8±223 | 3736±118 | 464.15 | 31.45 |
| J092035+002330 | 1.31±0.10 | 8113±638 | 3430±270 | 2.48998156 | 12 | 24.59±1.39 | 6484.7±280 | 4476±253 | 189.49 | 17.65 |
| J094113+114532[†] | 0.96±0.09 | 6232±609 | 2633±257 | 3.19338967 | 10 | 11.69±0.53 | 2621.9±132 | 3704±168 | -57.58 | 22.01 |
| J102429−005255 | 3.92±0.13 | 5630±197 | 2377±83 | 2.55605854 | 28 | 28.65±0.95 | 2757.2±66 | 3614±120 | 221.03 | 29.98 |
| J104257+074850 | 3.11±0.27 | 6823±596 | 2822±246 | 2.65984046 | 11 | 9.15±0.73 | 4136.9±369 | 4241±339 | 147.42 | 12.48 |
| J110344+023209 | 6.04±0.26 | 5032±217 | 3344±144 | 2.51275370 | 23 | 21.81±1.25 | 5935.3±800 | 4080±234 | -0.53 | 17.38 |
| J111857+123441 | 36.77±2.38 | 5978±388 | 2522±163 | 2.12674483 | 15 | 30.74±0.92 | 3310.8±154 | 4034±120 | 30.23 | 33.34 |
| J112338+052038 | 6.77±0.12 | 2989±56 | 2061±38 | 2.18274227 | 52 | 13.48±0.69 | 4684.8±207 | 3565±184 | 519.25 | 19.28 |
| J115901+065619 | 9.73±0.31 | 5906±192 | 2492±81 | 2.18311544 | 30 | 7.71±0.97 | 8750.9±255 | 3643±461 | 2819.44 | 7.90 |
| J120301+063441 | 14.86±0.36 | 4120±101 | 2724±67 | 2.17975559 | 40 | 8.47±0.61 | 2482.4±242 | 3200±233 | -37.95 | 13.72 |
| J121255+245332 | 2.69±0.23 | 4931±434 | 2081±183 | 2.40561193 | 11 | 5.510±0.94 | 5620.9±722 | 3861±664 | 2164.23 | 5.81 |
| J121911−004345 | 12.78±0.23 | 3590±67 | 2258±42 | 2.30407006 | 53 | 13.56±0.84 | 4323.5±182 | 3689±231 | 2064.21 | 15.96 |
| J122836+101841 | 6.23±0.20 | 4310±141 | 1965±64 | 2.30220348 | 30 | 12.12±0.80 | 3793.1±614 | 3500±232 | -100.02 | 15.06 |
| J133932−031706 | 7.62±0.25 | 5471±182 | 3515±117 | 2.31004297 | 29 | 16.59±1.27 | 4691.1±1403 | 4765±364 | -79.39 | 13.06 |
| J140445−013021 | 22.85±1.11 | 4262±208 | 3675±179 | 2.51798028 | 20 | 29.46±1.02 | 2552.3±2151 | 4534±157 | 168.99 | 28.71 |
| J141906+055501 | 3.20±0.19 | 7656±456 | 3790±225 | 2.29473715 | 16 | 9.73±0.84 | 5507.6±336 | 4103±356 | 187.76 | 11.50 |
| J143331+190711 | 7.07±0.35 | 5728±289 | 2416±122 | 2.35857408 | 19 | 23.10±0.76 | 3518.4±321 | 3884±129 | -133.65 | 30.05 |
| J145301+103617 | 6.49±0.23 | 4508±165 | 3386±124 | 2.27681782 | 27 | 10.19±0.90 | 5592.1±497 | 3833±341 | -273.64 | 11.24 |
| J151508+213345 | 13.08±0.55 | 6372±269 | 2693±113 | 2.24844579 | 23 | 28.56±0.95 | 3171.5±180 | 4812±160 | 294.71 | 30.01 |
| J153124+075431 | 1.13±0.06 | 3896±205 | 1643±86 | 2.47392896 | 18 | 6.46±0.40 | 3369.8±571 | 3633±229 | 1083.40 | 15.86 |
| J153727+231826 | 4.35±0.28 | 6717±446 | 2838±188 | 2.26599180 | 15 | 2.61±0.88 | 8007.8±2386 | 4237±1431 | 1766.47 | 2.96 |
| J153925+160400 | 1.75±0.11 | 3215±203 | 1349±85 | 2.55083196 | 15 | 5.00±0.72 | 4743.1±751 | 4429±641 | 1227.27 | 6.91 |
| J154459+040746 | 26.55±0.61 | 5480±126 | 2314±53 | 2.18572880 | 43 | 19.57±0.84 | 2275.8±249 | 3655±158 | 317.50 | 23.05 |
| J160016+183830 | 20.94±2.37 | 4205±476 | 1778±201 | 2.40598540 | 8 | 19.95±0.67 | 4543.5±270 | 3322±111 | 547.80 | 29.74 |
| J160154+135710 | 11.03±0.24 | 4942±108 | 3296±72 | 2.23799308 | 45 | 17.34±0.71 | 3312.5±186 | 3500±144 | -119.23 | 24.27 |
| J160212+241010 | 19.79±0.98 | 4796±238 | 2005±99 | 2.52917977 | 20 | 16.06±0.68 | 3789.9±194 | 4133±176 | 431.34 | 23.46 |
| J230011−102144 | 4.05±0.10 | 4313±113 | 2749±72 | 2.31862924 | 38 | 8.92±1.00 | 5145.6±683 | 3919±443 | 1315.68 | 8.84 |
| J231607+010012 | 5.77±0.30 | 3739±194 | 2472±128 | 2.64938761 | 19 | 9.31±1.32 | 6840.3±502 | 4499±640 | 2797.38 | 7.03 |
| Non-CARLA quasars having $M_{BH}$(C IV) $> 10^{10}$ M$_\odot$ | | | | | | | | | | |
| J005814+011530 | 9.08±0.35 | 3391±132 | 2797±109 | 2.52805982 | 25 | 17.50±1.97 | 8050.9±452 | 4303±486 | 3218.35 | 8.84 |
| J081014+204021 | 40.27±0.90 | 3776±84 | 3222±72 | 2.52432666 | 44 | 25.51±1.93 | 8328.7±807 | 4281±325 | 3245.79 | 13.16 |
| J115301+215117 | 20.58±0.78 | 6108±231 | 2573±97 | 2.37276010 | 26 | 76.71±3.97 | 6708.6±206 | 4700±243 | 2568.54 | 19.31 |
| J130331+162146 | 2.94±0.17 | 4067±245 | 1703±102 | 2.30183001 | 16 | 22.74±1.91 | 8390.7±348 | 4773±402 | 3640.50 | 11.85 |
| J210831−063022 | 15.07±0.37 | 4672±117 | 3003±75 | 2.37686673 | 39 | 20.27±1.46 | 10511.0±519 | 4584±331 | 5312.81 | 13.83 |

[a] Fluxes are given in units of $10^{-15}$ erg s$^{-1}$ cm$^{-2}$.

[†] Due to the high redshift of this source, the measurements were made using H$\beta$

## 4.4 Results

### 4.4.1 Black hole masses

Single epoch BH masses can be determined under the assumption of virial motions using two parameters, the velocity of the gas and its distance from the black hole. The strong $R-L$ relation between the continuum luminosity at 5100 Å and the BLR radius obtained from RM allows us to use the $L_{5100}$ as a measure of the BLR radius, while the FWHM of the Balmer lines serve as a proxy for the velocity of the gas. Both parameters were obtained in Section 3, and we can thus estimate the black hole mass using the FHWM of H$\alpha$ and $L_{5100}$. The general equation to estimate the black hole mass takes the form of equation 4.1(Shen et al. 2011):

$$\log(M_{BH}/M_{\odot}) = a + b \times \log(\frac{FWHM}{10^3\,km\,s^{-1}}) + c \times \log(\frac{\lambda L_{\lambda}}{10^{42}\,erg\,s^{-1}}) \tag{4.1}$$

Shen et al. (2011) presented BH masses for the entire SDSS quasar sample using the equations derived by Vestergaard & Peterson (2006) for C IV (at high redshift) and H$\alpha$ (at low redshift). Since the CARLA sample of quasars was selected from the SDSS as well, the BH masses of our quasars were previously determined based on C IV. Using the results from Section 3 we have used the H$\alpha$ line to obtain new BH masses. The new measurements should be relatively free from the type of uncertainties that affect determinations based on C IV. We use Equation 4.1 with the parameters (a,b,c)=(6.91,2.0,0.50) as in Vestergaard & Peterson (2006), by converting the FWHM of H$\alpha$ to FHWM of H$\beta$ using the equation presented by Coatman et al. (2017). Table 4.4 summarizes the values obtained. We compare the values obtained using H$\alpha$ and C IV in Figure 4.7. Panel (a) shows that there is a large scatter between the two estimates, as expected. The $M_{BH}$ from C IV is systematically lower by 0.11 dex on average, and has a scatter of 0.43 dex in either direction. The $M_{BH}$ estimated from H$\alpha$ concentrates around $\log(M_{BH}/M_{\odot}) \sim 9$ with only one source having $\log(M_{BH}/M_{\odot}) > 10$ compared to five sources when using C IV. Panel (b) of Figure 4.7 shows the distribution in $M_{BH}$ estimated from C IV and H$\alpha$. The figure shows that most of the objects having a C IV-based $\log(M_{BH}/M_{\odot})$ lower and higher than 9 and 10, respectively, are shifted into a region around $\log(M_{BH}/M_{\odot}) \sim 9.5$ when using H$\alpha$.

The role of C IV in SE BH mass determinations has been discussed by several authors, leading to novel attempts for providing reliable $M_{BH}$ based on this line. Here we test several empirical calibrations that have been proposed for improving the $M_{BH}$ estimate using C IV by comparing them with our results obtained using H$\alpha$.

Denney et al. (2012) used a combination of RM data with SE BM mass estimates based on C IV in order to investigate any offsets. Their results showed that in several cases C IV has a non-reverberating component (such outflows, for example) which varies from source to source. Comparing with the $M_{BH}$ estimated from H$\beta$ they showed that the scatter between the estimates based on these lines correlates with the shape of C IV. They suggested a correction for $M_{BH}$

Table 4.3: Peak ratio and UV and optical continuum luminosities.

| SDSS Name | Peak Ratio $\lambda$1400 | $L_{1350}$ (erg $s^{-1}$) | $L_{5100}$ (erg $s^{-1}$) |
|---|---|---|---|
| Radio-loud quasars from CARLA | | | |
| J012514−001828 | 0.173 | 46.539±0.02 | 46.00±0.05 |
| J082707+105224 | 0.203 | 46.146±0.02 | 45.92±0.09 |
| J090444+233354 | 0.378 | 46.952±0.02 | 46.73±0.06 |
| J092035+002330 | 0.184 | 46.547±0.03 | 46.11±0.03 |
| J094113+114532 | 0.211 | 46.430±0.02 | 45.49±0.05 |
| J102429−005255 | 0.161 | 46.702±0.02 | 46.29±0.12 |
| J104257+074850 | 0.285 | 46.448±0.04 | 46.41±0.10 |
| J110344+023209 | 0.380 | 46.529±0.03 | 46.38±0.03 |
| J111857+123441 | 0.172 | 46.396±0.02 | 45.88±0.04 |
| J112338+052038 | 0.272 | 46.032±0.03 | 45.83±0.04 |
| J115901+065619 | 0.195 | 45.650±0.05 | 46.03±0.05 |
| J120301+063441 | 0.129 | 45.693±0.03 | 46.26±0.03 |
| J121255+245332 | 0.604 | 46.420±0.07 | 45.77±0.11 |
| J121911−004345 | 0.500 | 46.822±0.04 | 46.13±0.02 |
| J122836+101841 | 0.298 | 46.354±0.09 | 46.19±0.08 |
| J133932−031706 | 0.175 | 46.526±0.04 | 46.13±0.09 |
| J140445−013021 | 0.172 | 46.778±0.02 | 46.29±0.05 |
| J141906+055501 | 0.203 | 46.050±0.04 | 45.59±0.04 |
| J143331+190711 | 0.106 | 46.454±0.02 | 46.01±0.11 |
| J145301+103617 | 0.317 | 46.010±0.04 | 45.83±0.01 |
| J151508+213345 | 0.202 | 46.590±0.02 | 46.32±0.02 |
| J153124+075431 | 0.367 | 46.159±0.03 | 45.65±0.01 |
| J153727+231826 | 1.010 | 46.250±0.15 | 46.36±0.15 |
| J153925+160400 | 0.318 | 46.180±0.06 | 45.70±0.14 |
| J154459+040746 | 0.113 | 46.384±0.02 | 46.13±0.04 |
| J160016+183830 | 0.241 | 46.386±0.02 | 46.08±0.15 |
| J160154+135710 | 0.219 | 46.384±0.02 | 46.24±0.03 |
| J160212+241010 | 0.265 | 46.435±0.02 | 46.30±0.06 |
| J230011−102144 | 0.561 | 46.730±0.05 | 46.13±0.11 |
| J231607+010012 | 0.408 | 46.690±0.06 | 46.32±0.02 |
| Non-CARLA quasars having $M_{BH}$(C IV) > $10^{10}$ $M_\odot$ | | | |
| J005814+011530 | 0.837 | 46.920±0.05 | 46.50±0.10 |
| J081014+204021 | 0.678 | 47.133±0.03 | 46.68±0.05 |
| J115301+215117 | 0.514 | 47.346±0.03 | 46.79±0.02 |
| J130331+162146 | 0.594 | 46.870±0.04 | 46.30±0.04 |
| J210831−063022 | 1.002 | 47.032±0.03 | 46.65±0.02 |

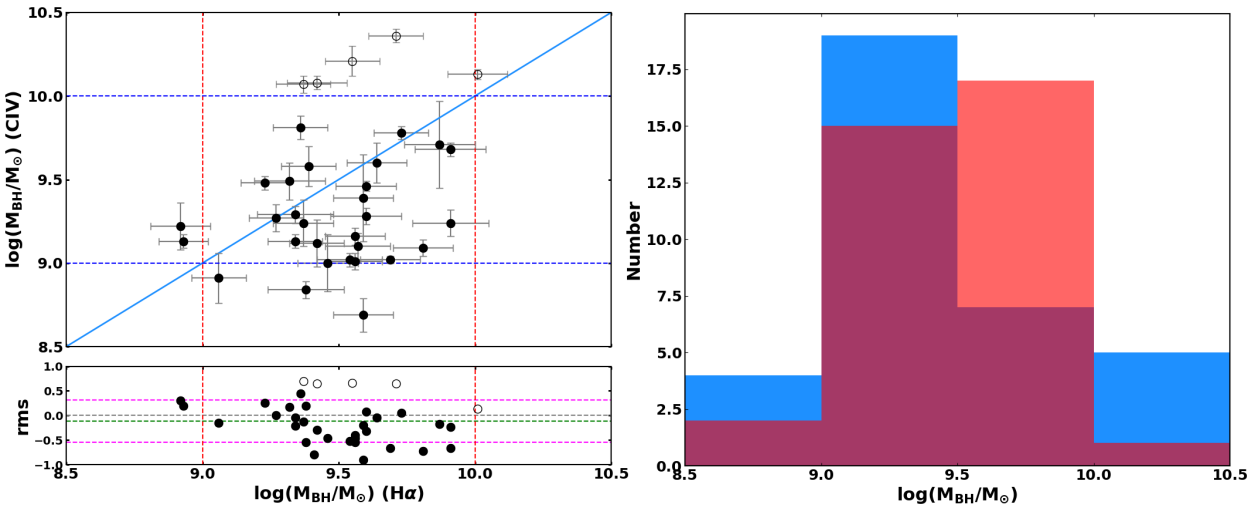


FIGURE 4.7. Black hole masses estimated using H$\alpha$ and C IV. Left panel (a): values obtained using Vestergaard & Peterson (2006) for C IV and H$\alpha$ (upper left panel) and the difference between the two (left bottom panel). Filled circles show the CARLA quasars and empty circles show the quasars not present in CARLA. Dotted lines (red for H$\alpha$ and blue for C IV) separate the regions where the $M_{BH}$ are below $10^9$ and above $10^{10}$ $M_\odot$. Right panel (b): the distribution of $M_{BH}$ for our sample (blue for C IV and red for H$\alpha$). While the H$\alpha$-based masses are higher on average, the number of sources above $10^{10}$ $M_\odot$ is reduced with respect to that of the C IV-based masses.

using C IV based on the ratio between the FWHM and dispersion ($\sigma_{l,CIV}$). We compare the $M_{BH}$ corrected by this method with the ones obtained from H$\alpha$. Panel (a) of Figure 4.8 shows the results. The Denney et al. (2012) method significantly reduces the scatter between H$\alpha$ and the (corrected) C IV by a factor of ~0.16 dex. The average value for C IV is now the same as that of H$\alpha$ and the scatter is 0.27 dex. We note that Denney et al. (2012) developed their method using relatively low luminosity, radio quiet sources with $\log(M_{BH}/M_\odot)$ between 7 and 9. Our results obtained here indicate that the method extends to luminous radio-loud quasars with higher black hole masses as well.

With the same goal, Runnoe et al. (2013) suggested that discrepancies between the $M_{BH}$ from C IV and H$\beta$ are mainly due to the fact that C IV often presents a non-virial component. Using a sample of 85 bright low-to-intermediate redshift quasars, they found that the residual width of C IV and H$\beta$ correlate with the peak of Si IV+O IV]$\lambda$1400. Using this parameter (Peak Ratio $\lambda$1400 in Table 4.3) they derived an empirical correction to the virial equation that reduces the scatter from 0.43 to 0.33 dex in their sample. Panel (b) of Figure 4.8 shows how the Runnoe et al. (2013) method compares with our estimates based on H$\alpha$. This method also reduces the scatter between the $M_{BH}$ estimated from H$\alpha$ and C IV, but with a tendency to underestimate

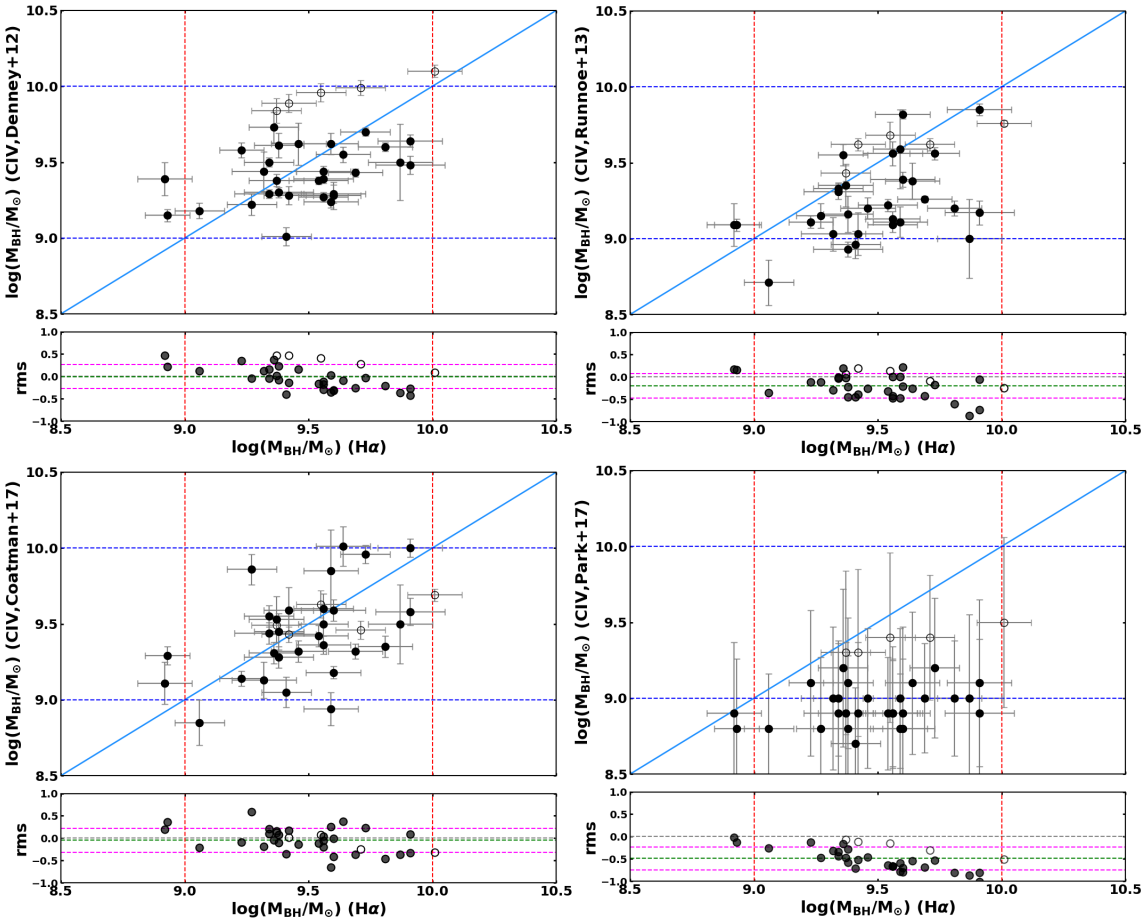


FIGURE 4.8. Rehabilitation methods for C IV-based $M_{BH}$ estimates compared to our H$\alpha$-based estimates. Panel (a) shows the method from Denney (2012). Panel (b) shows the method of Runnoe et al. (2013). Panel (c) shows the method of Coatman et al. (2017). Panel (d) shows the C IV single epoch estimates using the Park et al. (2017) new RM results. In all panels, filled circles show the quasars from CARLA and empty circles are the quasars that are not in CARLA. The red and blue dashed lines demarcate the range $9 < \log(M_{BH}/M_{\odot}) < 10$. Below each panel we show the absolute differences between the corrected C IV values and the corresponding H$\alpha$-based values.

the (H$\alpha$) $M_{BH}$. The average black hole mass has an offset of -0.2 dex with a scatter of 0.27 dex. Note that the scatter is similar to that obtained using the Denney et al. (2012) method, but with a larger negative offset from zero. Furthermore, this method depends strongly on a line that is significantly weaker than C IV. This means that in low S/N spectra the correction factor can drop close to zero, reducing the corrected $M_{BH}$ to the original C IV-based estimate.

Coatman et al. (2017) presented another possible solution to rehabilitate C IV BH mass estimators. Analyzing a large sample of 230 quasars, they found a strong correlation between

the blueshift of C IV and the FWHM ratio between C IV and H$\alpha$. Their results show that in order to estimate the BH mass using the FWHM of C IV it is necessary to first correct its width by a parameter that is a function of the C IV blueshift. We estimated the BH masses using the Coatman et al. (2017) method for our sample. Panel (c) of Figure 4.8 shows the corrected BH masses compared with our measurements based on H$\alpha$. The results are similar to those obtained with the Denney et al. (2012) method. The scatter between the BH masses from H$\alpha$ and C IV are reduced by a factor of 0.16 dex, with a tendency towards smaller values (the mean value of the offset of 0.05 dex).

Finally, Park et al. (2017) presented new RM results based on a larger sample than that presented by Park et al. (2013). By using a sample of 35 high S/N AGN they derived a new equation for SE BH masses using C IV. The main difference between their results and previous determinations of SE C IV-based BH mass estimates is the value of the exponent in the luminosity term of the equation. Their method reduces the contribution of the luminosity in the virial equation, and as a result the values obtained are smaller compared with C IV-based estimates based on Vestergaard & Peterson (2006). Panel (d) of Figure 4.8 shows the BH masses estimated by the Park et al. (2017) method compared with our results using H$\alpha$. Although the scatter (0.25 dex) is indeed reduced, we find a large systematic offset of -0.49 dex. This is in agreement with the results shown in Figure 11 of Park et al. (2017). They point out that their method overpredicts the masses of low mass BHs ($<10^{8.5}M_{\odot}$), and underpredicts those of high mass BHs ($>10^{8.5}M_{\odot}$). The offset seen in panel (d) is consistent with this trend given that our CARLA sample is biased toward very massive BHs that tend to be underestimated by Park et al. (2017).

### 4.4.2 Eddington Ratio

The Eddington luminosity ($L_{edd}$) is a theoretical maximum to the luminosity that an AGN can emit while balancing the outward radiative pressure and inward gravitational force. The Eddington ratio ($L/L_{Edd}$) is an estimate of the accretion rate of the black hole, and is believed to be the main driving mechanism of the Eigenvector 1 which correlates with most of the spectral features in Type-I AGN spectra, such as the ratio of Fe II/H$\beta$, the soft X-ray slope, and the blueshift of C IV (Boroson & Green 1992, Marziani et al. 2001, Shen & Ho 2014).

The Eddington ratio can be obtained by applying a bolometric correction factor, $f_l$, to the measured optical luminosity, and then dividing this bolometric luminosity by the Eddington luminosity for a given black hole mass. This correction factor, $f_l$, depends on the luminosity and for our sample ($45.5 < \log(L_{5100}) < 47.5$ erg s$^{-1}$) its range is 5-7 (Marconi et al. 2004). In this paper we follow the approach of Netzer et al. (2007), which assumes an $f_l = 7.0$. $L/L_{Edd}$ can then be estimated through (Netzer et al. 2007)

$$L/L_{\rm edd} = \frac{f_l\, L_{5100}}{L_{\rm edd}} = \frac{7.0\, L_{5100}}{(1.5 \times 10^{38}\, M_{BH}/M_{\odot})} \tag{4.2}$$

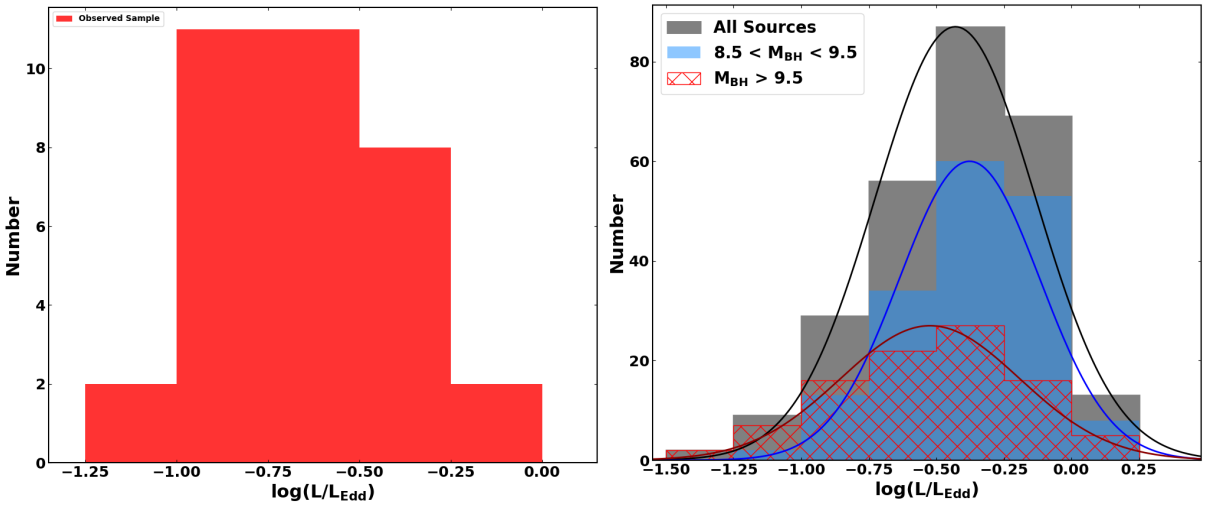


FIGURE 4.9. Distribution of $L/L_{Edd}$ for the quasars. Left panel: distribution of $L/L_{Edd}$ for the CARLA subsample observed with SINFONI. Right panel: Distribution of $L/L_{Edd}$ for the quasars in our sample combined with the quasars from the Coatman et al. (2017) sample (grey shaded histogram and black line). The red-hatched histogram and red line show the distribution for $M_{BH} > 10^{9.5}$ $M_{\odot}$, while the blue shaded histogram and blue line show distribution for $M_{BH} < 10^{9.5}$ $M_{\odot}$.

We use Equation 4.2 to estimate $L/L_{Edd}$ for our sample, as well as for the Coatman et al. (2017) sample for comparison. The results are shown in Figure 4.9. The left panel shows the distribution of $L/L_{Edd}$ for the CARLA sample. The values have a relatively broad distribution (0.26 dex) with a mean value of $10^{-0.67}$. In the right panel of Figure 4.9 we compare these results to a larger sample by adding our sample to that of Coatman et al. (2017) composed of both radio quiet and radio loud quasars. We split the combined sample into a high ($\log(M_{BH}/M_{\odot}) > 9.5$) and low mass black hole mass ($\log(M_{BH}/M_{\odot}) < 9.5$) sample. The lower mass BHs have both a higher mean $L/L_{Edd}$ ($\log(L/L_{Edd}) = -0.37$) and a narrower range ($0.25\,dex$) than the higher mass BHs (mean of $\log(L/L_{Edd}) = -0.52$ and range of 0.33 dex). The latter distribution is very similar to that found for the CARLA sample shown in the left panel, which is expected because the CARLA sample is exclusively composed of radio-loud quasars with high BH masses. The grey histogram shows the distribution we get when we combine the quasars of Coatman et al. (2017) with our sample, with an intermediate mean ($\log(L/L_{Edd}) = -0.43$) and spread (0.29 dex).:

In order to understand where these differences in the Eddington ratios come from, we plot $L/L_{Edd}$ as function of the observables FWHM(H$\alpha$), luminosity ($L_{5100}$) and BH mass ($M_{BH}$). Panel (a) of Figure 4.10 shows a high dependency of $L/L_{Edd}$ on FWHM(H$\alpha$), both for the Coatman et al. (2017) sample (mostly radio quiet quasars, grey circles) and for our SINFONI quasars (all radio loud, red squares). A Spearman rank correlation test gives a strong anti-correlation ($S_c = -0.79$ for our sample and $S_c = -0.74$ for the Coatman et al. 2017, sample) with a high significance

($p$-Value$< 10^{-8}$). As can be seen, objects with the broadest lines are accreting at lower rates than objects with narrower ones. This indicates that as the velocity of the gas increases, quasars accrete at slower rates.

Panel (b) of the same figure shows a trend of increasing $L/L_{Edd}$ with $L_{5100}$. The large scatter in the plot results in a weaker ($S_c = 0.54$ for our radio-loud quasars and $S_c = 0.46$ for the radio quiet quasars in the Coatman et al. (2017) sample), but high significance ($p$-Value$< 10^{-14}$), correlation between these quantities. This trend is expected and consistent with the physical scenario suggested by panel (a), because as the accretion rate increases the luminosity has to increase as well in order to give the same Eddington ratio.

Last, panel (c) of Figure 4.10 shows that there is a general trend of decreasing $L/L_{Edd}$ with increasing $M_{BH}$. The correlation in this case, as with the luminosity, is weak ($S_c = 0.25$ for radio loud and $S_c = 0.27$ for radio quiet), but also has a high significance ($p$-Value$< 10^{-5}$). The large scatter in this correlation is likely a reflection of the scatter of the luminosity observed in panel (b). These correlations suggest a scenario in which as the black holes increase their mass, the surrounding gas gains momentum increasing its velocity dispersion and hence reducing the accretion rate. However, the gain in luminosity is not sufficient to overcome the gain in the velocity resulting in the trends observed.

### 4.4.3 Growth Time

To estimate black hole growth times ($t_{grow}$) we will assume that the BH experiences a period of continuous growth during their duty cycle starting from a seed BH mass. We use the original expression from Salpeter (1964):

$$t_{grow} = t_{edd}\ \frac{\eta/(1-\eta)}{L/L_{edd}}\ \log\left(\frac{M_{BH}}{M_{seed}}\right)\ \frac{1}{f_{active}}\ \mathrm{yr}, \tag{4.3}$$

where $t_{edd} = 3.5 \times 10^8$ yr is the Eddington time, $\eta$ is the accretion efficiency, and $f_{active}$ is the duty cycle. The efficiency depends on BH spin and values range two orders of magnitude ($\eta = 0.004 - 0.4$) from retrograde to prograde accretion or BH spin of $a = \pm 1$, with typical values around $\eta = 0.2$ reflecting a non-zero angular velocity King et al. (2004). The black hole seed can have a low mass ($M_{seed} = 10^{2-4} M_\odot$) when resulting from Population-III stars, or larger ($M_{seed} = 10^{4-6} M_\odot$) when resulting from direct gas cloud collapse Begelman et al. (2006). In this work we follow Netzer et a. (2007), assuming $\eta = 0.2$, $M_{seed} = 10^4 M_\odot$, and $f_{active} = 1$. Additionally, we calculate the growth time using a lower efficiency, $\eta = 0.1$. From these parameters and Equation 4.3 we estimate the growth time for our sample as well as the Coatman et al. (2017) sample which is dominated by radio-quiet quasars (383 out of 409). The values obtained for $t_{growth}$ for our sample are listed in Column 9 of Table 4.4, where we divided the values by the age of the universe at each redshift for the adopted cosmology. We plotted the distribution of growth times

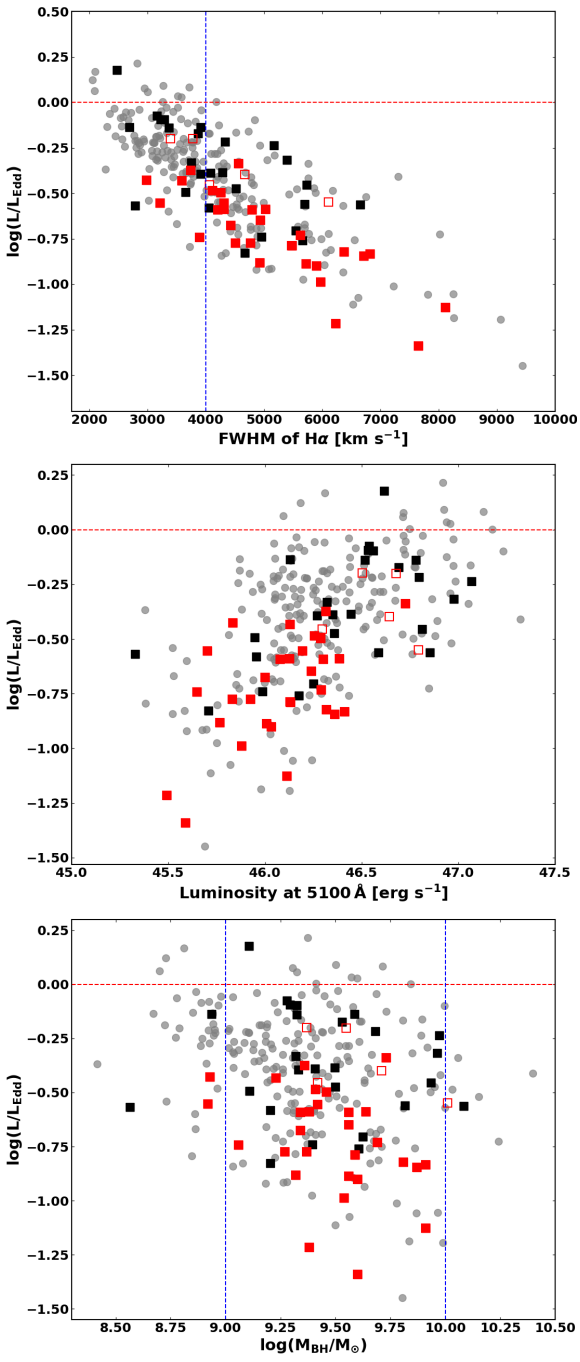


FIGURE 4.10. Quasar properties as function of Eddington ratio. Panels show (a) the correlation between $L/L_{Edd}$ and FHWM(H$\alpha$), (b) $L/L_{Edd}$ and $L_{5100}$, and (c) $L/L_{Edd}$ and $M_{BH}$. In all panels red filled and open squares, respectively, show the CARLA and non-Carla quasars from this paper, while the black squares and grey dots show the radio loud and quiet quasars from Coatman et al. (2017), respectively.

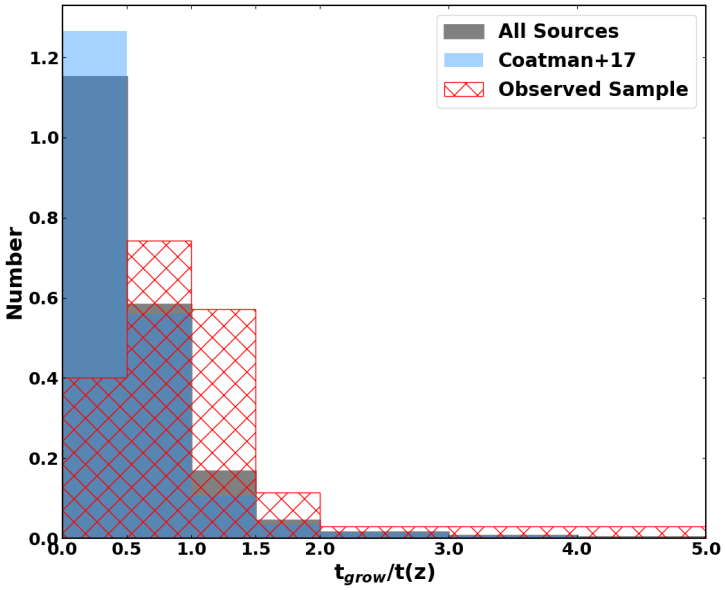


FIGURE 4.11. Distribution of the quasar growth times. The red dashed histogram shows the values derived for the CARLA sample, the blue solid histogram shows the Coatman et al. (2017) sample and the grey histogram shows the two samples combined. See Section 4.3 for details.

in Figure 4.11. For the assumed efficiency, 15 of our 35 quasars have $t_{grow}/t(z) > 1$[2], indicating that the typical efficiencies assumed are perhaps too high. Comparing the two samples in Figure 4.11, we find that radio-quiet and radio-loud quasars follow somewhat different distributions in $t_{grow}$, with radio-quiet quasars having, on average, lower growth times compared to radio-loud quasars.

In order to explore where these differences in growth times may come from, we plot $t_{grow}$ against the FWHM(H$\alpha$), optical luminosity, black hole mass and accretion rate in Figure 4.12. Panel (a) shows a strong correlation between $t_{grow}$ and FWHM(H$\alpha$) both for the CARLA sample ($S_c = 0.84$ and p-V$< 10^{-16}$) and for the (mostly) radio-quiet quasars from Coatman et al. (2017) ($S_c = 0.82$ and p-V$< 10^{-56}$). The correlation suggests that as the velocity of the gas increases, the growth of the BH is slowed down, and the similar distribution of the RL and RQ sources shows that this trend does not depend on radio-loudness. Panel (b) shows a weak, but highly significant, anti-correlation between the optical luminosity and the growth time, which is stronger for the radio-loud quasars ($S_c = -0.47$ and p-V$< 0.004$) than for the radio-quiet quasars ($S_c = -0.27$ and p-V$< 10^{-4}$). Despite the large scatter, brighter quasars appear to be growing faster. For the $M_{BH}$ shown in panel (c), a Spearman test indicates a moderate correlation with $t_{grow}$. We obtained $S_c = 0.33$ (with an p-V$< 0.05$) for the CARLA sample and $S_c = 0.44$ (with an p-V$< 10^{-20}$ for the radio-quiet quasars. Given the strong correlation with the FWHM(H$\alpha$) (panel a), and the weak anti-correlation with the luminosity (panel b), the scatter in panel (c) may reflect the luminosity

[2] t($z$) is the age of the universe at given redshift

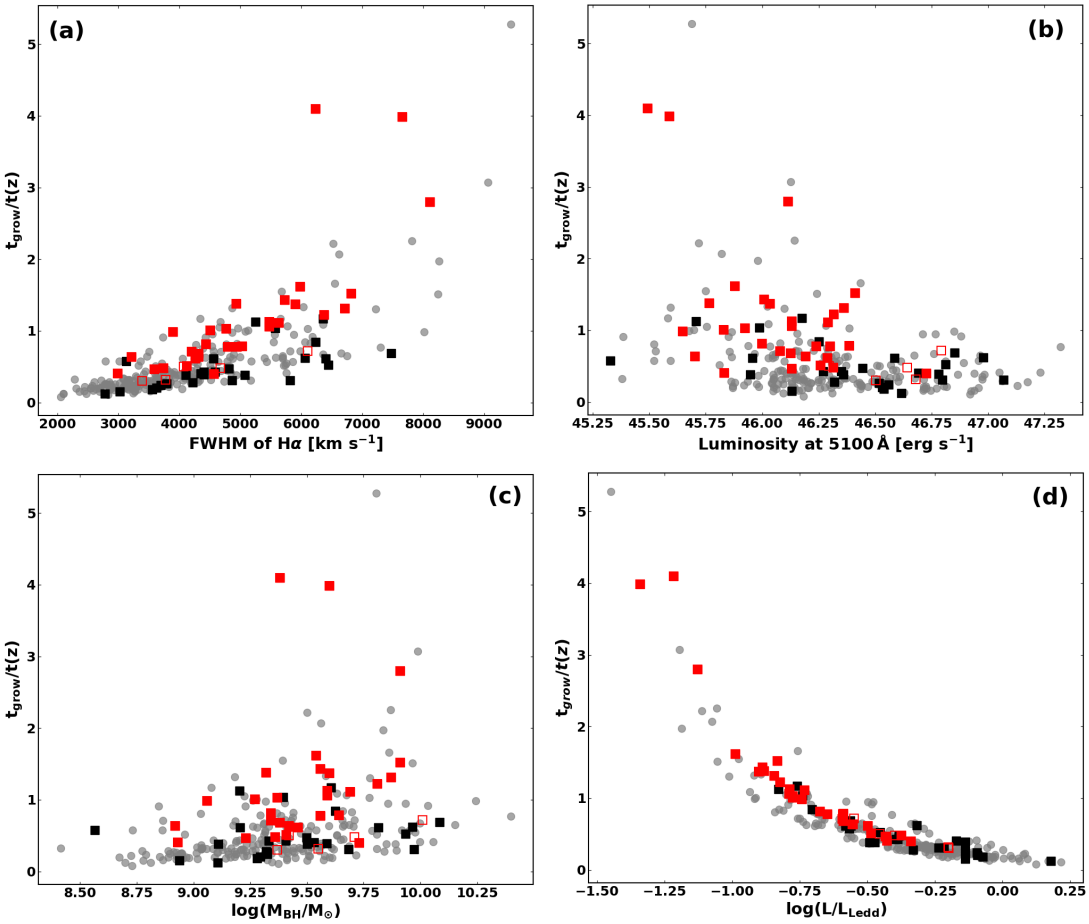


FIGURE 4.12. Quasar properties as function of the growth time. Panels show $t_{grow}$ versus FHWM of H$\alpha$ (panel (a)), $t_{grow}$ versus $L_{5100}$ (panel (b)), $t_{grow}$versus $M_{BH}$ (panel (c)), and $t_{grow}$ versus $L/L_{Edd}$ (panel (d)). In all panels, red filled squares show the quasars from CARLA, red empty squares show the quasars in our sample that are not in CARLA, and black squares (grey dots) show radio loud (quiet) quasars from Coatman et al. (2017). See Section 4.3 for details.

contribution to the $M_{BH}$, which is a function of the FWHM and $L_{5100}$. Last, in panel (d) we plot the growth rate against the Eddington ratio, finding that they are strongly correlated ($S_c = -0.98$ and p-V$< 10^{-29}$) as expected given that $t_{grow} \propto (L/L_{edd})^{-1}$.

Table 4.4: Black Hole masses, Eddington ratios and growth times.

| SDSS Name | H$\alpha$ | C IV | Rehabilitated C IV measurements | | | | | |
|---|---|---|---|---|---|---|---|---|
| | $\log(M_{BH}/M_\odot)$ | $\log(M_{BH}/M_\odot)$ | $\log(M_{BH}/M_\odot)$ (Denney+12) | $\log(M_{BH}/M_\odot)$ (Runnoe+13) | $\log(M_{BH}/M_\odot)$ (Coatman+17) | $\log(M_{BH}/M_\odot)$ (Park+17) | $L/L_{Edd}$ | $t_{growth}/t(z)$ |
| Radio-loud quasars from CARLA | | | | | | | | |
| J012514−001828 | 9.34±0.10 | 9.13±0.04 | 9.50±0.03 | 9.32±0.04 | 9.54±0.07 | 8.95±0.38 | 0.21 | 0.81 |
| J082707+105224 | 9.36±0.11 | 9.23±0.14 | 9.38±0.04 | 9.35±0.14 | 9.52±0.15 | 8.85±0.47 | 0.16 | 1.03 |
| J090444+233354 | 9.73±0.10 | 9.77±0.04 | 9.70±0.03 | 9.56±0.04 | 9.96±0.06 | 9.24±0.46 | 0.45 | 0.39 |
| J092035+002330 | 9.91±0.13 | 9.68±0.04 | 9.64±0.04 | 9.85±0.04 | 9.99±0.06 | 9.09±0.55 | 0.07 | 2.79 |
| J094113+114532 | 9.37±0.14 | 8.83±0.05 | 9.29±0.03 | 8.93±0.05 | 9.28±0.07 | 8.84±0.48 | 0.06 | 4.09 |
| J102429−005255 | 9.69±0.11 | 9.02±0.02 | 9.43±0.03 | 9.26±0.02 | 9.31±0.05 | 8.97±0.36 | 0.18 | 1.11 |
| J104257+074850 | 9.91±0.14 | 9.24±0.08 | 9.47±0.06 | 9.17±0.08 | 9.57±0.09 | 8.94±0.49 | 0.14 | 1.52 |
| J110344+023209 | 9.64±0.11 | 9.59±0.12 | 9.55±0.05 | 9.37±0.12 | 10.01±0.13 | 9.06±0.47 | 0.25 | 0.78 |
| J111857+123441 | 9.53±0.12 | 9.01±0.04 | 9.37±0.02 | 9.22±0.04 | 9.41±0.07 | 8.87±0.37 | 0.10 | 1.61 |
| J112338+052038 | 8.92±0.09 | 9.12±0.04 | 9.15±0.04 | 9.08±0.04 | 9.28±0.06 | 8.78±0.46 | 0.37 | 0.40 |
| J115901+065619 | 9.60±0.11 | 9.68±0.03 | 9.28±0.09 | 9.81±0.03 | 9.18±0.04 | 8.93±0.57 | 0.12 | 1.37 |
| J120301+063441 | 9.41±0.10 | 8.60±0.09 | 9.00±0.06 | 8.96±0.09 | 9.04±0.10 | 8.67±0.37 | 0.32 | 0.50 |
| J121255+245332 | 9.31±0.13 | 9.49±0.11 | 9.44±0.13 | 9.02±0.11 | 9.13±0.12 | 9.00±0.47 | 0.13 | 1.37 |
| J121911−004345 | 9.23±0.09 | 9.47±0.04 | 9.58±0.05 | 9.11±0.04 | 9.14±0.05 | 9.12±0.48 | 0.36 | 0.46 |
| J122836+101841 | 9.41±0.10 | 9.11±0.14 | 9.27±0.06 | 9.02±0.14 | 9.59±0.15 | 8.88±0.47 | 0.27 | 0.63 |
| J133932−031706 | 9.58±0.11 | 9.39±0.26 | 9.62±0.07 | 9.58±0.26 | 9.85±0.27 | 9.01±0.46 | 0.16 | 1.12 |
| J140445−013021 | 9.45±0.11 | 8.99±0.17 | 9.62±0.14 | 9.19±0.07 | 9.31±0.07 | 8.99±0.46 | 0.31 | 0.61 |
| J141906+055501 | 9.59±0.13 | 9.27±0.05 | 9.28±0.06 | 9.38±0.05 | 9.58±0.07 | 8.83±0.46 | 0.04 | 3.98 |
| J143331+190711 | 9.56±0.12 | 9.10±0.08 | 9.39±0.03 | 9.56±0.08 | 9.59±0.10 | 8.91±0.36 | 0.12 | 1.43 |
| J145301+103617 | 9.27±0.10 | 9.27±0.08 | 9.22±0.07 | 9.14±0.08 | 9.86±0.10 | 8.81±0.47 | 0.16 | 1.00 |
| J151508+213345 | 9.80±0.11 | 9.08±0.05 | 9.59±0.03 | 9.20±0.05 | 9.34±0.07 | 8.95±0.38 | 0.15 | 1.22 |
| J153124+075431 | 9.05±0.10 | 8.90±0.15 | 9.18±0.05 | 8.70±0.15 | 8.85±0.15 | 8.77±0.36 | 0.18 | 0.98 |
| J153727+231826 | 9.87±0.13 | 9.70±0.26 | 9.47±0.25 | 8.97±0.26 | 9.45±0.26 | 9.00±0.55 | 0.14 | 1.31 |
| J153925+160400 | 8.92±0.11 | 9.21±0.14 | 9.38±0.11 | 9.09±0.14 | 9.11±0.14 | 8.85±0.47 | 0.27 | 0.63 |
| J154459+040746 | 9.58±0.11 | 8.68±0.10 | 9.24±0.04 | 9.11±0.10 | 8.93±0.11 | 8.79±0.36 | 0.16 | 1.05 |
| J160016+183830 | 9.33±0.14 | 9.28±0.05 | 9.28±0.03 | 9.31±0.05 | 9.43±0.07 | 8.94±0.46 | 0.25 | 0.71 |
| J160154+135710 | 9.55±0.10 | 9.01±0.05 | 9.27±0.03 | 9.08±0.05 | 9.50±0.08 | 8.87±0.35 | 0.22 | 0.77 |
| J160212+241010 | 9.56±0.11 | 9.15±0.05 | 9.43±0.03 | 9.13±0.05 | 9.35±0.06 | 8.92±0.44 | 0.25 | 0.77 |
| J230011−102144 | 9.38±0.10 | 9.58±0.12 | 9.60±0.08 | 9.15±0.12 | 9.45±0.12 | 9.12±0.43 | 0.25 | 0.68 |
| J231607+010012 | 9.35±0.10 | 9.80±0.07 | 9.72±0.10 | 9.54±0.07 | 9.31±0.07 | 9.16±0.52 | 0.42 | 0.47 |
| Non-CARLA quasars having $M_{BH}$(C IV) $> 10^{10}$ $M_\odot$ | | | | | | | | |
| J005814+011530 | 9.36±0.10 | 10.06±0.05 | 9.84±0.08 | 9.42±0.05 | 9.49±0.06 | 9.30±0.54 | 0.63 | 0.30 |
| J081014+204021 | 9.54±0.10 | 10.21±0.09 | 9.95±0.06 | 9.68±0.09 | 9.62±0.09 | 9.40±0.56 | 0.62 | 0.31 |
| J115301+215117 | 10.01±0.11 | 10.13±0.03 | 10.10±0.04 | 9.75±0.02 | 9.68±0.04 | 9.45±0.56 | 0.28 | 0.71 |
| J130331+162146 | 9.41±0.11 | 10.07±0.04 | 9.89±0.06 | 9.61±0.04 | 9.42±0.05 | 9.29±0.55 | 0.35 | 0.50 |
| J210831−063022 | 9.70±0.10 | 10.35±0.04 | 9.99±0.05 | 9.62±0.04 | 9.46±0.06 | 9.41±0.41 | 0.39 | 0.47 |

### 4.4.4 Black holes and radio power

Early studies on nearby quasars have shown that radio-loud quasars harbor SMBHs that lie on the high end of the mass function ($M_{BH} > 10^8 M_\odot$) (Laor et al. 2000), up to three orders of magnitude higher than radio-quiet quasars (Mclure et al. 2001). This correlation between radio-loudness and black hole mass suggests that the properties of the SMBH play some role in the formation of the jet (Gu et al. 2001, Lacy et al. 2001). Our sample is characterized by powerful radio-loud quasars ($P_{500MHz} > 27.5$ W Hz$^{-1}$) and extremely massive black holes ($M_{BH} > 10^9 M_\odot$). In this section we investigate if the radio activity is related with any of the other properties of the sample derived in the previous sections.

We plot in Figure 4.13 the radio power versus the FWHM(H$\alpha$), $L_{5100}$, $L/L_{Edd}$, $M_{BH}$, and $t_{grow}$ in panels (a)–(e), respectively. We do not find significant evidence that any of these properties depend on $P_{500MHz}$, although we note that our sample spans only about one order of magnitude in radio power, optical luminosity and black hole mass. The weak (or absent) correlation between the $M_{BH}$ and $P_{500MHz}$ appears to be in contrast with Xiong et al. (2013), who found a strong correlation between the $M_{BH}$ and radio luminosity at 5 GHz for 97 local RLQs. Their sample consisted of quasars having lower radio luminosities but equally massive BHs compared to the CARLA sample studied here. We do not confirm this trend among our sample of high radio power quasars at $z \sim 2$.

Besides the existence of a minimum threshold $M_{BH}$ above which radio emission can be triggered (Laor et al. 2000, Magliocchetti et al. 2004, Sabater et al. 2018), the lack of correlation between $P_{500MHz}$ and $M_{BH}$ shows that once the radio activity is triggered the $M_{BH}$ does not control the radio output. Because both $L/L_{Edd}$ and $t_{grow}$ are estimated from the properties of quasars that have already experienced significant evolution, it is perhaps not surprising that these properties do not correlate with the current radio power. However, the fact that the optical luminosity and accretion rate do not correlate with radio power, suggests that radio power is also not a good proxy for the strength of possible feedback effects associated with the radio jets in these quasars.

As shown in panel (f) of Figure 4.13, we do, however, find an interesting trend for the C IV blueshift in the sense that the highest C IV blueshifts are exclusively found for the lowest radio power sources.

## 4.5 Discussion

### 4.5.1 Black hole mass determinations based on C IV and H$\alpha$

Among the methods used to estimate the $M_{BH}$ of quasars from SE spectra, the most reliable are those based on the Balmer lines for at least three reasons: (i) most RM studies were done using the continuum luminosity at 5100 Å and H$\beta$; (ii) the Balmer lines are 'well behaved' lines, showing highly symmetrical profiles; (iii) the Balmer lines are located in a spectral region of low

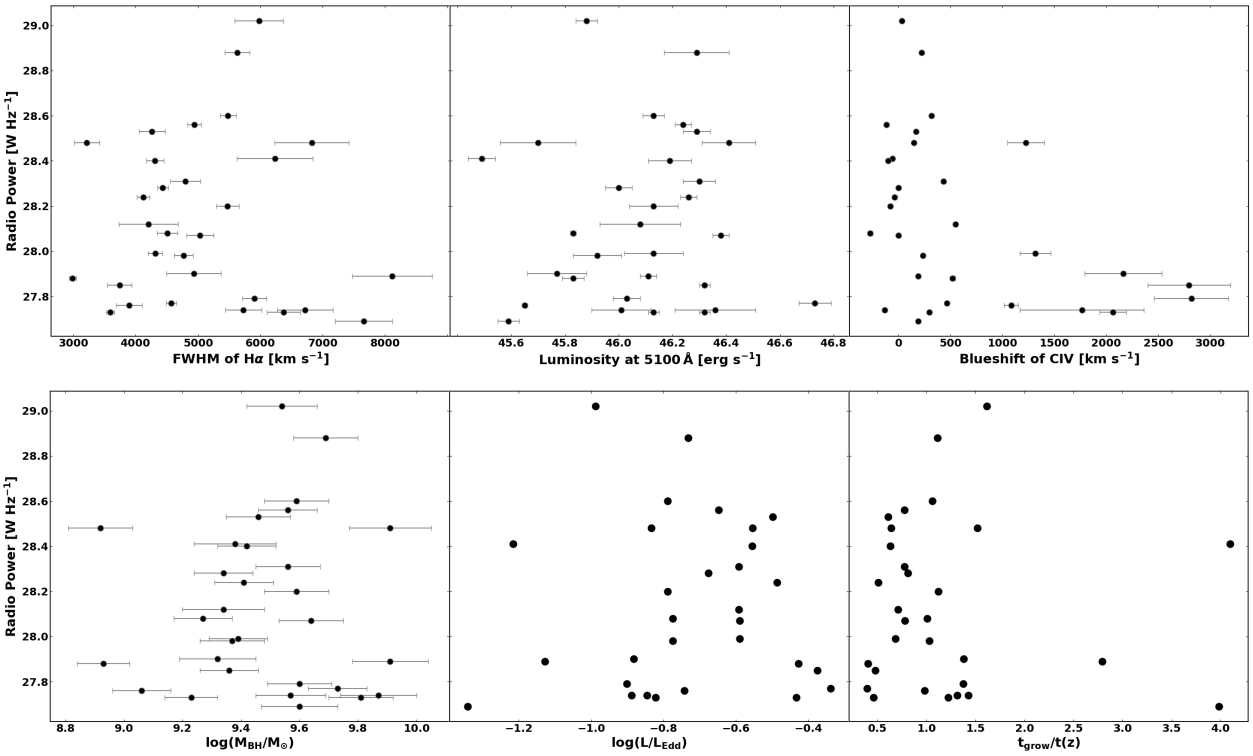


FIGURE 4.13. Radio power versus other quasar properties derived in this work. Panels show $P_{500MHz}$ versus FWHM of H$\alpha$ (a), optical luminosity (b), $M_{BH}$ (c), $L/L_{Edd}$ (d), $t_{grow}$ (e), and C IV blueshift (f).

contamination. In section 4.1 we used *K*-band spectroscopy of CARLA quasars to estimate $M_{BH}$ using the H$\alpha$ line, thereby obtaining new estimates that should be significantly more reliable than the previous ones that were based on C IV. We found that the black hole masses obtained using H$\alpha$ are significantly different from those based on C IV. One important check that needs to be performed on H$\alpha$-based masses is to make sure they are not affected by double peaked emission lines. Jun et al. (2017) warn that lines with a FWHM in excess of 8000 km s$^{-1}$ could be indicative of double-peaked lines which could bias the $M_{BH}$ estimates. Their analysis of 26 SDSS quasars at $0.7 < z < 2.5$ with extremely high BH masses ($M_{BH} > 10^{9.5} M_\odot$) showed that in 7 quasars a double peak was present (5 of which had FWHM> 8000 km s$^{-1}$). In our sample 4 out of 35 quasars have FHWM(H$\alpha$)> 8000 km s$^{-1}$, but we do not find any evidence for double peaks based on the high level of symmetry of the lines.

The results obtained with H$\alpha$ have some contrast with the ones obtained using C IV. The asymmetric shape of C IV is one of the main factors causing the problems in the C IV-based methods. A possible non-reverberating component of C IV would imply that not all of the flux observed comes from a region that is virialized. Denney et al. (2012) show that this component is

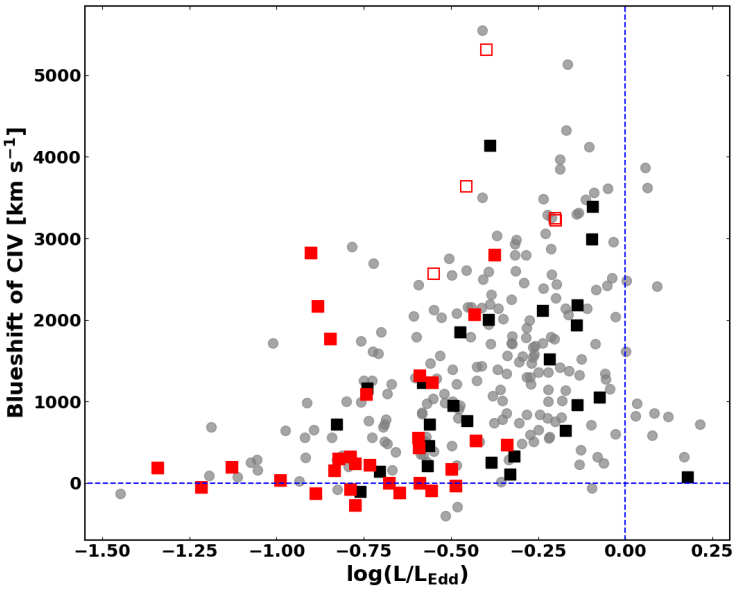


FIGURE 4.14. Blueshift of C IV as a function of the Eddington ratio. Red filled and empty squares, respectively, show the CARLA and non-CARLA quasars observed in this work. Black squares (grey dots) show the radio-loud (radio-quiet) quasars from Coatman et al. (2017). Vertical and horizontal blue dashed lines indicate the Eddington limit and a zero blueshift of C IV, respectively.

often present, and their correction is based on the correlation between the non-variable component of the line and the C IV shape profile. The non-reverberating component of C IV is also associated with outflows and winds originating from the very central region of the AGN (Bachev et al. 2004, Baskin & Laor 2005). Coatman et al. (2016) found for a small sample of quasars that the large blueshift of C IV is present in sources accreting around the Eddington limit. We therefore plot in Figure 4.14 the blueshift of C IV as a function of the Eddington ratio. There is a weak correlation ($S_c = 0.40$ with $p - V = 0.002$) between these quantities, showing that the non-variable component of C IV may indeed be associated with feedback from the AGN. We note, however, that the correlation observed between the accretion rate and the blueshift is a necessary but not sufficient condition for the presence of quasar outflows. Further discussion of this topic is outside the scope of this work.

Among the various methods for C IV rehabilitation that we tested in Section 4.1, the Denney et al. (2012) method better reproduced the BH masses estimated from H$\alpha$ for our sample. The Coatman et al. (2017) method also provides a good approximation, but, as pointed out by Park et al. (2017) (see their Figure 11), the Coatman et al. (2017) method overestimates $M_{BH}$ (which can predict $M_{BH}$ as large as $10^{12} M_\odot$) when the C IV blueshift is negative. A sample covering a broad range of negative blueshifts would be necessary for a complete rehabilitation of this line in this regime. Coatman et al. (2017) warn about this extrapolation of the estimates in the negative

blueshift regime, since their sample does not cover a large dynamic range. However, we still prefer these two methods over the Runnoe et al. (2013) correction method, because the $S/N$ of the peak at 1400 Å is usually low in faint high-redshift sources and negative C IV blueshifts are furthermore rare.

Other factors may contribute to the scatter between the C IV and Balmer methods such as differences in the mass scale relationships for each line (McGill et al. 2008). Another common source of error is contamination of H$\beta$. Most studies focus on the problems with C IV since H$\beta$ has been studied in detail in RM studies. However, this line has its own problems such as a strong narrow line component (although not important in our sample), host galaxy contamination, and a strong underlying Fe II pseudo-continuum (Bentz et al. 2009, Park et al. 2012). These problems are worse in low $S/N$ spectra (Assef et al. 2011).

### 4.5.2 The growth history of CARLA quasars

In this work we obtained robust black holes masses for 35 quasars at $z \sim 2$, finding masses ranging from $\sim 10^9$ M$_\odot$ to $\sim 10^{10}$ M$_\odot$. The results in Sections 4.2 and 4.3 show that these quasars are actively accreting, and have likely been growing for billions of years. We have also shown that at fixed accretion rates, the growth times for radio-loud quasars tend to be longer than those of radio-quiet quasars, but this is mainly a consequence of the fact that the black hole masses of the radio-loud quasars are higher. In this section we will explore a few simple evolutionary scenarios that may approximate the growth history of the CARLA quasars (Figure 4.15).

The first scenario we will explore is that the CARLA quasars have always accreted at their L/L$_{\rm Edd}$ measured at $z \sim 2-3$. This is indicated by the dashed tracks in Figure 4.15. These tracks are much too shallow, requiring the existence of seeds that are likely much too massive ($\gtrsim 10^7$ M$_\odot$) too early ($z \gtrsim 45$). This is a consequence of the long growth times we found for a significant fraction of the CARLA quasars. These growth times are often longer than the age of the universe (much longer in some cases). It is worth pointing out that this discrepancy is exacerbated by the fact that the values estimated here are actually a lower limit for the growth time. For example, an $f_{active}$ smaller than unity, a lower seed mass or a lower accretion rate would result in even longer growth times. Similar results were found by Netzer et al. (2007) for a significant fraction of quasars at $z = 2.3-3.4$.

The second, extreme scenario we consider is that the CARLA quasars grew at or near the Eddington limit for most of their lifetime (red solid track). This scenario easily reproduces the observed masses from relatively small seeds ($\sim 1000$ M$_\odot$) at relatively late times ($z \lesssim 6$), but probably is also not very realistic given the much lower values of L/L$_{\rm Edd}$ measured. Dietrich et al. (2009) analyzed a small sample of 9 quasars at $z = 1.1-2.2$. They studied the case of evolution for BHs with seed masses of 10, $10^3$, and $10^5$ with an L/L$_{\rm Edd}$=1 during the entire active phase of the quasar, and found that in this case, the growth time ranges 0.1–1 Gyr, much less than the cosmic age at $z \simeq 1-2$. Despite these growth times being smaller than the age of the universe,

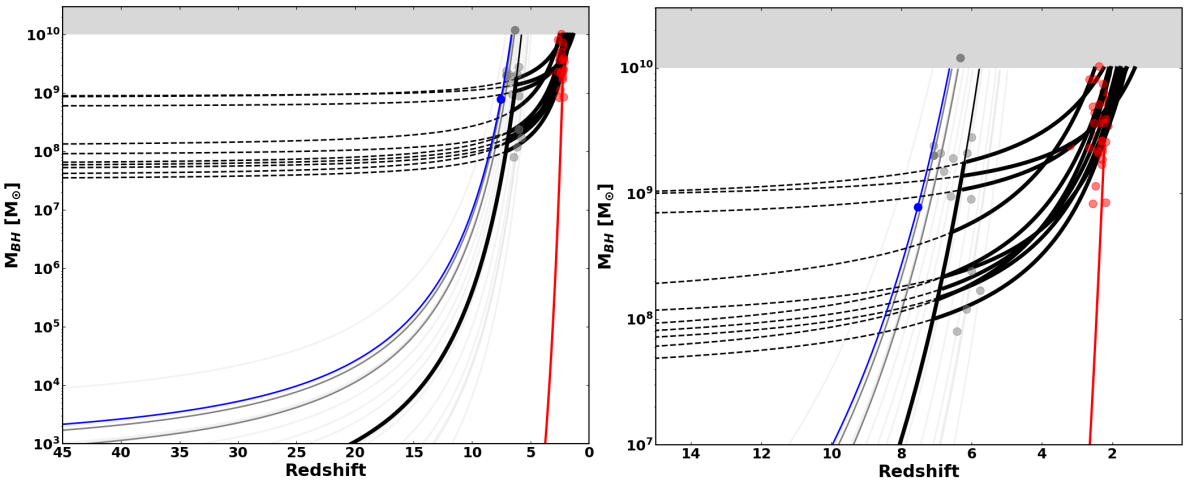


FIGURE 4.15. Black hole masses and possible evolutionary tracks for high redshift quasars in the $z = 0-45$ (left-hand panel) and the $z = 0-15$ redshift range (right-hand panel). Red filled circles at $z \simeq 2-3$ show the CARLA quasars from this paper. The blue circle shows the quasar at $z = 7.56$ from Banãdos et al. (2018), and the grey circles a sample of quasars at $z = 6-7$. Lines trace the possible growth histories of these SMBHs. The blue line shows the Eddington-limited growth of a 1000 $M_\odot$ seed at $z \gtrsim 45$ that is consistent with the $z = 7.56$ quasar (blue circle) from Banãdos et al. (2018), while the grey lines show the same tracks for $z \sim 6-7$ quasars (grey circles). Black dashed lines trace the masses of CARLA quasars back in time assuming they always grew at their observed Eddington ratios. These tracks require extremely large seed masses at high redshifts that are likely not physical (i.e., $> 10^7$ $M_\odot$ at $z \sim 45$). The solid black lines assume Eddington-limited growth that can produce the population of $\gtrsim 10^8$ $M_\odot$ BHs observed at $z \simeq 6-7$ (grey circles). Extending these curves to $z \sim 2-3$ at the Eddington ratios measured for the CARLA quasars (red circles) can reproduce their measured black hole masses (red circles). The red line shows a track of Eddington-limited growth starting from a $\sim 1000$ $M_\odot$ seed at $z < 5$, which can also reproduce the black hole masses of the CARLA quasars. The grey shaded region marks masses above the empirical limit of $\sim 10^{10}$ $M_\odot$.

they are still higher than the typically assumed quasar active phase of $\sim 10^{7-8}$ yr (Martini et al. 2003). However, when the values of $L/L_{Edd}$ used were set to those measured for their sample, these growth times increased by one order of magnitude.

The last scenario we consider here is that the CARLA quasars are direct descendants of the objects hosting the most distant SMBHs known at $z \simeq 6-8$ (e.g. Banãdos et al. 2019, Wu et al. 2015, Mortlock et al. 2011) analysed the possible formation history of a quasar at $z = 7.56$ with a SMBH of $\sim 8 \times 10^8$ $M_\odot$(blue circle). They presented an evolutionary track for a seed mass of 1000 $M_\odot$ at $z = 40$ growing at the Eddington limit with an efficiency of 10%. In Figure 4.15 we show

this evolutionary track (blue line). Similarly, we indicate Eddington-limited tracks (grey lines) for other quasars at $z \sim 6-7$ (grey circles). If we want to force a scenario in which the lower redshift SMBHs in CARLA quasars are the direct descendants of those in the higher redshift quasars, the latter must either drastically reduce their accretion rates after $z \sim 6$ (assuming a constant efficiency, $\eta$) or grow more intermittently by decreasing their duty cycle (Trakhtenbrot et al. 2012). Interestingly, we can easily unite the two populations by assuming that the SMBHs first grow at or near the Eddington limit reaching about 10% of their observed masses by $z \simeq 6-8$, followed by a phase of slower accretion given by the actual Eddington ratios measured for the CARLA quasars at $z \sim 2-3$ (thick black curves in Figure 4.15). Such a fast accretion phase at close or equal to the Eddington limit of BHs at early times, followed by a slower accretion phase at later times is also supported by the results of Marconi et al. (2004), although they proposed such a scenario to explain the black hole masses of quasars at $z \sim 1$ instead of $z \sim 2-3$. Interestingly, following these evolutionary tracks from $z \sim 2$ down to lower redshifts shows that most of our quasars do not pass the empirical $10^{10}$ $M_\odot$ threshold (grey shaded region in Figure 4.15), not even by $z = 0$, especially if we assume that the accretion rate will keep falling with decreasing redshift as the gas supply is exhausted. This scenario is consistent with the idea that the present-day descendants of the CARLA quasars are massive galaxies hosting $\simeq 10^{9-10}$ $M_\odot$ black holes.

The calculations thus far considered assume that the growth of the black hole is through efficient accretion only. However, theoretical studies show that in order to build $M_{BH} \sim 10^9$ $M_\odot$ SMBHs, both black hole mergers and radiatively (in)efficient accretion are necessary ingredients (Volonteri et al. 2007, Volonteri et al. 2008). These models show that a $10^9$ $M_\odot$ SMBH can be built in 100 Myr if the efficient accretion regime starts as soon as the seed reaches 10% of the final desired mass of the $M_{BH}$. In this scenario, mergers could drive the black hole growth up to the 10% seed mass, after which accretion of gas provided during those mergers takes over the growth. Such a scenario could give the range of $M_{BH}$ observed in our sample without requiring extreme accretion scenarios. In terms of the mass growth, this scenario would not be very different quantitatively from the slow-fast accretion scenario considered above (black solid tracks in Figure 4.15). This scenario also agrees with the results of Merloni et al. (2004) and Trakhtenbrot et al. (2012). They show that more massive BHs grow faster at higher redshifts, and that these BHs reach their final masses close to $z \sim 2$. They argue that these BHs are probably the progenitors of relic BHs in the centers of giant elliptical galaxies such as M87 and other brightest cluster galaxies that dominate the massive end of the $M_{BH} - \sigma_*$ relation (McConnell et al. 2011). Moreover, they conclude that $M_{BH} > 10^9$ $M_\odot$ SMBHs probably no longer accrete near the Eddington limit at $z < 2$ (see their Fig. 16), with such periods instead occurring at earlier epochs of $z > 3$.

If the most massive SMBHs are furthermore preferentially located in the most massive halos (see Section 5.3), they may have experienced a relatively high merger rate at early times. These mergers would increase the black hole spin, which would favor both the accretion rate and the

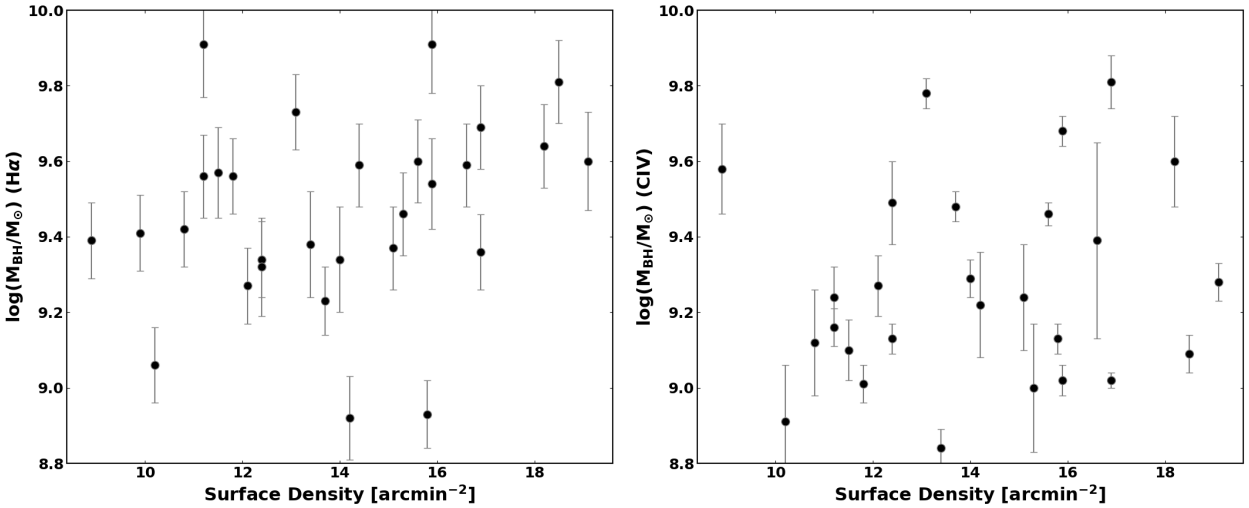


FIGURE 4.16. Galaxy surface density as measured by Wylezalek et al. (2013) versus black hole mass for the CARLA quasars studied in this paper. The left panel shows the H$\alpha$-based $M_{BH}$, while the right panel shows the C IV-based $M_{BH}$ corrected following the Denney et al. (2012) method.

formation of radio jets (Cattaneo et al. 2002, Volonteri et al. 2007). Although the results shown in Figure 4.10 point to a general scenario where the more massive black holes in our sample typically have lower accretion rates than less massive black holes, there is substantial scatter with some of the most massive BHs also having some of the highest accretion rates. These cases could be caused by massive black holes experiencing a secondary fast accretion event, perhaps as the result of a recent major merger in which the gas supply of a quasar or inactive SMBH is momentarily replenished.

### 4.5.3 Does black hole mass correlate with environment?

The main motivation for the CARLA project was to systematically study the environments of radio-loud AGN (radio galaxies and radio-loud quasars) at high redshifts (Galametz et al. 2012, Wylezalek et al. 2013, Hatch et al. 2014). One of the major results from this project was a clear excess in the number of (projected) galaxy counts for CARLA sources compared to carefully constructed control samples of radio-quiet quasars or stellar mass selected galaxies. Hatch et al. (2014) showed a 4$\sigma$ significance effect that radio-loud AGN from CARLA reside in denser environments compared to the control samples. The environmental parameter used in this study is, by necessity, defined as the surface density of color-selected galaxies measured within a few arcminutes (~1 Mpc) away from the target objects. The redshift accuracy of the color-selection is not very high, but by analysing a large sample the effects of fore- and background interlopers is expected to average out. The fact that the environmental measure does not correlate with

any of the radio properties of the sample (radio size, luminosity or spectral index), led Hatch et al. (2014) to the conclusion that it is the triggering of the radio jets that somehow depend on the environment of the host galaxies. It has been suggested that denser environments are conducive to higher merger rates between galaxies and thus of their black holes. This will in turn increase black hole spins that are needed to launch powerful jets. At the same time, the enhanced mergers or gas inflow rates in denser environments lead to higher accretion rates, which boost the luminosity of these active black holes.

The existence of a strong $M_{BH}-\sigma_*$ relation at the present-day demonstrates that at some point in the evolution, black hole masses began to correlate with galaxy bulge masses. Because the most massive SMBHs locally are furthermore often found in the massive central galaxies in galaxy clusters, we also expect an (albeit indirect) correlation between environment and black hole mass. The CARLA project traces some of the most massive SMBHs at high redshift that are found in, on average, high density environments suggestive of (proto)clusters of galaxies (Wylezalek et al. 2013, Overzier 2016). This sample therefore offers a unique chance to investigate at what epochs the correlation between black hole mass and environment may have been established. Hatch et al. (2014) tried to address this question by analysing if radio-loud quasars from CARLA with more massive SMBHs are found in denser environments. Although a weak correlation was found using the $\sim 200$ quasars studied by CARLA (Spearman rank coefficient of 0.16 with $P$-value of 0.02), that study was based on C IV black hole mass measurements. We have shown that C IV-based BH masses are less reliable than those based on H$\alpha$. In order to further investigate whether BH mass correlates with local galaxy density at $z \sim 2-3$, we plot in Figure 4.16 the $M_{BH}$ determined in Section 4.1 against the galaxy surface densities for the 35 CARLA quasars observed as part of this work. Panel (a) shows that there is indeed a weak trend for more massive SMBHs to be found in denser environments with a Spearman rank correlation of $S_c = 0.31$, but it is not significant ($P = 0.10$). When we substitute the H$\alpha$-based masses with their original C IV-based masses used in Hatch et al. (2014), the correlation coefficient is somewhat weaker than before, but again with a high $P$-value ($= 0.21$). This result is shown in panel (b).

Despite the fact that we do not find conclusive evidence for a positive correlation between black hole mass and environment, we have shown that the distribution of black hole masses changes significantly between the C IV- and H$\alpha$-based measurements (Figure 4.7). This shows that this kind of analysis should ideally be extended to the full CARLA sample in order to make a proper assessment of the question whether black hole mass correlates with environment. Although the sample size of H$\alpha$-based black hole masses for CARLA quasars is currently very limited, a possible improvement is to use the C IV-rehabilitation method by Denney et al. (2012) applied to the SDSS spectra. As shown in panel (a) of Fig. 4.8), this offers a substantial improvement over the direct C IV-based measurements (0.27 dex without any systematic offset).

A second, and perhaps larger, complication is that the density parameters estimated from the CARLA data suffer from projection effects and large redshift uncertainties. Besides accurate

black hole masses, improved density measurements should thus also be obtained in order to perform the kind of analysis presented in Hatch et al. (2014) and Figure 4.16 in the most accurate way possible.

## 4.6 Conclusions

We analyzed a sample of 35 high redshift quasars from the CARLA survey. We obtained spectroscopic observations with VLT/SINFONI in the $K$-band in order to estimate their BH masses and study the correlation between black hole mass and other physical properties. We used H$\alpha$ to obtain more accurate BH masses and to estimate accretion rates and black hole growth times. We then studied whether the properties of the quasars correlate with radio power and with the large-scale environmennt. The results are summarized as follows:

1. We used the H$\alpha$ line (redshifted to the $K$-band) to estimate more accurate BH masses for the quasars of the sample. The results show a large scatter (0.43 dex) between the masses obtained using H$\alpha$ and previously available C IV-based masses from SDSS spectra.

2. Using various recent methods proposed for rehabilitating measurements based on C IV, we analyze which best reproduce the BH masses obtained based on H$\alpha$. We found that the methods of Denney et al. (2012) and Coatman et al. (2017) reduce significantly the scatter between the $M_{BH}$ determinations (to 0.27 dex), while the methods of Park et al. (2017) and Runnoe et al. (2013) do not reproduce the $M_{BH}$(H$\alpha$) very well, resulting in a systematic offset and a larger scatter.

3. We calculate the $L/L_{Edd}$ for our sample and find a range of 0.04-0.64. We compare $L/L_{Edd}$ with the FWHM of H$\alpha$, $L_{5100}$, and $M_{BH}$. We obtained a strong correlation between $L/L_{Edd}$ and the first two, and only a moderate correlation with $M_{BH}$. The large scatter observed between $L/L_{Edd}$ and $M_{BH}$ is probably the result of the scatters in both $L_{5100}$ and FWHM propagated into the $M_{BH}$ estimate.

4. we compared the radio power of our quasars with all measured quantities $M_{BH}$, FHWM(H$\alpha$), $L_{5100}$, $L/L_{Edd}$, $t_{grow}$, and C IV blueshift. Our results show only very weak (or no) correlations between $P_{500MHz}$ and these quantities, except for the C IV blueshift.

5. Considering a typical scenario of exponential growth of a seed black hole mass accreting at the $L/L_{Edd}$ and an assumed efficiency and duty cycle, we estimate the black hole growth times for our sample. Although the median growth time of the sample is lower than the age of the universe at the redshifts of the quasars, almost half of the objects have growth times above one. We explore various simple evolutionary tracks for the black hole growth history of CARLA black holes, finding that a scenario in which the BH first accretes at or near the Eddington limit until $z \sim 6-8$ and then switches to a slower accretion rate given by the

$L/L_{Edd}$ measured at $z \sim 2-3$ perhaps best explains the observations. In this scenario, the CARLA quasars could be direct descendants of the SMBHs observed in quasars at $z \sim 6-8$. The scenario is also consistent with the empirical limit of $\sim 10^{10}$ $M_{\odot}$, even if the CARLA quasars were to continue to accrete at their measured rates, and predicts that CARLA SMBHs will be found near the upper end of the local $M_{BH} - \sigma_*$ relation.

6. In order to shed new light on the origin of the local $M_{BH} - \sigma_*$ relation, we repeated the analysis of Hatch et al. (2014) to study whether black hole masses are correlated with environment already at $z \sim 2-3$. We use the H$\alpha$-based black hole masses and galaxy surface density measurements from the CARLA survey as a proxy for environment. We find a weak correlation at very low significance. In future work, it will be important to extend the sample size of H$\alpha$-based $M_{BH}$, and address the large source of uncertainty related to the environmental measurement.

## 4.7 Additional Figures: Sample Spectra

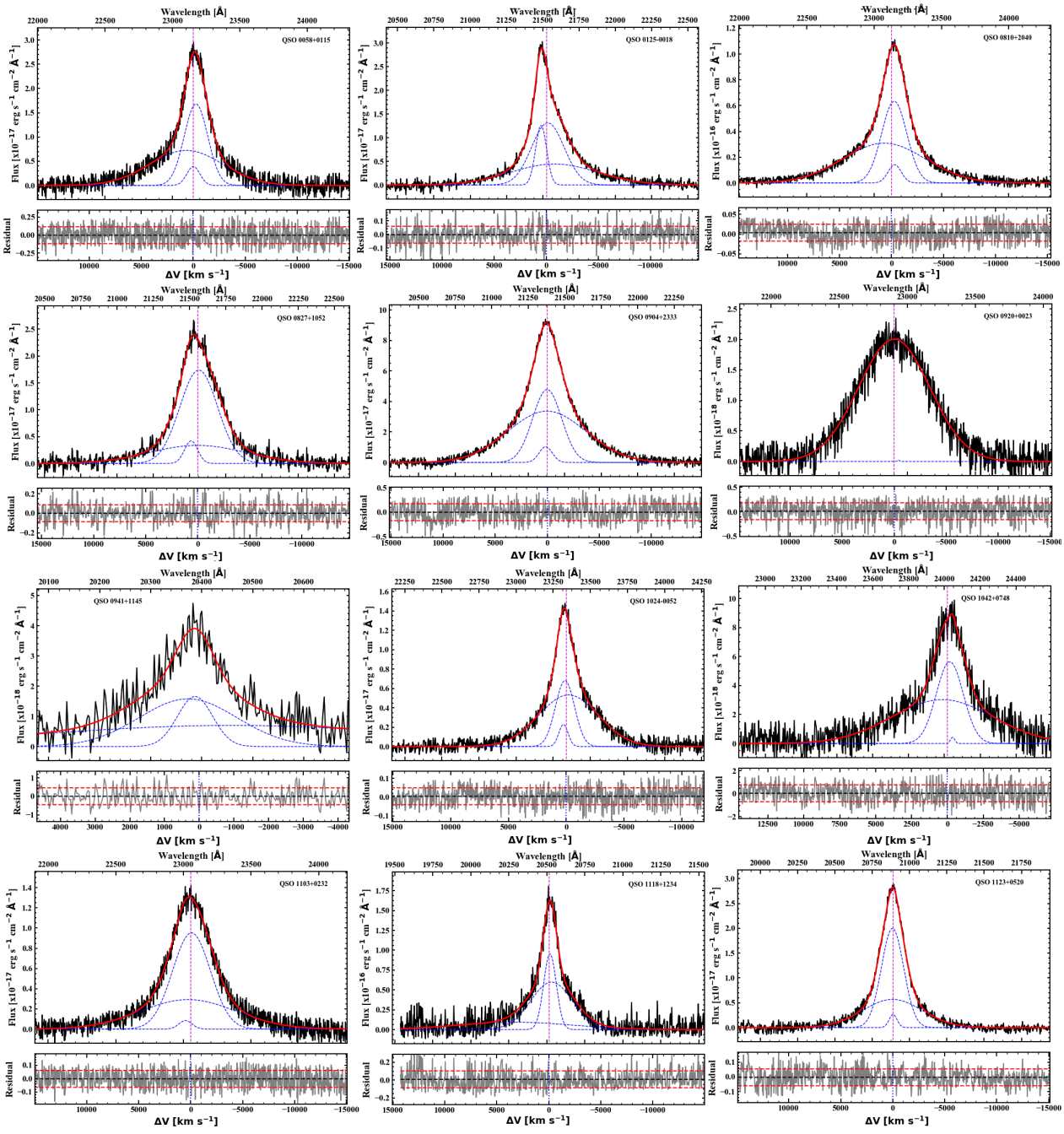


FIGURE 4.17. H$\alpha$ fit for the entire CARLA sample. Top panels show the observed spectrum in black, the best fit components in dashed blue, and the sum of all components in red. Bottom panels show the residual from the subtraction of the best fit from the observed spectrum in grey. The dashed black line shows the zero-level and the dashed red lines the standard deviation. Vertical dashed lines show the center of the line.

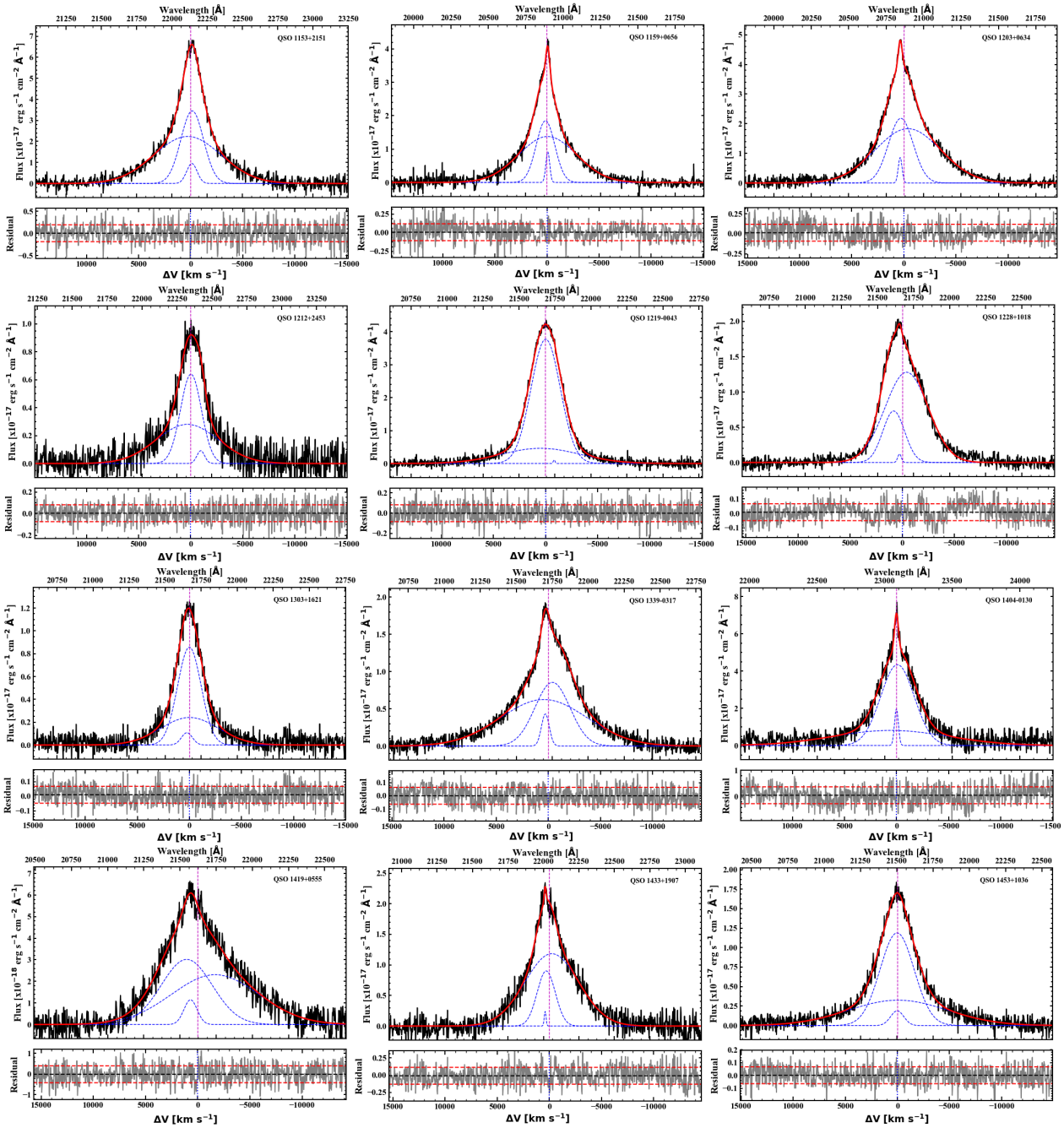


FIGURE 4.18. Continuation of Figure 4.17.

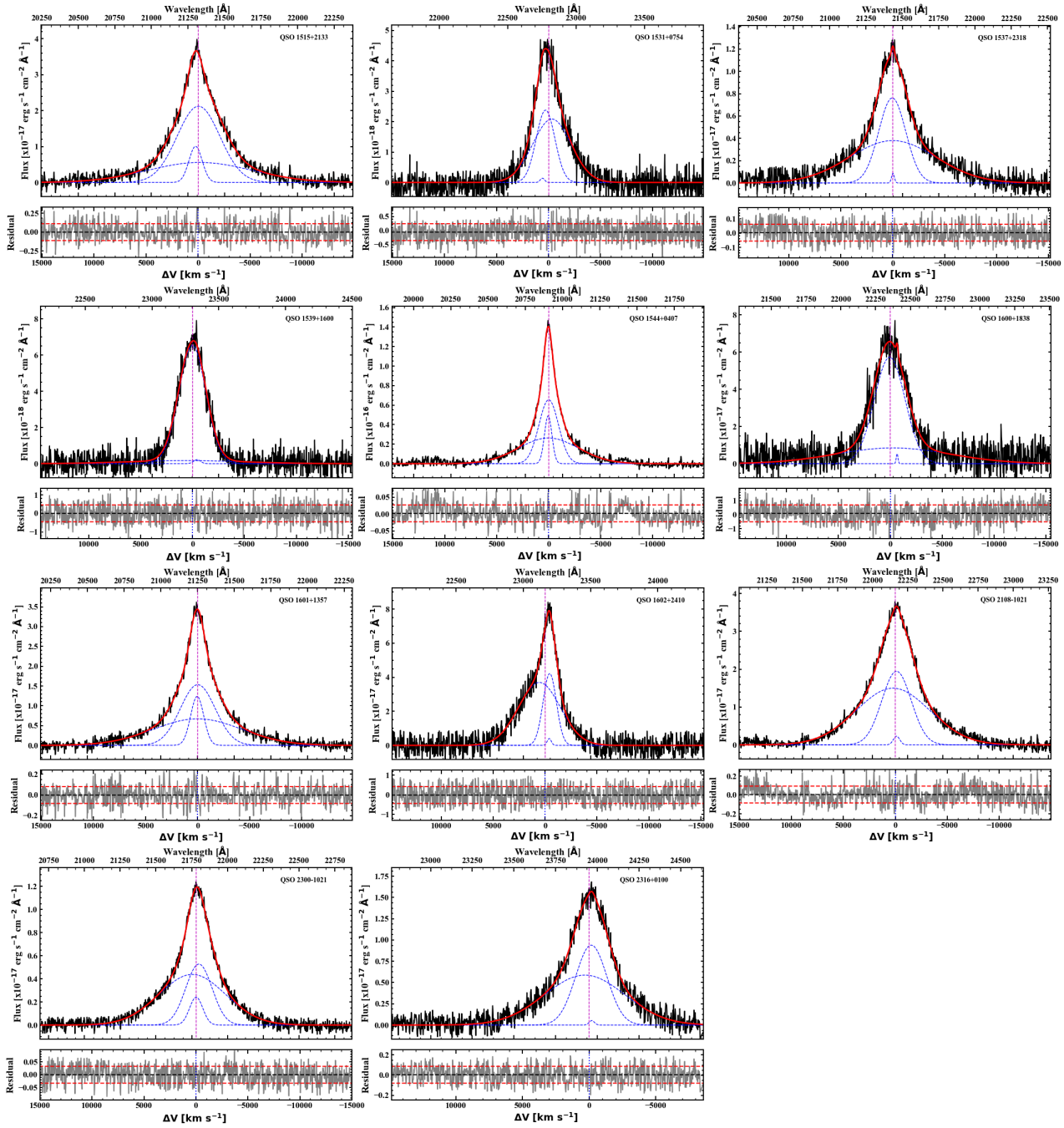


FIGURE 4.19. Continuation of Figure 4.17

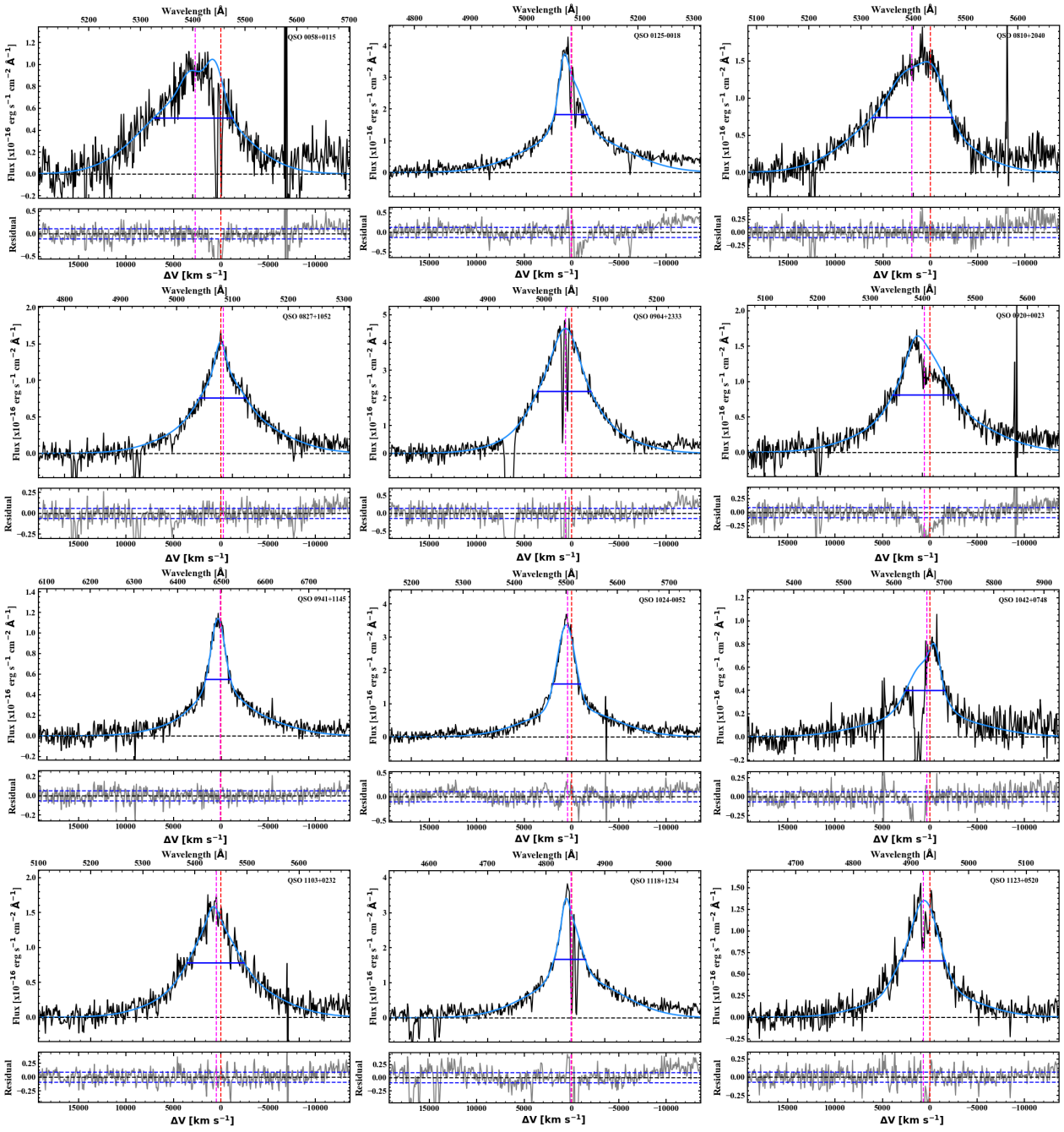


FIGURE 4.20. C IV fit for the entire CARLA sample. Top panels show the observed spectrum in black and the sum of all components in blue. Bottom panels show the residual from the subtraction of the best fit from the observed spectrum in grey. The dashed black line shows the zero-level and the dashed blue lines the standard deviation. Vertical red and magenta dashed lines show the center and centroid of the line, respectively.

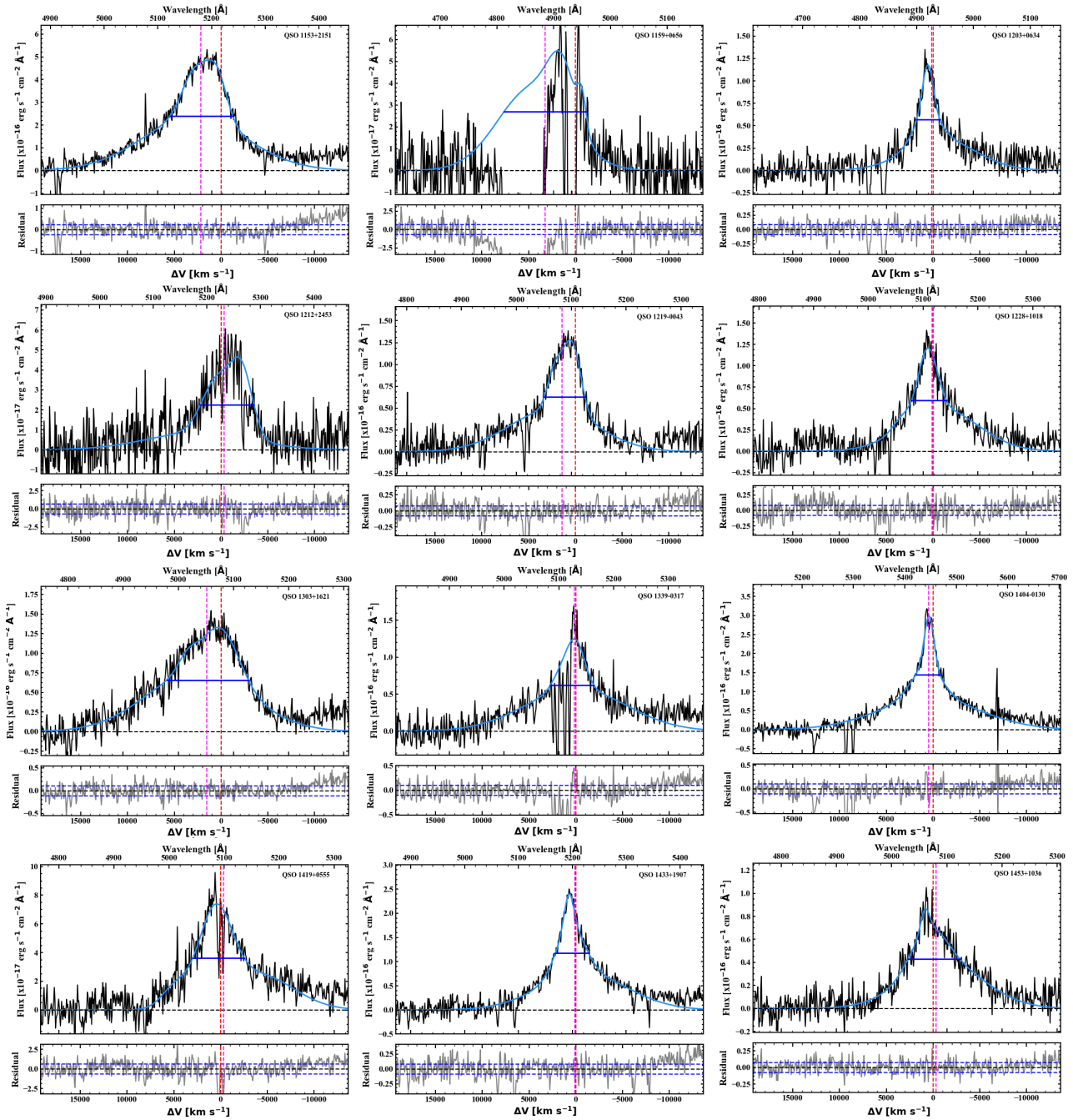


FIGURE 4.21. Continuation of Figure 4.20.

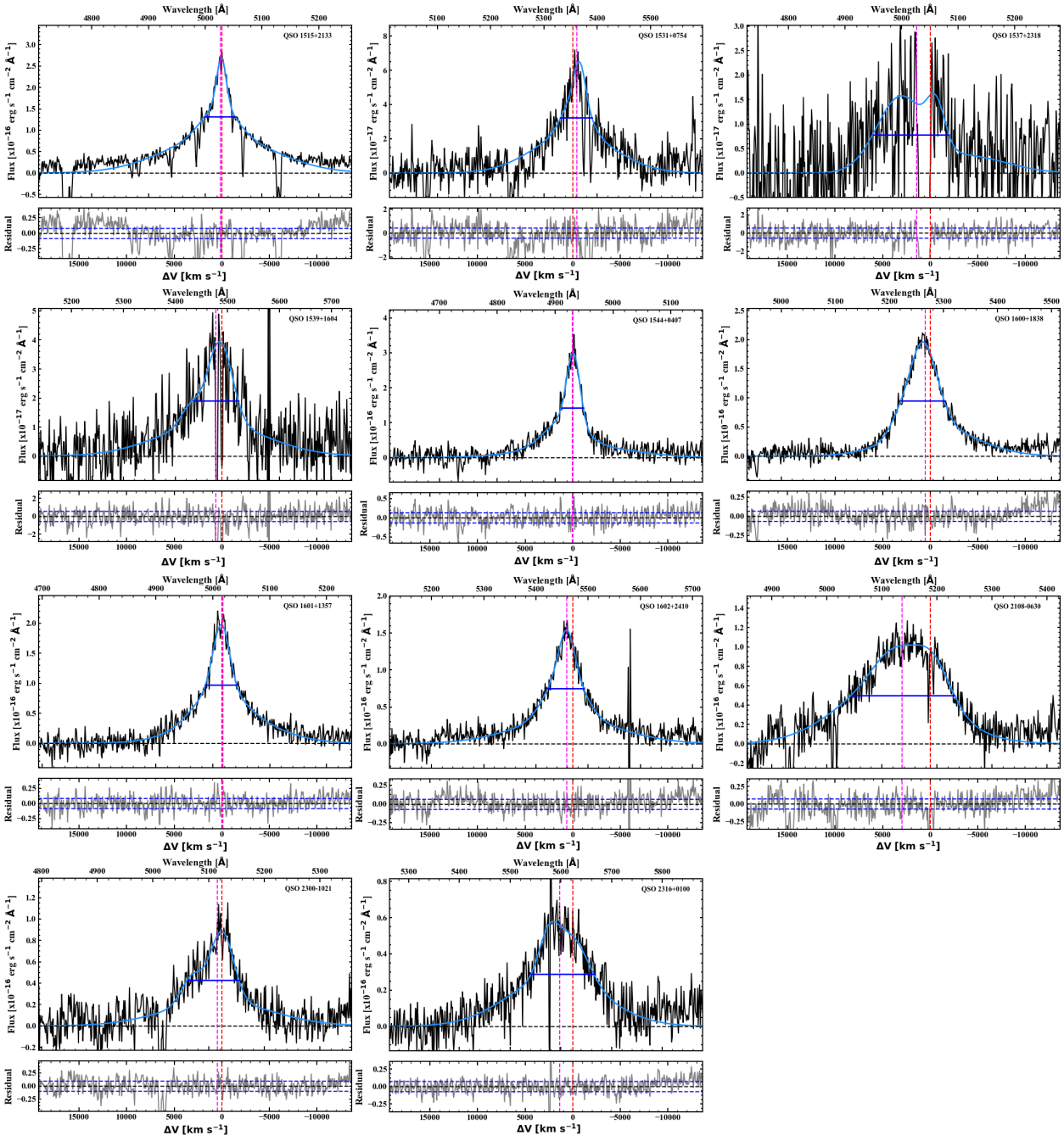


FIGURE 4.22. Continuation of Figure 4.20

CHAPTER 5

# CONCLUSIONS

In this chapter we provide a brief summary of the main conclusions from the three science chapters of this thesis.

In chapter 2 we investigate the physic of the Fe II emission in AGN. We analysed a sample of 25 AGN spectra using NIR cross-dispersed spectroscopy with IRTF/SpeX in order to test suitability of the Garcia-Rissmann et al. (2012) NIR Fe II template in measuring this emission. In the spectra of our sample we identify the 9200 Å bump, the key component predicted in the models of Sigut & Pradhan (1998, 2002). This feature confirms the presence of the Ly$\alpha$-fluorescence as excitation mechanism in the production of the Fe II emission. Using the Fe II template from Garcia-Rissmann et al. (2012) we measured the intensity of the 1$\mu$m lines finding that these lines remain constant from source to source, which suggests a common excitation mechanism for these lines, most likely collisional excitation. Comparing the NIR and optical Fe II emission we found that these two are strongly correlated in the $R_{4570}$, $R_{1\mu m}$, and $R_{9200}$ parameter space, which suggests that Ly$\alpha$-fluorescence plays an important role in the Fe II production. We count the number of Fe II photons in the NIR and optical which allows us to estimate an average contribution of the Ly$\alpha$-fluorescence of 18%. By comparing the line profiles of the Fe II lines with other lines of the BLR we found that they have similar widths as O I, and Ca II. On the other hand they are systematically narrower than Pa$\beta$, with an average of 30%. This result suggests Fe II, O I, and Ca II are produced co-spatially in an outer region of the BLR, white Pa$\beta$ is emitted closer in. Assuming virialized movement of the emitting clouds of the BLR, this means that Fe II is emitted in a region twice far as Pa$\beta$. Using the BLR radius from reverberation campaigns we estimate that the Fe II emitting region is located in a wide range, varying source to source. We found that this value can vary from just a few ($\sim$ 9 in NGC4051) up to a couple hundred of light days ($\sim$200 in Mrk509).

In chapter 3 we report the discovery of the most distant radio galaxy to date, TGSS J1530+1049, at $z = 5.72$. The discovery is a result of GEMINI/GMOS optical spectroscopic follow up observations of a sample selected at 150 MHz from TGGS (Saxena et al. 2018). The long-slit observations revealed one single emission line at 8170Å identified as Ly$\alpha$ after excluding other possibilities. The absence of other emission lines and blue asymmetry of the line supports our results. We took deep $J$ and $K$ band imaging using LBT/LUCI, which led us to no detection of the host galaxy at $3\sigma$. These observations constrain the magnitudes to $K > 22.4$ and $J > 24.4$. Considering these limits the $k-z$-diagram for radio galaxies also suggests redshift $z > 5$. This constraint also ruled out the possibility that the identified line is [O II]$\lambda\lambda$3726,3729, which would place the galaxy at $z = 1.2$. The observed line is best modeled by a skewed Gaussian, again consistent with $z \sim 6$. We measured an integrated flux of $F_{Ly\alpha} = 1.16 \times 10^{-17}$erg s$^{-1}$ cm$^{-2}$, a luminosity of $L_{Ly\alpha} = 5.7 \times 10^{42}$erg s$^{-1}$, an equivalent width of EW<40Å, and a FWHM=370 km s$^{-1}$. These values are consistent with non-radio Ly$\alpha$ emitting galaxies at this redshift. We found that TGSS J1530+1049 has radio properties ($L_{150MHz} = 29.1$ W Hz$^{-1}$) comparable to other radio galaxies at $z > 4$, and its compact radio size (~3.5kpc) suggests a galaxy in the early stages of evolution. We estimate the stellar mass of the galaxy using the $K$-band limit and a maximally old stellar population. We found $M_{stars} <\sim 10^{10.25}$M$_\odot$ for $A_v = 0.15$ mag and $M_{stars} <\sim 10^{10.5}$M$_\odot$ for $A_v = 0.5$ mag, which suggest a relatively young galaxy.

In chapter 4 we present a detailed study of black holes in high redshift radio loud quasars from the CARLA survey. We obtained VLT/SINFONI $K$-band IFU data of 35 quasars in the redshift range $2.2 < z < 3.5$. We used H$\alpha$ to estimate their BH masses and derive the accretion rate and the BH growth times. Our results show that H$\alpha$ gives much more accurate BH masses than C IV, which has a scatter of 0.43 dex compared with H$\alpha$. In order to test recent methods for rehabilitating C IV we analysed which one best reproduced the H$\alpha$-based BH masses. We found that the Denney et al. (2012) and Coatman et al. (2017) methods reduce the scatter between C IV-based and H$\alpha$-based BH masses to 0.27 dex. On the other hand, the Park et al. (2017) and Runnoe et al. (2013) methods lead to significant offsets of the averages masses. The L/L$_{\rm Edd}$ measured ranges 0.04–0.64. By comparing with other quasar features, such M$_{\rm BH}$, L$_{5100}$, and FWHM, we found that the first two are strongly correlated with L/L$_{\rm Edd}$ and the latter is only moderately correlated. These quantities are also correlated with the radio power of the quasars (P$_{\rm 500MHz}$). We found no correlation between P$_{\rm 500MHz}$ and these quantities, except for the C IV blueshift. We consider an exponential growth at a fixed L/L$_{\rm Edd}$ efficiency and duty cycle for BHs in our sample. We found on average that the quasar SMBHs can form within the cosmological age of the universe at their redshift, however around half of the quasars have growth times larger than the universe age. We discuss different scenarios that could explain the high BH masses of these quasars observed. A possible scenario consists of BH seeds growing at the Eddington limit until $z \sim 7$ and then reducing their L/L$_{\rm Edd}$ to the measured L/L$_{\rm Edd}$ at $z \sim 2$. In this scenario the BHs from CARLA quasars would be direct descendents of the SMBHs observed in the quasars at

$z \sim 7$. This scenario is also consistent with the BH mass limit of $10^{10}\,M_{\odot}$ observed in local massive elliptical galaxies. Thereby, even if the CARLA quasars continue to accrete at their measured $L/L_{Edd}$ they would still be consistent with the high end of the local $M-\sigma$ relation. Last, in order to study whether the $M-\sigma$ relation started to form already at $z \sim 2$ we look for a correlation between the environments and the BH masses of the quasars in our sample, finding only a weak correlation. In the future, larger samples with accurate BH masses, host masses and environment measurements will help to address the open questions studied in the chapter.

APPENDIX A

# APPENDIX: PUBLICATION LIST

The work performed during this PhD project has resulted in the following publications:

- THE Fe II EMISSION IN ACTIVE GALACTIC NUCLEI: EXCITATION MECHANISMS AND LOCATION OF THE EMITTING REGION
  **M. Marinello**, A. Rodríguez-Ardila, A. Garcia-Rissmann, T. A. A. Sigut, and A. K. Pradhan
  Astrophysical Journal, 2016, 820, 116 **Presented in Chapter 2**

- LUMINOUS QUASARS DO NOT LIVE IN THE MOST OVERDENSE REGIONS OF GALAXIES AT $z \sim 4$
  H. Uchiyama, J. T. Toshikawa, N. K. Ashikawa, R. Overzier, Y.-K. Chiang, **M. Marinello**, M. T. Anaka, Y. Niino, S. Ishikawa, M. Onoue, K. Ichikawa, M. Akiyama, J. Coupon, Y. Harikane, M. Imanishi, T. Kodama, Y. Komiyama, C.-H. Lee, Y.-T. Lin, S. Miyazaki, T. Nagao, A. J. Nishizawa, Y. Ono, M. Ouchi, S.-Y. Wang
  Publications of the Astronomical Society of Japan, 2018, 70, 32S

- DISCOVERY OF A RADIO GALAXY AT $z = 5.72$
  A. Saxena, **M. Marinello**, R. A. Overzier, P. N. Best, H. J. A. Rottgering, K. J. Duncan, I. Prandoni, L. Pentericci, M. Magliocchetti, D. Paris, F. Cusano, F. Marchi, H. T. Intema and G.K. Miley
  Monthly Notices of Royal Astronomical Society, 2018, 480, 2733 **Presented in Chapter 3**

- A VLT/SINFONI STUDY OF BLACK HOLE GROWTH IN HIGH REDSHIFT RADIO-LOUD QUASARS FROM THE CARLA SURVEY
  **M. Marinello**, R. A. Overzier, H. Röttgering, J. Kurk, C. De Breuck, J. Vernet, D. Wylezalek, K. Duncan, N. Hatch, N. Kashikawa, Y.-T. Lin, R. Nemmen, A. Saxena, D. Stern

Submitted to the Monthly Notices of the Royal Astronomical Society, **Presented in Chapter 4**

- SILVERRUSH. VIII. SPECTROSCOPIC IDENTIFICATIONS OF EARLY LARGE SCALE STRUCTURES WITH PROTOCLUSTERS OVER 200 Mpc at $z \sim 6-7$: STRONG ASSOCIATIONS OF DUSTY STAR-FORMING GALAXIES
  Y. Harikane, M. Ouchi, Y. Ono, S. Fujimoto, D. Donevski, T. Shibuya, A. L. Faisst, T. Goto, B. Hatsukade, N. Kashikawa, K. Kohno, T. Hashimoto, R. Higuchi, A. K. Inoue, Y.-T. Lin, C. L. Martin, R. Overzier, I. Smail, J. Toshikawa, H. Umehata, Y. Ao, S. Chapman, D. Clements, M. Im, Y. Jing, T. Kawaguchi, C.-H. Lee, M. M. Lee, L.-H. Lin, Y. Matsuoka, **M. Marinello**, T. Nagao, M. Onodera, S. Toft, W.-H. Wang
  Submitted to the Astrophysical Journal

- SEARCH FOR FAINT HIGH-REDSHIFT RADIO GALAXIES II: SPECTROSCOPIC AND NEAR-INFRARED OBSERVATIONS
  A. Saxena, H. J. A. Röttgering, P. N. Best, K. J. Duncan, G. J. Hill, B. L. Indahl, **M. Marinello**, R. A. Overzier, L. Pentericci, I. Prandoni
  Submitted to the Monthly Notices of the Royal Astronomical Society

# Bibliography